PSFC/RR-05-5 **DOE/ET-54512-351**

The Motional Stark Effect Diagnostic on Alcator C-Mod

Howard Yung-Hao Yuh

June 2005

Plasma Science and Fusion Center
Massachusetts Institute of Technology
Cambridge MA 02139 USA

This work was supported by the U.S. Department of Energy, Grant No. DE-FC02-99ER54512. Reproduction, translation, publication, use and disposal, in whole or in part, by or for the United States government is permitted.

The Motional Stark Effect Diagnostic on Alcator C-Mod

by

Howard Yung-Hao Yuh

S.B. Materials Science and Engineering (1997)
S.B. Nuclear Engineering (1997)
University of California at Berkeley

Submitted to the Department of Nuclear Science and Engineering
in partial fulfillment of the requirements for the degree of

Doctor of Philosophy in Nuclear Science and Engineering

at the

MASSACHUSETTS INSTITUTE OF TECHNOLOGY

June 2005

Author . . . .
Department of Nuclear Science and Engineering
May 23, 2005

Certified by . . . .
Steven D. Scott
Principal Research Physicist, Princeton Plasma Physics Laboratory
Thesis Supervisor

Read by . . . .
Ian H. Hutchinson
Professor and Head of Nuclear Science and Engineering
Thesis Reader

Accepted by . . . .
Professor J.A. Coderre
Chairman, Department Committee on Graduate Students

The Motional Stark Effect Diagnostic on Alcator C-Mod

by

Howard Yung-Hao Yuh

Submitted to the Department of Nuclear Science and Engineering
on May 23, 2005, in partial fulfillment of the
requirements for the degree of
Doctor of Philosophy in Nuclear Science and Engineering

Abstract

A ten channel **M**otional **S**tark **E**ffect diagnostic has been installed on Alcator C-Mod to measure the plasma internal magnetic pitch angle profile. The C-Mod MSE measures the local electric field direction by measuring the polarization angle of Balmer-α (n=3 → n=2) emission from a radially injected hydrogen **D**iagnostic **N**eutral **B**eam (50 keV, 5 A, 50 ms). The Lorentz electric field ($\mathbf{E_L} = \mathbf{v}_\perp \wedge \mathbf{B}$) and the magnetic field cause the nominally fully degenerate Balmer-α to split into a partially degenerate multiplet whose components are polarized relative to the local fields. Through careful spectral filtering, MSE measures the polarization angle of select multiplet components using a photoelastic modulator based polarimeter.

Investigation of hydrogenic Balmer-α transitions in crossed **E** and **B** fields typical of MSE has led to the discovery of new features of the Stark-Zeeman Balmer-α multiplet. Three different transitions are found for this $\mathbf{E}\wedge\mathbf{B} = (\mathbf{v}_\perp\wedge\mathbf{B})\wedge\mathbf{B}$ configuration. In the regime where the Stark effect dominates over the Zeeman effect, transitions polarize parallel to **E**, **B**, or $\mathbf{v}_\perp$ with ellipticity a function of the beam velocity. More important for MSE diagnostics is the discovery that multiplet lines (summed over degenerate transitions) will be observed to be orthogonally polarized *only for statistical (i.e. equally) upper hybrid state populations.* This contradicts the pure Stark case that is typically assumed for MSE, where Stark-σ lines are *always* observed to be orthogonal to Stark-π lines. Non-statistical upper hybrid states populations are *expected* in certain situations including the propagation of beam neutrals through neutral gas, which is often used to calibrate MSE diagnostics *in situ*.

Implementation of MSE on C-Mod required significant optical and optomechanical engineering. Satisfying MSE viewing geometry requirements for a radial beam on C-Mod resulted in an extended periscope inside the vacuum vessel. A successful design with robust performance against disruption accelerations, fatigue, creep, thermal stresses, and impact while being vacuum compatible has been developed for mounting the necessary polarization preserving optics.

Full Stokes polarimeter modeling and calibration has been performed for the C-Mod MSE. An invessel apparatus has been constructed that is capable of generating pure, linearly polarized light absolutely aligned (to gravity) at arbitrary angles, circularly polarized light, as well as unpolarized light. This device has been used *in situ* to measure the MSE response to all possible Stokes vectors. Results have been compared to a Müeller matrix model of MSE including real geometry and one imperfect mirror with an arbitrary s&p phase shift and s&p reflectivity ratio. Geometric and optical properties of MSE have been deduced by matching measured responses with modeled responses. A method for concurrently measuring the PEM retardances has been developed as part of this effort.

A complementary calibration technique using DNB injection into a gas-filled torus with known fields capable of measuring *in situ* optical Faraday rotation was also performed. Results show possible molecular deuterium contamination arising from the fill gas used in the calibration. MSE polarization measurements displayed discrepancies of over 20° with expected values from a vacuum field reconstruction. Motivated by spectral observations, an inclusion of Zeeman polarized D_2 molecular emission reconciled measured and modeled values of the linear angle and polarization fraction. Observed non-linearities in angular response and the strong viewing geometry dependency are also reproduced in the model when Zeeman polarized D_2 emission is included. Experiments testing this hypothesis are proposed.

Pitch angle measurements in plasmas show that MSE has statistical uncertainties of $\leq 0.4^\circ$ for all but the edge channel up to plasma densities of $\bar{n}_e = 1.5 \times 10^{20}$ m^{-3}. This is insufficient to explain remaining discrepancies with magnetic reconstruction results at the plasma edge. While Faraday rotation and PEM retardance changes could play a role, these instrumental effects are also insufficient. Radial electric fields and beam induced charge exchange emission have been suggested as causes for errors in MSE measurements of plasma.

Thesis Supervisor: Steven D. Scott
Title: Principal Research Physicist, Princeton Plasma Physics Laboratory

Acknowledgments

A heartfelt thanks goes to Dr. Steve Scott who has made it possible for me to complete this work. From pulling me back to see the forest to pointing out individual leaves on the trees, he has patiently and enthusiastically worked with me to get to this point. He has been willing to do everything, from getting his hands dirty with garnet grit in a waterjet cutter to getting his brain dirty with unclear thoughts reading early drafts of this thesis.

I would also like to sincerely thank Prof. Hutchinson for his counseling, advice, and mentoring over the course of my graduate education. His clarity of thought and ability to grasp at the heart of so many scientific issues has been a continuous source of inspiration. Special thanks to Dr. Bob Granetz, who selflessly, patiently, and for some unknown reason eagerly worked inside the tokamak on behalf of MSE. He tirelessly removed broken glass, and put in new glass in what appeared to be an infinite while loop. He also provided his keen experimental know-how with a much appreciated willingness. I wish to thank Dr. Earl Marmar for providing, on several occasions, concise and deeply insightful advice that dramatically changed my course of action; always in the correct direction. I'd like to thank Dr. Steve Wolfe for his spirited assistance on numerous occasions, though with marked frequency immediately before APS conferences. Dr. Martin Greenwald of course showed me the ropes when I was still wet behind the ears and provided sound advice for a beginning graduate student, and for this I thank him. My gratitude to Dr. Miklos Porkolab for his continued interest in and support of my progress towards graduation. I'd like to thank the rest of the "beam" team, Drs. Ron Bravenec, Ned Eisner, Bill Rowan, Norton Bretz, and Matt Sampsell. My sincere thanks to the other scientists, Drs. Jim Irby, Steve Wukitch, Jim Terry, Bruce Lipschultz, John Rice, Ron Parker, Gerd Schilling, Jeff Friedberg, Paul Bonoli, Amanda Hubbard, Catherine Fiore, Brian Labombard, and Joe Snipes.

To the folks who actually make things happen, my sincere thanks goes to Ed Fitzgerald, Rui Vieira, Dexter Beals, Sam Pierson, Bill Parkins, Joe Bosco, Maria

Silveira, Bob Childs, Jason Thomas, and Paul Rivenberg, each of whom has gone out of their way to help me. I am especially indebted to Josh Stillerman and Tom Fredian for answering approximately innumerable questions arising from my frequent obtuseness. Thanks to Henry Bergler and Don Nelson for putting up with my rambunctious computing ways. Having Valerie Censabella on your side is like having the "Easy" button for the lab, and I appreciate her continued help throughout the years. I thank Megan Tabak for her friendship, understanding, and sympathetic ear. I thank Corrinne Fogg for her cheerful disposition, the occasional cookie, and always a warm smile.

To my colleagues, although I use the word loosely since being a graduate student is not a profession, all my best. Each of you have enriched my life, but the following people deserve to see their names. Jerry W. Hughes has been a terrific friend and officemate, and has shown me much appreciated support while simultaneously putting up with all of my peculiarities, incoherent ramblings, and incessant complaining. I have enjoyed my friendships, lively scientific and mostly not-so-scientific discussions with Vincent Tang, Tim Graves, W. Davis Lee, Sanjay Gangadhara, Chris Boswell, Joe DeCiantis, Ishtak Karim, Jennifer Ellsworth, John Liptac, Noah Smick, Kirill Zhurovich, Natalia Krashennikova, Dave Schmittdiel, Rob Nachtrieb, Karyn Green, Loretta Weathers, and Khashayar Shadman. I thank Jinseok Ko for the hard work he's already put into MSE and wish him the best of luck in future work.

I wish to acknowledge my good friends outside of the PSFC, who have been through it all with me. I thank Elva for her amazing unwavering cheerfulness, especially when I'm downtrodden. Mike and Carsten are two great friends that I've had the fortune of finding first as roommates. To Jill, thanks is obviously not enough, I owe you immensely for seeing me through thick and thin, bad and worse, and now a moment previously thought unattainable, the last words written for this thesis.

Finally, to my family, a gratitude that cannot really be expressed. To my mother and father, who have provided me with all my opportunities in life, often through great sacrifices in their own, my deepest thanks. I thank my brother Patrick for his continual moral support through this and all other endeavors in my life.

Contents

1 Introduction **21**

1.1 Fusion Energy 21

1.2 Magnetic confinement 22

1.3 The tokamak magnetic confinement scheme 23

    1.3.1 Major tokamaks around the world 25

    1.3.2 Advanced steady state tokamaks 25

1.4 Internal magnetic topology measurement using the motional Stark effect diagnostic 28

1.5 Introduction to MSE on C-Mod 29

1.6 Thesis goals and outline 31

2 Diagnostic Theory **33**

2.1 Unperturbed, pure Stark, and pure Zeeman conditions 34

    2.1.1 Unperturbed Eigenstates 35

    2.1.2 Pure Electric Fields - Stark Effect 36

    2.1.3 Pure Magnetic Field - Zeeman Effect 40

2.2 Combined $\mathbf{E} \wedge \mathbf{B}$ as encountered in MSE 43

    2.2.1 Hybridization of the n=3 and n=2 states in $\mathbf{E} \wedge \mathbf{B}$ fields . . . 43

    2.2.2 Hα transition classification in $\mathbf{E} \wedge \mathbf{B}$ fields 50

    2.2.3 Hα transition probabilities in $\mathbf{E} \wedge \mathbf{B}$ fields 51

    2.2.4 Polarization pattern of Stark-Zeeman Lines 60

    2.2.5 Comparison of Stark-Zeeman to pure Stark polarization 60

2.3 Excited State Populations 62

2.3.1 Stark-Zeeman polarization in non-statistical populations . . . 62
2.3.2 Beam-into-gas Excited Populations 63
2.3.3 Beam into Plasma Excited Populations 65
2.4 Chapter Summary and Next Steps 66

3 Diagnostic Hardware 67
3.1 Polarization mapped to the C-Mod MSE viewing geometry 68
3.2 Angular Sensitivity and Radial Resolution 71
3.3 Invessel components 76
3.3.1 Optics Configuration 76
3.3.2 Mechanical design of optical mounts 76
3.3.3 Additional Mechanical Improvements 87
3.3.4 Optical Properties of Invessel Components 90
3.3.5 Bench testing of the Verdet constant of MSE optics 91
3.4 Air-side components 92
3.4.1 Air-side relay optics 93
3.4.2 Photoelastic modulators and linear polarizer 93
3.4.3 Image dissector and transfer fibers 95
3.4.4 Interference Filter & Filter tuning 96
3.4.5 CAMAC hardware and control software 98
3.4.6 Photomultipliers 98
3.5 Digital Lockins 99
3.5.1 Analog lockin amplifiers 100
3.5.2 Fast digitization 100
3.5.3 Phase locking reference signal 101
3.5.4 Windowing and Apodization 102
3.5.5 Determination of individual harmonics 104
3.5.6 Hardware background detector 105

4 Diagnostic Modeling and an Absolute Invessel Calibration 109
4.1 A mathematical model of MSE 110

4.1.1 The MSE Stokes vector 110
4.1.2 Müeller matrix representation of MSE optical components . . 111
4.1.3 Intensity calculations for an ideal polarimeter 120
4.1.4 Intensity calculations for the C-Mod polarimeter 123
4.1.5 Measuring the PEM retardances even with imperfect optics . . 125
4.2 Absolute invessel calibration using known Stokes vectors 126
4.2.1 LED light source 127
4.2.2 Generating unpolarized light 127
4.2.3 Generating linearly polarized light 127
4.2.4 Generating circularly polarized light 129
4.2.5 Invessel alignment and calibration procedure 132
4.2.6 Reflection measurements from ICRF antennas 134
4.3 Results from invessel calibration 135
4.3.1 Measured calibration retardances 136
4.3.2 Measured and fitted responses 137
4.3.3 Values of optical properties used in MSE simulation 145
4.3.4 Geometric properties used in MSE simulation 149
4.3.5 Additional optical properties 150
4.3.6 Limitations of the single-mirror model 152
4.3.7 Effect of unpolarized and circularly polarized light 153
4.4 Chapter summary 153

5 Beam-into-gas Calibration **155**
5.1 Spectra Simulation 156
5.1.1 Beam effect on observed spectra 157
5.1.2 Broadening Mechanisms 158
5.1.3 Simulated spectra 160
5.2 Measured spectra 162
5.2.1 Beam-into-gas spectra 164
5.2.2 $\mathbf{D_2}$ molecular lines in beam-into-gas spectra 167

5.2.3 Excited state population for C-Mod beam-in-gas 175
5.3 MSE Beam-into-gas measurements 176
5.3.1 Beam-into-gas run parameters 178
5.3.2 Beam-into-gas measured angles 179
5.3.3 Unexpected polarization fraction 181
5.3.4 Non-statistical upper state populations 183
5.3.5 Instrumental effects 184
5.4 Resolution via molecular $\mathbf{D_2}$ lines 187
5.4.1 Zeeman-σ polarization response 188
5.4.2 Zeeman linear polarization fraction 193
5.5 Chapter conclusions & Next steps 194
5.5.1 Next steps 196

6 Plasma Measurements **199**
6.1 Uncertainty analysis of plasma MSE measurements 200
6.1.1 Sources of uncertainty 200
6.1.2 Plasma Background Subtraction 201
6.1.3 Beam current effect on MSE signal to noise 206
6.1.4 Angular uncertainty 209
6.1.5 Uncertainties vs. density 210
6.2 Comparison with EFIT at the plasma edge 210
6.2.1 Faraday rotation 216
6.2.2 Radial electric field 217
6.2.3 PEM retardances during plasma measurements 220
6.2.4 EFIT discrepancies vs. density and $\mathbf{Z_{eff}}$ 222
6.3 Polarization fraction of beam emission 222
6.4 Observation of edge emission on MSE 229
6.4.1 Correlation with Dα diode data 231
6.5 Chapter Summary & Next Steps 236
6.5.1 Summary 236

6.5.2 Next Steps 238

7 Summary and Future work 241

7.1 Summary 241

7.1.1 Atomic Physics 241

7.1.2 Hardware 242

7.1.3 Calibration & Modeling 243

7.1.4 Beam-into-gas calibration 244

7.1.5 Plasma Measurements 244

7.2 Future Work 245

A Stokes Vectors and Müeller matrix representation for polarization optics 247

A.1 Stokes vector representation of partially polarized light 247

A.1.1 Common Stokes Vectors 249

A.2 Müeller Matrix representation for optical components 250

A.2.1 Polarization Optics 250

A.2.2 Rotation Matrices 251

A.2.3 An Example Optical Train 252

A.2.4 A low retardance waveplate 253

B Current interation of MSE invessel optics 255

Bibliography 265

List of Figures

1-1 A schematic of the tokamak configuration 24

1-2 Scaled renderings of several existing tokamaks operating around the world and ITER 26

1-3 MSE viewing chords, top view 30

1-4 MSE viewing chords, invessel view 31

2-1 Unperturbed hydrogen orbitals 37

2-2 Stark Polarization Pattern 40

2-3 Zeeman Polarization Pattern 42

2-4 Coordinate System 44

2-5 Transition probabilities for the Stark-Zeeman hybrid states in various viewing geometries 53

2-6 Lab Frame angles in tokamak geometry 55

2-7 Relative transition probabilities Stark-Zeeman hybrid states for MSE geometries 57

2-8 Dipole projections of the Stark-Zeeman hybrid transitions 59

3-1 Projected angles of each Stark-Zeeman hybrid polarization directions into the MSE view 70

3-2 F-port horizontal flange layout 72

3-3 Radial Resolution 73

3-4 Angular sensitivity and error magnification of MSE channels 74

3-5 MSE invessel optics canister 77

3-6 Damaged Mirror 1 from early designs 79

3-7 Reinforced Mirror 3 mount, circa 2001 80
3-8 Current MSE lens mount assembly, exploded view 81
3-9 MSE lens retaining ring Teflon gasket 82
3-10 Final assembled MSE lens module 82
3-11 Early mirror mounts, circa. 2000 83
3-12 Bolted Mirror 3 design, circa. 2002 84
3-13 Cracked mirrors, circa. 2003 85
3-14 Rendered drawing of latest MSE Mirror 2 design 86
3-15 Modified MSE split can allowing viewing angle adjustment 88
3-16 Inconel mirror backplates stiffened and designed to minimize eddy currents 89
3-17 MSE external optics diagram 93
3-18 MSE unshifted bandpass filter functions 97
3-19 MSE IDL Widget Control Panel 99
3-20 Fast digitized MSE signals 101
3-21 MSE signal showing a dynamic background 106
3-22 MSE background detector array 107

4-1 Raytracing results for Mirror 2&3 angles of incidence 113
4-2 Diagram defining χ as the 2D rotational angle for the MSE composite mirror 114
4-3 Manufacturers mirror phase shift specification 115
4-4 Ratio of J_3/J_1, the 3$^{\text{rd}}$ order to 1$^{\text{st}}$ order Bessel function of the first kind. 126
4-5 Unpolarized LED light source used for invessel calibration 128
4-6 Construction and measurement of the pure circularly polarized source 130
4-7 Circular source with rotating waveplate 131
4-8 Circular Source used invessel 132
4-9 Diagram of linear invessel calibration 133
4-10 MSE absolute calibration apparatus 134
4-11 MSE linear response curves of A40 and A44 for linearly polarized light 143

4-12 MSE linear response curves of A20 kHz and P_f to linearly polarized light 144
4-13 Ratio of 20 kHz to 40 kHz and 20 kHz to 44 kHz modulation amplitudes 147

5-1 Simulated spectra for a 6.1T shot (1040304027) 161
5-2 McPherson 2051 Instrument function 163
5-3 Measured spectra 165
5-4 Measured spectra 166
5-5 Deuterium molecular lines within the MSE spectral region 167
5-6 Polarization pattern of D_2 lines in high fields 168
5-7 Fitted neutral beam-into-gas specta in zero field 170
5-8 Fitted Zeeman components 171
5-9 Zoomed area blue of Dα showing possible D_2 lines 172
5-10 Polarization of D_2 lines on the blue side of Dα 175
5-11 Fitted MSE π components 177
5-12 MSE filter function overlaid on beam-into-gas spectra 179
5-13 Beam-into-gas calibration measured angles 180
5-14 Beam-into-gas operation polarization fraction, P_f 182
5-15 Beam-into-gas retardances compared with invessel calibration 186
5-16 MSE calibrated repsonses to Stark-π and Zeeman-σ light 189
5-17 Fitted response functions matching beam-into-gas measurements . . . 191
5-18 Beam-into-gas measured angles and expected angles with the addition of Zeeman-σ and unpolarized light 192

6-1 40 and 44 kHz (A40 and A44) amplitudes as a function of time 202
6-2 Estimate of uncertainties in the interpolated plasma background . . . 204
6-3 Beam current degredation over a single beam pulse 208
6-4 Uncertainty sensitivity for MSE channels 209
6-5 MSE uncertainties as a function of plasma density 211
6-6 MSE measured angles compared with EFIT 213
6-7 MSE uncertainties compared to discrepancies with EFIT 214
6-8 Variations in the EFIT/MSE discrepancies 215

6-9 Plasma retardances compared with invessel calibration 219

6-10 PEM retardance ratios vs. EFIT/MSE discrepancies 221

6-11 MSE discrepancies with EFIT vs. plasma density 223

6-12 MSE discrepancies with EFIT vs. plasma Z_{eff} 224

6-13 Average polarization fraction of plasma data set 225

6-14 Calibrated polarization fraction of plasma measurements 226

6-15 Calibrated polarization fraction of plasma measurements 227

6-16 Calibrated polarization fraction of plasma measurements 228

6-17 Calibrated polarization fraction vs. EFIT/MSE discrepancy 230

6-18 Plasma edge fluctuations as observed by the 10 channels of MSE, the Dα diode and the Z-meter 232

6-19 Plasma edge fluctuation brightness as a fraction of the total MSE intensity 233

6-20 Edge emission relative brightness 234

A-1 Change in linear angle through a low retardance waveplate 254

B-1 M2 retainer. An identically shaped piece of 20 mil thick Teflon is used as a gasket under the metal retainer, mechanically trapped by the bolts. 256

B-2 M2 rib. A 20 mil strip of Teflon is placed between the inner wall of the rib and the mirror. 257

B-3 M2 backplate. Constructed of Inconel with broken ribs on the back to increase stiffness but not increase eddy current loops. 258

B-4 M2 gasket shown by thick black lines. Cut from 30 mil Teflon sheet and placed under the mirror. 259

B-5 M3 retainer. An identically shaped piece of 20 mil Teflon is used as a gasket under the metal retainer, mechanically trapped by the bolts. . 260

B-6 M3 rib. A 20 mil strip of Teflon is placed between the inner wall of the rib and the mirror. 261

B-7 M3 Backplate. Constructed of Inconel with broken ribs on the back to increase stiffness but not increase eddy current loops. 262

B-8 M3 gasket shown by thick black lines. Cut from 30 mil Teflon sheet and placed under the mirror. 263

List of Tables

1.1 Major tokamaks machine parameters 27

1.2 MSE viewing radii and angles 32

2.1 Coefficients of linear and quadratic Stark shifts 39

2.2 Stark-Zeeman eigenstates, eignevectors, and transition classification . 54

2.3 Absolute Stark-Zeeman hybrid transition probabilities for C-Mod viewing geometry 56

2.4 Collisional ℓ-mixing cross-sections of $H^* + H_2$ with a relative velocity of 5km s^{-1}. ℓ-mixing mean free path lengths in 1 mTorr gas 64

2.5 Collisional excitation cross sections of $H(1s) + H_2$ at 50keV atomic energy, excitation mean free path at 1 mTorr, mean excited lifetime, and mean distance travelled before radiative de-excitation at 50keV. . . . 64

3.1 History of MSE invessel components design revisions 78

3.2 Summary of apodization errors introduced by using a non-integer number of cycles. The error amplitudes are relative to the amplitude of the signal (A_1 and A_2). Values of the errors themselves oscillate between zero and the listed maximum as a function of the sampling window length with periodicity given in the first column. 103

4.1 Invessel calibration angular fit parameters 136

4.2 Retardance values measured during the invessel calibration 137

4.3 Stokes vectors used to model the MSE invessel calibration response . 139

4.4 Measured and simulated 40.6 kHz responses from the MSE invessel calibration using linearly polarized light 140
4.5 Measured and simulated 44.6 kHz responses from the MSE invessel calibration using linearly polarized light 141
4.6 Measured and simulated 20.3 kHz responses from the MSE invessel calibration using linearly polarized light 141
4.7 Measured and fitted responses from the circular MSE invessel calibration 145
4.8 MSE Mirror Properties and geometric constants 146

5.1 Estimate of excited state population 176
5.2 Estimated mixture of MSE observed light during beam-into-gas . . . 188

6.1 Instrumental standard deviation of MSE 201
6.2 Uncertainty σ values for MSE plasma measurements 212
6.3 Estimate of Faraday rotation in MSE optics based on lab measured Verdet constants 216
6.4 Faraday rotation for MSE channels with error magnification 217
6.5 Radial electric field sensitivity 218

A.1 Table of common Stokes vectors 249
A.2 Müeller matrix representations of common polarization optics 250

Chapter 1

Introduction

1.1 Fusion Energy

Fusion energy is being actively researched around the world as an attractive replacement for current sources of energy, primarily the combustion of fossil fuels. Fusion energy combines many benign features such as:

- Universal availability and virtually inexhaustible fuel in the raw forms of heavy water and lithium
- No emission of greenhouse gases or other combustion polluants such as $\mathrm{SO_x}$ and $\mathrm{NO_x}$
- No long lived or high level radioactive waste
- High energy density traditional power plant model
- Inherent safety due to minimal energy inventory
- Significantly reduced weapons proliferation risks
- Lack of public fear and distrust

One significant downside to fusion is the difficulty of igniting a plasma, where a plasma becomes primarily self heating and releases net energy. Over fifty years of fusion research has made it possible for recent efforts to reach the brink of ignition.

Two major ongoing efforts are now underway to achieve the scientific goal of igniting a plasma such that it produces more energy than is required to assemble and heat the starting fuel. One major approach is the National Ignition Facility, NIF, being constructed at Lawrence Livermore National Lab, and is expected to acheive ignition using high-powered lasers to compress a deuterium-tritium pellet to fusion conditions. Inertial "confinement" exploits the fact that nuclear reactions take place on timescales much shorter than hydrodynamic forces to generate significant fusion energy before the fuel explodes, and is useful for simulating nuclear weaponry. The other major experiment expected to achieve ignition is the International Tokamak Experimental Reactor, ITER, a magnetically confined plasma in the tokamak configuration. ITER, is currently under negotiation by the participating members, the European Union, Japan, U.S., China, South Korea, and Russia.

This work will be focused on the implementation of an instrument that can measure the internal topology of the magnetic field in a tokamak plasma, and begins with an introduction to magnetic confinement and the tokamak configuration.

1.2 Magnetic confinement

Power from the first fusion reactor will very likely come from the deuterium tritium reaction due to its highly favorable fusion cross-section arising from a resonance in the ^{5}He nucleus.

$$\mathrm{D} + \mathrm{T} \rightarrow^{4} \mathrm{He}(3.5\mathrm{MeV}) + \mathrm{n}(14.1\mathrm{MeV}) \tag{1.1}$$

For fusion reactions to occur, nuclei must approach each other to sufficiently close distances, of order femtometers (10^{-15}m) in order for the strong nuclear force to dominate over Coulomb repulsion and fuse. Even when considering quantum mechanical tunnelling at the the tails of a thermal distribution, a plasma will still need to be heated to a thermal temperature of 10–20 keV (116–232 million K) for fusion reactions to occur in useful quantities. Further, the thermal distribution must be confined to conserve the kinetic energy of the particles because the Coulomb scattering cross-section is much larger than the fusion cross-section at all energies. The kinetic energy of the nuclei must not be lost after a small number of Coulomb interactions or else a reactor will not produce net energy. These criterian point to a scheme of confining and heating plasmas to thermonuclear temperatures without contact between the plasma and physical materials. Magnetic confinment fusion uses magnetic fields to fulfill these goals.

A benchmark goal for such a magnetic confinement device is to be capable of confining a plasma at a sufficiently *high density* for a sufficiently *long time* and being able to heat it to a sufficiently *high temperature* for the fusion power output to equal the energy lost. For a plasma to ignite, it must balance energy losses from the plasma with the heat from only the 3.5 MeV α particles which are confined by magnetic fields. Neutrons escape the magnetic field and do not heat the plasma directly. In a reactor, the neutron energy will be captured to produce power.

From [1], this goal can be written as,

$$nT\tau_E > 3 \times 10^{21} \text{ m}^{-3}\,\text{keV}\,\text{s} \tag{1.2}$$

where τ_E, the energy confinement time is defined by the energy loss rate of the plasma, P_{loss}, and the plasma total energy, $W = 3nT$, as $\tau_E = W/P_{loss}$. Plasma density is given by n, and T represents the plasma thermal temperature. This ignition triple product can be easily remembered as the criterion of confining a 10^{20}m^{-3}, 10keV plasma with an energy confinement time of 3 seconds.

The most successful configuration of magnetic fields for plasma confinement to date is the tokamak configuration.

1.3 The tokamak magnetic confinement scheme

Tokamaks can be described as a cylindrical solenoid which has been bent to form a torus, producing a magnetic field inside with field lines forming toroidal loops. A vacuum chamber is constructed within the torus for the plasma, which has particle densities about a million times below standard atmosphere. Charged particles which comprise the plasma cannot move across a magnetic field due to the Lorentz field, and are confined to the toroidal field lines. Equilibrium fields are produced to balance plasma expansion forces by poloidal coils placed around the plasma. A schematic of the tokamak configuration showing the coils just described is shown in Fig. 1-1.

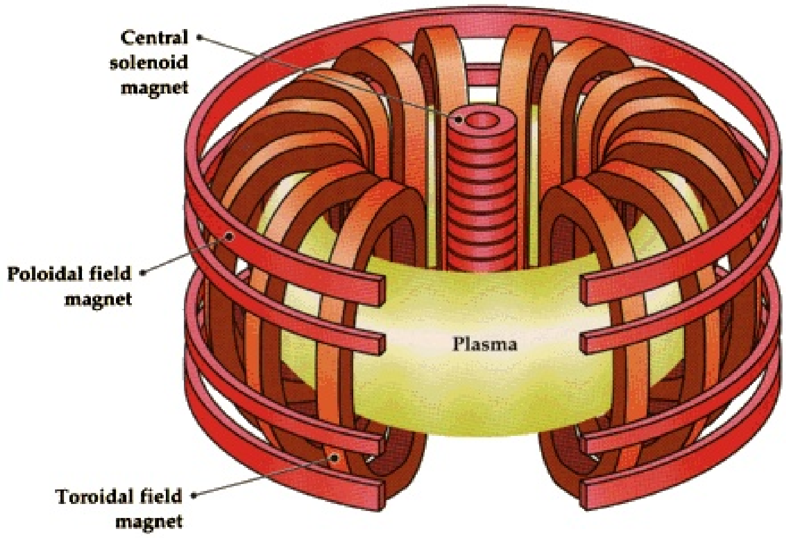

Figure 1-1: A schematic of the tokamak configuration showing the major components. The vacuum vessel is not shown but would enclose the plasma.

Although the vacuum field lines in the tokamak configuration wrap around themselves and have no ends, drifts will still result in single particle losses from vacuum fields. The curvature and major radial gradient of the vacuum toroidal field will cause ions and electrons will drifts vertically in opposite directions,

$$v_R + v_{\nabla B} = \frac{1}{q}(mv_\parallel^2 + \frac{1}{2}mv_\perp^2)\frac{\vec{R}_c \wedge \vec{B}}{R_c^2 B^2} \tag{1.3}$$

where $\vec{R}_c$ is the radius of curvature vector, $\vec{B}$ the magnetic field, $v_\parallel$ the particle velocity along the magnetic field line, and $v_\perp$ the particle velocity perpendicular to the magnetic field line.

For an ensemble of particles, these drifts further result in an electric field created by the charge separation. This vertical electric field will cause the bulk plasma to drift radially outwards resulting in the loss of confinement. To counteract this effect, the plasma must carry a toroidal current to produce a poloidal field (around the short way of the torus). This field adds rotational transform, i.e, makes the magnetic field lines helical. With helical fields, going around both the long way of the torus as well as the short, the vertical drifts now average to zero over a poloidal transit and confinement is acheived for sufficient values of plasma current.

The toroidal current that must flow in the plasma to produce the poloidal confinement field is produced in the standard tokamak by treating the plasma as a secondary in a transformer, inducing a loop voltage by changing the flux through a central solenoid aligned with the torus axis of symmetry. The central solenoid is also shown in Fig. 1-1.

1.3.1 Major tokamaks around the world

There are over a dozen research tokamaks currently operating around the world. A few, including the two largest operating U.S. tokamaks, Alcator C-Mod at MIT (where this work was completed), and DIII-D at General Atomics in San Diego, are shown as scaled cutaway renderings in Fig. 1-2. The proposed ITER design is also shown to scale next to the existing machines. Table 1.1 shows some key parameters of the tokamaks shown in Fig. 1-2.

1.3.2 Advanced steady state tokamaks

The toroidal plasma current in a standard tokamak is driven by the central solenoid via transformer action. However, the current cannot increase in the central solenoid without bound, and so the toroidal plasma current cannot be sustained steady state. From a reactor engineering point of view, a pulsed thermal source is highly undesirable. Therefore, a primary thrust in current tokamak research is the development of current drive mechanisms that can operate in steady state. These efforts include neutral beam current drive, where high energy neutrals are injected tangentially into the plasma to drive current, EM wave current drive, where electromagnetic waves are launched that preferentially heat particles moving on one toroidal direction, and optimizing the plasma pressure profile to maximize a natural plasma current called the bootstrap current.

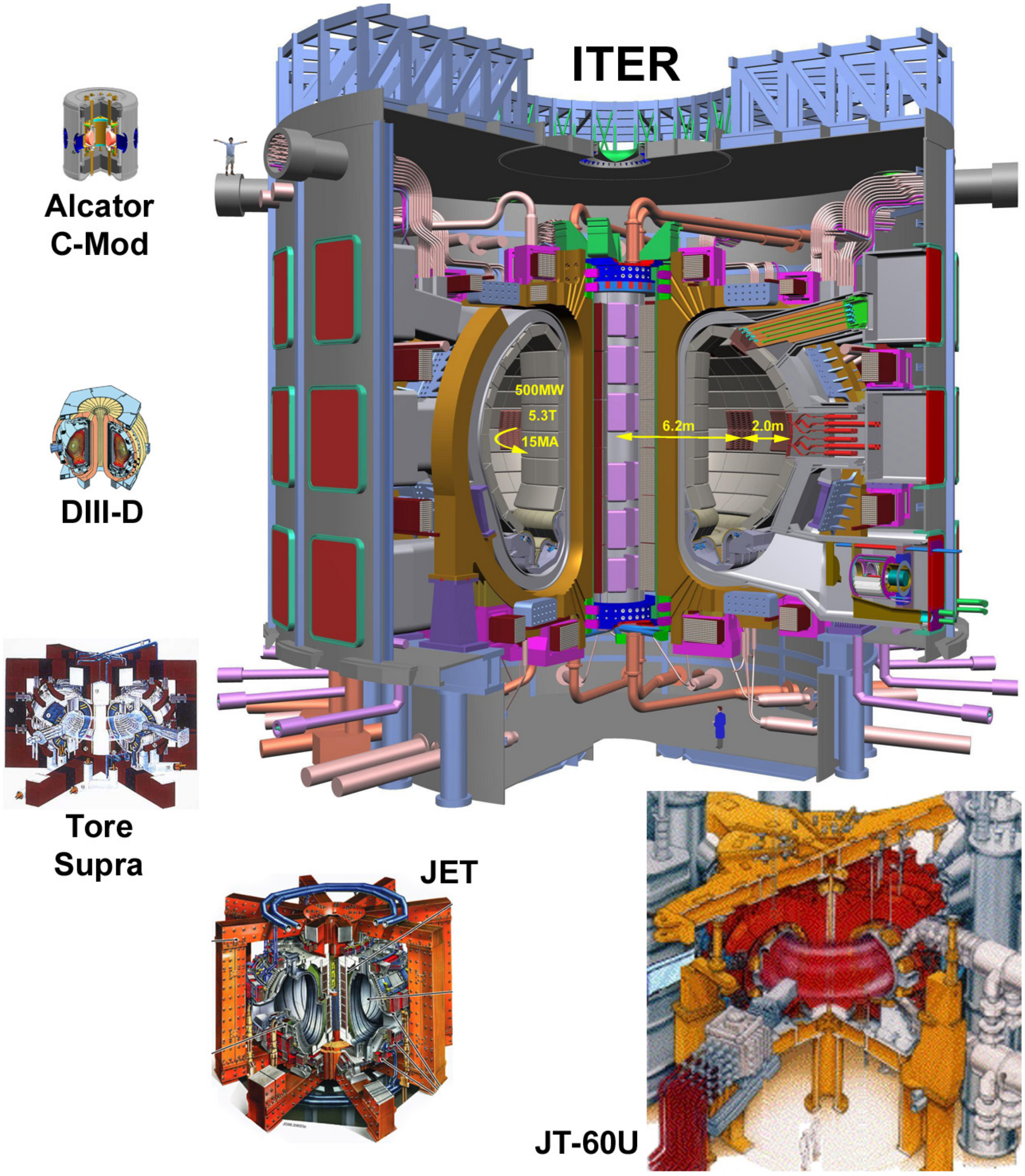

Figure 1-2: Scaled renderings of several existing tokamaks operating around the world and ITER. The two largest operating U.S. tokamaks are Alcator C-Mod at MIT, where this work was done, and DIII-D at General Atomics in San Diego.

	ITER	JT-60U	JET	TFTR	Tore Supra	DIII-D	Alcator C-Mod
Location	???	Japan	U.K.	U.S.A	France	U.S.A	U.S.A.
Major Radius [m]	6.2	3.45	2.96	2.48	2.25	1.67	0.67
Minor Radius [m]	2.0	1.2	1.25	0.85	0.80	0.67	0.21
Elongation, κ	1.7	1.4	1.7	1.0	1.0	2.0	1.8
Toroidal Field [T]	5.3	4.4	3.5	5.2	4.5	2.2	8.1
Featuring	Ignition	Negative Ion Beam 500 keV 10MW	D-T	D-T Shut-down 1997	SC Magnets	Adv. Diag.	High field, High Density

Table 1.1: Major tokamaks machine parameters. The ITER site had not been decided at the time of this work. D-T stands for deuterium-tritium operation, and SC stands for superconducting.

One necessity in advancing knowledge for any of these current drive experiments is to measure the local effect of the applied current driving mechanism on plasma current. To calculate the current distribution across the poloidal cross-section, one can measure the magnetic topology, or $B_{poloidal}$, which is created by the plasma current.

In addition to current drive experiments [2, 3, 4, 5, 6, 7, 8, 9, 10, 11, 12], the magnetic topology is a crucial parameter in a tokamak plasma and is necessary for understanding a variety of phenomena, including plasma transport and transport barriers [13, 14], magnetic island formation [15], MHD stability [16, 17, 18], sawteeth [19, 2, 20, 21], and the measurement and effect of a radial electric field in the plasma [22, 23, 24, 25, 26, 27].

1.4 Internal magnetic topology measurement using the motional Stark effect diagnostic

One successful method used to measure the internal magnetic topology is to measure the magnetic pitch angle profile across the plasma minor radius with the **M**otional **S**tark **E**ffect diagnostic, henceforth referred to as **MSE**.

MSE operates by viewing neutral, excited hydrogen atom decay emission generated by a high energy neutral beam crossing a magnetic field. In the rest frame of the emitting atom, the fields experienced by the particle are the static plus Lorentz electric fields $\mathbf{E_{tot}} = \mathbf{E} + (\mathbf{v} \wedge \mathbf{B})$, and also the magnetic field $\mathbf{B}$. Hydrogen lines such as the Balmer-α line (n=3 → n=2) typically used for MSE, experience energy splittings as well as polarize relative to the external fields. The atomic physics describing the line splitting and polarization is discussed in Chapter 2.

The fundamental idea behind MSE is to exploit the linearly polarized and spectrally separated hydrogen Balmer lines to measure the direction of the local electric field. By injecting high energy neutrals with known velocity $\mathbf{v_{beam}}$ across a magnetic field, one can make a local measurement of the magnetic field line pitch angle,

$$\gamma_{pitch} = \tan^{-1}(\frac{B_\theta}{B_\phi}) \tag{1.4}$$

where B_θ is the poloidal magnetic field and B_ϕ the toroidal magnetic field.

A magnetic pitch angle profile across the minor radius of a plasma allows the calculation of the plasma's internal magnetic configuration in the form of the safety factor profile, q(r). The MHD safety factor, q, is defined as the number of time a field line orbits in the toroidal direction (ϕ) for each single orbit in the poloidal (θ) direction. Mathematically q is given in [1] as,

$$q = \frac{1}{2\pi} \oint \frac{1}{R} \frac{B_\phi}{B_\theta} \, ds \tag{1.5}$$

where $ds = \dfrac{B_\theta}{B_\phi} \, R \, d\phi$ is the distance moved in the poloidal direction for a movement of $d\phi$ in toroidal angle, with the integral carried out over a single poloidal circuit.

For a large aspect ratio circular cross-sectional plasma, the analytical relationship between the measured pitch angle and q is given in [2],

$$q(R) = \frac{rB_t}{RB_\theta} = \frac{\rho(R)}{R\tan(\gamma_{pitch})}\frac{1}{[1+\Delta'(\rho)]} \tag{1.6}$$

where R is the major radius and ρ is the minor radius of the flux surface which crosses the midplane at major radius, R, with the Shafranov shift of the flux surface given as Δ. For shaped tokamak plasmas, the pitch angle profile is used as a constraint in an equilibrium construction program such as EFIT used on C-Mod.

1.5 Introduction to MSE on C-Mod

MSE is typically implemented to observe light from tangential neutral beam injection used for plasma heating, [28, 29, 30, 31]. C-Mod does not use neutral beam heating but rather uses **I**on **C**yclotron **R**adio **F**requency, ICRF, for auxiliary heating. Therefore, MSE on C-Mod observes a **D**iagnostic **N**eutral **B**eam. Due to the lack of large tangential ports in the vacuum vessel design, the DNB is installed to inject radially. The DNB used for this work is a 50ms duration hydrogen beam at 50 keV with a maximum current of 5A, built by the Budker Institute located in Novosibirsk, Russia.

Satisfying the viewing geometry and optical requirements of MSE with a radial DNB requires the use of a fairly complex invessel optics set. MSE requires that the beam emission be Doppler shifted away from the unshifted background plasma deuterium Balmer-α, or Dα, for noise rejection purposes, and this requires viewing the DNB away from perpendicular. Conversely, to achieve radial resolution requires views away from parallel to the DNB. The views on C-Mod are shown as a top view in Fig. 1-3. The figure is to scale, and depicts the DNB at its 1/e width of 9cm.

The MSE periscope inside the vacuum vessel is shown in Fig. 1-4, showing the invessel optics canister, a graphic representing the DNB, and sample viewing chords representing approximately the edge, optical axis, and innermost MSE views. The MSE objective lens is positioned slightly above the midplane, giving the viewing

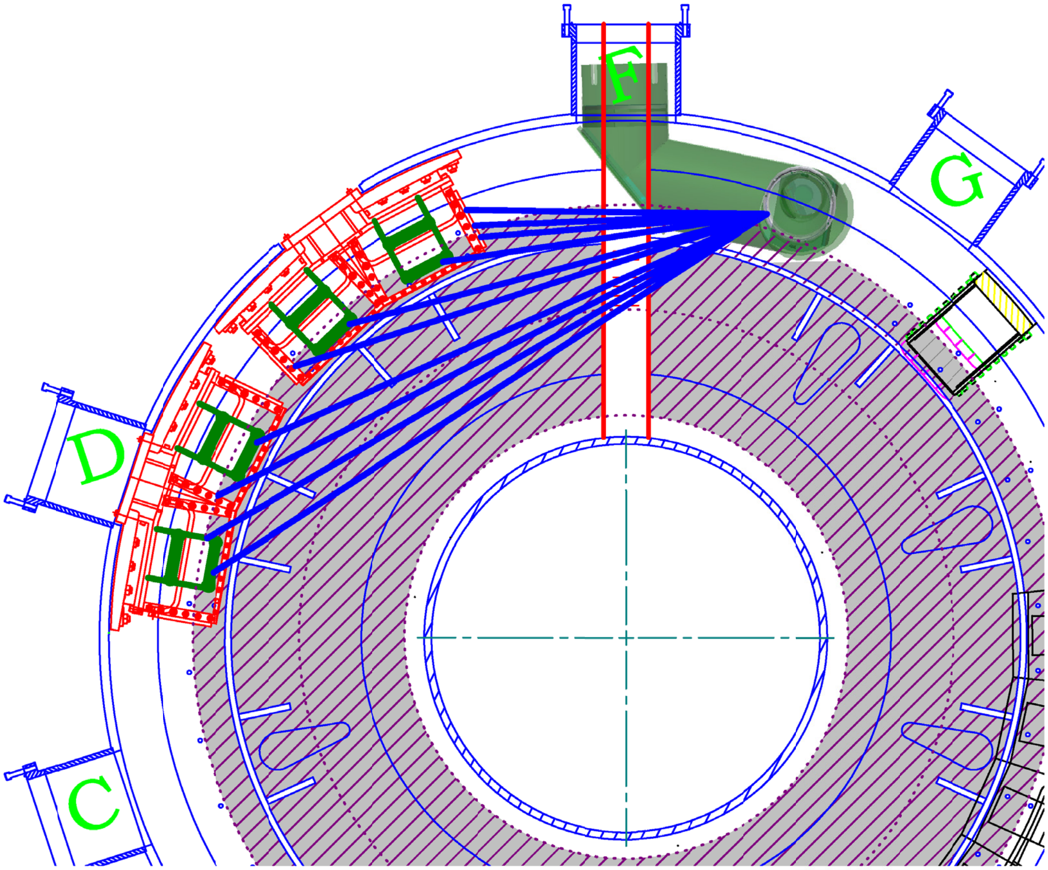

Figure 1-3: MSE viewing chords. Top view of C-Mod with MSE viewing chords. The beam shown is representative of the C-Mod DNB at 9cm 1/e width. Most MSE chords terminate at the ICRF anntennas. Hatched grey area indicates nominal plasma region at the midplane.

chords an inclination angle of $-4.9°$ down towards the beam[†], measured as part of the calibration process discussed in Chapter 4. The viewing radii at the DNB axis, the angle between the viewing chord and the beam velocity is listed in Table 1.2.

The angular sensitivity of MSE is dependent on viewing geometry, and a quantitative analysis of the angular sensitivity and radial resolution is presented in Sec. 3.2.

[†] Both the toroidal field and the plasma current on C-Mod are normally in the clockwise direction as seen from the top view in Fig. 1-3. Both these quantities are negative in a [R,ϕ,Z] right-handed coordinate system where +Z is up and +R is outward from the torus axis. In this coordinate system the magnetic pitch angles are negative on the low-field side of the plasma, where MSE makes all its measurements. The peak C-Mod pitch angle approaches $-14°$ for the highest plasma current pulses.

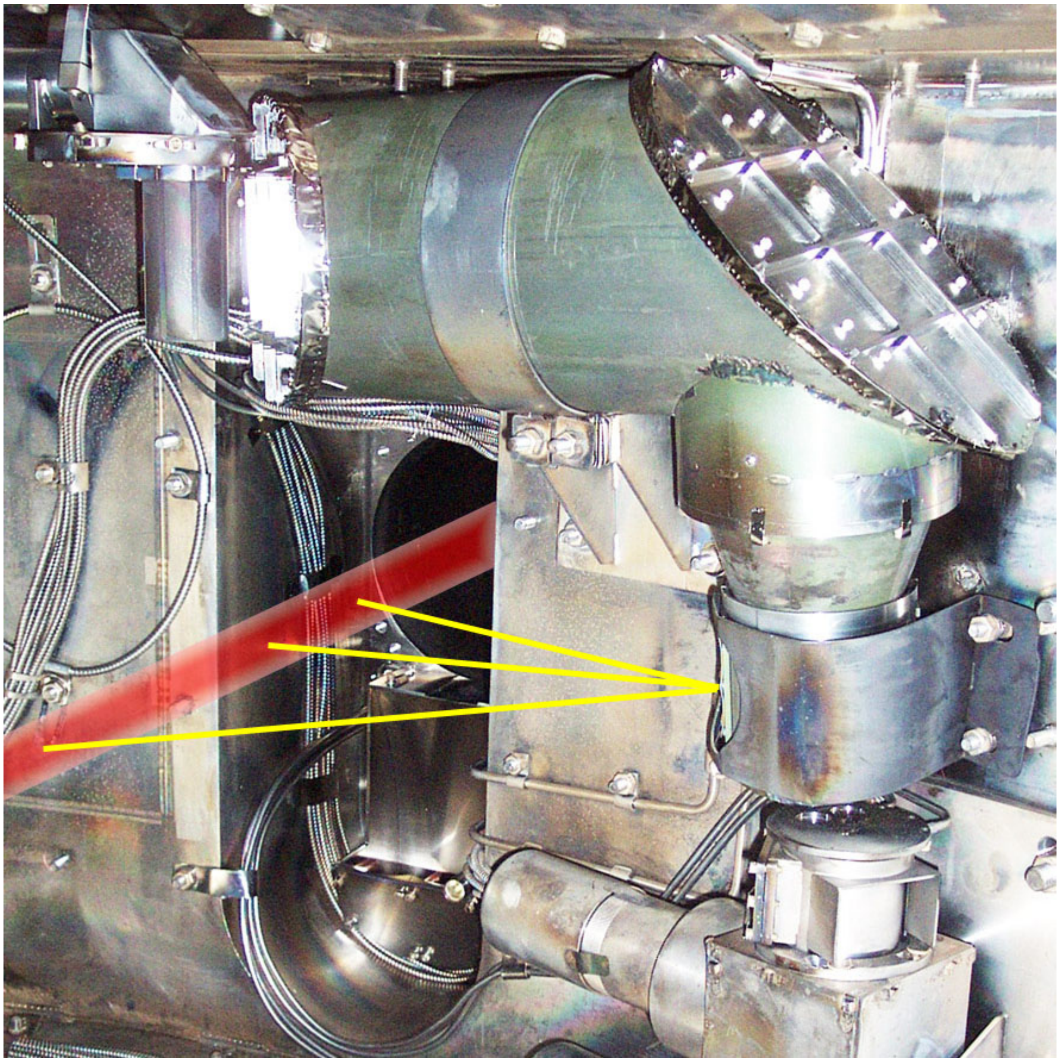

Figure 1-4: MSE viewing chords as seen from inside the vacuum vessel. The MSE periscope is shown with viewing chords, shown as yellow lines, emanating from the objective lens. A graphic is used to represent the DNB as a red beam entering through the port. Three viewing chords are shown for the edge, optical axis, and innermost MSE views.

1.6 Thesis goals and outline

The goals if this work will focus on understanding the principles behind the MSE diagnostic, starting with a discussion of the atomic physics that govern the energy splitting and polarization states of Hα in $\mathbf{E} \wedge \mathbf{B}$ fields in Chapter 2.

Implementing the optical components necessary to make the MSE measurement on Alcator C-Mod proved to require a significant engineering effort. The engineering

View Maj. Radius [cm]	86.8	85.2	83.6	82.0	78.5	76.7	74.7	72.6	70.1	67.6
View [r/a_0]	0.90	0.83	0.76	0.67	0.52	0.44	0.35	0.25	0.15	0.05
Viewing angle [deg]	79.9°	77.2°	74.3°	71.7°	66.2°	63.4°	60.6°	57.9°	54.7°	51.8°

Table 1.2: MSE viewing radii and angles. The minor radius used here is 22cm with a major radius of 67cm. The viewing angle is the angle between the beam velocity and the viewing chord.

lessons learned from designing the MSE optics set is presented in Chapter 3.

MSE requires absolute angle calibrations and also measurement of instrumental parameters that modify the input polarization angle. Calibrations using an invessel apparatus that generates polarized light are discussed in Chapter 4.

Another approach that could potentially provide MSE calibration using conditions more closely matched with plasma pulses is to measure magnetic pitch angles in vacuum fields. This calibration technique involves beam injection into a gas-filled-torus with toroidal and vertical magnetic fields. Results from this calibrations differed significantly from the invessel calibrations. Analysis of the beam-into-gas measurements and a discussion about the discrepancies between the two calibrations are discussed in Chapter 5.

Plasma measurements are discussed in Chapter 6, showing discrepancies with the magnetic reconstruction data. Uncertainty analysis of the MSE data is presented, and several mechanisms that may give rise to errors in the MSE measurement are discussed.

Finally, Chapter 7 summarizes the current status of the MSE diagnostic, pointing out the next steps that need to be taken to resolve remaining issues with the diagnostic.

Chapter 2

Diagnostic Theory

MSE measures the polarization direction of a Balmer line emitted from a fast hydrogenic atom travelling across a magnetic field. Hydrogenic atoms experience a linear Stark effect which separates nominally degenerate lines sufficiently to allow the measurement of only select components of the multiplet. Each component of the multiplet is polarized relative to the external field, so by measuring the angle of select components of the multiplet, one has measured the direction of the local fields. Under conditions normally encountered in fusion plasmas (see Sec. 2.3), components of the multiplet are polarized either exactly parallel (π components) or perpendicular (σ components) to the external electric field. Knowing the injected beam velocity allows calculation of the magnetic field line pitch angle (and in theory also the magnitude) when the static electric field can be neglected in the total electric field, $\mathbf{E_{tot}} = \mathbf{E_{static}} + (\mathbf{v} \wedge \mathbf{B})$.

Measurements of the magnetic field line pitch angle, $\gamma_{pitch} = \tan^{-1}(B_\theta/B_\phi)$, can be used to calculate safety factors for circular cross-section plasmas, see Eqn. 1.6, or can be used to constrain magnetic equilibrium reconstructions in codes such as EFIT used on C-Mod.

MSE was first used to measure the pitch angle of the local magnetic field in a magnetic confined plasma in 1990 by Levinton on the PBX experiment [28]. The emitting neutrals were introduced by injecting a high energy neutral hydrogen or deuterium beam across the magnetic field to be measured. The resultant localized magnetic field pitch angles provided for the first time a non-perturbative measurement of the internal magnetic topology of a high temperature plasma.

This chapter describes the atomic physics involved in MSE, starting with a discussion of the unperturbed quantum mechanical states. The pure Stark and Zeeman cases follow next, continuing with a new calculation showing the polarization states of Balmer-α in $\mathbf{E} \wedge \mathbf{B}$ fields, which accurately describe the MSE observed radiation. The general polarization calculations are then applied to the C-Mod viewing geometry, and the chapter concludes with a discussion of the effects due to the excited state population.

2.1 Unperturbed, pure Stark, and pure Zeeman conditions

MSE operates by viewing neutral, excited hydrogenic atom decay emissions from a high energy neutral beam crossing a magnetic field. In the rest frame of the emitting atom, the fields experienced by the particle are the static plus Lorentz electric fields $\mathbf{E_{tot}} = \mathbf{E_{static}} + (\mathbf{v} \wedge \mathbf{B})$, and also the magnetic field $\mathbf{B}$. In the discussions that follow, the velocity of the beam is much smaller then the speed of light ($v_{beam}/c = \beta \ll 1$), so relativistic effects are ignored. The shifts of interest for MSE are of sufficient magitude to neglect fine structure from effects the Lamb shift and L-S coupling, and hyperfine structure from nuclear spin effects. In this context, the effect of electric and magnetic fields on hydrogen Balmer emission is discussed.

An overview of the necessary atomic physics used in MSE follows. The discussion focuses on the Balmer-α line, (Hα 6562.79Å, Dα 6561.03Å, wavelengths through air), used in MSE because it is the most intense line that lies in the visible region allowing usage of conventional optics. Although the physics is applicable to other hydrogenic lines, such as the Lyman series ($n \rightarrow 1$ transitions) or other lines in the Balmer series (e.g. Hβ, $n = 4 \rightarrow n = 2$), the easiest line to use for MSE is Hα. Although much more intense, the Lyman series lies in the deep ultraviolet ($\lambda_{\mathrm{L}\alpha} = 121.6$nm) and thus is incompatible with conventional optics. Hβ ($\lambda_{\mathrm{H}\beta} = 486.1$nm) is not used primarily due to its more complex polarization structure and is lower intensity.

2.1.1 Unperturbed Eigenstates

Before a description of the quantum state transitions, it is helpful to clarify the nomenclature by describing the unperturbed eigenstates. In the following, **L** refers to the vector orbital angular momentum, L its magnitude, ℓ the orbital quantum number, and m_ℓ is the quantum number of the projected orbital angular momentum onto a preferred axis, such the direction of an external field (assumed to be $\hat{\mathbf{z}}$ for convenience). Similarly, **S**, S, s, and m_s refer to the spin angular momentum, and **J**, J, j, and m_j refer to the total angluar momentum. The principal quantum number is denoted by n. For each principal quantum number n, there are $2n^2$ quantum states.

Solutions to the unperturbed spherical Schrödinger's equation provide the following quantized quantities,

$$n = 1, 2, 3, \cdots \tag{2.1}$$

$$\ell = 0, 1, 2, \cdots, n-1 \tag{2.2}$$

$$s = \pm\tfrac{1}{2} \tag{2.3}$$

$$j = \ell + s \tag{2.4}$$

$$m_\ell = -\ell, (-\ell+1), (-\ell+2), \cdots, +\ell \tag{2.5}$$

$$m_j = -j, (-j+1), (-j+2), \cdots, +j \tag{2.6}$$

The quantum numbers relate to the vector magnitudes such that

$$L = \sqrt{\ell(\ell+1)}\hbar \tag{2.7}$$

$$S = \sqrt{s(s+1)}\hbar \tag{2.8}$$

$$J = \sqrt{j(j+1)}\hbar \tag{2.9}$$

The above states form a convenient basis set of eigenstates in polar coordinates with which hybrid states can be constructed. When using ket notation, this basis set is written as $| n, \ell, m_\ell, m_s\!>$. The normalized radial probabilities, a 3D visualization of the orbital shape, and a 2D cross-sectional plot of the probability function for hydrogen in each n=2 and n=3 state is shown in Fig. 2-1.

In the absence of external fields, the electron spin, **S**, is coupled to the orbital angular momentum, **L**. This spin-orbit coupling gives rise to the fine structure in hydrogenic lines, and results from the interaction between the electron spin and the magnetic field produced by the electron's own orbital motion around the nucleus.

To represent this partially degenerate system, the total angular momentum, **J** = **L**+**S**, can be used to represent the energetically distinguishable eigenstates in the form $| n, \ell, m_j >$. This set of states can also be specified using spectroscopic notation where n and m_j are represented numerically but $l = 0, 1, 2, 3, 4, 5$ is represented by the spectroscopic notation s, p, d, f, g, h, resulting in an equivalent representation of $| \, 3, \, 2, \frac{3}{2} >$ as $3p_{\,3/2}$.

2.1.2 Pure Electric Fields - Stark Effect

The Stark effect is the effect of an electric field on line radiation. The theoretical calculations for the perturbed hydrogen state eigenfunctions were solved analytically by Schrödinger and Epstein [33, 34]. Perturbations to the state functions by an electric field and a derivation of the consequent change in transition energies are discussed in books by Condon and Shortley [35], as well as Bethe and Salpeter [36]. A summary of results important for MSE is presented here.

In an electric field, the hydrogen orbitals are no longer fully degenerate, and form hybridized states. Having introduced the polar coordinate basis set in the last section, one could construct a perturbation matrix by using polar coordinate eigenfunctions to solve for the perturbed eigenvalues, as will be done for the $\mathbf{E} \wedge \mathbf{B}$ case. This would allow the Stark hybrid states to be represented using the polar basis set. However, a simpler method used by Schrödinger and Epstein [33, 34] transforms the wave equation into parabolic coordinates resulting in analytic solutions for hydrogenic atoms in uniform external electric fields. The result is a partially degenerate set of hy-

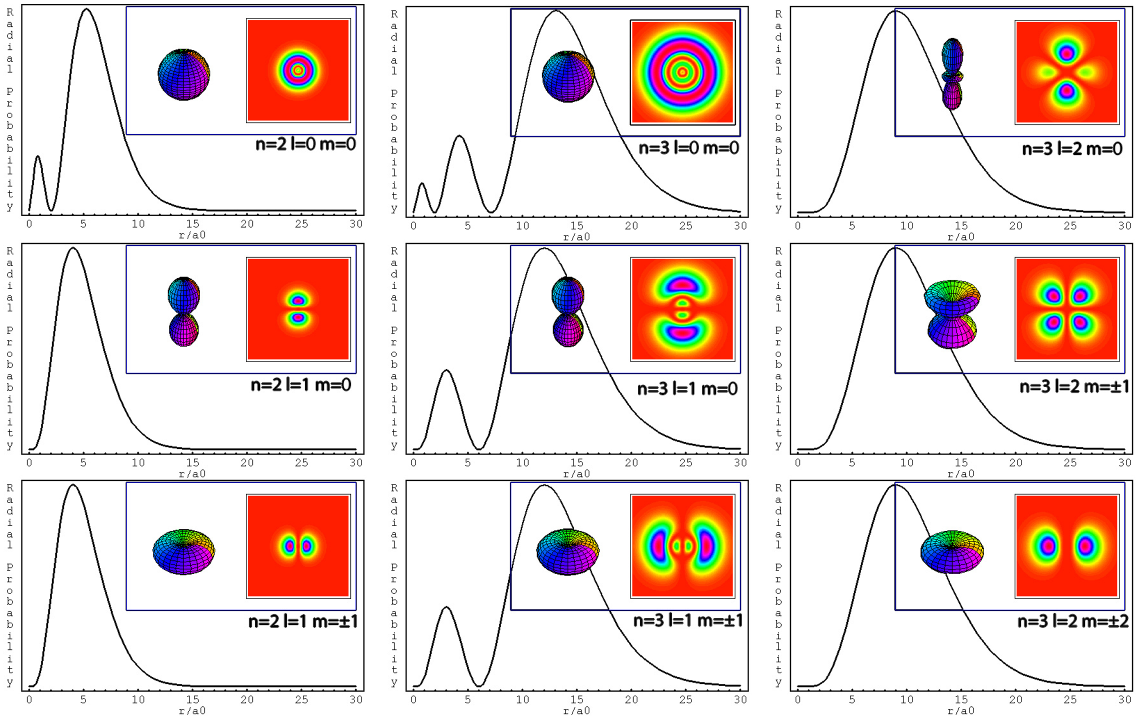

Figure 2-1: Unperturbed hydrogen orbitals for n=2 and n=3, generated from [32]. Normalized radial probabilities are shown, with r/a$_0$ on the abscissa. A 3D visualization the shape of the orbital and a cross sectional view of the probability density is shown in each inset.

brid states where unperturbed eigenstates with different ℓ but identical m_ℓ have been mixed. The Stark eigenstates are specified by n, the principal quantum number and the "electric" quantum numbers, n_1 and n_2 as used by Bethe and Salpeter [36] (also used here) or identially using different notation, k_1 and k_2 by Condon and Shortley [35]. These electric quantum numbers have integers values zero or greater and follow the relation,

$$n_1 + n_2 = n - |m_\ell| - 1 \tag{2.10}$$

The Hamiltonian of each Stark states can be characterized as

$$\mathsf{H}^S = -\frac{3}{2} n(n_1 - n_2) e a_0 E \tag{2.11}$$

where $a_0 = \frac{4\pi\epsilon_0\hbar^2}{m_e e^2}$ is Bohr's radius, and E is the electric field magnitude, and e is the electron charge. Rewriting explicitly for Hα yields the following,

$$\mathsf{H}^S_{n=3} = \tfrac{3}{2} e a_0 \, (\pm 6, \pm 3, 0) \, E \tag{2.12}$$

$$\mathsf{H}^S_{n=2} = \tfrac{3}{2} e a_0 \, (\pm 2, 0) \, E \tag{2.13}$$

$$\Delta\mathsf{E}^S_{H\alpha} = \tfrac{3}{2} e a_0 (\pm 8, \pm 6, \pm 5, \pm 4, \pm 3, \pm 2, \pm 1, 0) \, E \tag{2.14}$$

From the above Stark states, one can see that there are five different energies for $n=3$, and three energies for $n=2$. This leads to 15 transitions with differing energies in the Balmer-α transition. This is still partially degenerate, as there are 36 total possible Balmer-α transitions when electron spin is neglected.

Inserting numeric values for the constants, and rewriting $\Delta\mathsf{E}^S_{H\alpha}$ in wavelength, the following is a useful form of the Stark splitting for spectroscopy use. The lines below have been separated by the polarization directions σ and π discussed later on.

$$\Delta\lambda^{\sigma}_{H\alpha} \, (\text{Å}) = 0.277 \, (0, \pm 1, \pm 5, \pm 6) \, E \, (\text{MV/m}) \tag{2.15}$$

$$\Delta\lambda^{\pi}_{H\alpha} \, (\text{Å}) = 0.277 \, (\pm 2, \pm 3, \pm 4, \pm 8) \, E \, (\text{MV/m}) \tag{2.16}$$

where E is given in MV/m and $\Delta\lambda$ in angstroms.

For hydrogenic atoms, the Stark potential energy perturbations go linearly as $n \, m_\ell \, E$, and this first order linear term dominates up to 10 MV/m. In C-Mod, the beam velocity is 3×10^6 m/s and magnetic fields have values of 5 to 8 Tesla, the electric fields reach values of 15 to 24 MV/m. It is therefore worthwile to briefly address the quadratic Stark effect. Values for calculating the quadratic effect are given in [35] for Hα Stark lines as (2.17) and the results are summarized in Table 2.1. For lines that experience linear Stark shifts, the quadratic effect is negligible at 15 MV/m. Interestingly, the 0σ lines, unaffected by the linear term, experiences a small *redshift* of up to 1.5% of the 1σ shift.

$$\Delta(cm^{-1}) = \pm aE - bE^2 \tag{2.17}$$

Table 2.1: Coefficients of linear and quadratic Stark shifts

$3, n_1, n_2, m \rightarrow 2, n_1, n_2, m$	Label	a	b	$\frac{bE^2}{aE}$ (E=15MV/m)
002 → 001	0σ	0	5.177	-
110 → 001	0σ	0	6.705	-
101 → 100	1σ	64.39	6.156	1.43%
110 → 010	2π	128.78	6.715	0.78%
101 → 001	3π	193.17	6.207	0.48%
200 → 100	4π	257.56	6.309	0.37%

The discussion up until now has focused on the energy splitting of the Stark lines, however, equally important to the MSE measurement is the polarization of each line. In addition to the energy splitting, π and σ lines are also polarized relative to the external electric field. It is useful to first understand the polarization in the pure Stark case before moving on to the $\mathbf{E} \wedge \mathbf{B}$ scenario in actual MSE measurements.

The transitions labeled as π are produced with no change in the angular orbital momentum in the direction of the electric field, that is $\Delta m_\ell = 0$. This can be visualized using a classical analog as emission from an electron oscillating along the direction of **E**. Transitions labeled σ have $\Delta m_\ell = \pm 1$ and can be visualized as emission from an electron orbiting around the nucleus with the orbital axis aligned with **E**. Consequently, when viewed transverse to the electric field, the π emission is linearly polarized parallel to **E** (π for **p**arallel) and the σ is perpendicular (σ from the German for perpendicular, *senkrecht*). Looking in the longitudinal direction (along **E**), the π emission intensity is zero, and the σ is circularly polarized, with the handedness dependent on the sign of Δm_ℓ. However, Stark circularly polarized transitions are degenerate, unlike with the Zeeman effect, so right and left-handed polarization cannot be distinguished through observation. Longitudinal observation of Stark spectra will yield equal intensities of incoherently mixed right and left handed radiation giving rise to no net polarization. Fig. 2-2 shows the Stark polarization pattern viewed transverse and longitudinal to **E**.

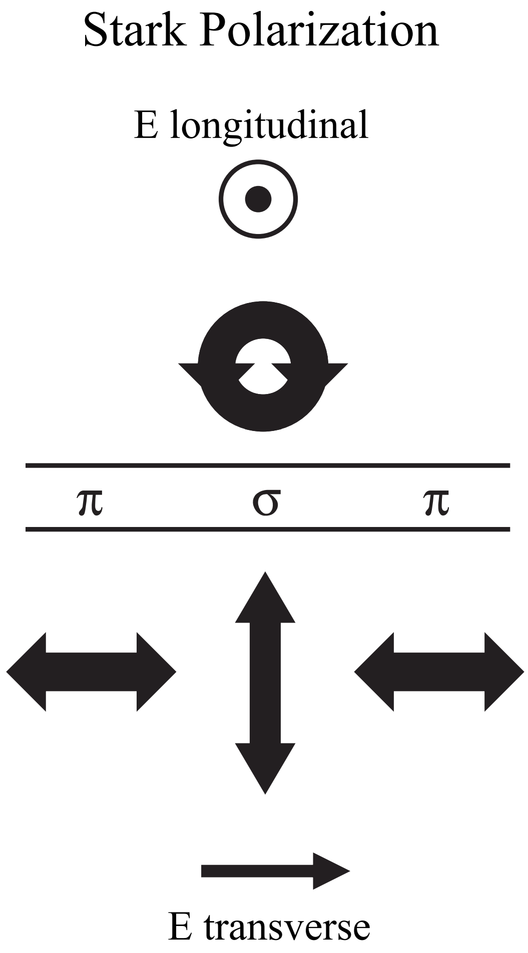

Figure 2-2: The Stark effect polarization pattern

2.1.3 Pure Magnetic Field - Zeeman Effect

It is important to consider the case when emission occurs in a pure magnetic field because emission from non-beam species will behave with characteristics of Zeeman splitting and polarization. This will become very important for the beam-into-gas calibrations.

In a pure magnetic field, the Hα lines split due to the Zeeman effect. The energy perturbations are much weaker for hydrogen when compared to the linear Stark effect. The Hamiltonian for the Zeeman effect is

$$\mathsf{H}^Z = \mu_B B_{\|}(g_\ell m_\ell + g_s m_s) \tag{2.18}$$

where $\mu_B = e\hbar/2m_e$ is the Bohr magneton in SI units, $g_\ell = 1.000$ is the g-factor for the orbital angular momentum, $g_s = 2.0023$ is the spin g-factor, and $B_\parallel$ is the parallel component of B to **L**.

When the external mangetic field is much greater than the field created by the electron orbital motion, the electron spin is decoupled from the electron orbit. The intrinsic orbital field can be estimated using the Bohr atom using classical orbits as,

$$B_{orbit} = \frac{\mu_0 ev}{4\pi r^2} = \frac{\mu_0 ZeL}{4\pi m_e r^3} = \frac{\mu_0 Z^4 eL}{4\pi m_e a_0^3 n^6} \tag{2.19}$$

where L is the orbital angular momentum from Eqn. 2.7, $L = m_e rv$ has been used for the classical electron velocity, and $r = n^2 a_0/Z$, the Bohr atom electron radius. The maximum value of this field occurs at $n = 2, \ell = 1$ to give a field of about 0.3 Tesla. Since the fields considered in this work are of order 5 Tesla, the external fields are much greater than the orbital fields. This high field regime where spin is fully decoupled from orbital angular momentum is known as the complete Paschen-Back effect.

In the complete Paschen-Back regime, the electron spin is conserved in radiative transitions. This comes from the fact that transition probabilities for $\Delta m_s \neq 0$ transitions is zero [36]. Since the spin quantum number is invariant, the eigenstate can be represented using just $\mid n, \ell, m_\ell >$, halving the number of unique states to n^2. The spin term in Eqn.2.18 can also be omitted in this regime.

The Zeeman effect creates a polarization pattern parallel and perpendicular to the magnetic field as well as a symmetric energy splitting for the σ polarized line from the unshifted line. As with the pure Stark case, Zeeman lines are labeled for their polarization, but with the linear component of σ perpendicular to the **magnetic** field and π parallel. Visualization of the orbitals that lead to Zeeman splitting is similar to that of the pure Stark situation in Sec. 2.1.2, with $\Delta m_\ell = \pm 1$ transitions producing σ lines, and $\Delta m_\ell = 0$ transitions producing π lines. In this case, the classical analogy can be extended even further to illustrate the energy splittings as the circular σ dipoles can be described classically as having a magnetic dipole moment either parallel or

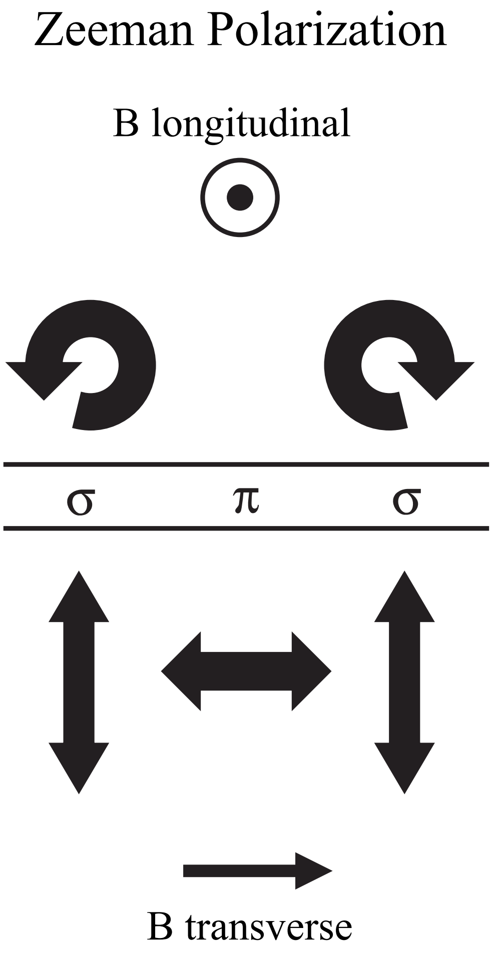

Figure 2-3: The Zeeman effect polarization pattern

antiparallel to the external field, resulting in the Zeeman energy splitting of the σ lines. The π lines are again pictured as produced from linear dipoles aligned with $\mathbf{B}$, and so absent when looking along $\mathbf{B}$ as well as having no perturbation in energy.

The intensities of the Zeeman components are related to the angle of observation,

$$I(\text{Zeeman-}\pi) \propto \sin^2(\psi) \tag{2.20}$$

$$I(\text{Zeeman-}\sigma) \propto \frac{1}{2}[1+\cos^2(\psi)] \tag{2.21}$$

where ψ is the angle between the viewing chord and $\mathbf{B}$.

2.2 Combined $\mathbf{E} \wedge \mathbf{B}$ as encountered in MSE

Having discussed both the pure Stark and pure Zeeman effects, it is important to point out that neither describe the state of emitting beam atoms used in MSE. Because the electric field is the Lorentz field from $\mathbf{v} \wedge \mathbf{B}$, the atom is always resting in both an $\mathbf{E}$ field as well as a perpendicular $\mathbf{B}$ field.

In the pure Stark effect, there is only one preferred axis, that of the electric field. Symmetry exists about the single axis, and thus π and σ can be defined relative to $\mathbf{E}$ for any observation angle. With the addition of a magnetic field, however, a second preferred direction becomes defined and the rotational symmetry about $\mathbf{E}$ is lost. In the case of a Lorentz electric field, conveniently $\mathbf{B} \perp \mathbf{E}$, and a Cartesian coordinate system is fully defined. With rotational symmetry removed, the observed polarization becomes dependent on viewing geometry.

2.2.1 Hybridization of the n=3 and n=2 states in $\mathbf{E}\wedge\mathbf{B}$ fields

The $\mathbf{E}\wedge\mathbf{B}$ fields found in MSE measurements establish a Cartesian coordinate system. The coordinate system used here follows the convention in other works [37, 38, 39]. $\hat{z}$ is defined by $\mathbf{B}$, $\hat{s}$ is the viewing chord, and $\hat{x}$ is constructed such that $\hat{s}$ lies in the x-z plane, $\hat{x} = \hat{s} - (\hat{s} \cdot \hat{z})\hat{z}$. The y-axis is define as $\hat{y} = \hat{z} \wedge \hat{x}$.

The polarization direction must be projected into the viewing 2D plane defined by $\mathbf{e_1}$ and $\mathbf{e_2}$, both perpendicular to $\hat{s}$. $\mathbf{e_1} = \hat{y}$ and $\mathbf{e_2} = [-\cos(\psi)\hat{x} + \sin(\psi)\hat{z}]$, where ψ is the angle between $\hat{s}$ and $\hat{z}$. The beam velocity has been separated into parallel and orthogonal components to the magnetic field, $\mathbf{v} = v_z\hat{z} + \mathbf{v}_r = v\cos(\theta)\hat{z} + \mathbf{v_r}$. The orthogonal component, $\mathbf{v}_r = v\sin(\theta)[\cos(\phi)\hat{x} + \sin(\phi)\hat{y}]$, makes an angle ϕ with $\hat{x}$. In the following calculations, only $\mathbf{v_r}$ affects the atomic transitions, with $\mathbf{v_z}$ contributing only to the Doppler shift.

Fig. 2-4 illustrates this coordinate system, as well as the 2-D coordinate system perpendicular to $\hat{\mathbf{s}}$, $\mathbf{e_1}$ and $\mathbf{e_2}$, in which the angle of polarization is determined.

To calculate the Hα spectrum, one finds the eigenvalues and eigenstates of the pertrurbed states. This can be done by calculating the perturbation matrix from

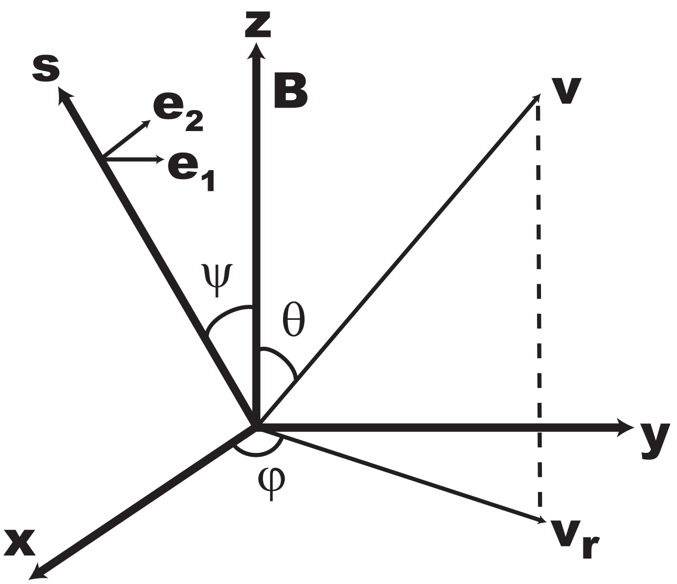

Figure 2-4: Coordinate system used for the $\mathbf{E} \wedge \mathbf{B}$ field calculations. $\hat{z}$ is defined by $\mathbf{B}$ and $\hat{s}$ is the viewing chord. $\hat{x}$ is constructed such that $\hat{s}$ lies in the x-z plane, i.e. $\hat{x} = \hat{s} - (\hat{s} \cdot \hat{z})\hat{z}$, and $\hat{y} = \hat{z} \wedge \hat{x}$. The 2D projection plane perpendicular to $\hat{s}$ is defined $\mathbf{e_1} = \hat{y}$ and $\mathbf{e_2} = [-\cos(\psi)\hat{x} + \sin(\psi)\hat{z}]$, where ψ is the angle between $\hat{s}$ and $\hat{z}$. The beam velocity is separated into parallel and orthogonal components to the magnetic field, $\mathbf{v} = v_z\hat{z} + \mathbf{v}_r,$. The orthogonal component, $\mathbf{v}_r = v\sin(\theta)[\cos(\phi)\hat{x} + \sin(\phi)\hat{y}]$ makes an angle ϕ with $\hat{x}$.

the Hamiltonian, $\mathsf{H}^S + \mathsf{H}^Z$, then diagonalizing it to solve for the eigenvalues (energies) and the eigenvectors that relate each of the perturbed states back to the unperturbed polar coordinate basis, $|\, n, \ell, m_\ell\!>$. These eigenvectors form the matrix $<\!n, k|\, \mathsf{H}^S + \mathsf{H}^Z |\, n, \ell, m_\ell\!>$, where $|\, n, k\!>$ is used to designate $\mathbf{E} \wedge \mathbf{B}$ hybrid states.

The 4×4 matrix, $<\!2, k|\, \mathsf{H}^S + \mathsf{H}^Z |\, 2, \ell_2, m_{\ell_2}\!>$ and the 9×9 $<\!3, k|\, \mathsf{H}^S + \mathsf{H}^Z |\, 3, \ell_3, m_{\ell_3}\!>$ was calculated by Isler [37] along with the eigenvalues (energy states) of each hybrid state. Also needed is the dipole matrix that governs the radiative transition between the unperturbed eigenstates, $<\!2, \ell_2, m_{\ell_2}|\, \vec{\mathbf{r}}\, |\, 3, \ell_3, m_{\ell_3}\!>$. The instuctions for constructing this matrix using the dipole approximation are described by Bethe and Salpeter [36], save for one important step. In each published work dealing with Hα in $\mathbf{E} \wedge \mathbf{B}$ fields [37, 38, 39], the primary interest has been focused on the transition probabilities or intensities of the radiated lines, which is calculated using the *square* of the dipole matrix. More important for MSE purposes, however, is the polarization state of each transition. By using the signed solutions for the radial overlap functions, worked out by [40] and given in Eqns. 2.34, 2.35, and 2.36, one can retain the phase information in the dipole components.

The approach taken by [37, 38, 39] are all similar in that each directly calculates the transition probability in each orthogonal coordinate, discarding the coherent phase information. Without using the phase to construct the complex vector dipole, much of polarization information is lost, giving only the intensity observed in $\mathbf{e_1}$ and $\mathbf{e_2}$ as if linear polarizers had been place along each direction. Information about ellipticity or equivalently the linear polarization fraction is not retained, and different transition types are not as readily identified.

To properly retain the phase, one must solve for the dipole matrices for each hybrid state in each coordinate direction and then vectorally sum the radiation fields coherently before taking the intensity. This is done in the following calculations, which is otherwise analogous to the previous work in [37, 38, 39].

To begin, the electric dipole matrix for the unperturbed hydrogen states are solved. For the Balmer-α series, the dipole matrix can be represented as a 9×4×3 array, where the indices represent the 9 eigenstates in n=3, 4 eigenstates in n=2, and 3 coordinate directions. For each transition $nlm \rightarrow n'm'l'$, the dipole vector is given in [36] as

$$\mathbf{D}^{nlm}_{n'l'm'} = \int \psi^*_{n'l'm'} \sum_i \mathbf{r}_i \; \psi_{nlm} d\mathbf{r} \tag{2.22}$$

where i refers to the coordinate directions and the state function

$$\psi_{nlm} = \frac{1}{\sqrt{2\pi}} R_{nl}(r) \mathcal{P}_{lm}(\theta) e^{im\phi} \tag{2.23}$$

is expressed in polar coordinates using the radial eigenfunctions and Legendre functions. Solutions are given in $\hat{z}$, and the left and right handed polarizations $\hat{x} + i\hat{y}$ and $\hat{x} - i\hat{y}$ for transitions between the unperturbed hydrogen eigenstates (n,l,m) as:

$$\begin{aligned}
\langle n', l{+}1, m \,|z|\, n, l, m\rangle &= \sqrt{\frac{(l+1)^2 - m^2}{(2l+3)(2l+1)}}\; R_{nl}^{n'l+1} \\
&= P_z^{n'l+1} R_{nl}^{n'l+1} \qquad (2.24)
\end{aligned}$$

$$\begin{aligned}
\langle n', l{-}1, m \,|z|\, n, l, m\rangle &= \sqrt{\frac{l^2 - m^2}{(2l+1)(2l-1)}}\; R_{nl}^{n'l-1} \\
&= P_z^{n'l-1} R_{nl}^{n'l-1} \qquad (2.25)
\end{aligned}$$

$$\langle n', l', m \,|z|\, n, l, m\rangle = 0 \quad \text{for all other } l\text{'}$$

$$\begin{aligned}
\langle n', l{+}1, m{+}1 \,|x{+}iy|\, n, l, m\rangle &= \sqrt{\frac{(l+m+2)(l+m+1)}{(2l+3)(2l+1)}}\; R_{nl}^{n'l+1} \\
&= P_{x+iy}^{n'l+1} R_{nl}^{n'l+1} \qquad (2.26)
\end{aligned}$$

$$\begin{aligned}
\langle n', l{-}1, m{+}1 \,|x{+}iy|\, n, l, m\rangle &= -\sqrt{\frac{(l-m)(l-m-1)}{(2l+1)(2l-1)}}\; R_{nl}^{n'l-1} \\
&= P_{x+iy}^{n'l-1} R_{nl}^{n'l-1} \qquad (2.27)
\end{aligned}$$

$$\begin{aligned}
\langle n', l{+}1, m{-}1 \,|x{-}iy|\, n, l, m\rangle &= -\sqrt{\frac{(l-m+2)(l-m+1)}{(2l+3)(2l+1)}}\; R_{nl}^{n'l-1} \\
&= P_{x-iy}^{n'l+1} R_{nl}^{n'l-1} \qquad (2.28)
\end{aligned}$$

$$
\begin{aligned}
\langle n', l\!-\!1, m\!-\!1\, | x\!-\!iy |\, n, l, m\rangle &= \sqrt{\frac{(l+m)(l+m-1)}{(2l+1)(2l-1)}}\, R_{nl}^{n'l-1} \\
&= P_{x-iy}^{n'l+1} R_{nl}^{n'l-1} \qquad (2.29)
\end{aligned}
$$

$$
\begin{aligned}
\langle n', l', m'\, | x \pm iy |\, n, l, m\rangle &= 0 \quad \text{for all other } l\text{'}m\text{'} \\
R_{nl}^{n'l'} &= \int R_{n'l'}(r) R_{nl}(r) r^3 dr \qquad (2.30)
\end{aligned}
$$

Where $R_{nl}^{n'l'}$ is the radial overlap integral between the nl and $n'l'$ state. Its solution is given in [36] and is reproduced here,

$$
\begin{aligned}
R_{nl}^{n'l-1} = \; & \frac{(-1)^{n'-l}}{4(2l-1)!}\sqrt{\frac{(n+l)!(n'+l-1)!}{(n-l-1)!(n'-l)!}}\; \frac{(4nn')^{l+1}(n-n')^{n+n'-2l-2}}{(n+n')^{n+n'}} \times \\
& \left\{ F\left(-n_r, -n_r', 2l, -\frac{4nn'}{(n-n')^2}\right) - \right. \\
& \left. \left(\frac{n-n'}{n+n'}\right)^2 F\left(-n_r\!-\!2, -n_r', 2l, -\frac{4nn'}{(n-n')^2}\right) \right\} \qquad (2.31)
\end{aligned}
$$

with F, the hypergeometric function, defined below, note the summation begins at zero. $n_r = n - l - 1$ and $n_r^{'} = n' - l$ are the radial quantum numbers.

$$
\begin{aligned}
F(a, b, c, x) &= \sum_{\nu=0} \frac{[a(a+1)\ldots(a+\nu-1)]\,[b\ldots(b+\nu-1)]}{\nu!\,[c\ldots(c+\nu-1)]} x^{\nu} \qquad (2.32) \\
&= 1 + \frac{ab}{1!\; c}x + \frac{a(a+1)b(b+1)}{2!\; c(c+1)}x^2 \\
&\quad + \frac{a(a+1)(a+2)b(b+1)(b+2)}{3!\; c(c+1)(c+2)}x^3 + \ldots \qquad (2.33)
\end{aligned}
$$

The signed solutions of the radial integral for the Balmer-α transitions are,

$$(2s-np) \qquad R_{20}^{n1} = \left[\frac{2^{17}n^7(n^2-1)(n-2)^{2n-6}}{(n+2)^{2n+6}}\right]^{\frac{1}{2}} \tag{2.34}$$

$$R_{20}^{31} = \boxed{3.065}$$

$$(2p-nd) \qquad R_{21}^{n2} = \left[\frac{2^{19}n^9(n^2-1)(n-2)^{2n-7}}{3(n+2)^{2n+7}}\right]^{\frac{1}{2}} \tag{2.35}$$

$$R_{21}^{32} = \boxed{4.748}$$

$$(2p-ns) \qquad R_{21}^{n0} = \left[\frac{2^{15}n^9(n-2)^{2n-6}}{3(n+2)^{2n+6}}\right]^{\frac{1}{2}} \tag{2.36}$$

$$R_{21}^{30} = \boxed{0.9384}$$

From these solutions of the Legendre functions and radial functions, each element of (2.22) can be solved for each direction. $\mathbf{D}_{\mathbf{i}}^{\mathbf{n}\to\mathbf{n}',\ell,\mathbf{m}}$ is used to denote the unperturbed dipoles. The transpose of the resultant dipole matrices are shown for typographical reasons.

$$(\mathbf{D}_{\hat{\mathbf{z}}}^{\mathbf{3}\to\mathbf{2},\mathbf{l},\mathbf{m}})^{\mathbf{T}} = \begin{array}{c|cccc} \frac{2lm\rightarrow}{3lm\downarrow} & 200 & 211 & 21\text{-}1 & 210 \\ \hline 300 & 0 & 0 & 0 & \sqrt{\frac{1}{3}}R_{21}^{30} \\ 310 & \sqrt{\frac{1}{3}}R_{20}^{31} & 0 & 0 & 0 \\ 311 & 0 & 0 & 0 & 0 \\ 31\text{-}1 & 0 & 0 & 0 & 0 \\ 320 & 0 & 0 & 0 & \sqrt{\frac{4}{15}}R_{21}^{32} \\ 321 & 0 & \sqrt{\frac{1}{5}}R_{21}^{32} & 0 & 0 \\ 32\text{-}1 & 0 & 0 & \sqrt{\frac{1}{5}}R_{21}^{32} & 0 \\ 322 & 0 & 0 & 0 & 0 \\ 32\text{-}2 & 0 & 0 & 0 & 0 \end{array} \tag{2.37}$$

$$
(\mathbf{D^{3\rightarrow 2,l,m}_{\hat{x}+i\hat{y}}})^{\mathbf{T}} =
\begin{array}{c|cccc}
\frac{2lm\rightarrow}{3lm\downarrow} & 200 & 211 & 21\text{-}1 & 210 \\
\hline
300 & 0 & \sqrt{\frac{2}{3}}R^{30}_{21} & 0 & 0 \\
310 & 0 & 0 & 0 & 0 \\
311 & 0 & 0 & 0 & 0 \\
31\text{-}1 & -\sqrt{\frac{2}{3}}R^{31}_{20} & 0 & 0 & 0 \\
320 & 0 & -\sqrt{\frac{2}{15}}R^{32}_{21} & 0 & 0 \\
321 & 0 & 0 & 0 & 0 \\
32\text{-}1 & 0 & 0 & 0 & -\sqrt{\frac{2}{5}}R^{32}_{21} \\
322 & 0 & 0 & 0 & 0 \\
32\text{-}2 & 0 & 0 & -\sqrt{\frac{4}{5}}R^{32}_{21} & 0
\end{array}
\tag{2.38}
$$

$$
(\mathbf{D^{3\rightarrow 2,l,m}_{\hat{x}-i\hat{y}}})^{\mathbf{T}} =
\begin{array}{c|cccc}
\frac{2lm\rightarrow}{3lm\downarrow} & 200 & 211 & 21\text{-}1 & 210 \\
\hline
300 & 0 & 0 & -\sqrt{\frac{2}{3}}R^{30}_{21} & 0 \\
310 & 0 & 0 & 0 & 0 \\
311 & \sqrt{\frac{2}{3}}R^{31}_{20} & 0 & 0 & 0 \\
31\text{-}1 & 0 & 0 & 0 & 0 \\
320 & 0 & 0 & \sqrt{\frac{2}{15}}R^{32}_{21} & 0 \\
321 & 0 & 0 & 0 & \sqrt{\frac{2}{5}}R^{32}_{21} \\
32\text{-}1 & 0 & 0 & 0 & 0 \\
322 & 0 & \sqrt{\frac{4}{5}}R^{32}_{21} & 0 & 0 \\
32\text{-}2 & 0 & 0 & 0 & 0
\end{array}
\tag{2.39}
$$

The right and left hand solutions above can simply be combined to form x and y dipole due to the following relations,

$$\langle n', l', m' \,| x |\, n, l, m\rangle = \frac{1}{2}[\langle n', l', m' \,| x{+}iy |\, n, l, m\rangle + \langle n', l', m' \,| x{-}iy |\, n, l, m\rangle] \tag{2.40}$$

$$\langle n', l', m' \,| y |\, n, l, m\rangle = \frac{-i}{2}[\langle n', l', m' \,| x{+}iy |\, n, l, m\rangle + \langle n', l', m' \,| x{-}iy |\, n, l, m\rangle] \tag{2.41}$$

From these unperturbed dipole matrix elements, and the hybridization matrices, the hybrid dipoles for the $\mathbf{E} \wedge \mathbf{B}$ states can finally be constructed, where $\mathbf{D_i^k}$ is used to denote the hybrid dipoles, and i each of the coordinate axes.

$$\mathbf{D_i^k} = < 2, k |\, \mathsf{H}^S + \mathsf{H}^Z |\, 2, \ell_2, m_{\ell_2} >^* \cdot (\mathbf{D_{\hat{i}}^{l,m}} \cdot \; < 3, k |\, \mathsf{H}^S + \mathsf{H}^Z |\, 3, \ell_3, m_{\ell_3} >) \tag{2.42}$$

The results of (2.42) are complex vector dipoles for each of the possible 36 hybrid transitions. Dipole elements for the same transition must be vectorially added (coherently) together utilizing the phase, while different transitions should be added incoherently weighed by their amplitude. Finally the dipole vectors in (x,y,z) can be projected to ($\mathbf{e_1}$, $\mathbf{e_2}$) to determine the observed polarization, and the transition probability is determined by the magnitude of the dipole.

2.2.2 Hα transition classification in $\mathbf{E} \wedge \mathbf{B}$ fields

The equations in Sec. 2.2.1 were incorporated into routines written in the IDL environment to calculate the polarization patterns and intensity of Hα in $\mathbf{E} \wedge \mathbf{B}$ fields.

The combination of Stark and Zeeman effects produces three types of transitions, compared to two states (Stark-π, σ and Zeeman-π, σ) for the pure Stark and pure Zeeman conditions. The $\mathbf{E} \wedge \mathbf{B}$ transitions will be referred to as Stark-Zeeman-(E,B, and v) states, with the following polarization characteristics.

- **Stark-Zeeman-E** — Elliptically polarized with the major axis (linear angle) parallel to **E**. The ellipticity varies as a function of γ/ϵ from Eqns. 2.45 and 2.46. The ellipticity handedness depends on the sign of the energy perturbation.

- **Stark-Zeeman-v** — Elliptically ($\Delta E \neq 0$) or linearly ($\Delta E = 0$) polarized with the major axis (linear angle) parallel to $\mathbf{v_r}$, the component of the beam velocity responsible for the Lorentz electric field. The major axis (linear angle) is also perpendicular to **E** when viewed along **B**. The ellipticity handedness depends on the sign of the energy perturbation.

- **Stark-Zeeman-B** — Linearly polarized along **B**. These transitions are found to occur degenerately with both Stark-Zeeman-E and Stark-Zeeman-v lines.

2.2.3 Hα transition probabilities in $\mathbf{E} \wedge \mathbf{B}$ fields

The basic energy splitting units in the Stark-Zeeman splitting are shown in Eqns. 2.43 and 2.44, where q_0 is the basic energy splitting of n=2 and $\frac{q_1}{2}$ of n=3. The Zeeman term, γ, is simply (2.18) omitting the electron spin term in the complete Paschen-Back regime and choosing $m_\ell = 1$. The Stark term, ϵ, is (2.11) having chosen n=2 and $(n_1 - n_2) = 1$.

$$q_0 = \sqrt{\gamma^2 + \epsilon^2} \tag{2.43}$$

$$\frac{q_1}{2} = \frac{\sqrt{4\gamma^2 + 9\epsilon^2}}{2} \tag{2.44}$$

$$\gamma = \mu_B B_{\|} \tag{2.45}$$

$$\epsilon = 3ea_0E \tag{2.46}$$

In this work, $\gamma \ll \epsilon$ is satisfied unless otherwise noted, includes the preceeding descriptions of the polarization Stark-Zeeman states.

Comparing Stark and Zeeman Energetic Splittings

The contribution from the magnetic field to the MSE observed Hα is usually neglected completely, (this is implicit in the name of the diagnostic, it's called the motional Stark diagnostic, Zeeman is not mentioned). From an energetic perspective, one can show that this approximation is valid for MSE by comparing the contribution to the energy splitting resulting from the combination of both fields.

To do this, one can compare the ratio of γ^2 to ϵ^2 in Eqns. 2.45 and 2.46.

$$\begin{aligned}
\frac{\gamma^2}{\epsilon^2} &= \left(\frac{\mu_B B_{\|}}{3ea_0 v_r B_{\|}}\right)^2 && (2.47) \\
&= \left(\frac{\alpha}{3n\beta}\right)^2 && (2.48) \\
&= 0.014\ (n=2, \beta = v_r/c = 0.0103) \\
&= 0.006\ (n=3, \beta = v_r/c = 0.0103)
\end{aligned}$$

where v_r is the beam velocity perpendicular to $\mathbf{B}$, and the electric field used for ϵ is $E = v_r B$. On C-Mod, the 50 keV hydrogen beam is injected perpendicular to the magnetic field. $\beta = v_r/c$, and α is the fine structure constant.

One can see that the magnetic field accounts for a small fraction of the energy splitting observed for MSE emission, and depends only on the beam velocity. For high energy beams, the Stark splitting will be the dominant effect. Therefore, for energetic purposes, the Stark-Zeeman energy splittings can be treated as essentially equal to the pure Stark case.

The importance of the magnetic field comes from the fact that it removes an important symmetry from the pure Stark effect, and results in three transition types with varying ellipticity.

Transition degeneracy and energies

Since there are nine n=3 and four n=2 $\mathbf{E} \wedge \mathbf{B}$ hydrid states, 36 Stark-Zeeman transitions are possible. Each transition type and its energy shift in units of $q_0/2 \approx q_1/6$

(a) $\psi = 90°$, $\phi = 0°$ (b) $\psi = 0°$, $\phi = 0°$

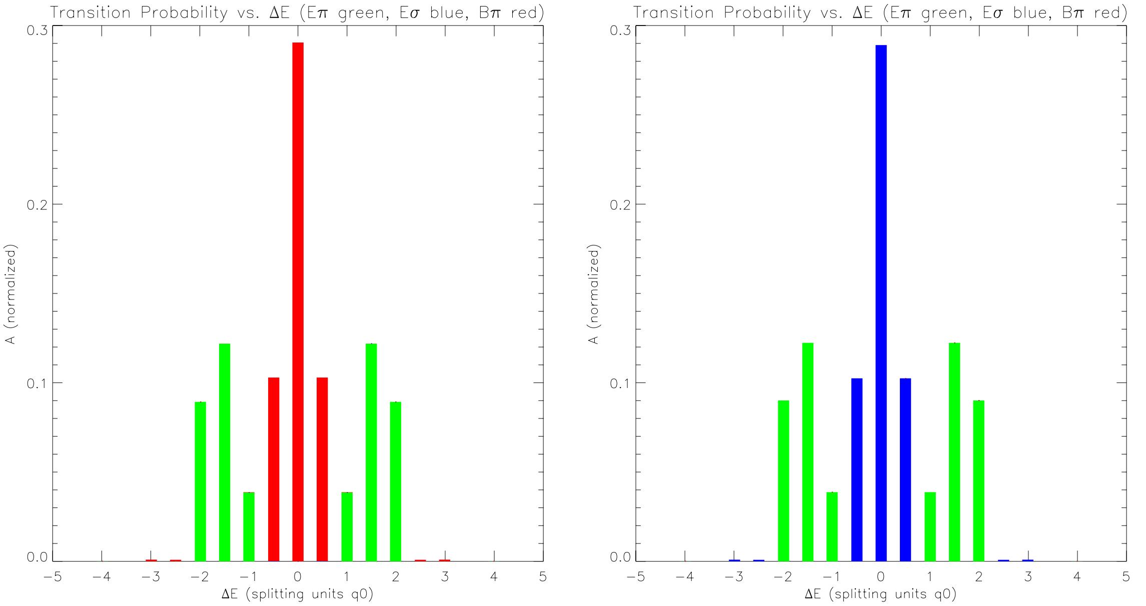

(c) $\psi = 90°$, $\phi = 90°$ (d) $\psi = 45°$, $\phi = 45°$

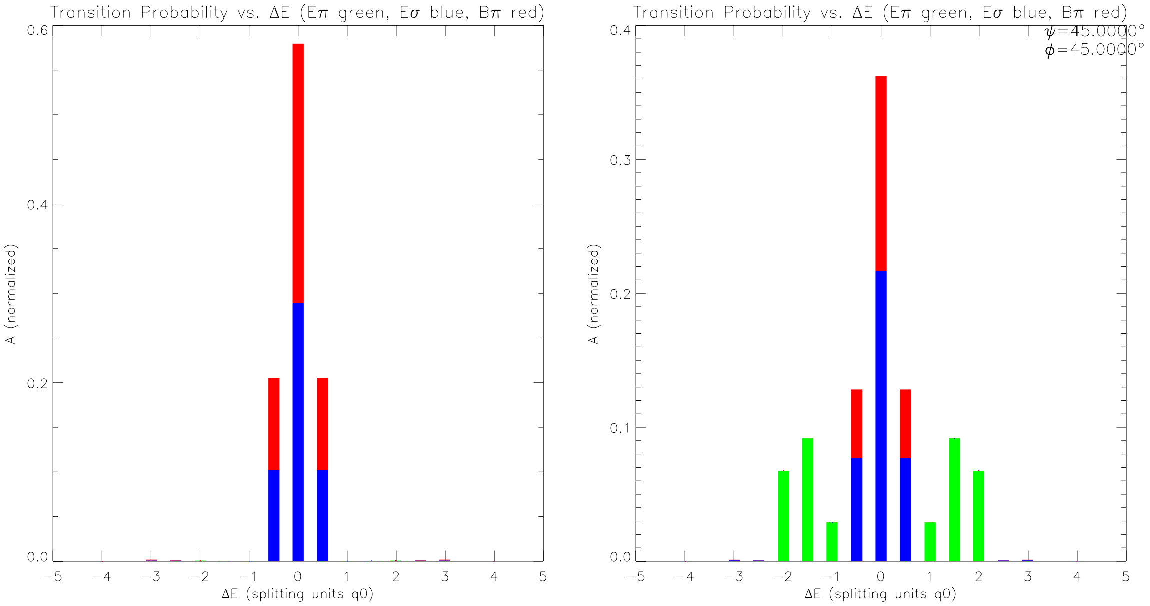

Figure 2-5: Calculated transition probabilities for each energy in the Stark-Zeeman Balmerα spectra. Transition probabilities are summed over degenerate transitions, and the polarization is indicated using green for Stark-Zeeman-E, blue for Stark-Zeeman-v, and red for Stark-Zeeman-B. Fig. a-d compares results for various geometries. All cases are for a field of 4.1T and a beam energy of 50keV. Energy splitting are in units of $q_0 \approx q_1/3$.

$3k \downarrow 2k \rightarrow$	0	q_0	$-q_0$	0	Isler[37]
0	0 v	-2 E	2 E	0 B	Tbl.I 6^{th}
0	0 v	-2 E	2 E	0 B	Tbl.I 5^{th}
0	0 B	-2 B	2 B	0 v	Tbl.II 1^{st}
$\frac{q_1}{2}$	3 E	1 v	5 v	3 B	Tbl.I 3^{rd}
$-\frac{q_1}{2}$	-3 E	-5 v	-1 v	-3 B	Tbl.I 4^{th}
$\frac{q_1}{2}$	3 B	1 B	5 B	3 E	Tbl.II 2^{nd}
$-\frac{q_1}{2}$	-3 B	-5 B	-1 B	-3 E	Tbl.II 3^{rd}
q_1	6 v	4 E	8 E	6 B	Tbl.I 1^{st}
$-q_1$	-6 v	-8 E	-4 E	-6 B	Tbl.I 2^{nd}
Isler[37]	Tbl.III 1^{st}	Tbl.III 2^{nd}	Tbl.III 3^{rd}	Tbl.III 4^{th}	

Table 2.2: Hybrid state eigenvalues and Stark-Zeeman hybrid transition classification. E and v refer to Stark oriented transitions, and B refer to Zeeman-π transitions. The numerical label represents the energy ordering of the lines in the Stark dominant case. For $\gamma \ll \epsilon$, the numerical labels are in units of $q_0/2 \approx q_1/6$ given by Eqn. 2.43. MSE on C-Mod is designed to observe the -2,-3, and -4 lines.

(for $\gamma \ll \epsilon$) is shown in Table 2.2. Row and columns are labelled by the eigenvalue (perturbed energy) of the Stark-Zeeman hybrid state, using units of q_0 and q_1 from Eqns. 2.43 and 2.44. The energy of each transition is determined by taking the hybrid state (3k) initial energy (rows) and subtracting the hybrid state (2k) final energy (columns). Since the eigenvalues are not unique, the last column and row references unique columns in Tables I–III from Isler [37] so the reader may find the corresponding hybrid eigenvectors.

Table 2.2 shows that the number of eigenvalues (energies) have not changed from the pure Stark case, so Stark-Zeeman transitions are partially degenerate.

Fig. 2-5 shows the calculated transition probabilities for each type of transition in several orientations matching previous works. The calculated intensities agrees with previous works [37, 38, 39, 41]. Degenerate states are summed in Fig. 2-5, with the polarization type designated using different colors.

To verify the validity of the calculations, several checks were performed. First, the hybridization matrices were checked such that the summed magnitude of each unperturbed and hybrid states were unity. Second, the total transition probability was verified not to vary with geometry or fields. Third, the total radiation summed over the 4π solid angle was verified to be unpolarized. Finally, the total transition probability for all 36 transitions were found to match the total unperturbed transition probability for n=3 → n=2 found in Bethe and Salpeter [36].

Transition probability results for the C-Mod viewing geometry

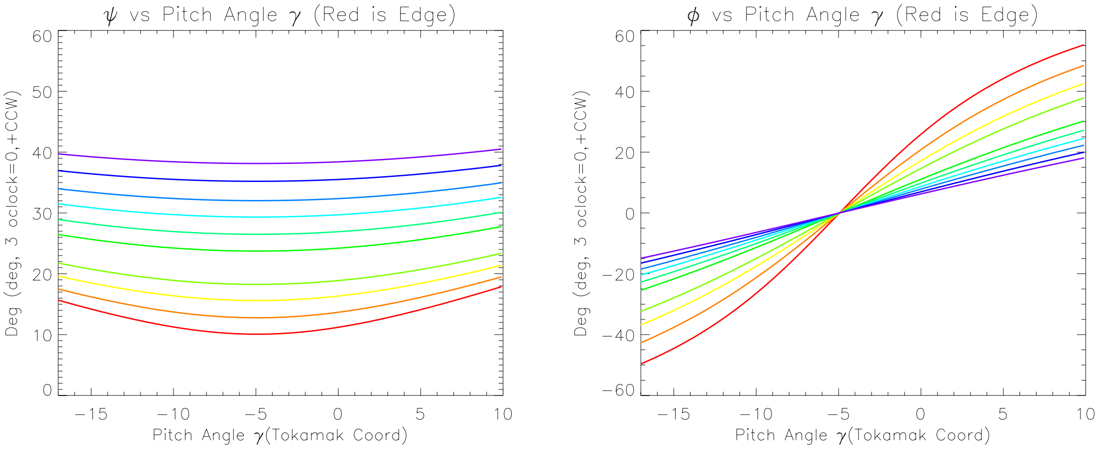

Figure 2-6: ψ and ϕ as a function of magnetic pitch angle in C-Mod for all MSE channels, red (edge) to violet (core). Note the large apparent change of ϕ due to a modest change of γ.

Although the fully general coordinate system shown in Fig. 2-4 is natural for use in the lab frame, in a tokamak it is the magnetic field that changes angle while the sightline and beam directions are maintained. As $\mathbf{B}$ determines $\hat{\mathbf{z}}$, changing $\mathbf{B}$ will affect both ϕ and ψ differently for each viewing chord. These angles need to be calculated for each MSE channel, and the results used to calculated transition probabilities. Fig. 2-6 shows calculated angles for C-Mod MSE channels using the views listed in Table 1.2. Features in ψ and ϕ occur at the inclination angle of the MSE sightlines, $-4.9°$. Specifically, this is the angle at which the MSE sightline is most parallel to **B**, thus ψ is minimized. Also at this pitch angle, the viewing chord lies in the **B**-**v** plane, so $\phi = 0$.

The transition probability of each transition varies with ϕ and ψ. However, each Stark-Zeeman-E transition behaves the same as a function of ϕ and ψ when normalized by the maximum value. The same is true of Stark-Zeeman-v, and Stark-Zeeman-B transitions. All that is necessary to determine the transition probabilities for all transitions at all pitch angles are these normalized functions, and the absolute values of the transition probabilities at the minima/maxima.

The normalized functions are shown in Fig. 2-7 and the absolute transition probabilies are given in Table 2.3

Channel		Energy Splitting in q_0, $(\gamma \ll \epsilon)$							
		0	±1	±2	±3	±4	±5	±6	±8
R=86.7cm	σ	2.5853	0.9166	-	-	-	0.0076	0.0083	-
	π	-	-	0.3573	1.1286	0.8308	-	-	0.0005
	B	0.0819	0.0290	0.0000	0.0000	-	0.0002	0.0003	-
R=81.9cm	σ	2.4052	0.8528	-	-	-	0.0071	0.0078	-
	π	-	-	0.3572	1.1283	0.8303	-	-	0.0005
	B	0.2629	0.0930	0.0001	0.0000	-	0.0008	0.0009	-
R=74.6cm	σ	2.0271	0.7190	-	-	-	0.0060	0.0066	-
	π	-	-	0.3569	1.1277	0.8293	-	-	0.0005
	B	0.6429	0.2274	0.0004	0.0001	-	0.0019	0.0021	-
R=67.6cm	σ	1.6502	0.5856	-	-	-	0.0050	0.0054	-
	π	-	-	0.3567	1.1271	0.8283	-	-	0.0005
	B	1.0217	0.3614	0.0006	0.0002	-	0.0029	0.0033	-

Table 2.3: Absolute Stark-Zeeman hybrid transition probabilities for the C-Mod viewing geometry. Values are given for four MSE channels each at the the maxima/minima in Fig. 2-7. Figures are given in units of $10^7\ s^{-1}$. The total transition probability matches the value in Bethe and Salpeter [36] at 9.225×10^7.

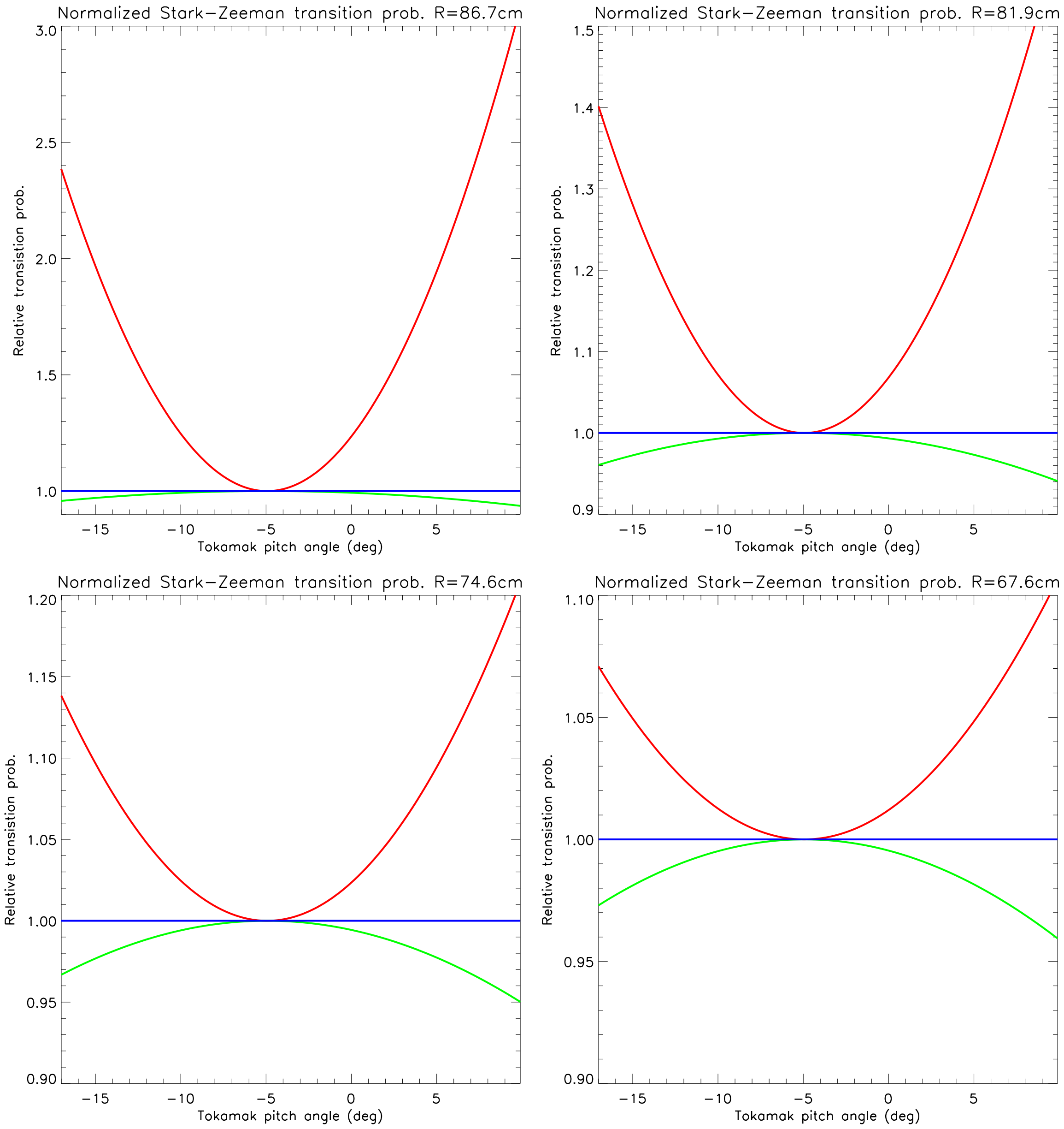

Figure 2-7: Relative transition probabilities Stark-Zeeman hybrid states for MSE geometries. Green is used for Stark-Zeeman-E, blue for Stark-Zeeman-v, and red for Stark-Zeeman-B. Each transition type follows the same relative curves, with minima/maxima occuring at the pitch angle equal to the MSE view inclination. The absolute value of the transition probability for each transition energy can be found in Table 2.3.

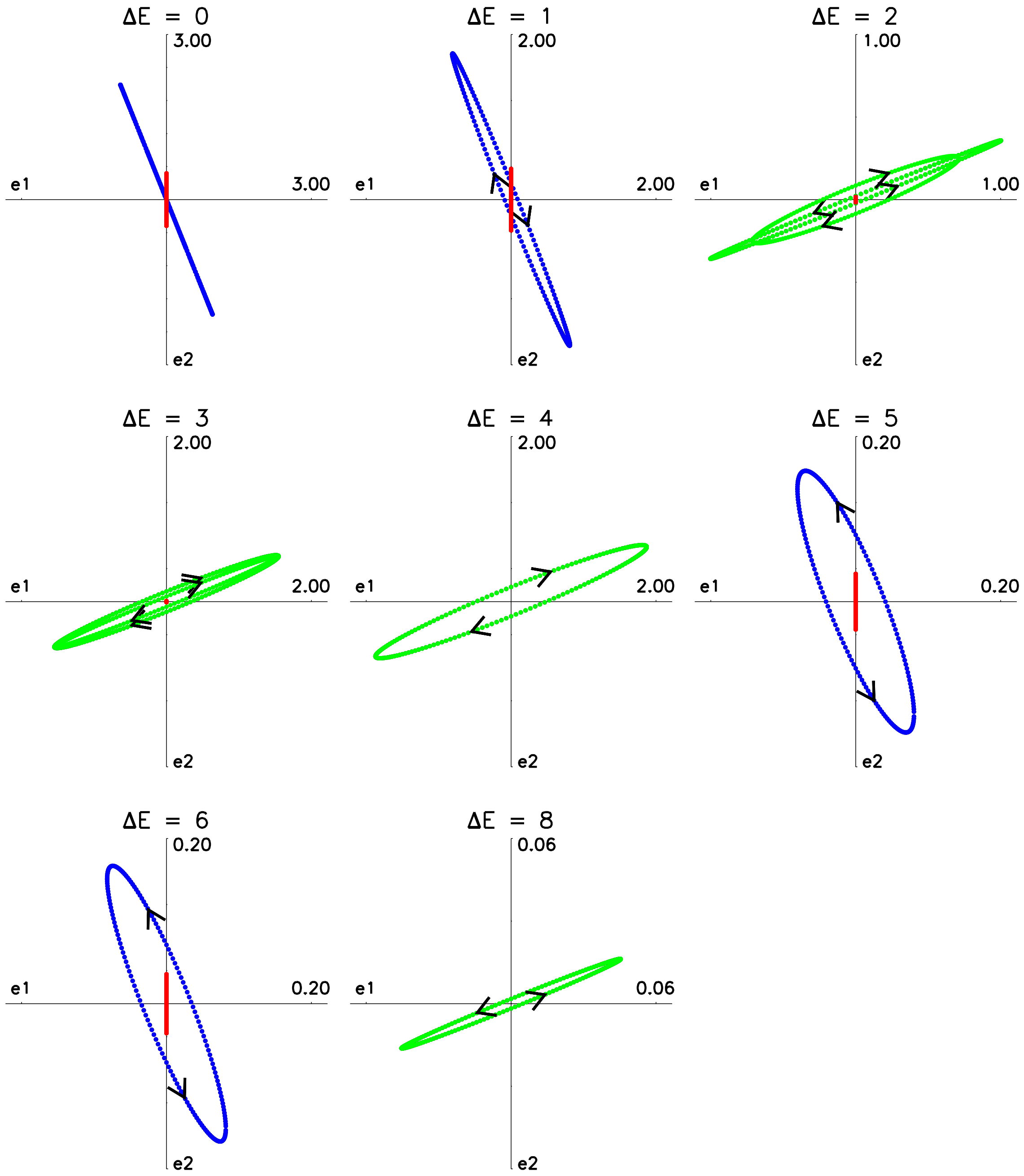
ΔE = 0
3.00
e1
3.00
e2
ΔE = 1
2.00
e1
2.00
e2
ΔE = 2
1.00
e1
1.00
e2
ΔE = 3
2.00
e1
2.00
e2
ΔE = 4
2.00
e1
2.00
e2
ΔE = 5
0.20
e1
0.20
e2
ΔE = 6
0.20
e1
0.20
e2
ΔE = 8
0.06
e1
0.06
e2

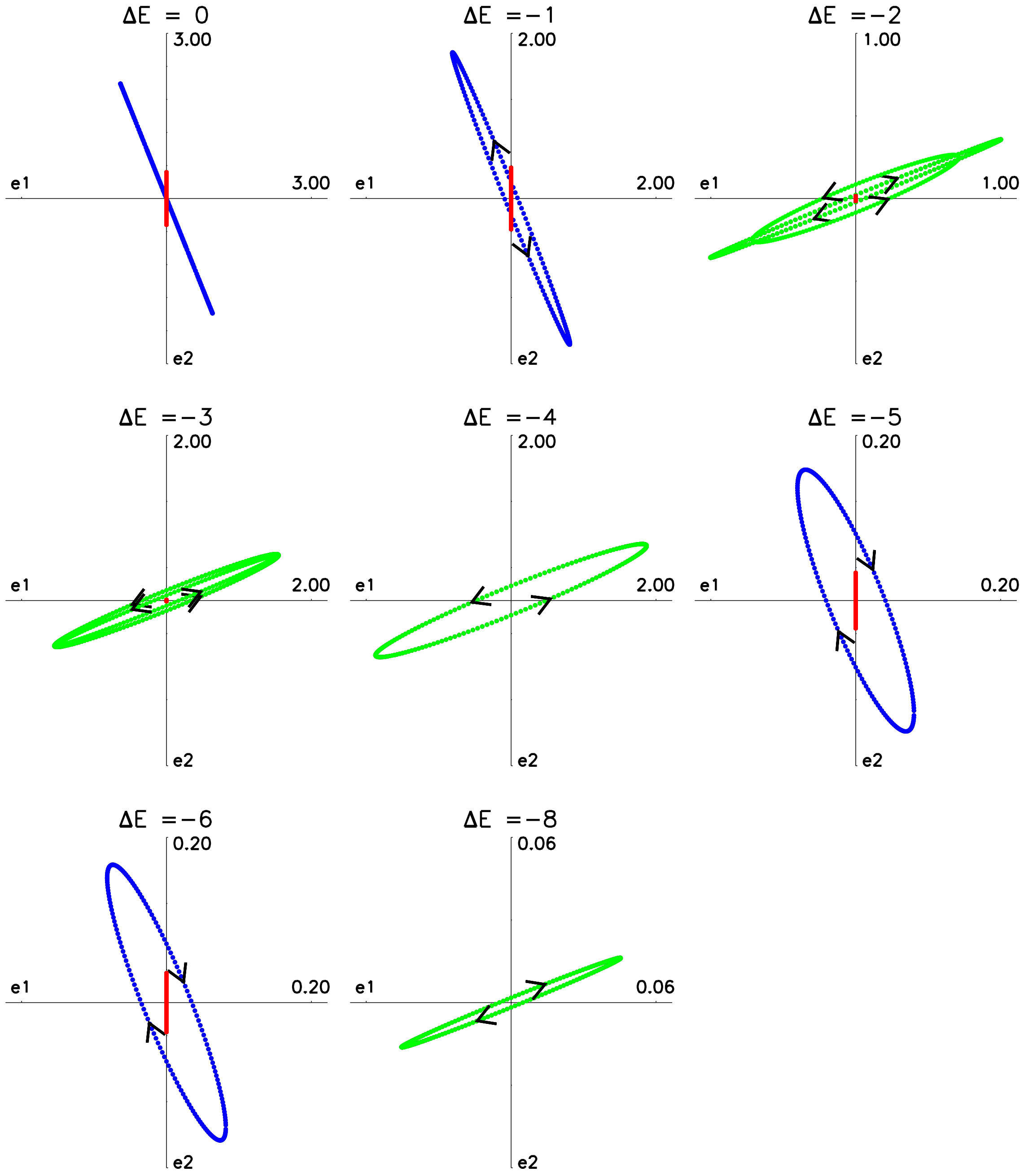

Figure 2-8: Projected dipoles for negative [this page] and positive [previous page] energy perturbation transition of Stark-Zeeman hybrid transitions. For this calculation, ϕ=21.7°, ψ=10.8° (which happens to be the values for the MSE edge channel at a tokamak pitch angle γ=-9.0°). Stark-Zeeman-**B** lines (red) are always oriented parallel to $\mathbf{e_2}$ (z-axis) which is the projected direction of **B**, Stark-Zeeman-**v** lines are shown in blue, and Stark-Zeeman-**E** lines in green. Degenerate lines are plotted in the same window using the colors, with arrows indicating left- or righthanded ellipticity. The ΔE=0 plot is included on both pages for symmetry. MSE nominally observes the -2,-3,and -4 energy lines.

2.2.4 Polarization pattern of Stark-Zeeman Lines

Projected dipoles (polarization patterns) for all transitions are shown for a sample angle in Fig. 2-8. Degenerate transitions are overplotted on the same axis, using the same colors as Fig. 2-5 to distinguish the transition type. Arrows are shown for transitions with non-zero ellipticity to indicate the handedness. Transition probabilities shown in Fig. 2-5 are the sums of the dipole magnitudes shown in Fig. 2-8.

For general viewing geometries, the projected direction of Stark-Zeeman-v is not necessarily perpendicular to Stark-Zeeman-E. These transtitions are only perpendicular when viewed along **B**. When viewing in this orientation, as in Fig. 2-5(b), the Stark-Zeeman-B intensity goes to zero and the multiplet intensity is identical to the pure Stark case.

Fig. 2-8 shows ellipticity in the Stark-Zeeman-E and Stark-Zeeman-v lines. These transitions show characteristics indicating that they are hybrid mixtures of Stark-π with Zeeman-σ and Stark-σ with Zeeman-σ, respectively. The ellipticity changes with the ratio γ/ϵ (for Lorentz electric fields, as the beam velocity shown in Eqn. 2.47). The linear polarization direction (major axis) of both Stark-Zeeman-E and Stark-Zeeman-v transitions go from being aligned relative to $\mathbf{E}$ to being aligned perpendicular to $\mathbf{B}$ as $\epsilon/\gamma \rightarrow 0$, i.e. the transitions reduce to the pure Zeeman case.

In the limit approaching the pure Stark case, $\gamma/\epsilon \rightarrow 0$, ellipticities for Stark-Zeeman-E go to zero, but all three transition types remain. The conclusion from this observation is that the introduction of the coordinate system with zero degrees of freedom allows one to distinguish between Stark-Zeeman-v and Stark-Zeeman-B, whereas only Stark-σ existed for the pure Stark case due to rotational symmetry.

2.2.5 Comparison of Stark-Zeeman to pure Stark polarization

The observed photon rate per solid angle of each transition is equal to the number of excited atoms in each hybrid upper state multiplied by the transition probability, a function of the observation geometry. Since there is no way to seperate degenerate transitions, the incoherently summed radiation (using Stokes vectors, see Appendix A) from all degenerate transitions comprising an energy component of the Stark-Zeeman multiplet will be referred to as a Stark-Zeeman line from here on. To begin, each excited upper hybrid state will be assumed to be populated equally, i.e., *statistically populated excited states.*

The energy differences between the Stark-Zeeman lines and pure Stark lines are also neglegible ($q_0 \approx \epsilon$), so Stark-Zeeman lines will be compared to the corresponding pure Stark lines in energy.

It should be no surprise that for $\gamma/\epsilon \rightarrow 0$, lines with Stark-Zeeman-v transitions have polarization identical to Stark-σ and lines with Stark-Zeeman-E are identical to Stark-π. This allows results from this calculation to reduce back to the pure Stark case. Calculations also show that for real MSE cases of small γ/ϵ, the net linear angles of the Stark-Zeeman lines are, for practical measurement purposes, the same as Stark-σ and Stark-π. The circular fraction remains for Stark-Zeeman-E however, for $\gamma/\epsilon \neq 0$, as shown in Fig. 2-8.

In these calculations, statistically populated upper states were assumed. The linear angle of the Stark-Zeeman $\Delta E = 0, \pm 1$ lines depends on two differently directioned Stark-Zeeman-v and Stark-Zeeman-B transitions, coming from different upper states, as shown in Fig. 2-5(d) and Table 2.2. This means that *Stark-Zeeman lines are only polarized in the same direction as pure Stark lines for statistically populated upper states.*

The C-Mod MSE observes the Stark-Zeeman $\Delta E = -2, -3, -4$ components, where calculations show that degenerate Stark-Zeeman-B transition probabilities are three orders of magnitude smaller than that for Stark-Zeeman-E, making an extremely skewed excited state population necessary to result in a deviation in polarization direction away from **E**. However, many MSE diagnostics observe the $\Delta E = 0, \pm 1$ lines. The conventional assumption is that the $\Delta E = 0, \pm 1$ are aligned perpendicular to **E**, but this work now shows that this assumption is only true for statistically populated n=3 hybrid states.

Of particular concern are MSE diagnostics that rely on multiplet component amplitudes, such as MSE on Textor-94 [42]. Spectral MSE instruments currently make assumptions about both the intensity and ellipticities of components in the Stark-Zeeman multiplet to make angular measurements based on line ratios, but must actually take into account the real ellipticities of the Stark-Zeeman transitions as well as excited state populations.

2.3 Excited State Populations

The assumption that degeneracy summed Stark-Zeeman lines have identical linear polarizations compared to the corresponding (in energy) pure Stark transition was shown to depend on statistical upper state populations in the last section.

Upper state populations have been shown to be *non-statistical* for beam-into-gas calibrations on TFTR by Levinton [41] using measured spectra from a heating beam injected into a gas-filled torus.

2.3.1 Stark-Zeeman polarization in non-statistical populations

There are several ways for Stark-Zeeman lines to become polarized differently than the expected direction, the most dramatic effect occurs with the nominally Stark-σ oriented lines. Table 2.2 shows that the unshifted line is six way degenerate, with three transitions each in the Stark-Zeeman-v and Stark-Zeeman-B directions. Each upper state produces both types of transitions, but the ratio of Stark-Zeeman-v to Stark-Zeeman-B transition probabilities is dramatically different for each upper state. Therefore, when the Stokes vectors of all six transitions are added, the result will only be perpendicular to $\mathbf{E}$ when the three upper states contributing to the unshifted line are equally populated. Otherwise, an angle weighted more towards $\mathbf{B}$ or $\mathbf{v}$ will be produced.

The $\Delta E = \pm 1$ and the much lower intensity $\Delta E = \pm 5$ lines are only two-fold degenerate, with different upper states contributing the Stark-Zeeman-v and Stark-Zeeman-B polarizations. Again, the summed Stokes vector will be linearly perpendicular to $\mathbf{E}$ for statistical populatons only, and can be biased towards the projected direction of **B** or **v** for non-statistical populations.

Figure 2-5(d) illustrates the previous points. The $\Delta E = 0$ and ± 1 lines show comparable intensities for both Stark-Zeeman-v and Stark-Zeeman-B polarizations. These polarizations appear to the observer at different angles, about 35° apart. The Stark-Zeeman-v and Stark-Zeeman-E polarizations are about 70° apart. Only by adding the Stokes vectors of all six degenerate transitions for the $\Delta E = 0$ and both of the transitions for $\Delta E = \pm 1$ does one get the angle of Stark-σ, i.e. perpendicular to **E**.

The situation is somewhat improved when discussing the Stark-π lines. For these lines, the $\Delta E = \pm 2, \pm 3$, the transition probabilities for the Stark-Zeeman-B transitions are 3 orders of magnitude smaller (see Table 2.3) than that for the Stark-Zeeman-E polarization, the angle will remain unaffected unless the population becomes extremely skewed. $\Delta E = \pm 4, \pm 8$ transitions are not degenerate, and are always oriented in the Stark-Zeeman-E direction.

2.3.2 Beam-into-gas Excited Populations

One key issue of concern for the use of beam-into-gas calibrations is understanding if there are differences in collisional ℓ-mixing of the beam atoms traversing D_2 gas versus traversing plasmas. Several works [43, 44, 45] have attempted to address the issue of collisional mixing of states with neutral gas, including experimental work to measure the actual cross-section for $3\ell \rightarrow 3\ell'$ in $H^* + H_2$ collisions. No data is currently available for the high field Stark-Zeeman hybrid states, so data on the unperturbed states is used here to try to provide qualitative insight. The best available data comes from Glass-Maujean et al. [43] in which ℓ-mixing cross-sections are given directly, summarized in Table 2.4. Next to these cross sections a calculation of the ℓ-mixing mean free paths for beam-into-gas is listed.

Several important caveats need to be pointed out when looking at the data from [43] for MSE scenarios. The listed cross-sections are for slow moving excited atoms in unperturbed states, and are to decrease as $v^{-\frac{1}{3}}$ [46], and so the cross sections may be *much* smaller for high energy atoms. No experimental measurements yet exist for the specific conditions found in MSE. Therefore the following discussion should be treated as a qualitative argument.

Table 2.5 shows the cross sections and mean free paths for for excitation of H + H_2 at 50keV [47], and the mean distance travelled before radiative de-excitation for the unperturbed ℓ states.

$\sigma_{3\ell\to 3\ell'}$	Cross Section [Å^2]	Mean Free Path
σ_{3sp}	53 ± 12	5.3 cm
σ_{3sd}	77 ± 12	3.7 cm
σ_{3ps}	18 ± 4	15.7 cm
σ_{3pd}	95 ± 12	3.0 cm
σ_{3ds}	15 ± 3	18.8 cm
σ_{3dp}	60 ± 22	4.7 cm

Table 2.4: Collisional ℓ-mixing cross-sections of $H^* + H_2$ with a relative velocity of 5km s^{-1} [43]. ℓ-mixing mean free path lengths in 1 mTorr gas using these cross sections.

When the excitation, radiative de-excitation, and ℓ-mixing mean free paths are all compared, one can see that that ℓ-mixing lengths are not much shorter than the radiative lifetimes. This suggests that upper state populations in MSE beam-into-gas

$\sigma_{1s\to 3\ell}$	Excitation Cross Section [$\times 10^{-2}$Å^2]	Excitation MFP [m]	Mean Excited Lifetime [ns]	De-excitation Mean Distance [cm]
σ_{3s}	3.30 ± 0.41	85.6	158 (3s)	47.4
$0.12\sigma_{3p} + \sigma_{3d}$	1.17 ± 0.41	241	5.4 (3p)	1.6
			15.6 (3d)	4.7

Table 2.5: Collisional excitation cross sections of [H(1s) + H_2] at 50keV atomic energy [47], excitation mean free path at 1 mTorr, mean excited lifetime, and mean distance travelled before radiative de-excitation at 50keV. Due to the methods used in [47], only the sum of $0.12\sigma_p + \sigma_d$ excitation cross sections are given.

calibrations are dynamic rather than quasistatic, and may not be statistical.

Thus, the population dynamics need to be considered carefully with respect to the actual observed intensities in each polarization direction. Further, it appears that the range of gas pressures used in gas calibrations (0.5 - 2 mTorr) can affect state populations. All these factors combine to introduce a level of complexity undesirable in a diagnostic calibration.

In situations where the excited states are non-statistical, an MSE calibration into a gas filled torus can observe nominally σ lines that are not completely perpendicular to $\mathbf{E}$. However, it is important to note that all of the effects due to non-statistical populations should not affect the C-Mod MSE, which observes the most redshifted nominally π lines of the full energy beam component. Since only the σ components polarization angles can be noticably affected by excited state populations, their effect on the C-Mod MSE can been eliminated through careful spectral filtering. Great care has been taken to completely exclude the nominally σ lines to maximize polarization fraction. Therefore, non-statistical populations should not affect the angles measured by the C-Mod MSE.

2.3.3 Beam into Plasma Excited Populations

Since ℓ-mixing is achieved by the electric fields from surrounding particles in a process similar to the Stark broadening of atomic lines, in neutral gas the scale length for interaction is the atomic or molecular size. In plasmas, this interaction distance will approach the much longer Debye length for transitions between nearly degenerate states. Previous work by Fonck et. al. [48] shows that ℓ-mixing should reach statistical equilibrium in plasmas with densities of greater than $n_e = 10^{19}\mathrm{m}^{-3}$. This is confirmed experimentally with spectroscopic measurements in plasma from Levinton, [41].

2.4 Chapter Summary and Next Steps

In this chapter, the atomic physics of the Stark, Zeeman, and Stark-Zeeman hybrid states have been discussed, including energetic splitting as well as polarization effects. Two new discoveries about the polarization of Stark-Zeeman hybrid states were revealed. One was the ellipticity of the Stark-Zeeman transitions, and the other was the discovery of three distinct polarization directions, which have been labelled in this work as Stark-Zeeman-E ($\parallel \mathbf{E}$), Stark-Zeeman-v ($\parallel \mathbf{v}_\perp$), and Stark-Zeeman-B ($\parallel \mathbf{B}$).

Summed over degenerate transitions, Stark-Zeeman lines are similar to pure Stark line when $\epsilon \gg \gamma$ in Eqns. 2.46 and 2.45 as is the case for MSE observations involving high energy neutrals. In this regime, the Stark effect dominates and the energy splitting for Stark-Zeeman approachs those of the pure Stark lines.

The polarization directions of Stark-Zeeman lines can be treated as identical to the Stark lines only in the case of statistical upper hybrid state populations. The observed Stark-Zeeman polarization angles for the $\Delta E = 0, \pm 1, \pm 5$ depend upon the intensities of both the Stark-Zeeman-v and Stark-Zeeman-B transitions, and so for non-statistical excited state populations, it may be possible to observe $\Delta E = 0, \pm 1, \pm 5$ transitions that are not perpendicular to $\mathbf{E}$. It is theoretically possible for $\Delta E = \pm 2, \pm 3$ lines to be polzarized at an angle deviating from $\mathbf{E}$, but it would be require an extremely skewed upper state population, as the transition probability for the Stark-Zeeman-B at these energies are three orders of magnitude below that of Stark-Zeeman-E. $\Delta E = \pm 4, \pm 8$ are not degenerate, and contain only a single Stark-Zeeman-E transition.

Based on data from unperturbed, low velocity ℓ-mixing cross-sections, a qualitative argument for the possibility of observing non-statistical populations in beam-into-gas MSE calibrations was discussed. This confirms the experimental measurements from Levinton on TFTR [41] and suggests further effort to verify statistical populations in MSE beam-into-gas calibrations, especially for those MSE systems that observe the nominally σ, $\Delta E = 0, \pm 1$ lines.

Chapter 3

Diagnostic Hardware

Implementing MSE on C-Mod requires a complex optical system with demanding requirements in the areas of mechanical toughness, polarization preservation, and vacuum compatibility. The MSE invessel periscope provides views with good radial resolution only for the plasma edge, and good angular resolution only for the plasma center. These limitations are due to the geometric constraints imposed by a radial neutral beam, which in turn is constrained by the lack of large tangential ports on the vacuum vessel. A number of mirrors and lenses both inside and outside the vacuum vessel are required to bring the light beyond the port extension where the polarimeter can be physically mounted. Before entering the polarimeter, any alterations to the polarization state will affect the MSE measurement, so polarization preservation must be carefully maintained and calibrated.

The optical mounts must be designed to be robust enough to ensure the survival and stationary positioning of all optics, especially those inaccessible inside the vacuum vessel. During disruption events, large transient forces can be experienced by the vacuum components. Over the typical run year, MSE optics may experience over 300 such large transient force events. All invessel component must be constructed from high vacuum compatible components, which excludes common optical cushioning materials such as rubber. Invessel components must also be able to withstand temperatures of 150°C during the vacuum vessel bake. These conditions combine to require that invessel optics be designed against vibration, fatigue, creep, outgassing, thermal stresses, eddy current forces, and impact.

This chapter will discuss the current successful hardware implementation used in MSE, emphasizing lessons learned from past implementations. To begin, the geometric projection of polarization angles to the MSE view will discussed, followed by a discussion of radial resolution and angular sensitivity.

3.1 Polarization mapped to the C-Mod MSE viewing geometry

When measuring angles, it is crucial to map angles in free space into the MSE viewing geometry, discussed in Sec. 1.5. This geometric mapping converts between pitch angles in the tokamak coordinate system, and angles measured by MSE. To be certain this was done correctly, both trignometic and vectoral calculations were carried out independently and reconciled. The full expression for $\gamma_{measured}$, which is the angle between the direction of $\mathbf{v} \wedge \mathbf{B}$ and the vertical direction projected perpendicular to the viewing chord, is reproduced here for fully general viewing geometries from [29],

$$
\begin{gathered}
\tan(\gamma_{measured}) = \frac{E_{horizontal}}{E_{vertical}} = \\
[-B_V \cos\Delta \cos(\alpha+\Omega) + \sin\Delta(B_R \sin\Omega - B_T \cos\Omega)] \Big/ \\
[-B_V \cos\Delta \sin\Theta \sin(\alpha+\Omega) + \sin\Theta \sin\Delta(B_T \sin\Omega + B_R \cos\Omega) + \\
\cos\Theta \cos\Delta(B_R \cos\alpha - B_T \sin\alpha)]
\end{gathered}
\tag{3.1}
$$

where B_V, B_T, and B_R are the vertical, toroidal, and radial components of the magnetic field (the magnetic pitch angle would be defined here as $\gamma_{pitch} = \tan^{-1}[B_V/B_T]$). α is the midplane projected angle between the beam velocity and the toroidal field, Ω is the midplane projected angle of the viewing chord and the toroidal field (note that Ω is the complement of the values given in Table 1.2), Θ is the angle between the viewing chord and the midplane, and Δ is the angle between the beam velocity and the midplane. Capital letters are used to avoid confusion between these angles and those used for MSE optics properties in Chapter 4 while being consistent with previously published works. For C-Mod, the beam velocity is in the radial direction with no inclination angle, and the viewing chords have an inclination angle of $\Theta = -4.9°$ with respect to the midplane. This allows a simplified form of the projection that is accurate to a few hundredth of a degree,

$$\tan\left(\gamma_{measured}\right) \approx -\frac{B_V \sin\Omega}{B_V \sin\Theta \ \cos\Omega - B_T \cos\Theta} \tag{3.2}$$

A vectoral method of calculating the same quantity projects the vectors of interest to a plane perpendicular to the viewing chord. A series of vectors defines the magnetic field, viewing chords, and beam velocities. Vector operations are used to determine the projected angles.

$$\hat{\mathbf{v}} = [-1, 0, 0] \tag{3.3}$$

$$\mathbf{B} = [0, 1, \arctan(\gamma_{pitch})] \tag{3.4}$$

$$\hat{\mathbf{s}} = \overline{\mathrm{P_{views}P_{L1}}} \Big/ \, \|\, \overline{\mathrm{P_{views}P_{L1}}} \,\| \tag{3.5}$$

$$\hat{\mathbf{E}} = \mathbf{v} \wedge \mathbf{B} \tag{3.6}$$

$$\mathbf{E_{MSE}} = -(\mathbf{E} \wedge \hat{\mathbf{s}}) \wedge \hat{\mathbf{s}} \tag{3.7}$$

$$\mathbf{B_{MSE}} = -(\mathbf{B} \wedge \hat{\mathbf{s}}) \wedge \hat{\mathbf{s}} \tag{3.8}$$

$$\hat{\mathbf{z}}_{\mathbf{MSE}} = -(\hat{\mathbf{z}} \wedge \hat{\mathbf{s}}) \wedge \hat{\mathbf{s}} \tag{3.9}$$

$$\gamma^{\mathrm{E}}_{\mathrm{MSE}} = \arccos\left[\frac{\mathbf{E_{MSE}} \cdot \hat{\mathbf{z}}_{\mathbf{MSE}}}{\|\,\mathbf{E_{MSE}}\,\| \ \|\,\mathbf{R_{MSE}}\,\|}\right] \tag{3.10}$$

$$\gamma^{\mathrm{B}}_{\mathrm{MSE}} = \arccos\left[\frac{\mathbf{B_{MSE}} \cdot \hat{\mathbf{z}}_{\mathbf{MSE}}}{\|\,\mathbf{B_{MSE}}\,\| \ \|\,\mathbf{R_{MSE}}\,\|}\right] \tag{3.11}$$

where the vector components have been defined in the order $[\hat{\mathbf{R}}, \hat{\phi}, \hat{\mathbf{z}}]$, as radial toroidal, and vertical components. Position coordinates of L1 (the objective lens) location are given as $\mathrm{P_{L1}}$ and the viewing radii at the beam axis as $\mathrm{P_{views}}$, with $\overline{\mathrm{P_{views}P_{L1}}}$ representing the ray connecting the two points, and $\hat{\mathbf{s}}$ representing the normalized viewing chord vector.

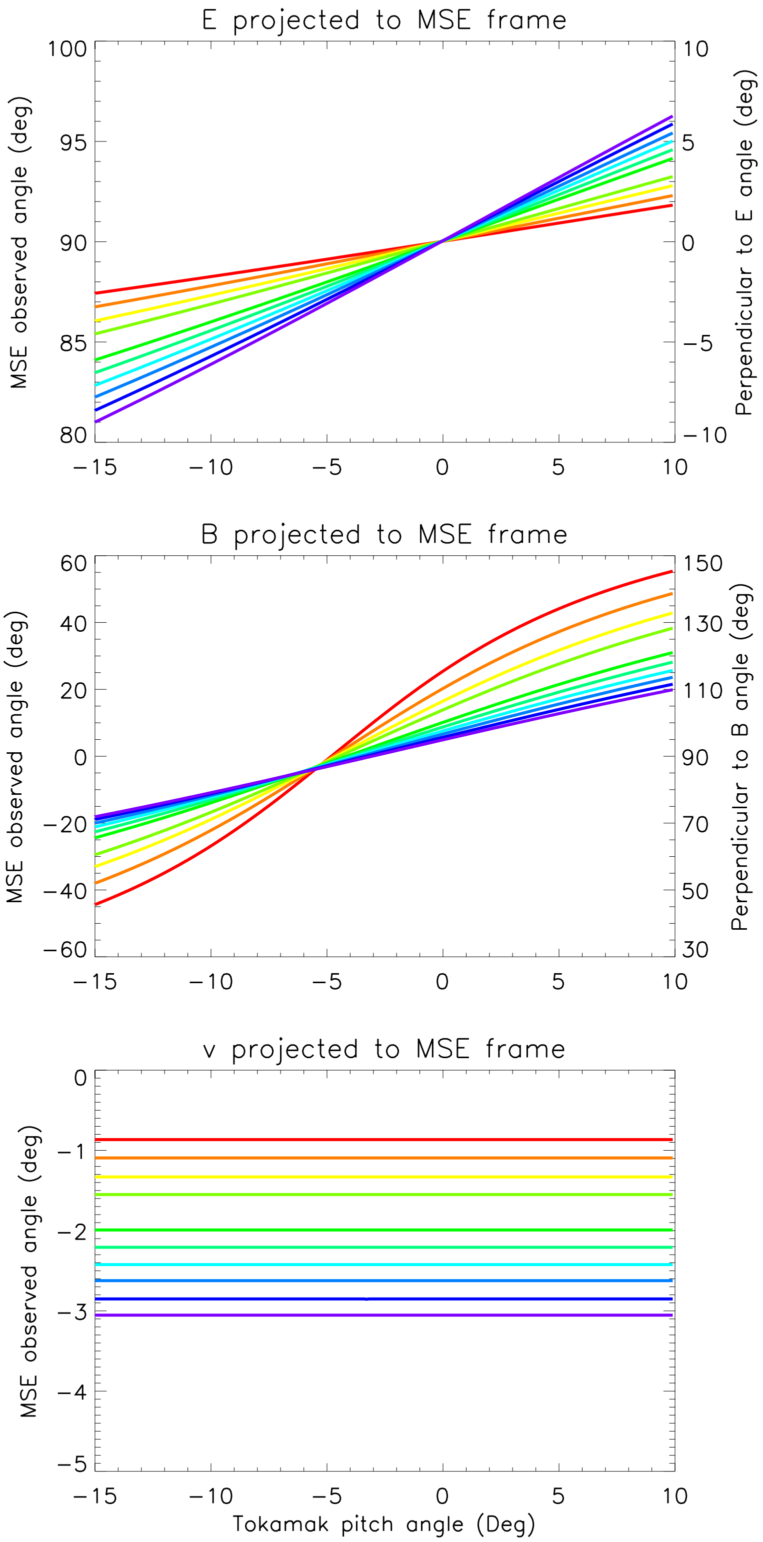

Figure 3-1: Projected angles of the three Stark-Zeeman hybrid polarization directions, Stark-Zeeman-E ($\parallel \mathbf{E}$), Stark-Zeeman-v ($\parallel \mathbf{v}$), and Stark-Zeeman-B ($\parallel \mathbf{B}$) into the MSE view as a function of the C-Mod defined pitch angle. Red is the edge MSE channel, going to violet for the core channel.

The vector approach is quite amenable to calculation using measured quantities, such as objective lens coordinates, and the intersection radii between the beam axis and the viewing chord.

Figure 3-1 shows the calculated polarization direction projected to the MSE reference viewing plane. The 2D coordinate is based on placing the projected z-axis at 90° and 0° at 3 o'clock.The perpendiculars of the given angles are shown for **E** and **B** using the right y-axis.

Stark-Zeeman-E is aligned parallel to **E** [TOP:LEFT AXIS], Stark-Zeeman-B parallel to **B** [MIDDLE:LEFT AXIS], and Stark-Zeeman-v to $\mathbf{v_{beam}}$ [BOTTOM]. Since the viewing chord, $\hat{\mathbf{s}}$, and $\mathbf{v_{beam}}$ do not change with pitch angle, the observed angles for Stark-Zeeman-v do not change with magnetic pitch angle. However, the intensities and angles of the Stark-Zeeman-B changes in such a way, see Fig. 2-7, that lines containing Stark-Zeeman-v align perpendicular to **E** [TOP:RIGHT AXIS] for statistical populations.

The projected angles can be used for pure Stark and pure Zeeman transitions as well, with Stark-$\pi \parallel \mathbf{E}$ [TOP:LEFT AXIS], Stark-$\sigma \perp \mathbf{E}$ [TOP:RIGHT AXIS], Zeeman-$\pi \parallel \mathbf{B}$ [MIDDLE:LEFT AXIS], and Zeeman-$\sigma \perp \mathbf{B}$ [MIDDLE:RIGHT AXIS].

3.2 Angular Sensitivity and Radial Resolution

The C-Mod MSE viewing geometry is constrained by the radially injected DNB. A radial beam forces any possible MSE viewing chord to tradeoff between radial resolution and angular sensitivity. Because views from adjacent ports would be distant and nearly perpendicular to the beam, MSE was designed to gather light using an invessel periscope that provides midplane viewing with an aperture between F-port and G-port by reflecting the light out of the vacuum vessel directly over the beam drift duct, as shown in Fig 3-2. The MSE periscope also provides light for the Beam Emission Spectroscopy diagnostic, or BES.

Radial resolution is determined by the beam width and the viewing chord angle, with resolution improving as the viewing angle becomes more perpendicular to the

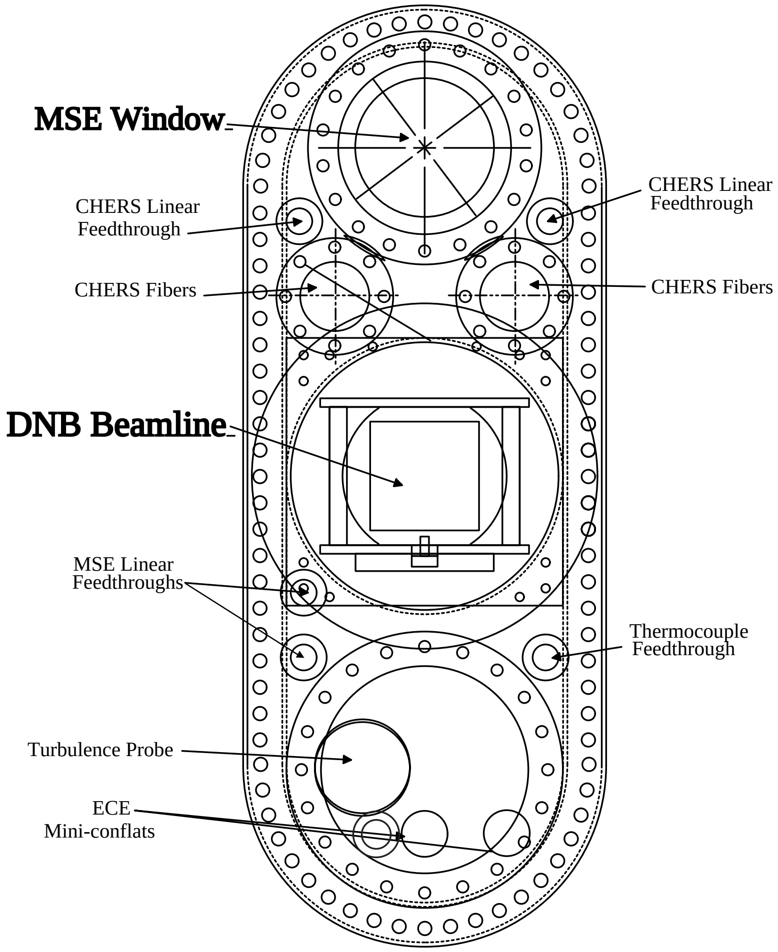

Figure 3-2: F-port horizontal flange layout. MSE light exits the vessel through the MSE window, directly above the DNB drift duct.

DNB. This can be seen by looking at the top view of Fig. 1-3 and the radial resolution plot of Fig. 3-3, where the solid line shows the radial resolution of MSE views as a function of major radius for the 9cm beam used, and the dashed and dotted lines show MSE resolution for a beam that has been apertured down to a width of 2 or 3cm.

The problem and solution for radial resolution had been recognized early on [49] during the MSE design process. MSE was designed with the premise that the neutral beam would be reduced to a 2-3cm width inside the DNB drift duct before entering the plasma. Plans to aperture the beam have been shelved due to engineering concerns, cost, the reduction of beam signal to other diagnostics as well as the loaned nature of the DNB used for this work. If MSE is to achieve the radial resolution shown as the

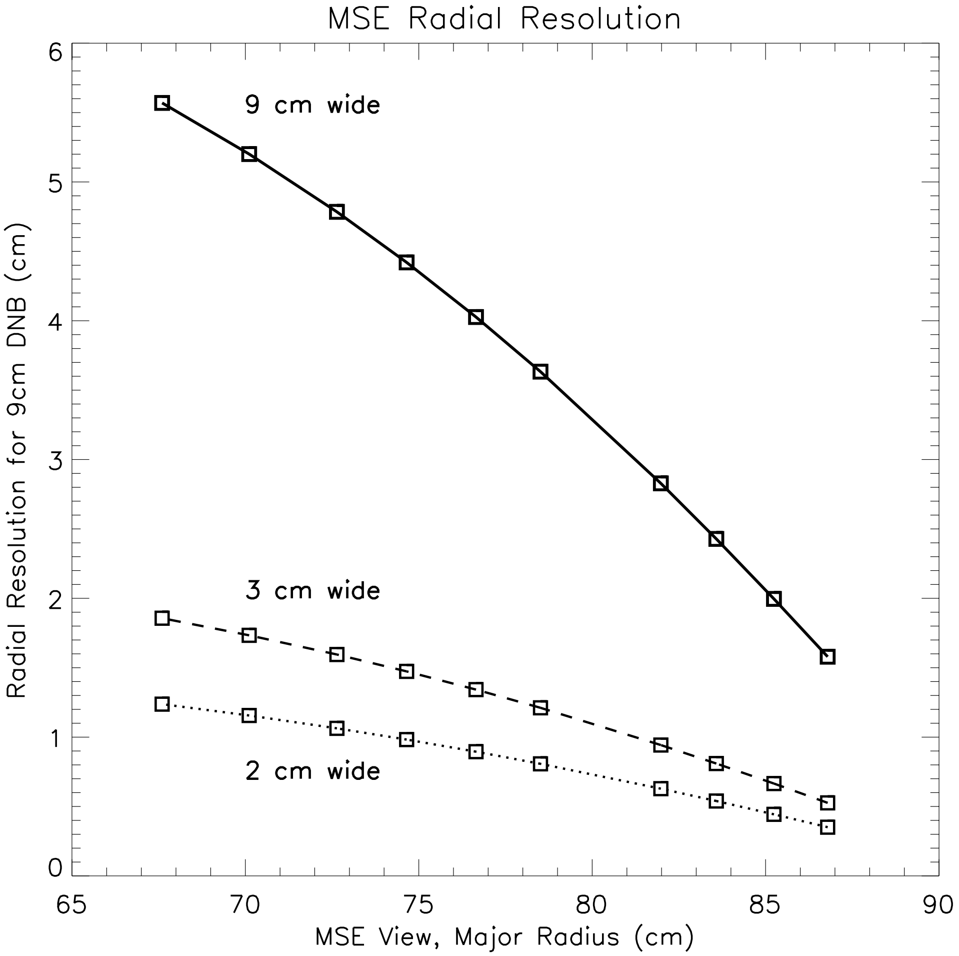

Figure 3-3: Radial Resolution as a function of viewing chord. This results from the finite extent of the DNB, which has been measured to be have a 1/e diameter of 8–10 cm, combined with the angle between the viewing chord and the DNB direction. Dashed and dotted lines show the resolution for a DNB that is apertured down to 2 or 3cm, as originally planned.

dashed or dotted curve in Fig. 3-3, a renewed effort to aperture the newly acquired C-Mod DNB must be pursued.

Angular sensitivity and spectral separation from the unshifted Balmer-α line are improved by looking more along the DNB, as seen by the angle sensitivity factors plotted in Fig. 3-4[TOP]. The reason for low angle sensitivity is due purely to the unfavorable geometric projection of the $\mathbf{v} \wedge \mathbf{B}$ direction to the MSE measurement plane, which can also be seen in Fig. 3-1[TOP]. For the range of MSE pitch angles, the angular sensitivity is essentially equal to $\sin(\Omega)$ in Eqn. 3.2. The inverse way of

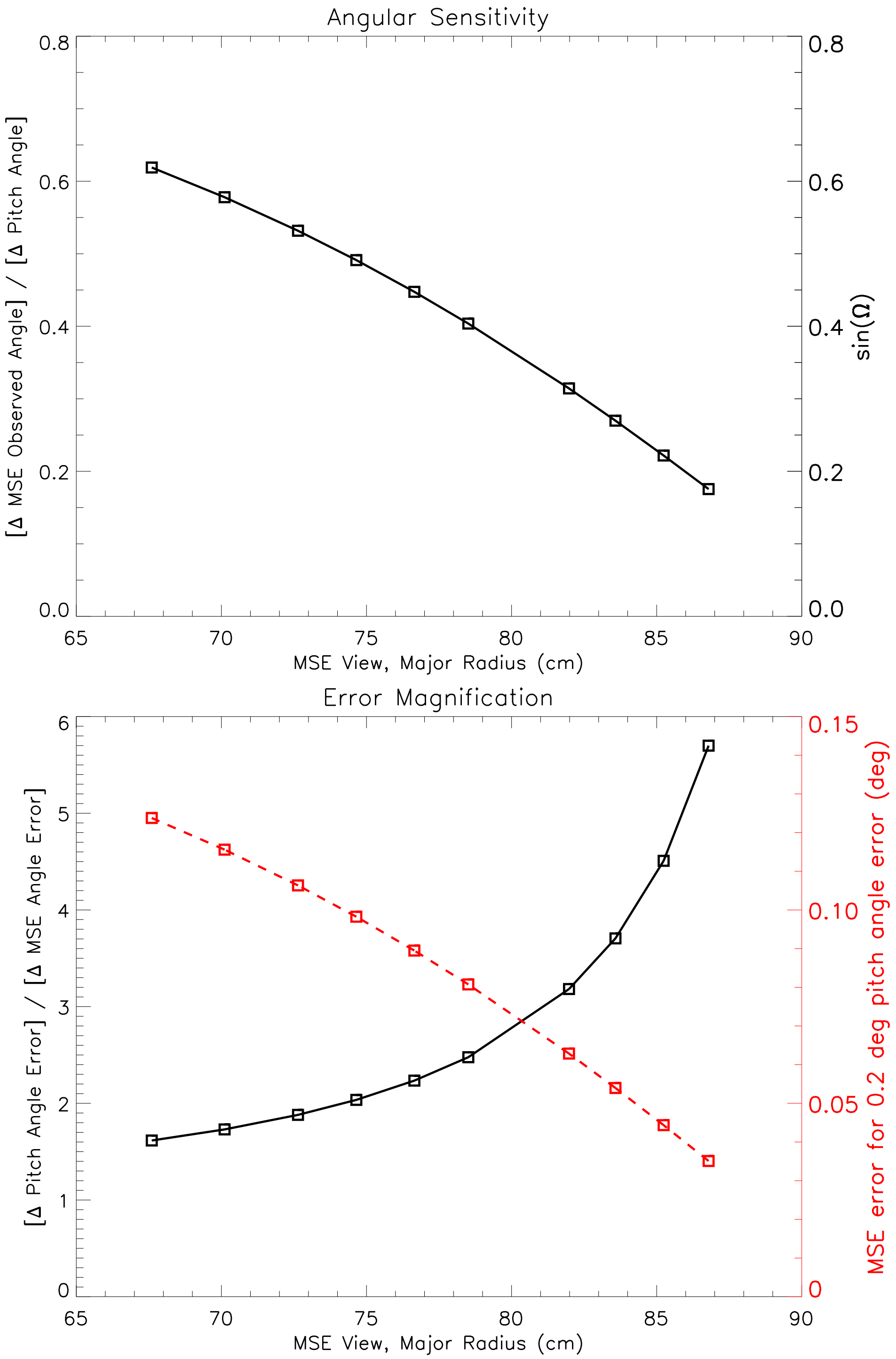

Figure 3-4: Top: Angular sensitivity as a function of viewing chord. This results from the geometric projection of **E** to the MSE viewing plane, and is equal to sin(Ω) for the range MSE measurements. Bottom: Low angle sensitivity is equivalent to high error magnification, or the multiplication factor of uncertainties, shown in the solid line as a function of MSE channel. The dashed red line using the right hand axis shows MSE measurement uncertainties corresponding to a typical “desired” 0.2° accuracy in pitch angle.

looking at the low angular sensitivity issue is a large uncertainty magnification, where uncertainties meaasured in the MSE view in must be multiplied by a large factor due to the reverse projection. This effect is shown in 3-4 [BOTTOM]. For comparison, MSE on the DIII-D tokamak has angular sensitivity factors ranging from 0.6 to 0.9 [30] using a tangential beam and tangential viewing chords.

The low angular sensitivity at the plasma edge presents a particular challenge for the C-Mod MSE. The widely accepted benchmark for MSE measurements is to reproduce the edge pitch angle calculated by the magnetic reconstruction code, which is EFIT on C-Mod. Achievable real world instrumental errors for MSE including background subtraction errors, calibration errors, and systematic errors, may range between 0.1° to 0.4°. With an edge sensitivity of 0.8, the upper end estimate translates into pitch angle errors of 0.5°. For the C-Mod edge MSE channel, meeting this same benchmark of 0.5° would require a pitch angle measurement of no more than 0.086° error. This will prove to be a considerable challenge considering that C-Mod uses same polarimeter as other MSE installations, but is trying to make the measurement in a plasma with considerably higher density with the added complexity of an extended optics set. Therefore, it might be necessary to create a new benchmark for the C-Mod MSE.

Since a primary goal for MSE is to measure lower hybrid driven current, which for a typical shot will be driven at r/a = 0.7–0.8, this might be a more suitable location to benchmark MSE on C-Mod. To do this, one would make an inner-column limited, low density plasma with a small minor radii, only 80–90% of the typical value. This would place the plasma edge at the fourth MSE channel at 81.9cm, with a more favorable projection angle. At this location, a 0.16° MSE uncertainty would magnify to the tolerable benchmark of 0.5° error in pitch angle. This is nearly a factor of two reduction in the error magnification factor, and may be achievable under ideal conditions.

Other benchmarks exist, such as measuring the pitch angle at the sawtooth inversion radius, rather than at the plasma edge. Other well characterized rational surfaces of q can also be used for this purpose. The advantage of these method is that they can be run in combination with other plasma experiments, rather than requiring a dedicated small minor radius plasma. Disadvantage will likely include larger error bars and more difficulty in interpretation, as additional measurements will be required to locate these internal surfaces.

3.3 Invessel components

In this section, the optomechanical configuration and design guidelines distilled from past experiences will be discussed. Optical concepts that affect the preservation of polarization will be introduced, with more detailed calibration and simulation results found in Chapter 4.

3.3.1 Optics Configuration

Fig. 3-5 shows a rendering of a 3D model of the invessel periscope. Each lens is labeled L, and each mirror with an M. There are nine total optical elements in invessel assembly, including a custom designed vacuum window made to suit MSE optical requirements not shown in the figure.

3.3.2 Mechanical design of optical mounts

Over the past several years, every MSE invessel component has undergone multiple redesigns motivated by the mechanical failure of the optics. This section discusses the design principles learned from previous attempts and describes the latest implementation, which has proven to be the most successful design thus far, having survived a one year run campaign without sustaining any damage that affects the collected data.

Although actual C-Mod vacuum vessel accelerations during disruptions are not fully known, past measurements place the value for the vacuum vessel at roughly 100g in the radial direction. From MSE experiences, this figure may be conservative for the forces on the MSE periscope. MSE invessel optics must be mounted such that

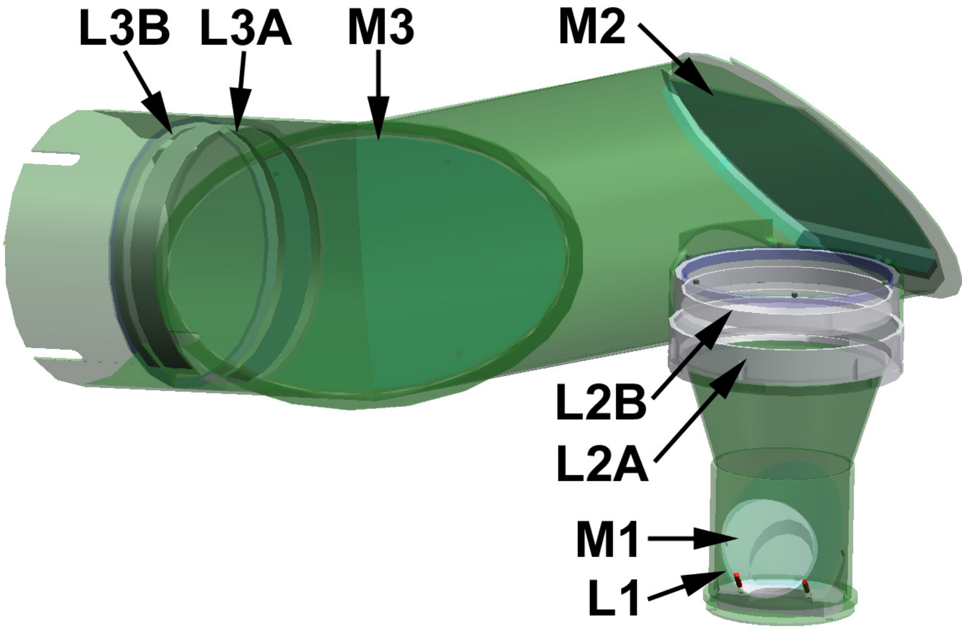

Figure 3-5: MSE invessel optics canister. 3D rendered translucent model showing the locations of invessel mirrors and lenses used by MSE. L denotes each lens, M each mirror.

it can withstand repeated disruptions (over 300 on one run campaign year) without displacement or breakage.

MSE uses a number of large invessel glass optics in C-Mod. A considerable effort over several years has gone into mechanical designs that combine the requisite shock tolerance, vacuum compatibility, and durability. Expertise with such designs was in retrospect quite lacking, evident by the number of unsuccessful attempts despite the large number of participants in the design process from MIT, U.Texas, and PPPL. The design history of each component in the MSE invessel system is summarized in Table 3.1.

This section discusses four crucial design principles learned through past design attempts. Optics damage as a consequence of diverging from one or more design principle will be summarized and contrasted with newer designs.

	L1	M1	L2 A&B	M2	M3	L3 A&B	V.Window
Jan 1999	PPPL	PPPL	PPPL	PPPL	PPPL	PPPL	Pyrex
Feb 2000	PPPL	PPPL	Inaccessible	PPPL	PPPL	Inaccessible	Pyrex
May 2002	PPPL	PPPL	PPPL/MIT	PPPL	PPPL	PPPL/MIT	SFL6
Mar 2003	OK	OK	OK	MIT	MIT	OK	OK
Dec 2004	MIT	MIT	OK	OK	OK	OK	OK

Table 3.1: History of MSE invessel components design revisions, L refers to lenses, and M refers to mirrors. V.Window refers to the vacuum window.

I. Prevent any metal to glass contact

Every MSE optomechanical design where metal contacted glass has resulted in damaged optics. The vibrational forces resulting from C-Mod disruptions has proven to always provide sufficient relative movement between the metal and glass to cause chipping and fragmentation damage.

Examples of this can be found by looking the 1999 design for the invessel M1 mounts in Fig. 3-6. These mechanisms were based on metal clips holding the mirrors with a small contact area, with small (≈ 0.5 cm^2) Teflon tabs about 1mm thick separating the clips from the glass. Over time, vibrations caused the Teflon tabs placed in between the metal tabs and the mirrors to dislodge. Even this small freedom caused subsequent motion to chip and dislodge the mirrors. The steel mirror mounting plates also had a shallow lip to trap the perimeter of the mirror and prevent in-plane movement. This steel lip caused damage on the underside of the mirror and accumulated glass shards, wedging the mirror away from its original calibrated position.

In 1999, all lenses were secured in this manner, using small area metal tabs with Teflon friction trapped between glass and metal. The result was chipping damage around the lens perimeter followed by misalignment of the lens. Lenses could not be replaced without removing the MSE optics canister from the vacuum vessel. Lens repairs were delayed until 2001 because the original optics canister was not designed to be removable through reentrant ports.

Figure 3-6: Early MSE mirror mounts had many metal to glass interfaces. Every instance of metal to glass contact resulted in damaged optics, like this early M1, which rested on a a steel base, held by metal tabs. Damage occured on both front and back surfaces of the mirror.

Displacements of MSE optics at unknown times during a run campaign renders all MSE calibrations inaccurate. Since the location of the mirrors were not known as a function of time, data taken from campaigns in which mirrors changed positions could not be used. Mirrors, unlike the lenses, could be repaired invessel, but conservative upgrades of the 1999 concept with additional reinforcements proved unsuccessful in 2000, see Fig. 3-7.

Figure 3-8 shows the 2001 PPPL designs for the lens mounts. All pieces shown in Fig. 3-8 are steel except for the lenses (parts 7 & 12) and and a Vespel spacer ring (parts 5 & 10). Upon delivery to the PSFC, serious concerns over the possibility for additional vibrational damage resulted in modifications to the design. The devised solution is shown in fig 3-9, a complex Teflon gasket constructed from 20 mil Teflon sheeting with numerous staggered folds at three different depths to seperate steel from glass. Although nearly impossible to assemble, this single piece of Teflon completely eliminated all metal to glass contact and is volumetrically trapped between the glass

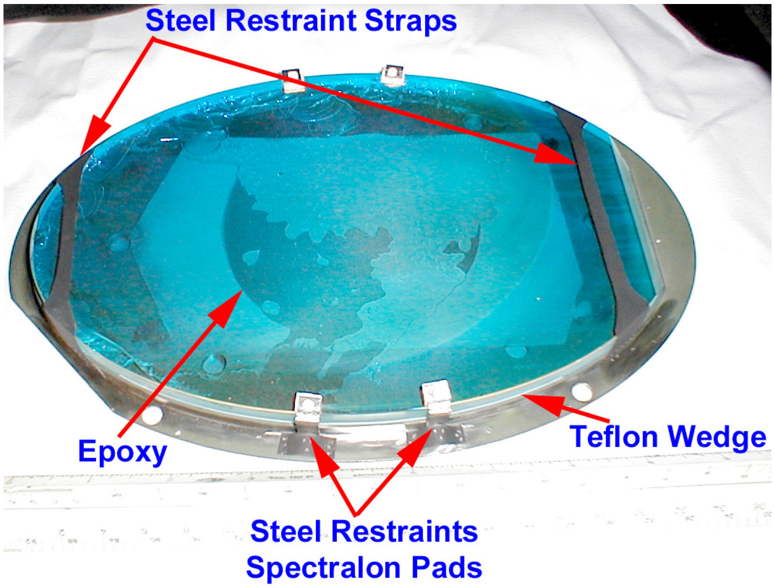

Figure 3-7: A conservative upgrade of the MSE mirrors mount perfomed under tight time restaints using additional restraints, a low outgassing vacuum compatible epoxy, and improved tabs was insufficient to prevent further damage.

and metal components, unable to vibrate out of position. The resulting assembled lens module is seen in Fig. 3-10. The teflon tabs that separate steel from glass can be seen clearly from the angle in the figure, but protrude miniminally when viewed along the lens axis. With this important refinement, the lens assembly satisfies all four design principles and has survived invessel without incurring any damage since May 2002.

The current design for all lenses and mirrors surrounds each optical component with stainless steel and/or Inconel, but separates the components with a Teflon layer. The contact area between the optic and its support is maximized to reduce local stresses.

II. Trap all Teflon volumetrically or mechanically

In 20/20 hindsight, it is easy to criticize the engineering decision to rely on friction to trap the slipperiest material ever invented in a vibrational environment, but for the original MSE design, this was thought to be sufficient [50]. When the Teflon tabs inevitably dislodged, the lack of compressional forces holding the mirror to the steel

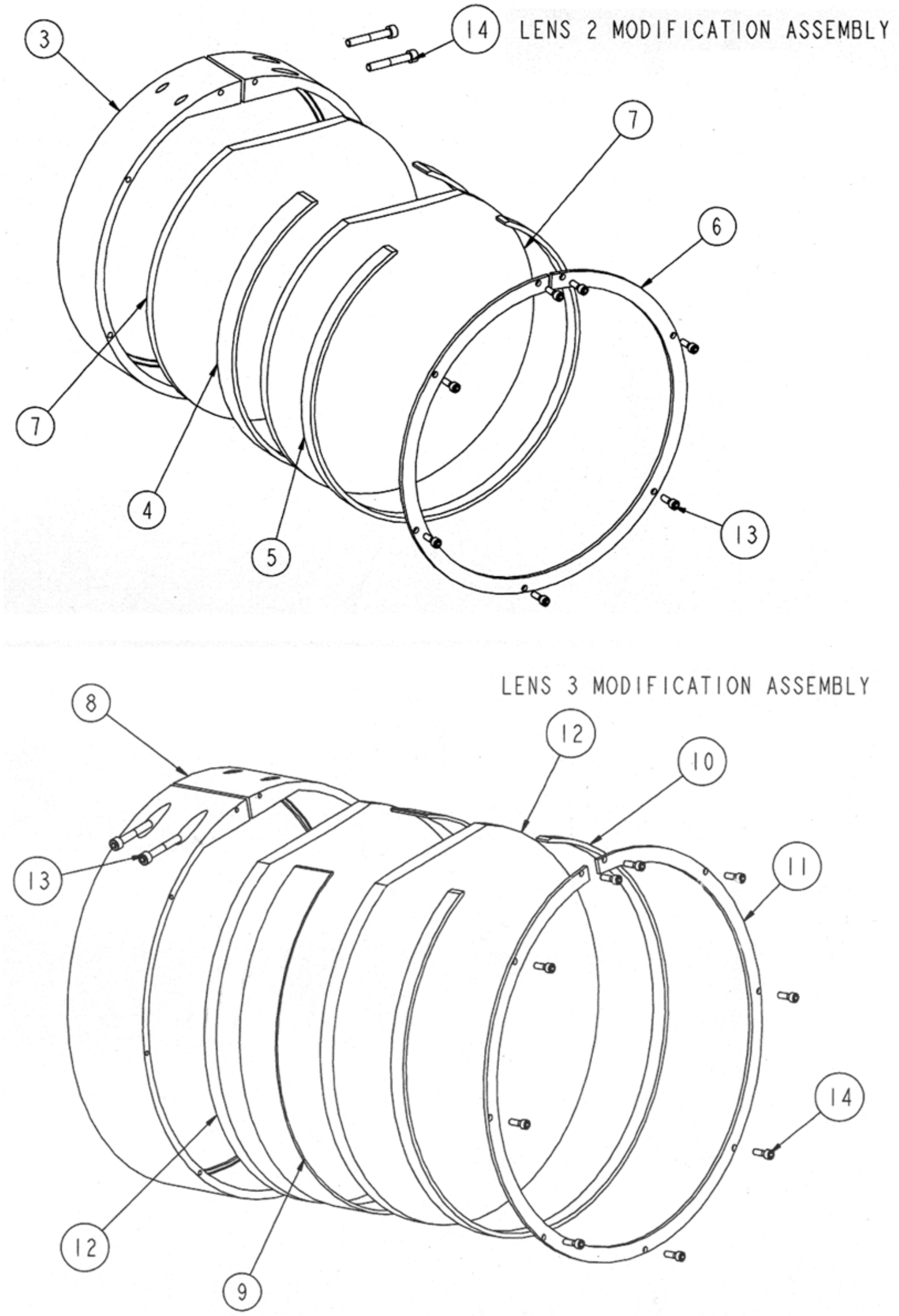

03	02	01	PART NO.	NOMENCLATURE OR DESCRIPTION	DRAWING NO.	MATERIAL
	2	2	14	HEX HD SCREW #4-40 UNC X 7/8 LG	COML	STEEL
	7	9	13	HEX HD SCREW #2-56 UNC X 1/2 LG	COML	STEEL
	2		12	LENS 3 MODIFIED	E-MIT117-2	SEE SPEC
	1		11	LENS 3 RETAINING RING	E-MIT117-5	SEE DWG
	1		10	LENS 3 RETAINER	E-MIT117-4	SEE DWG
	1		9	LENS 3 SPACER	E-MIT117-3	SEE DWG
	1		8	LENS 3 MOUNT	E-MIT117-1	SEE DWG
		2	7	LENS 2 MODIFIED	E-MIT116-2	SEE SPEC
		1	6	LENS 2 RETAINING RING	E-MIT116-5	SEE DWG
		1	5	LENS 2 RETAINER	E-MIT116-4	SEE DWG
		1	4	LENS 2 SPACER	E-MIT116-3	SEE DWG
		1	3	LENS 2 MOUNT	E-MIT116-1	SEE DWG
			02	LENS 3 MODIFICATION ASSEMBLY	THIS DRAWING	----
			01	LENS 2 MODIFICATION ASSEMBLY	THIS DRAWING	----

Figure 3-8: MSE lens mount assembly drawing showing the successful design implemented in 2001 to house the invessel MSE lenses.

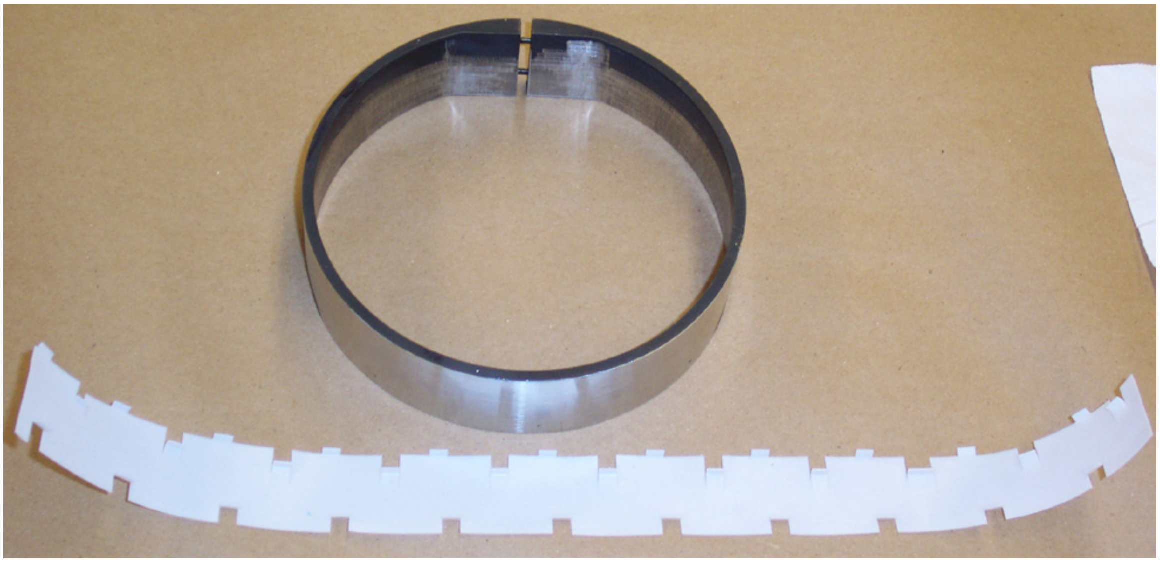

Figure 3-9: MSE lens retainer ring shown next to the Teflon gasket designed at MIT. The Teflon gasket utilized numerous folded 1/4" tabs staggered for each of the three metal to glass interfaces it was designed to eliminate. Note that the lens retaining ring was remachined to allow room for the Teflon gasket, so original dimensional drawings are no longer accurate.

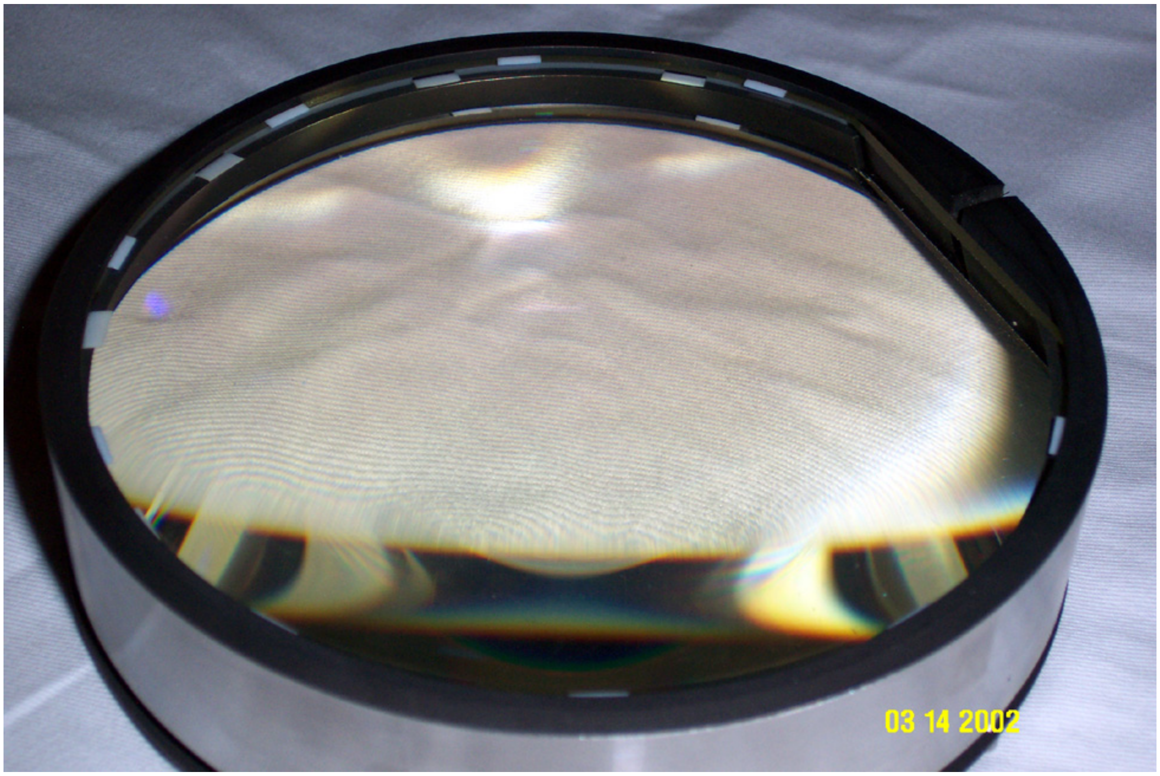

Figure 3-10: MSE lens mount assembly drawing showing the successful design implemented in 2001 to house the invessel MSE lenses. This implementation survived invessel without incurring any damage since May 2002.

backplate caused the mirrors to break after subsequent disruptions.

The tabs were remanufactured by PPPL in 2000 out of a harder polymer (Spectralon) with an extended button designed to minimize in-plane motion. This conservative redesign also proved to to be inadequate, failing much in the same way as the 1999 design, with the loss of the Spectralon tabs leading to metal to glass contact. Fig. 3-11 shows the 2000 design.

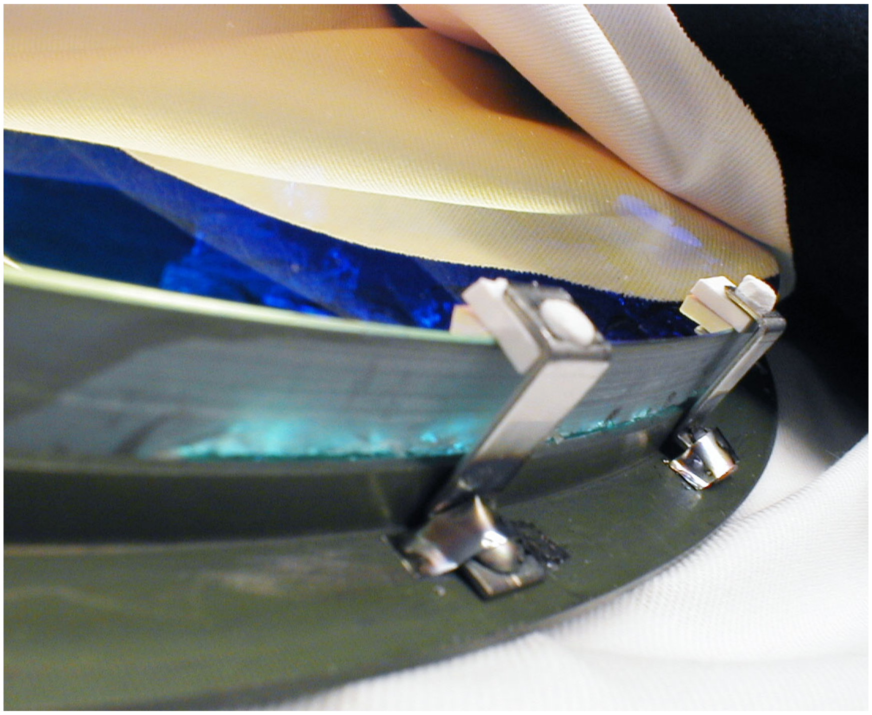

Figure 3-11: Early MSE mirror mounts relied on small metal tabs with a Teflon cushion. The earliest iterations used frictional trapping for the Teflon, while the iteration illustrated here used a protruding button. Neither method worked successfully.

The repeated failure of the critical cushion between metal and glass due to vibration leads to the second design tenet. *All crucial interface materials should be volumetrically trapped or mechanically fastened.* Teflon sheeting is now the preferred material due to its compliance and wide availability in a variety of thicknesses. Outgassing of water from Teflon had been an initial concern, but has not proven to be a problem possibly due to the the high surface area to volume of thin sheets. Care is still taken to use the minimal amount, see Fig. B-4 and B-8.

Volumetric trapping calls for the full enclosure of Teflon, eliminating the possibility of migration by not allowing any open volumes around the Teflon. This is the current mechanism for holding the Teflon gasket in the L2 and L3 assembly, as well as all Teflon used the mirror assemblies save the top gaskets. Mechanical fastening uses physical fasteners to anchor the Teflon rather than friction. This is the method used in the the current M2/M3 gaskets, which have a series of through holes for bolts, see Appendix B.

III. Put only compressive stresses on optics

The 2001 mirror mounts are shown in Fig. 3-12. This design was based on directly bolting the mirror to the support plate, avoiding the hold-down clips in previous designs. Vespel bushings were used to avoid metal to glass contact. This implementation failed during the 2002 run campaign, with new failure mechanisms compared previous implementations. While the 2000 tabs based design suffered incremental vibrational damage, the 2001 bolted mirrors suffered single event catastrophic cracks.

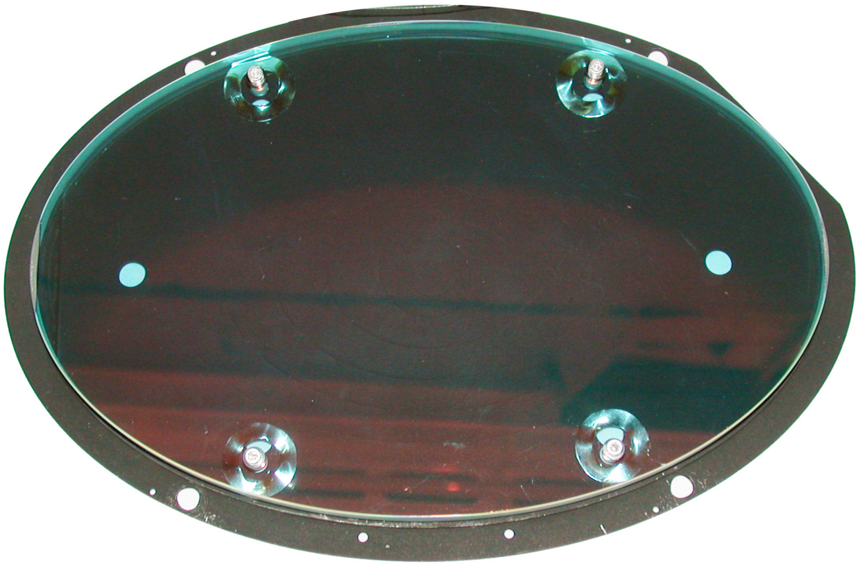

Figure 3-12: The second major design of the MSE Mirror 2 & 3 (shown here) mechanical mounts. This version drilled small holes through each mirror, and bolted them directly to the backplate. This configuration placed in-plane tensile stresses on the mirrors, and led to large single event failures of each mirror.

Both large mirrors, M2 and M3, cracked into two pieces after the 2002 summer campaign, Fig. 3-13. The exact failure mechanism was never identified, but two

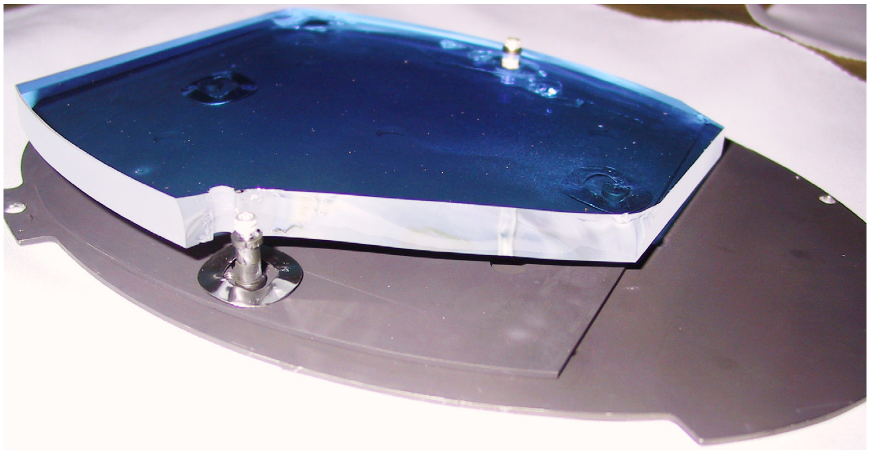

Figure 3-13: Both the bolted M3 and M2 (shown here) failed within a single run campaign. This single event catastrophic failure mode led to the design criterion of placing the mirror under only compressive stresses.

theories appear plausible. The first focuses on the difference in thermal expansion coefficients betweeen the Vycor® mirror subtrate and the stainless steel mounting plate. It was suggested that the damage occured during the pumpdown bake, when invessel components can reach 150°C. This theory would have the mirrors broken even before the run began, and may not be consistent with observations by BES, which reported changes in their viewing geometry during the middle of the run. An alternate theory postulates impact damage between the sides of the mirrors with the canister walls under disruption forces. There is chipping damage near the suspected impact locations that lends support to this conjecture, and fracture mechanics calculations show that a 1 m/s relative velocity impact between the glass and metal canister wall can create the necessary stress to propagate a crack in the mirror. Calculations show that this impact velocity is achievable with C-Mod disruption events.

Both of these failure mechanisms share the fact that the mirrors failed under tensile stresses, leading to the third design principle: *place only compressive stresses on optics.* Currently, no optical component is held using tensile forces, and all optical components are protected against tensile forces even in case of impact.

IV. Protect against direct impact

Disruption forces within the MSE optics canister arise from eddy currents induced by the rapid change of magnetic field resulting from the sudden termination of plasma current during a disruption. Because the MSE canister is a large cylinder, there is a possibility of gross elastic deformation of the toroidal section of the housing. As there are no such forces in the optical elements, this could have led to the relative velocities suspected to be responsible for the breakage of mirrors during the 2002 run campaign.

Up until 2003, the mirror perimeter was left open, with a small gap of 2mm between the edge of the mirror and the steel canister. After the suspected impact failure of 2002, protection against direct impact was added to the mirrors in the form of a steel rim. This design placed significantly more metal around the mirrors, and to satisfy design principles I and II, more Teflon was incorporated into the design.

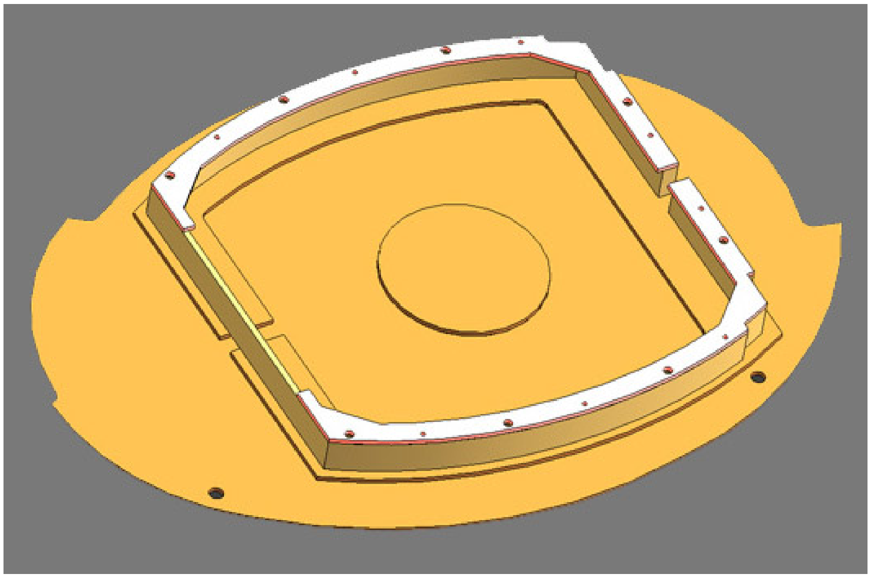

Figure 3-14: Rendered drawing of latest MSE Mirror 2 design showing all metal components. The mirror is held down around the entire perimeter, has zero glass to metal contact, is free of tensile stresses, and protected from impact. Drawings of the parts used in the lastest incarnation of the MSE mirrors are included in Appenix B.

The current mirror mount design is similar to the successful lens mounts, surrounding the mirror with a steel frame, and captured along the entire perimeter via a front retaining plate, eliminating the risk of direct impact. All glass to metal contact is eliminated by use of Teflon sheets, which are volumetrically trapped by surrounding components and rendered immobile through their geometric arrangement, see Fig. 3-14.

3.3.3 Additional Mechanical Improvements

Several additional improvements have been made to the MSE invessel components in the past several years, most notably the ability to change the field of view without sacrificing light throughput and the ability to remove the optics housing through a reentrant port. This was accomplished by separating the original single piece canister into two separate components, Fig. 3-15, in 2002. This separated the housing for M1 and L1, forming a freely rotating "turret" separate from the rest of the assembly. Prior to this modification, the desired viewing radii for MSE and BES was selected by rotating M1 relative to L1. This effectively misaligned the optical system, reducing the light gathering power of the system.

The splitting of the MSE periscope allowed for its removal from the vacuum vessel through a reentrant port. This is necessary to repair L2A/B and L3A/B, which had to be left unrepaired during the 2000 opening due to the inability to remove the original optics canister.

The original vacuum window was a commercially available product using a 1 cm borosilicate glass (BK7/Pyrex) as the transmissive media. This glass is known to have a Verdet constant of 4.1 rad/m $\cdot$ T. After some sample EFIT calculations of the stray fields at the window's location, 22 cm above the midplane, it was determined that the poloidal feedback coils induced unacceptable Faraday rotations in this window with temporal variations much larger than 0.1°. The fields through the window also had spatial variations over the window diameter greater than 0.1° in certain conditions. At the plane of the vacuum window, the MSE light is defocused, so each channel can be transmitted over an unknown large section of the vacuum window. Since there was no obvious method of measuring the local field with high spatial and temporal resolution, the decision was made to construct a custom window from SFL6, a low

Figure 3-15: Modified MSE split can allowing viewing angle adjustment and removal through a reentrant port.

Verdet constant glass. A Viton sealed vacuum window was custom designed and maufactured at the PSFC, because no vendor could bond SFL6 to metal as is done with borosilicate glass. Although the Viton seal has held for several years, a more permanent solution would be desirable, so any advances in vacuum bonding custom glasses to metal should be of interest to the MSE group.

The MSE mirror mounting plates were also redesigned to reduce eddy currents and increase stiffness, shown installed in Fig. 3-16. Large time derivatives of magnetic fields from a disrupting plasma cause loop currents in the mounting plates, which in turn experience $\mathbf{J} \wedge \mathbf{B}$ forces with the confinement field. This results in bending moments in the plate but not in the nonconducting optics. In the current design, the mirrors are well coupled mechanically to the mounting plate, such that bending forces would be transmitted from the plate to the mirrors. To minimize bending moments in the glass, the plates were redesigned to minimize cross sectional area susceptible to eddy currents. Protruding ribs with broken sections were added to the back to increase bending stiffness without adding to eddy currents. The entire piece was

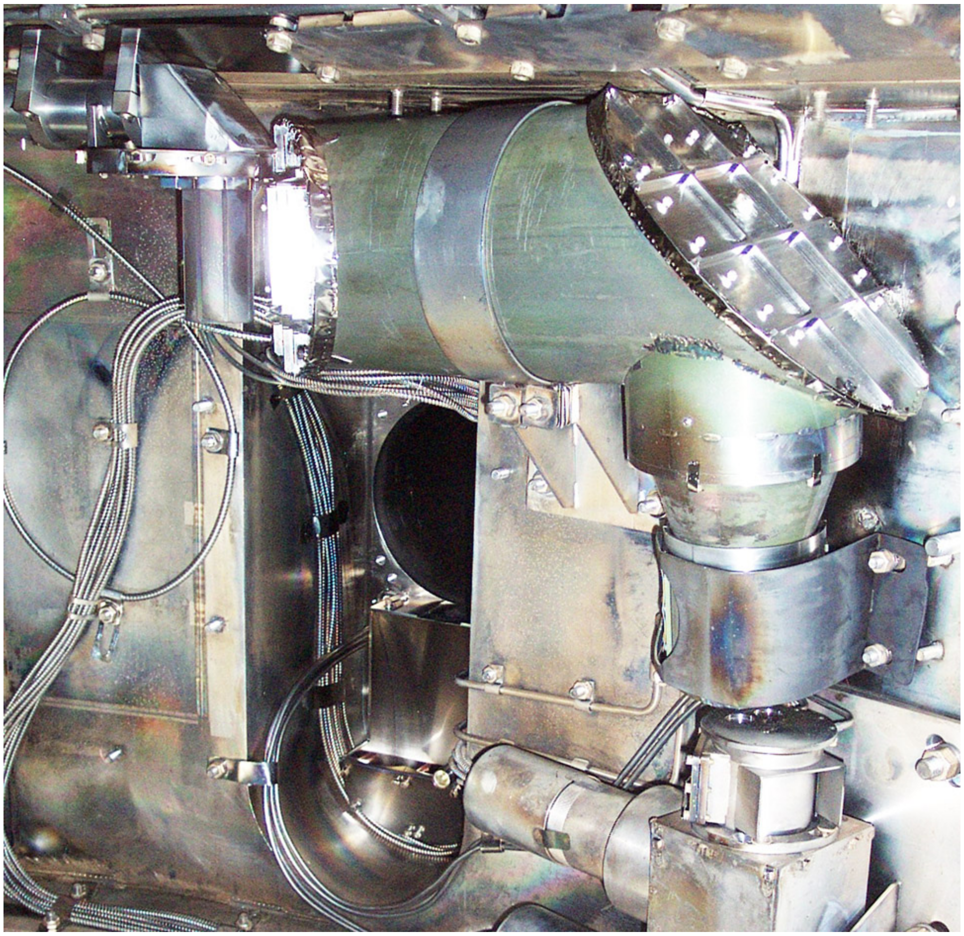

Figure 3-16: Inconel mirror backplates stiffened and designed to minimize eddy currents. Seen here installed for its maiden voyage in March 2003.

constructed not from stainless but from Inconel, which has half the conductivity of original stainless steel and greater stiffness, thereby reducing both bending moment and the bending deflection.

The MSE mirrors are designed to make approximate right angle reflections to the incident light and are mounted in a cylindrical canister. The resultant basic shape of such mirrors are elliptical. Fabrication of optics had always been through outside vendors at high expense and long lead times.

There was insufficient time to procure properly shaped optics from an external vendor in 2003, so a new rapid in-house method was developed to modify existing spare mirrors for use in the new design. A procedure was developed to make a set of high precision elliptical cuts on an abrasive water jet at MIT. Using the water jet cutter allowed complex 2D shapes to be cut, even through brittle materials such as glass. A great deal of development time was spent cutting prototypes before there was enough confidence in the procedure to cut the irreplacable (within the 2003 maintenance period) mirrors.

As a valuable side benefit to using water jet cutting, the speed and low cost of making prototypes allowed, for the first time, a MSE mirror design to be destructively tested. This was done for the 2003 design. A series of tests were performed on a full mockup of the final components. A steel mounting plate was used in the test using a plate glass dummy mirror. The prototype survived a bending test with a point load of 2000N, exceeding the worst calculated case for a disruption scenario by 150%, direct side impacts with a steel head hammer causing 200g of acceleration to the assembly, and 800g of vibrational accelerations. The prototype was finally tested to failure at over 1200g of impact bending acceleration, many times beyond the worst case scenario expected inside the tokamak.

3.3.4 Optical Properties of Invessel Components

Much of the cost and long lead times required to procure MSE optics comes from the fact that they must meet stringent polarization preservation properties.

With reflective optics such as mirrors, there are two possible methods for affecting the polarization state. One is a difference in reflectivity for the p- (TE or transverse electric, polarization parallel to the plane of reflection) and s- (TM or transverse magnetic, polarization direction perpendicular to the plane of reflection, from the German "senkrecht" meaning perpendicular). The other is a relative phase change introduced between the s- and p- components of the reflected light. The mirrors used in MSE are front surface dielectric mirrors on a Vycor$^{\circledR}$ substrate. While dielectrics can be tailored to minimize differences in s/p reflectivity and phase shifts, the operating range limits incidence angles and wavelengths. The mirror properties were calibrated *in situ* via polarized light calibrations. See Chapter 4 for details of this invessel calibration.

For transmissive optics such as lenses, the primary concern is with the Verdet constant of the media. Faraday rotation introduced by a uniform material with Verdet constant V, magnetic field **B**, and ray path ℓ through the material is

$$\Delta\theta = \int V\mathbf{B} \cdot \mathrm{d}\ell \tag{3.12}$$

In order to minimize Faraday rotation through transmissive optics, every transmissive element in front the polarimeter is constructed from Schott SFL6 glass, which exhibits a very low Verdet constant of $< 0.05\,\mathrm{radian}\cdot\mathrm{Tesla}^{-1}\cdot\mathrm{meter}^{-1}$. The thickness of the only lens (L1) with a component in the toroidal direction is minimized (5mm) Although these efforts are made to minimize Faraday rotation effects, calibration is still required. Beam-into-gas calibrations were originally intended to measure the residual Faraday rotation, see Chapter 5. However, suspected contaminant polarized light has kept the beam-into-gas measurements from being useful for this purpose. Suggestions on how to solve the beam-into-gas issues will be discuss in Chapter 5. Another techinique of using a fixed invessel linear polarizer to measure the Faraday effect is also currently underway. Also, a lab measurement of the Faraday rotation in each MSE optic was performed.

3.3.5 Bench testing of the Verdet constant of MSE optics

Spare lenses and a spare vacuum window purchased at the same time as those currently in use were tested in the lab using high field permanent magnets, with measured average fields through the optics reaching about 0.25 Tesla.

The results showed all invessel components were within the specified Verdet constant of $< 0.05\,\mathrm{rad/T\cdot m}$, but several lenses were tested at 2-3 times the specified Verdet constant value, but not exceeding a high anomalous value of $0.15\,\mathrm{rad/T\cdot m}$. All lenses measured with a high Verdet constant are oriented in the radial direction outisde the toroidal field coils, and would only be affected by the stray radial magnetic field, $\mathrm{B_r}$. Typical expected values of $\mathrm{B_r}$ in the location of the external lenses are below 0.25T, which would create Faraday rotation angles totaling approximately 0.1°. To calculate the apparent errors caused by Faraday rotations to pitch angle measurements, one needs to multiply by the uncertainty multiplication factor shown in Fig. 3-4[BOTTOM]. For the edge channel with the highest uncertainty multiplication, a Faraday rotation of 0.1° is equal to a 0.6° in pitch angle. Things improve rapidly going towards the core, such that by the fifth chord at 78cm, the 0.1° only magnifies to 0.25°.

Two additional transmissive elements, described in the next section, are photoeleastic modulators made of fused silica, which has a high Verdet constant. The crystals are about 1cm thick, and are in locations that can experience stray radial magnetic fields. An estimate of the effect of Faraday rotation by the PEM crystals places the maximum effect at under 0.3°, but because the crystals are active optics modifying the polarization of incident light, a more detailed calculation or simulation needs to be done, particularly for the effect of two PEMs in series. If the results show significant effects, the PEMs may need to be magnetically shielded from stray fields.

The bench measurements show the necessity of measuring the total *in situ* Faraday rotation induced by the entire MSE optics set. While not sufficiently accurate to replace *in situ* calibration using full fields, these bench measurements have place upper limits on the effect Faraday rotation can have on MSE measurements. In particular, even the maximum values given in this section cannot explain the difference between invessel calibrations and angles measured during beam-into-gas calibrations. These Faraday rotations are also lacking in sufficient dynamic range to explain differences between multiple plasma measurements with similar fields. For both plasma and beam-into-gas, other mechanisms need to considered to explain the observed angles and polarization fractions.

3.4 Air-side components

After the MSE light exits the vacuum vessel, it traverses a set of relay optics to clear the toroidal coil cryostat and concrete shielding before it can enter the polarimeter and image dissector. This section describes the optical components outside the vacuum vessel.

3.4.1 Air-side relay optics

Space constraints around the F-port flange does not permit the polarimeter to be situated directly outside the vacuum window, so a set of relay optics is used to transmit the light approximately 30 cm radially outwards to clear the cowl. Although these lenses are not subjected to the strong fields found inside the vacuum chamber, they too are constructed from SFL6 to minimize Faraday rotation from stray fields. The external lenses are enclosed in a blackened cylinder to minimize surface reflections. Figure 3-17 show L4A/B and L5A/B pairs of plano-convex lenses inside the relay optics tube.

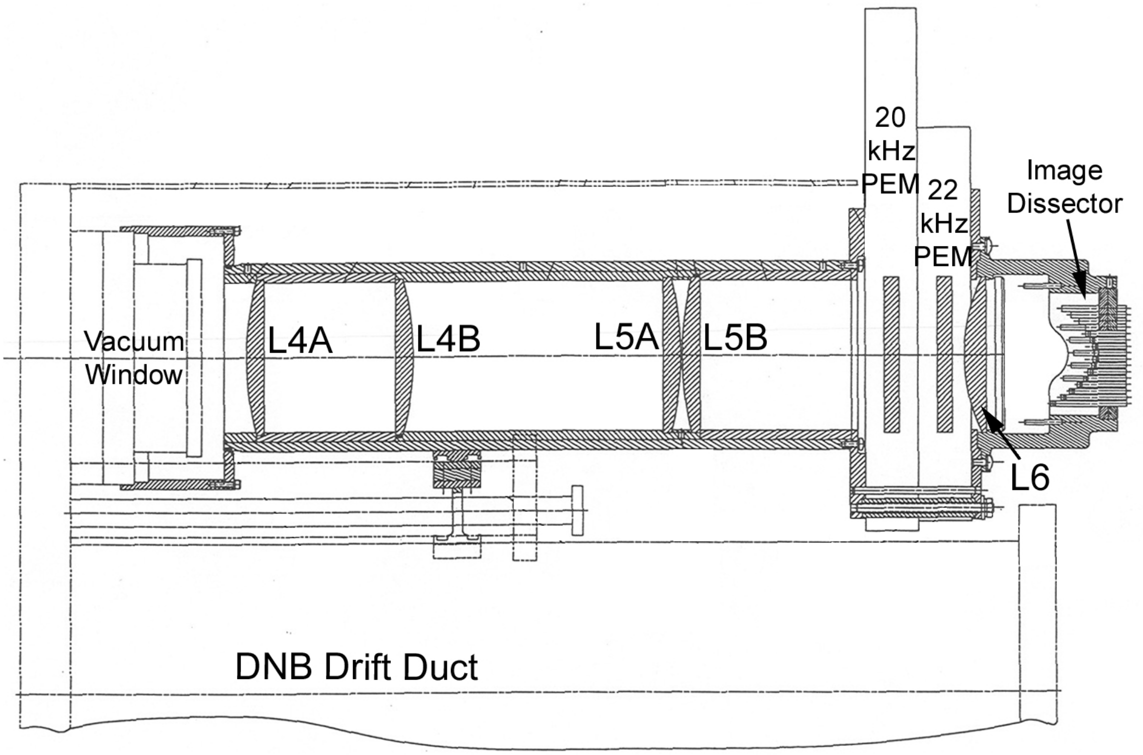

Figure 3-17: MSE air-side optics layout, showing the vacuum window, relay optics train, PEMs, and image dissector.

3.4.2 Photoelastic modulators and linear polarizer

The polarimeter consists of the next three optical components, two photoelastic modulators and a linear polarizer. These components make up the core of the diagnostic, encoding the polarization information of the Stokes vector into amplitude modulations detectable with photodetectors.

The photoelastic modulators, or PEMs, are waveplates with time varying retardance. They operate using the principle of stress induced birefringence, where a stress is used to alter the index of refraction of a material anisotropically. The C-Mod MSE (as well as most other MSE implementations) uses commercial PEMs made by Hinds Instuments. The PEM operates by resonating a solid crystal with non-unity stress birefringence coefficients with a piezoelectric transducer. The birefringent material varies depending on the operating wavelength to achieve the proper retardance. For Hα, fused silica is used, and for the two model PEM-90 PEMs used on C-Mod, the crystal is approximately 1 cm thick, and roughly 12 cm square with an open aperture of roughly 10 cm. By inducing a uniaxial, time varying stress in the crystal, the index of refraction in one direction of the crystal is varied in time. Each PEM in the pair is modulated at different resonance frequencies, so the encoded frequency can be separated using their resonance frequency. The PEMs used on C-Mod are inherited from the TFTR MSE, and operate at 20.17 and 22.17 KHz, varying slightly as a function of temperature.

PEMs are used in a full Stokes polarimeter as half-wave waveplates with time varing retardance. A waveplate has different indices of refraction in each principle axis, often called the "fast" and "slow" axis, which introduces a phase difference, or retardance, between electric fields in each axis. A n$^{\text{th}}$-order half-wave waveplate introduces a $(2n + 1)\pi$ phase difference such that linearly polarized light at angle θ relative to the axes will emerge with the polarization angle reflected across the axes at $-\theta$. During normal operation, the MSE PEMs oscillate between a positive half wave plate to a negative half wave plate. Polarized light passing through the PEM undergoes time varying changes in ellipticity and polariation direction, which results in intensity modulations after passing through a linear polarizer. Section 4.1.3 models this modulation mathematically.

3.4.3 Image dissector and transfer fibers

Through the polarimeter and the final focusing lens, L6, the MSE optical sytem has maintained and processed the entire invessel image, much like a camera optics set. The image detector is the apparatus by which individual channels are separated within the MSE image. The optical image is shared with the Beam Emission Spectroscopy (BES) diagnostic, viewing different regions of the image.

The original 1999 image dissector consisted of an array of through circular holes in a block of aluminum. Quartz transfer fibers used to relay the light to remote detectors were mounted into ferrules made from stainless steel tubing and inserted. The image plane was not a flat plane, but rather an ashperical surface because a planar image would have required a costly custom lens fabricated from SFL6. Instead, the fiber ends were inserted to differing depths such that their ends were on the image plane.

To accommodate two separate diagnostics, MSE and BES, about half the image dissector was filled by a rectangular array of holes sized for 4 fiber ferrules. This was done to allow MSE and BES fibers to be interchangable. In channels desirable to both MSE and BES, MSE ended up with view locations several centimeters from the beam centerline, leading to poor signals. Each of these edge MSE channels used a total of 16 fibers split into 4 ferrules. For views near the core, where BES is not interested in viewing, a more optimal 7 fiber ferrule sized hole was used exclusively by MSE, with view locations near the neutral beam axis. These core MSE channels employed 14 fibers divided into two ferrules in the dissector.

In 2001, after early measurements revealed an signal to noise ratio too low to make meaningful MSE measurments for several MSE channels, steps were taken to improve the MSE light gathering capabilities. A new image dissector and fiber ferrule scheme was devised to allow MSE to view the brightest portion of the beam, as well as more narrowly confining the vertical extent of the MSE view. Due to the cost of increasing the number of optical fibers, significant increases in the number of fibers per channel was not possible, but the core channels were upgraded from 14 to 16 fibers each. The dissector ends of the fibers were all repolished to repair scratches and broken ends that had occured during previous operation.

Due to space constraints in the tokamak cell, as well as to isolate electronic noise, the remaining components of MSE are kept in an external diagnostic lab. As the polarimeter has encoded the Stokes vector information into amplitude modulations, polarization preserving optics are not necessary after the polarimeter. To carry the light to the photodetectors in the diagnostic lab, about 30 meters away, a set of large diameter solid core silica fibers are used. The fibers used in MSE are 1.1 mm in diameter, consisting of a 1 mm transmissive core of fused silica surrounded by a buffer coating, and a nylon sheath. The transfer fibers are recycled from the TFTR MSE experiment to reduce cost, and would be a high cost item in an upgrade to the MSE channel count.

3.4.4 Interference Filter & Filter tuning

The fibers run approximately 30 meters from the tokamak cell to a diagnostic lab where they enter a filter cavity. Up to this point, no intentional spectral filtering has been imposed by MSE optics, although the dieletric mirrors do have a limited reflective range in wavelength. Isolation of one component of the Stark-Zeeman emission is performed using narrow bandpass interference filters. MSE uses custom central wavelength 2" dia. bandpass filters from Andover with FWHM transmission of about 9Å. Because each MSE channel views beam emission at a different angle, each channel requires a filter centered at a different wavelength to compensate for the varying Doppler shift. The MSE filter functions are shown in Fig. 3-18.

viewing chord The passband of interference filters can be varied in wavelength in two ways, using temperature or the incidence angle. Both methods change the apparent interface spacing to incoming radiation, thus changing the constructively interfering wavelength that is passed. MSE currently uses temperature tuning by placing the filters in an electric oven. The oven has a capability of reaching 60°C and the filters have a tuning coefficient of 0.17 Å/°C. This translates to a one way (red) tunable range of +6.5Å. This capability allows the MSE filters to be precisely tuned to the right passband to maximize the polarization fraction.

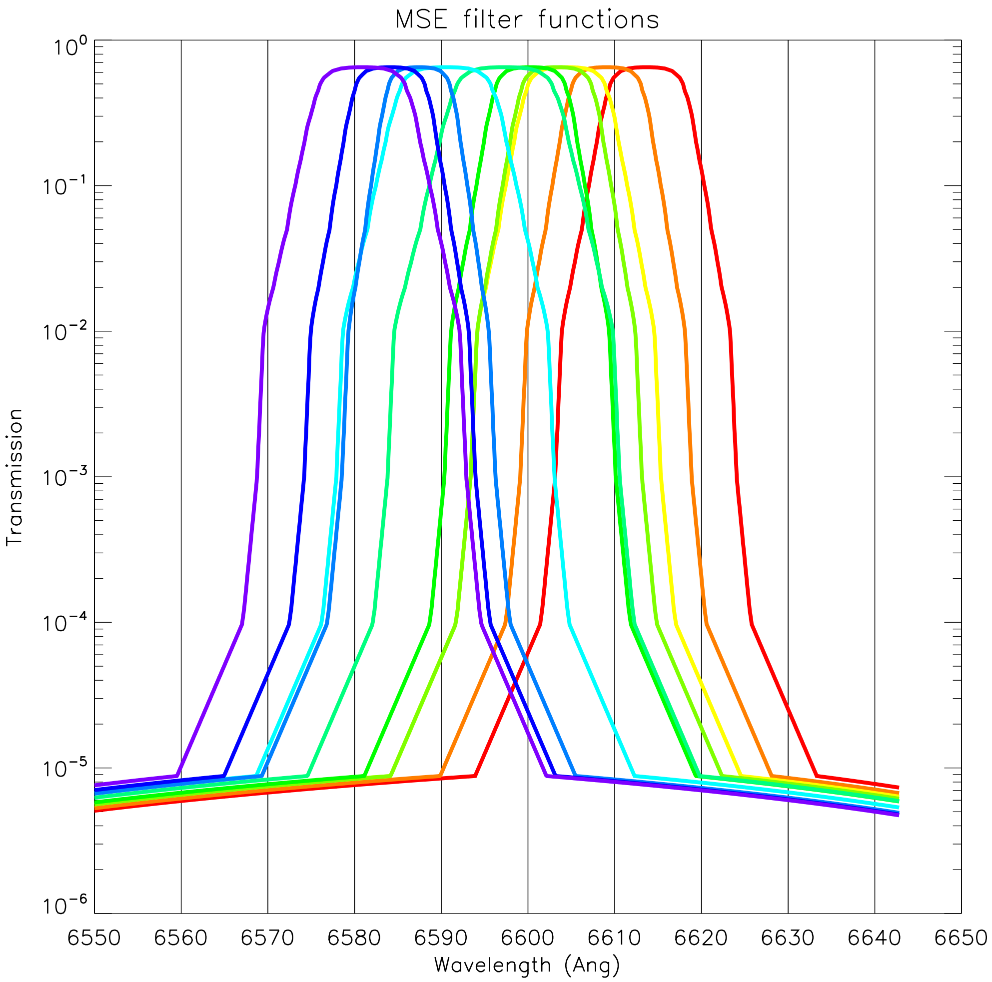

Figure 3-18: MSE bandpass filter functions. Exponential falloff shapes taken from manufacturer, Andover Corp., with central wavelengths and full with 10% max transmission widths measured using a spectrometer. Heated filters can shift filters up to 6.5Å higher in wavelength. Red shows filter function for innermost channel going to violet for the edge channel.

Recognizing incidence angle as a parameter that affect the passband, the MSE filter cavity uses an collimating lens set to reduce the incidence angle range. The entrance light is expanded from the 4 mm square image from the fiber bundle to about a 7cm diameter circle reducing the incidence angle range on the filter. The final lens focuses the filtered light to the 1 square cm active area of Hamamatsu R943 photomultipliers [51].

3.4.5 CAMAC hardware and control software

Several MSE components must be controlled in real time, independent of the tokamak shot cycle, the most important being the filter temperatures which must be tuned to match magnetic field conditions. The time required to reach a new temperature setting is about 15 minutes to tune further red, but over 30 minutes to decay to a lower temperature. The high voltage supplied to the photomultipliers need to be adjusted according the incident light intensity, varying mostly with the background bremsstrahlung level. Commands issued through an RS-232 interface control the PEM controllers, which are located inside the tokamak cell.

CAMAC hardware that provided communications with the various components were provided as part of the PPPL collaboration, but no compatable software or drivers were available at MIT. A custom realtime control and monitoring program for MSE was developed in the form of an IDL widget program using MDSPlus to perform direct CAMAC I/O in real time, independent of the shot cycle. Fig. 3-19 shows the control panel that is used to operate and monitor the diagnostic. The MSE settings used for each plasma pulse is automatically recorded to the experimental database.

3.4.6 Photomultipliers

The optical path of MSE data ends at the photomultiplier, after having travelled from the plasma to the polarimeter as polarized light, and then for another 30 meters through fiber optics with the polarization state encoded as amplitude modulations. The photons are converted to a current by the photomultiplier, and the output is amplified by a EG&G Princeton Applied Research Model 181 current to voltage preamps. Prior to the installation of fast digitizers, the signal would then be run through an antialiasing filter before going to the lockin amplifiers. The signal was split to each of the two lockins, which would multiply the signal by two different references electronically. The result was then digitized by the PPPL model H981 digitizers at 1 kHz, limited by the bandwidth of the lockin amp.

The photomultiplier tube is powered by four high voltage power supplies and

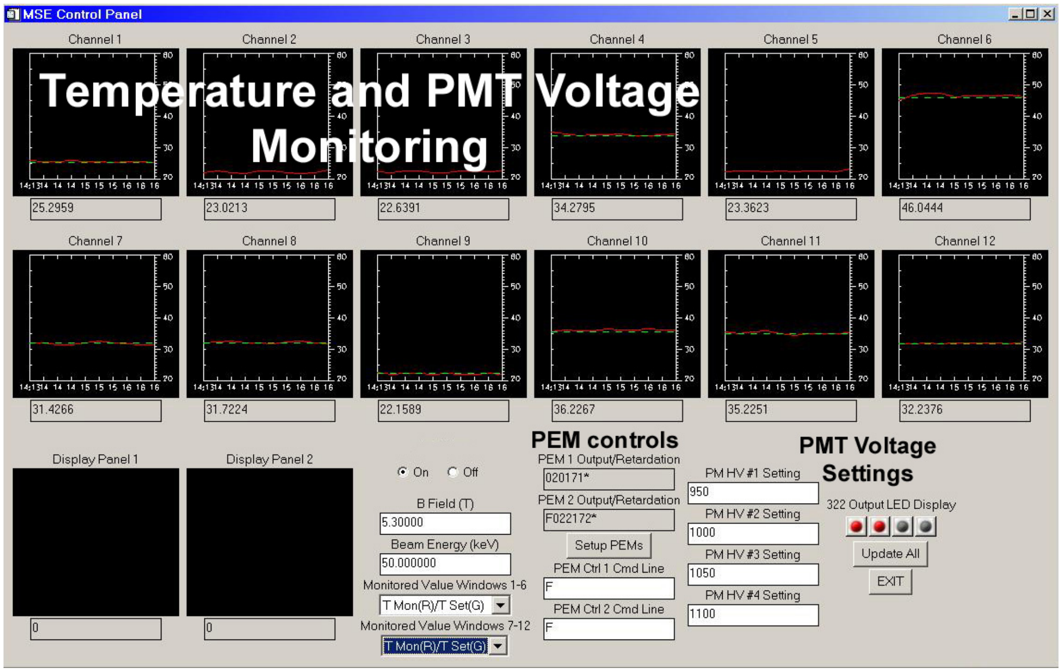

Channel 1: 25.2959
Channel 2: 23.0213
Channel 3: 22.6391
Channel 4: 34.2795
Channel 5: 23.3623
Channel 6: 46.0444
Channel 7: 31.4266
Channel 8: 31.7224
Channel 9: 22.1589
Channel 10: 36.2267
Channel 11: 35.2251
Channel 12: 32.2376
Display Panel 1: 0
Display Panel 2: 0
● On ○ Off
B Field (T): 5.30000
Beam Energy (keV): 50.000000
Monitored Value Windows 1-6: T Mon(R)/T Set(G)
Monitored Value Windows 7-12: T Mon(R)/T Set(G)
PEM 1 Output/Retardation: 020171*
PEM 2 Output/Retardation: F022172*
PEM Ctrl 1 Cmd Line: F
PEM Ctrl 2 Cmd Line: F
PM HV #1 Setting: 950
PM HV #2 Setting: 1000
PM HV #3 Setting: 1050
PM HV #4 Setting: 1100

Figure 3-19: Screenshot of the MSE control panel which provides real time control and monitoring of filter temperatures, PEM retardances and power, and photomultiplier high voltage. The MSE control panel is an IDL widget application.

respond logarithmically to the input voltage. Typical operating voltages ranges from 1000-1300V to encompass the large dynamic range of background bremsstrahlung varying with C-Mod operating densities.

3.5 Digital Lockins

Lockins are a common method of recovering signals that suffer from high background noise. A high frequency carrier wave is used to modulate the desired lower frequency signal, which would otherwise suffer from low signal to noise ratios. The same carrier signal is then used to demodulate the signal, acting as a narrow phase locked band-pass filter, thereby eliminating most of the background noise. Wireless technology is completely dependent on this method for transmitting information. Television, cellular phones, radio, and wireless networking are just a few examples.

MSE uses amplitude modulation to encode polarization information, meaning the signal is transmitted as the amplitude envelope function at the carrier frequency. This is very similar to AM radio, where the audio signal (<20 kHz) is used as the amplitude envelope for the carrier wave (∼800kHz). In MSE, Stokes vector components are the signal (<1kHz), and are used as the ampltude envelope of the PEM carrier wave (40kHz and 44kHz).

3.5.1 Analog lockin amplifiers

The MSE polarization signal is amplitude modulated by the polarimeter, and can be demodulation in several ways. The original equipment inherited from TFTR included a set of lockin amplifiers, an analog circuit that multiplies a reference signal with the measured signal. For MSE, the reference signal is a square wave TTL signal from the PEM controller. The output from the lockin amplifier was digitized at the lockin amplifier's bandwidth, which was about 1kHz.

Using simulated MSE signals created by frequency generators, it was determined that the rise and fall time of the analog lockins were too long. The analysis flexibility that analog electronics provided were quite limiting. Analog lockins also could not accommodate arbitrary phase shifts between the signal and the reference nor could they extract other frequency harmonics in the MSE signal. Therefore, in April 2002, MSE was upgraded to use fast digitizers and digital lockins.

3.5.2 Fast digitization

Starting in April 2002, the raw photomultiplier signal along with the PEM reference signal were digitized at 1 MHz using a pair of Joerger 612 fast CAMAC digitizers providing 12 digitization channels. The Joerger 612's were upgraded to the maximum available memory capacity of 256k samples, making the MSE digitization period for each pulse 256 ms. Figure 3-20 shows a sample fast signal. Each of the ten MSE raw intensity signal from the photomultiplier preamps is digitized at 1 MHz, along with the two reference signals from the photoelastic modulator controllers.

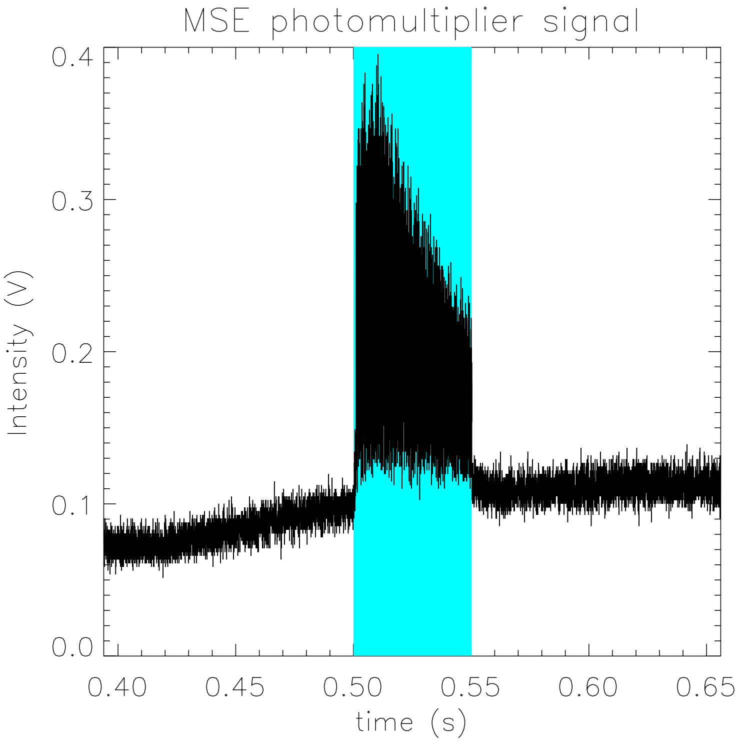

Figure 3-20: Fast digitized MSE signals prior to processing with digital lockins. The total digitization time is 256ms, filling available digitizer memory. Cyan shows beam duration of 50ms.

3.5.3 Phase locking reference signal

An IDL routine was written to perform the lockin function on the fast signals. The square wave TTL reference signals digitized are the piezoelectric drive signals. While these reference signals accurately captures the exact frequency of the PEM modulation, it is not an accurate representation of the retardance as a function of time. The retardance is linear with strain, and so is a sinusoidal in a material under resonant elastic vibration. Therefore, a sine wave is fitted to the reference via zero crossings for the entire digitization period.

A fixed phase lag was found between the PEM reference signals and the data signal likely due to signal propagation delays of the reference signal. The electronic reference signal from the PEM controllers is optically encoded for transmission to the MSE electronics rack where it is decoded then digitized whereas the MSE data signal takes all optical path. The phase difference was measured to be 0.42 radians for the

20kHz reference and 0.38 radians for the 22kHz reference. Using the proper phase lag measured during a calibration ensures the maximum signal extraction and noise rejection.

Once the exact fundamental frequency and phase is determined for each PEM, all harmonics and sum/difference frequencies can be computed and applied to the same fast signal.

3.5.4 Windowing and Apodization

Separating the MSE signal into separate time windows requires some care due to concerns of apodization, that is, errors due to using a non-integer numbers of cycles. The problem is compounded by the number of frequency components in the MSE signal. The optimized MSE analysis window is examined in this section.

The raw 1MHz intensity signals are broken down into user specified analysis windows, and the DNB injection period is distinguished from the background plasma. To choose the optimal size for the analysis period, a simple model of the the MSE signal is used for insight, shown as the sum of two frequency components and a DC noise level in Eqn. 3.13.

$$\begin{aligned} I(t) &= A_1 \sin(\omega_1 t) + A_2 \sin(\omega_2 t) + N && (3.13) \\ A_1 &= \frac{1}{t_2 - t_1} \int_{t_1}^{t_2} \sin(\omega_1 t) I(t) dt && (3.14) \\ A_2 &= \frac{1}{t_2 - t_1} \int_{t_1}^{t_2} \sin(\omega_2 t) I(t) dt && (3.15) \end{aligned}$$

This model signal is multiplied by the reference frequency and averaged over arbitrary time periods. The results reveal errors introduced by the choice of time period. Four main errors result from the choice of sampling window. The main errors in ω_1 are shown, ω_2 errors are analogous. ω_1 and ω_2 can be the PEM frequencies, 20 and 22KHz, or their harmonics. In reality, all PEM harmonics should be included.

Table 3.2 shows four frequencies and their normalized magnitudes, using Δt_{ms} as

Error Oscillation period	Peak Fractional Error (%)	Minimizing Solution
$\frac{1}{2\omega_1}$	$\frac{0.20}{\Delta t_{ms}}$	$>$ 2ms windows
$\frac{1}{\omega_1 - \omega_2}$	$\frac{4.0}{\Delta t_{ms}} \left(\frac{A_2}{A_1}\right)$	windows at multiples of 0.5ms
$\frac{1}{\omega_1 + \omega_2}$	$\frac{0.19}{\Delta t_{ms}} \left(\frac{A_2}{A_1}\right)$	$>$ 2ms windows
$\frac{1}{\omega_1}$	$\frac{0.80}{\Delta t_{ms}} \left(\frac{N}{A_1}\right)$	Zero center each window

Table 3.2: Summary of apodization errors introduced by using a non-integer number of cycles. The error amplitudes are relative to the amplitude of the signal (A_1 and A_2). Values of the errors themselves oscillate between zero and the listed maximum as a function of the sampling window length with periodicity given in the first column.

the window duration in milliseconds. A_1/A_2 is of order unity in the C-Mod MSE design, and the same error terms for ω_2 would depend on A_2/A_1 by symmetry. All the errors have characteristic frequencies, and each error would go to zero by choosing windows such that $(t_2 - t_1)\omega_{error} = 2n\pi$.

These results show that all apodization errors improve with longer window times as expected, and multi-millisecond windows would be adequate for reducing apodization effects for the first and third high frequency terms. Using long windows to reduce the second term at the beat frequency would reduce time resolution significantly. The DNB pulse used in this work is also limited to a 50ms duration. Therefore, the best solution to reduce beat frequency apodization is to choose sample windows at multiples of the beat time. The PEMs have fundamental beats of 2kHz, so time windows should be multiples of 0.5ms.

The final errors comes from the effect of a non-modulating DC background being multiplied by a fractional cycle of the reference signal. This effect goes as the amplitude of the noise over the amplitude of the modulation. This can be quite significant on C-Mod as the unpolarized background can often be several times the beam signal.

To get rid of this effect, each MSE time window is zero centered prior to the lockin function by subtracting the mean of the signal over the time window from the signal prior to demodulating, $\mathrm{I_{zero}} = \mathrm{I} - \langle \mathrm{I} \rangle$, there $\langle \mathrm{x} \rangle$ denotes time averages.

Combining all of these requirements and adding the fact that the DNB has a 1–2 ms of non-useful rise and decay time, the optimal window size for MSE currently is 4.5ms or 5ms. This allows each apodization error to be minimized while at the same time maintain sufficient time resolution and allows for use of most of the 50ms DNB pulse.

3.5.5 Determination of individual harmonics

Each signal window is multiplied by the corresponding reference window and the DC level is averaged over the window. For example, to find the 40 and 44 KHz modulation amplitudes for one time window, one does the following operation,

$$\mathrm{A40(t)} = \langle \mathrm{Signal(t - \Delta t, t + \Delta t) \cdot Reference_{40kHz}(t - \Delta t, t + \Delta t)} \rangle \tag{3.16}$$

$$\mathrm{A44(t)} = \langle \mathrm{Signal(t - \Delta t, t + \Delta t) \cdot Reference_{44kHz}(t - \Delta t, t + \Delta t)} \rangle \tag{3.17}$$

The result is frequency and phase matched with the reference, reducing background noise to a great extent. The results of the digital lockin are the desired amplitudes of each harmonic. These amplitude signal will be referred to with the preface **A** followed by the frequency, e.g. A40 and A44 will be used for the amplitude of the 40 and 44 kHz harmonics.

With the choice of a sufficiently long time window and zero centering the signal, Chapter 6 will show that when a plasma background is present, the statistical uncertainties from effects including digital lockin artifacts is essentially negligible, comprising only a few percent of the total uncertainty.

The MSE fast signal contains every harmonic and sum/difference frequencies of the harmonics. MSE analysis currently makes direct use of the 20, 22, 38, 40, 42, 44, and 46 kHz frequency components. To analyze the data for all frequency components including the plasma background for all MSE channels takes at roughly 20-30 seconds on a fast PC workstation.

3.5.6 Hardware background detector

One challenge for MSE in high density plasmas is background light. For MSE, the background is composed of light from bremsstrahlung and line radiation. Dα from the plasma edge, which can be about three orders of magnitude brighter than the beam emission, can be detected weakly by MSE channels. The beam components are only separated away from the unshifted Dα wavelength enough for filter transmissions to drop to 10^{-4}–10^{-5} (10^{-5} appears to be the limit for interference filters, see Fig. 3-18). The background has a large dynamic range, from being significantly lower than the beam signal, to a order of magnitude brighter depending on density. A small fraction of the background appears to be polarized and needs to be subtracted from the beam signal.

A linear interpolation of each harmonic amplitude signal due to background, e.g. light not produced as a consquence of beam injection, is made by analyzing a time window before the beam and one after the beam. This method assumes that the background polarized intensity changes linearly in time for the 50ms beam pulse from the 10ms immediately before the beam to the 10ms immediately after the beam. Fig. 3-21 shows conditions when this method works well, and when it would not. When the beam is intentionally modulated to include inactive periods for background measurements, these background measurements are included in the background interpolation.

This method provides an adequate treatment of the background when the plasma is in steady state during the beam pulse. However, measurements have shown that the polarized background changes dramatically during certain plasma events, particularly L-H or H-L transitions and RF power changes. This issue should be explored in more detail if MSE is expect to make measurements during such dynamic background conditions.

More advanced techniques for accurately determining the background during the beam pulse will be necessary to allow MSE measurement during dynamic plasmas. One attempt has been made to use the spectral region around the MSE wavelengths

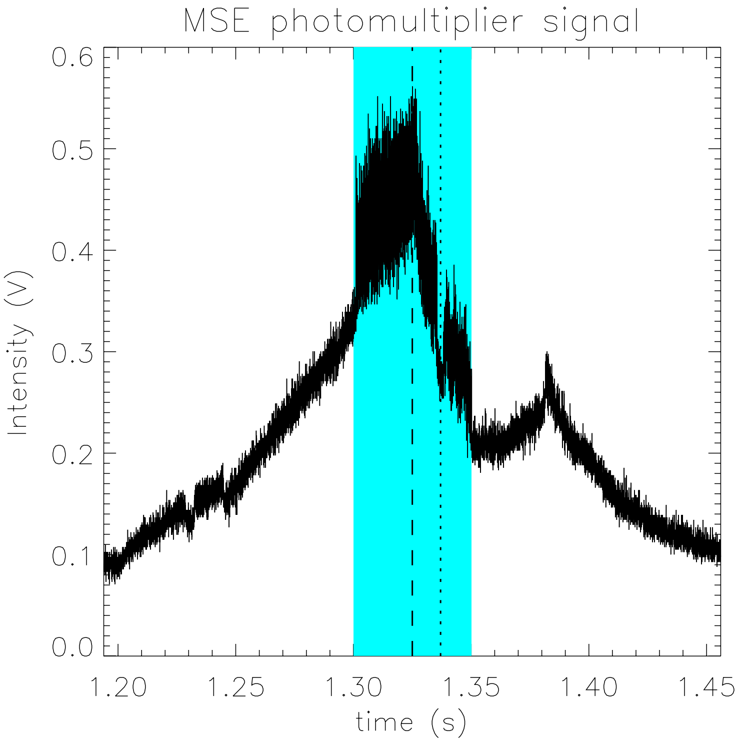

Figure 3-21: MSE signals showing the the background during a dynamic plasma. This MSE measurement, taken at r/a$_0$ = 0.53 of with $\overline{n}_e = 1.6\times10^{20}\text{m}^{-3}$ shows an ICRF heating trip at the dashed line, causing the plasma fall out of H mode at nearly the same time, and a beam trip at the dotted line. Background subtraction for this type of dynamic plasma currently has large uncertainties.

to measure the background during the beam pulse. Rejected light from interference filters reflected back from the surface was recycled to a bank of 1cm^2 active area photodiode detector with a Dα or 600nm interference filter about 10nm wide. Fig. 3-22 shows the bandpass filters and detector array for the background detector. Filters centered at 600nm were chosen because no strong impurity lines are be present within the bandpass. These filters allowed two spectral regions to be measured (not simultaneously for each channel). By using the Dα filter, one could determine if edge Dα would correlate with the MSE background, and the 600nm filter would allow a measurement of bremsstrahlung.

The advantages to this method including matching the actual MSE viewing chords, being inexpensive as no long length fiber was needed to be run from the cell (the entire background detector was constructed for less than $2k), and the measurement is simultaneous with MSE. Unfortunately, the data shows that the MSE background is not correlated with either the Dα intensity nor the bremsstrahlung in a consistent manner from one shot to the next.

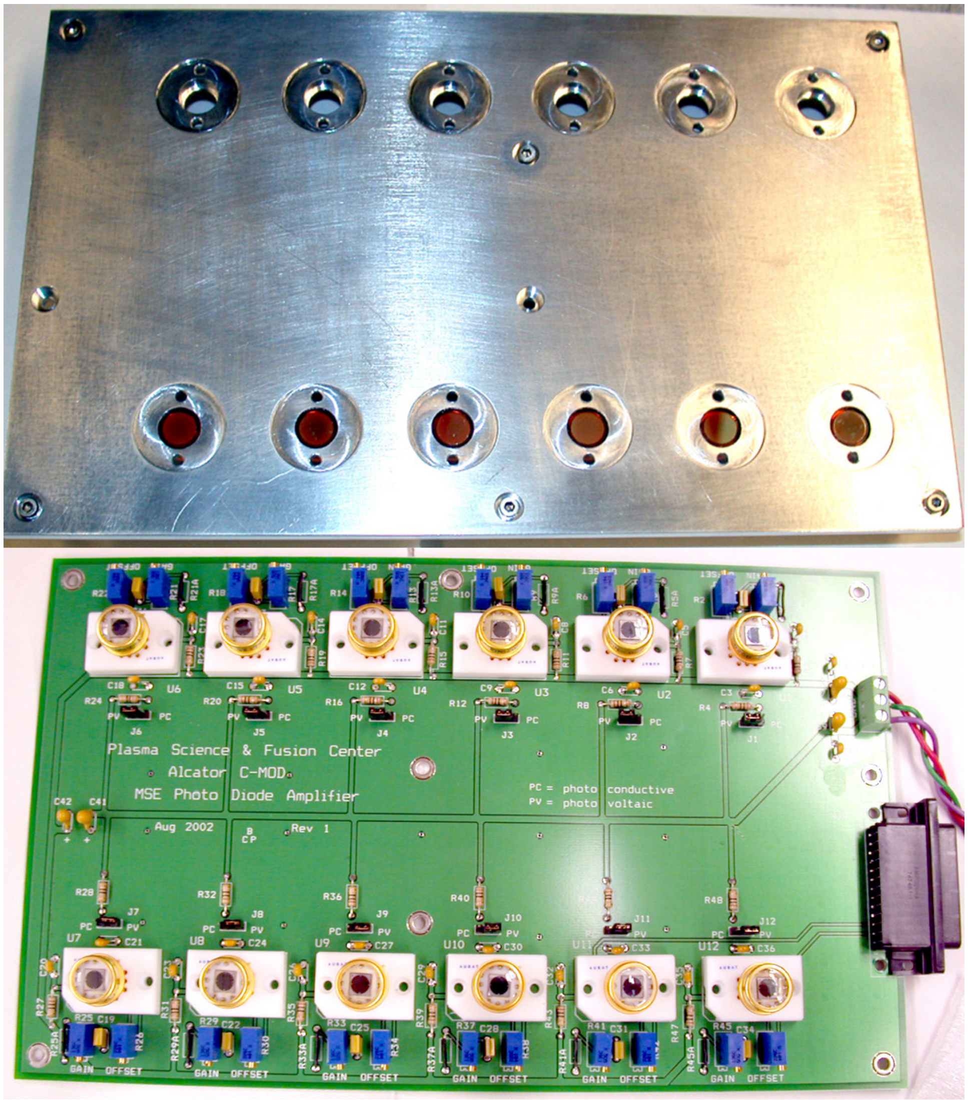

Figure 3-22: The MSE background detector array. The silicon photodiode array circuit board with filter holder assembly shown here just prior to assembly. This background diagnostic measured the reflected light from MSE interference filters in an attempt to make background measurements for MSE during the beam pulse.

The lack of correlation between the MSE polarized background and both the bremsstrahlung and Dα suggests that the source of the partially polarized light is not due to the originally proposed mechanism, which is polarization via reflection. Because most MSE chords end on the ICRF antennas, the original assumption had been that both bresstrahlung and Dα would become partially polarized after a reflection at the antennas. The was based on the fact that both the copper staps and boron nitride are both polarizing materials. However, measured results call this assumption into question. Sec. 4.2.6 will discuss the invessel test of the ICRF antenna reflectivity.

Chapter 4

Diagnostic Modeling and an Absolute Invessel Calibration

MSE on C-Mod makes use of many optical components to bring the beam emission to the polarimeter where the polarization measurement is actually made. Although stringent specifications were required of the optics, careful calibration and modeling is necessary to ensure the proper performance of the instrument. The concern is that optics used in the diagnostics modify the polarization state prior to measurement by the polarimeter leading to erroneous results. This chapter describes the effort made to perform an absolute calibration of MSE and the modeling used to interpret the results.

The invessel calibration consisted of inputing light with known polarization properties into the MSE diagnostic from inside the vacuum vessel. Along with linear polarized light at all angles, circularly polarized light and unpolarized light calibrations were also performed. Since the properties of the mirrors are dependent on reflection angles, calibrations of these properties must be performed *in situ*. Results from the invessel calibration were interpreted using an model of MSE which includes non-ideal optics effects.

A simplified mathematical model of MSE that generates simulated signals equivalent to the measured time-varying intensity was used to determine the optical parameters that give rise to the non-ideal behavior observed during the invessel calibration.

This chapter begins by describing this model, which also shows how MSE performs full Stokes polarimetry on incoming radiation.

4.1 A mathematical model of MSE

4.1.1 The MSE Stokes vector

Appendix A defines the Stokes vector, a way of representing incoherent light of arbitrary polarization, including partially polarized states.

In the specific case of MSE, the Stokes vector used is,

$$S_v = \begin{bmatrix} I_{unp} + I_\pi + I_\sigma + I_C \\ I_\pi \cos(2\gamma_\pi) + I_\sigma \cos(2\gamma_\pi + \pi) \\ I_\pi \sin(2\gamma_\pi) + I_\sigma \sin(2\gamma_\pi + \pi) \\ I_C \end{bmatrix} \tag{4.1}$$

$$\approx \begin{bmatrix} I_{unp} + I_\pi \\ I_\pi \cos(2\gamma_\pi) \\ I_\pi \sin(2\gamma_\pi) \\ I_C \end{bmatrix} \tag{4.2}$$

where I_π and I_σ are the intensities of the linearly polarized σ and π components, and I_{total} has been explicitly rewritten as the sum of the unpolarized, linear, and circular intensities. Note that the angle of the σ lines are assumed to be perpendicular to the angle of the π component, given by γ_π. As shown in Chapter 2, this assumption is only fully valid for statistical upper state populations.

Using interference filters, MSE is designed to reject σ wavelengths. The circular polarized light is expected to be of negligible intensity. Eliminating the I_σ terms shows an idealized Stoke vector, shown by Eqn. 4.2, composed of fully polarized π light from beam emission with a fully unpolarized source, such as plasma bremsstrahlung. The circular term is retained to account for the ellipticity of the Stark-Zeeman-E lines.

Using the simplified Stokes vector in Eqn. 4.2, it is trivial to to show how MSE is theoretically meant to operate. Eqn. A.10 shows the linear polarization angle in relation to the second and third Stokes elements, and the following section shows how MSE can measure each of the Stokes vector elements.

4.1.2 Müeller matrix representation of MSE optical components

Müeller matrices are mathematical represention of optical elements' effect on the polarization state of input light. Each optical element is represented by a four by four matrix and operates on the incoming Stokes vector. In this way, a chain of optical elements can be represented by operating on the Stokes vector in the order of light propagation. An introduction to Müeller matrices is found in Appendix A, with examples to familarize the reader.

For the C-Mod MSE system, the list of optical elements that must be considered for the polarization state include mirrors, lenses, a vacuum window, photoelastic modulators, and a linear polarizer. A simplified MSE optics train can be mathematically modeled as

$$\mathbf{S_{out}} = \mathbf{P}(\beta) \cdot \mathbf{PEM_2} \cdot \mathbf{PEM_1} \cdot \mathbf{D} \cdot \mathbf{R^{Faraday}_{CCW}}(\eta) \cdot \mathbf{R^{Offset}_{CCW}}(\theta) \cdot \mathbf{M}(\chi, \delta, \mathbf{r_m}) \cdot \mathbf{S_{in}} \quad (4.3)$$

with $\mathbf{S_{in}}$ and $\mathbf{S_{out}}$ the input and outgoing Stokes vectors. Every other term represents a polarization component in the form of a 4×4 matrix operator. $\mathbf{P}$ is a linear polarizer, $\mathbf{D}$ is a partial depolarizer, and $\mathbf{M}$ is a mirror. $\mathbf{PEM_1}$ and $\mathbf{PEM_2}$ are the photoelastic modulator operators, with the orientation of $\mathbf{PEM_1}$ defining $0°$ in this model. Matrices are typically defined for an orientation of $0°$, so rotation matrices are necessary to rotate them into the actual geometry. Rotation angles include β for the polarimeter polarizer and χ for the composite mirror. θ is the polarimeter offset which defines the zero angle, and η is the total Faraday rotation by all transmissive elements. The phase change imposed by a mirror reflection is represented by δ and the ratio of reflectivity for the two mirror axes is represented by $\mathrm{r_m}$. Each term in the optics train will be discussed individually in the following sections.

$\mathbf{R_{CCW}}$ and $\mathbf{R_{CW}}$ are the standard counter-clockwise and clockwise rotation operators defined in Appendix A. It might appear redundant to include both CW and CCW matrices, as $\mathbf{R_{CCW}}(-x) = \mathbf{R_{CW}}(x)$, but in a complex optical train such as MSE, using both can be helpful in avoiding signed angle confusion.

In reality, there are three mirrors and ten lenses, but the explicit inclusion of every component quickly leads to a model rendered useless by the number of fitting parameters. The model used here has combined the effect of all mirrors into one composite mirror and has combined the Faraday rotation of all lenses into a single rotation. This leaves the minimal model necessary to capture the effect of imperfect optics on the MSE measurement. The Müeller matrix representation of each element used in the model is described below.

Mirrors

C-Mod's MSE uses a set of invessel mirrors to reflect beam emission so it can exit the vacuum vessel directly above the neutral beam while maintaining the necessary MSE viewing geometry. Although dielectric mirrors were chosen to preserve the polarization state of the incoming radiation, they can only do so at one exact angle of incidence and wavelength. The mirrors are placed in defocused planes, and are used over much of their active reflection area. Raytracing models have shown that in many cases, the reflection angles exceed the specified range of polarization preservation, which is specified at $45^\circ \pm 5^\circ$. Fig. 4-1 shows the raytracing results for the optical axis. Views at the edges of the acceptance angle may experience even further deviations from 45° incidence angles.

Imperfections in mirror properties can affect the MSE measurement if the Stokes vector is modified before entering the polarimeter. The two effects an imperfect mirror can have on incident radiation are unequal reflectivity for s-polarization (transverse electric) and p-polarization (transverse magnetic) components and a mirror induced phase shift between the s&p reflected components. In order to simulate the effect of such an imperfect mirror, the combination of a partial polarizer and a partial retarder

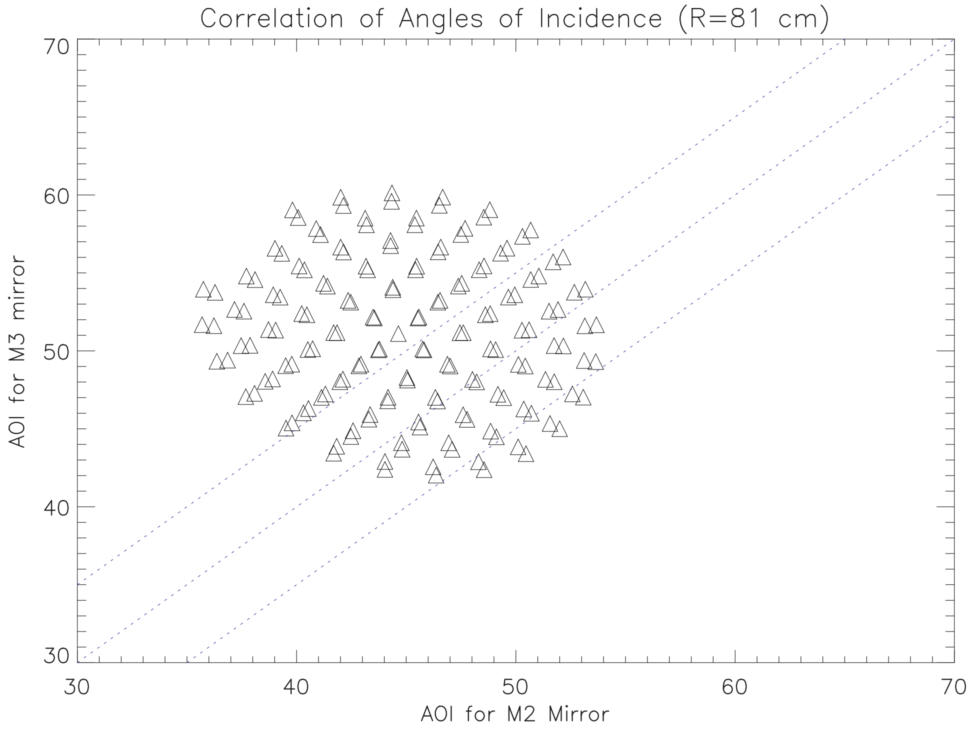

Figure 4-1: Raytracing results for Mirror 2&3 angles of incidence. Dotted lines represent the equality line and ±5° from equality. This results shows that many MSE rays are outside the optimal 45° ± 5°.

is used. These matrices may be combined because both of these operators must be aligned in the mirror s-p coordinate system.

$$\mathbf{M_{non-ideal}}(0^\circ) = \begin{bmatrix} \frac{1}{2}(r_m+1) & \frac{1}{2}(r_m-1) & 0 & 0 \\ \frac{1}{2}(r_m-1) & \frac{1}{2}(r_m+1) & 0 & 0 \\ 0 & 0 & \sqrt{r_m}\cos(\delta) & \sqrt{r_m}\sin(\delta) \\ 0 & 0 & -\sqrt{r_m}\sin(\delta) & \sqrt{r_m}\cos(\delta) \end{bmatrix} \tag{4.4}$$

$$\mathbf{M}(\chi) = \mathbf{R_{CCW}}(\chi) \cdot \mathbf{M_{non-ideal}} \cdot \mathbf{R_{CW}}(\chi) \tag{4.5}$$

Equation 4.4 shows the matrix for an imperfect mirror having non-unity reflectivities and non-zero phase shifts between s&p components in the horizontal dirction, where δ represents the phase shift introduced by the mirror and r_m represents the ratio of reflectivities between s and p components. An ideal mirror has $r_m = 1$ and $\delta = 0$, leaving the identity operator. Note that the mirror defined here is a *transmissive* element, and the image rotation resulting from mirror reflections is not included. Rather, the net effect of image rotation by all the mirrors as well as image inversions by lenses are grouped into the polarimeter offset term, $\mathbf{R}^{\mathbf{Offset}}_{\mathbf{CCW}}(\theta)$.

The matrices for polarization components are usually defined for the optical axis aligned at 0°, so rotation matrices are used to rotate the optical axis into the desired geometry. In practice, this effectively rotates the user coordinate system into that of the optical component prior to operating on the Stokes vector with the Müeller matrix, followed by the reverse rotation back to user coordinates. This is done with the mirror matrix in Eqn. 4.4, rotating the mirror to the angle χ as shown in Eqn. 4.5.

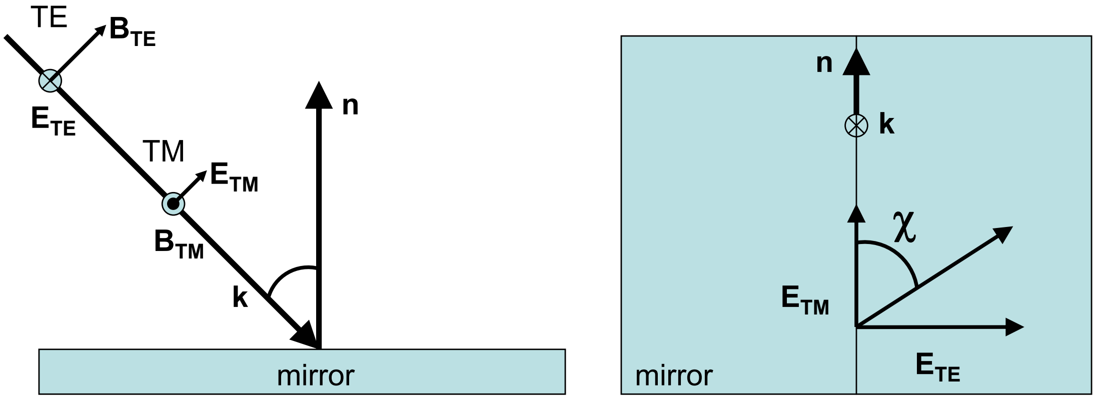

Figure 4-2: Diagram defining the 2D rotational angle, χ, for the MSE composite mirror. In the figure, **n** is the mirror normal, **k** the wave vector, TE and TM are the transverse magnetic and transverse electric components of the incoming plane wave, whose polarization is at 0°. A side view defining the reflection plane is shown on the left, and the right hand figure looks along **k** in the mirror plane defined by **n** and **k**.

Fig. 4-2 diagrams how χ is defined using **k** and **n**, the wave vector of the incident ray, and the mirror normal. From the figure, one can see that χ is related to the angle of incidence, and if phase changes between s and p components were introduced, that it may depend on the angle of incidence. This is shown in the vendor specifications for the mirrors shown in Fig. 4-3, where only three angles were measured, but over a wide wavelength range. The incidence angle sensitivity shows the each ray in Fig. 4-1 may experience different phase shifts.

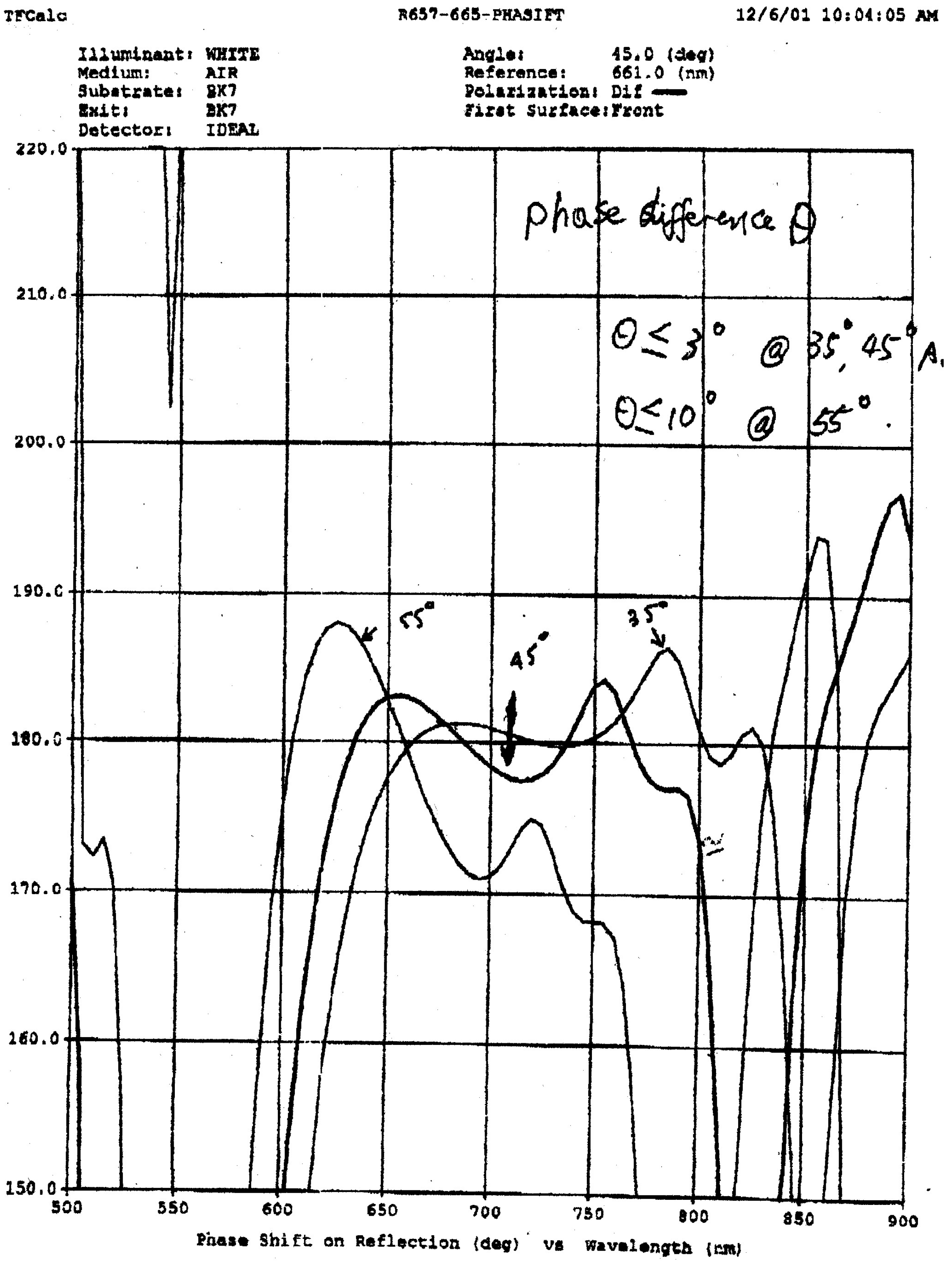 TFCalc R657-665-PHASIFT 12/6/01 10:04:05 AM

Illuminant: WHITE
Medium: AIR
Substrate: BK7
Exit: BK7
Detector: IDEAL

Angle: 45.0 (deg)
Reference: 661.0 (nm)
Polarization: Dif
First Surface: Front

phase difference θ

$\theta \leq 3^\circ$ @ $35^\circ, 45^\circ$ A.

$\theta \leq 10^\circ$ @ 55°.

Figure 4-3: Manufacturers mirror phase shift specification as a function of wavelength for three incidence angles labeled 35°, 45°, and 55°. Deviations from 180° is equivalent to δ in the model. The ranges of the specifications are not quite sufficient, as even the optical axis channel can have rays at 60°. Rays away from the optical axis can experience further deviations from the optimal 45°.

In the single mirror model of Eqn. 4.3, eight independent parameters have been introduced (neglecting the Faraday rotation term, which will not be present for an invessel calibration). Three of the terms are in the mirror element. For each mirror, both the reflectivity ratio, $\mathrm{r_m}$, and the imposed phase shift, δ, are functions of the angle of incidence. The apparent mirror rotation, χ, is a function of geometry. Both the angle of incidence and geometry are different for each mirror, so the inclusion of all three mirrors would introduce six additional parameters, increasing the current model to fourteen free parameters.

A brief study of a three mirror model was conducted, showing that the use of one composite mirror cannot accurately reproduce cross terms produced when perturbations from one mirror is reflected by the next mirror. However it also demonstrated the difficulty of working with the three mirror model, with so many terms as to make intuitive understanding of the equations extremely difficult. The number of free parameters in a three mirror model was originally thought to exceeded the number of measured parameters expected from a calibration (known now not to be true). The value of additional mirror parameters was questioned because the additional complexity still does not treat individual rays properly. In a complete model, each ray should be modeled individually, with each ray experiencing three mirror reflections with different effects because the angle of incidence varies. For these reasons, the first full optics train model of the C-Mod MSE described in this work uses a a single mirror to represent the composite effect of all mirrors across all rays in each channel.

Polarimeter Offset

A rotational matrix is included to account for the effect of a polarimeter rotational offset, shown in Eqn. 4.3 as $\mathbf{R}^{\mathbf{offset}}_{\mathbf{CCW}}(\theta)$. MSE was designed such that a polarization parallel to gravity would be measured as 22.5°. The C-Mod MSE measures the Stark-Zeeman-E polarized lines, which is parallel to $\hat{z}$ for a radial beam and a toroidal field. With the polarimeter thus oriented, the vertical direction would be measured as cos(45°). At this angle, the normalized error of the MSE measured ratio, A40/A44, is minimized.

Faraday rotation

A counter-clockwise matrix was arbitrarily chosen for the Faraday rotation, given as $\mathbf{R}_{\mathbf{CCW}}^{\mathbf{Faraday}}(\eta)$ in Eqn. 4.3. In the case of the invessel calibration, there are no magnetic fields and therefore no Faraday rotation, so η is zero for modeling the invessel calibration. Upper bounds and sensitivities on values of Faraday rotation were measured in the lab, see Sec. 3.3.5, but must be measured using a beam into gas calibration or with an invessel polarizer to obtain the actual operational values.

Partial Depolarizer

One effect of passing through the MSE invessel optical system, which includes twenty air/vacuum-glass transitions through lenses with antireflective coatings, two such transitions through the vacuum window without an AR coating, and three reflections, is a partial depolarization of the input light. The exact cause of this effect is not well known, but it can be caused by internal reflections, both from lens interfaces, as well as reflections off of non-optical components along the optics train, such as the support structure or the the metal canister. While angles measured do not depend on the polarization fraction, the simulation also accounts for the sensitivity to Stokes terms, so this effect needs to be accounted for.

A homogenous partial depolarizer has the following matrix,

$$\mathbf{D_{partial}} = \begin{bmatrix} 1 & 0 & 0 & 0 \\ 0 & (1-d) & 0 & 0 \\ 0 & 0 & (1-d) & 0 \\ 0 & 0 & 0 & (1-d) \end{bmatrix} \tag{4.6}$$

where d is the depolarization fraction.

Photoelastic Modulators

The polarimeter of the C-Mod MSE is comprised of a pair of photoelastic modulators (**PEM**) followed by a linear polarizer. How this combination of components encodes the polarization angle as amplitude modulations of intensity will be discussed in the next section, here the Müeller matrices of the individual polarimeter components is provided.

The PEMs are optically active devices consisting of a birefringent material under resonant cyclical strain causing time-varying retardance with adjustable retardance maxmima. The matrices for the PEMs are

$$\mathbf{PEM_1}(0^\circ) = \begin{bmatrix} 1 & 0 & 0 & 0 \\ 0 & 1 & 0 & 0 \\ 0 & 0 & \cos(A) & \sin(A) \\ 0 & 0 & -\sin(A) & \cos(A) \end{bmatrix} \tag{4.7}$$

$$\mathbf{PEM_2}(45^\circ) = \begin{bmatrix} 1 & 0 & 0 & 0 \\ 0 & \cos(B) & 0 & -\sin(B) \\ 0 & 0 & 1 & 0 \\ 0 & \sin(B) & 0 & \cos(B) \end{bmatrix} \tag{4.8}$$

$$A = A_0 \cos(\omega_1 t) \tag{4.9}$$

$$B = B_0 \cos(\omega_2 t) \tag{4.10}$$

where A_0 and B_0 are the maximum retaradation values for the PEMs, ω_1 and ω_2 are the vibrational frequencies of the respective PEMs. ω_1 and ω_2 are chosen distinctly to avoid overlap on any harmonics and are 20.3 kHz and 22.3 kHz in this case. The PEMs are positioned 45° relative to each other as to make them sensitive to the Q and U components of the Stokes vector.

Conceptually, it is perhaps easiest to consider the PEMs only at their zero and peak retardance values. The peak retardation values used in MSE for A_0 and B_0 is optimal at roughly half wave, so at the peak retardance, the linear polarization angle is reflected across the unmodified PEM axis while at zero retardance, the PEMs do not modify passing light. Combined with a fixed polarizer, such angle dependent manipulations result in intensity modulations proportional to incident polarization angle.

As mentioned in Sec. 3.3.5, there could be Faraday rotation through the PEMs, since fused silica is not a low Verdet constant material. The single total Faraday rotation term used in this model is unlikely to characterize this effect fully. Faraday rotation in the PEMs may require additional terms in the optics train.

Linear polarizer

A linear polarizer is the last polarization sensitive component and follows the PEMs in the MSE polarimeter. It is nominally oriented such that its passing angle bisects the angle between the PEMs, so if the PEMs were oriented at 0° and 45°, the passing angle of the polarizer would be 22.5°. The Müeller representations for ideal and imperfect (but nonbirefrigent and nondepolarizing) linear polarizers at 0° are

$$\mathbf{P_{ideal}}(0^\circ) = \frac{1}{2}\begin{bmatrix} 1 & 1 & 0 & 0 \\ 1 & 1 & 0 & 0 \\ 0 & 0 & 0 & 0 \\ 0 & 0 & 0 & 0 \end{bmatrix} \tag{4.11}$$

$$\mathbf{P_{non-ideal}}(0^\circ) = \frac{1}{2}\begin{bmatrix} (k_P + k_B) & (k_P - k_B) & 0 & 0 \\ (k_P - k_B) & (k_B + k_B) & 0 & 0 \\ 0 & 0 & 2\sqrt{k_P k_B} & 0 \\ 0 & 0 & 0 & 2\sqrt{k_P k_B} \end{bmatrix} \tag{4.12}$$

$$\mathbf{P}(\beta) = \mathbf{R_{CCW}}(\beta) \cdot \mathbf{P_{ideal}} \cdot \mathbf{R_{CW}}(\beta) \tag{4.13}$$

where k_P and k_B are the transmission fractions for the light parallel to the **p**assing direction and **b**locking directions. For the ideal polarizer $k_P = 1$ and $k_B = 0$. The polarizer used in the calibration apparatus was a dichroic sheet from OptoSigma with a quoted transmission of 36% (@550nm) and an extinction ratio of 10^{-4}. The extinction ratio is measured by the ratio of intensity between plane polarized light parallel and perpendicular to the passing direction of the polarizer, or k_B/k_P.

The non-ideal polarizer is included here only for completeness. Even though all physical polarizers are non-ideal, simulations results showed that these non-ideal properties did not affect the MSE measured quantities, as long as $k_B \ll k_P$, which is true for most polarizers, including the dichroic sheet polarizers used in MSE. An ideal polarizer is used in the simulation.

4.1.3 Intensity calculations for an ideal polarimeter

It is illustrative in understanding the operation of the PEM based polarizmeter by starting with an ideal case. The simplest ideal polarimeter is represented by

$$\mathbf{S_{output}} = \mathbf{P(22.5^\circ)} \cdot \mathbf{PEM_2} \cdot \mathbf{PEM_1} \cdot \mathbf{S_{input}} \tag{4.14}$$

where the rotation of each optical component has already been applied. PEM1 is oriented at 0°, PEM2 at 45°, and the linear polarizer would be at 22.5° with their operators given by Eqns. 4.7, 4.8, and 4.13. If the ideal Stokes vector from 4.2 is input into the ideal polarimeter, Eqn. 4.15 shows the first Stokes element, I (the total intensity), of the resultant Stokes vector after passing through the polarimeter.

$$\begin{aligned} 4I = {} & 2[I_{unp} + I_\pi] \\ & + \sqrt{2}\, I_\pi \;\; [\cos(B)\, \cos(2\,\gamma_\pi) - [\cos(A) + \sin(B)\, \sin(A)]\, \sin(2\,\gamma_\pi)] \\ & - \sqrt{2}\, I_C \;\; [\sin(A) - \sin(B) \cos(A)] \end{aligned} \tag{4.15}$$

$$\text{Amplitude}[\cos(A)] \;\; \propto -I_\pi \sin(2\gamma_\pi) \tag{4.16}$$

$$\text{Amplitude}[\cos(B)] \;\; \propto \;\; I_\pi \cos(2\gamma_\pi) \tag{4.17}$$

$$\text{Amplitude}[\sin(A)] \;\; \propto \;\; I_C \tag{4.18}$$

A and B are defined by eqns. 4.9 and 4.10. Note that in this ideal example, the polarimeter is insensitive to unpolarized light except to allow half its intensity to pass through the ideal polarizer, so it would not affect the measured polarization angle. Terms including $\cos(A)$, $\cos(B)$, and $\sin(A)$, will be shown as harmonic families, containing infinite series of even and odd harmonics of the PEM fundamental. Terms such as $\sin(B)\cos(A)$, which include products of harmonic families will be shown to include the sums and differences of harmonic frequencies. In the intensity equation, the harmonic families terms are multiplied by elements of the Stokes vector, making their amplitudes proportional to those Stokes vector elements, Eqn. 4.16 to 4.18.

One can now see how the linear angle γ_π information is now effectively conveyed by the total intensity term. The terms $\cos(A)$, $\cos(B)$, $\sin(A)$, and $\sin(A)$ are not trivial functions because A and B are also sinusoids. These functions can be expanded using the Jacobi-Anger expansion [52],

$$
\begin{aligned}
e^{iz\cos(\theta)} &= J_0(z) + 2\sum_{n=1}^{\infty} i^n J_n(z)\cos(n\theta) && (4.19)\\
\cos[A_0\cos(\omega_1 t)] + i\sin[A_0\cos(\omega_1 t)] &= \\
& J_0(A_0) - \ [2J_2(A_0)\cos(2\omega_1 t) - 2J_4(A_0)\cos(4\omega_1 t)] && (4.20)\\
& \qquad + i\ [2J_1(A_0)\cos(\omega_1 t) - 2J_3(A_0)\cos(3\omega_1 t)] + \ldots
\end{aligned}
$$

where J_n is the n^{th} order Bessel function of the first kind. The expansion of the first few terms of Eqn. 4.19 shows how $\sin(A)$ can be expressed as odd harmonics of ω_1 and $\cos(A)$ using even harmonics. Similarly, $\sin(B)$ and $\cos(B)$ can be expressed as harmonics of ω_2. Using this expansion in Eqn. 4.15, one can see that the amplitudes of the of the even harmonic terms are related via the linear polarization angle and that each harmonic in the series is independent of one another.

$$\frac{\sin(2\gamma)}{\cos(2\gamma)} = \tag{4.21}$$

$$-\frac{J_2(A_0)\text{Amplitude}[\cos(2\omega_1 t)]}{J_2(B_0)\text{Amplitude}[\cos(2\omega_2 t)]} = -\frac{J_4(A_0)\text{Amplitude}[\cos(4\omega_1 t)]}{J_4(B_0)\text{Amplitude}[\cos(4\omega_2 t)]}\cdots$$

$$= -\frac{J_2(A_0)\text{A40}}{J_2(B_0)\text{A44}} = -\frac{J_4(A_0)\text{A80}}{J_4(B_0)\text{A88}}\cdots \tag{4.22}$$

where the notation representing the modulation amplitude at each frequency has been introduced and defined for the C-Mod PEMs with $\omega_1 = 20\text{kHz}$ and $\omega_2 = 22\text{kHz}$.

Since each harmonic term is independent and can be isolated using lockins, a measurement of the *intensity modulation amplitudes* of any even harmonic pair ($2\text{n}\omega_1$ and $2\text{n}\omega_2$) will yield a measurement of the *linear polarization angle.* Note also that the Stokes intensities divide out in Eqn. 4.21, making the MSE measurement independent of the incoming intensity of polarized light. Although the same measurement can be done with each of the even harmonics, the largest amplitude occurs with the second harmonic at the retardation value of $A_0 = B_0 = 3.054$. This is the reason why the PEM's are operated at half wave (3.14), where the amplitude is very close to the optimal retardation (99.7%). At the same time, the amplitudes of the higher harmonics are significantly lower, 29% for 4ω and 2.6% for 6ω. It is important to maintain the ratio A_0/B_0 between calibration and plasma, as this can introduce a multiplier into the calibration. Section 4.1.5 discusses how one can make synchronous measurements of A_0 and B_0 for each MSE measurement using the harmonic sum and difference frequencies.

The circular Stokes element, I_C, is most easily measured using the odd harmonics in $\sin(A)$. The odd harmonics of PEM2, $\sin(B)$, do not appear alone in Eqn. 4.15 because it comes after the light has already been operated on by PEM1. Its odd harmonics are multiplied by the even harmonics of PEM1, resulting in the term $\sin(B)\cos(A)$. To lowest order, this has the effect of multiplying each odd harmonic by $J_0(A_0)$.

Cross terms in Eqn. 4.15 such as $\sin(B)\sin(A)$ are traditionally ignored (usually not measured) because they are not directly used to measure any of the Stokes components. They explain the appearance of the large number of sum and difference frequencies seen in the FFTs of the MSE fast signal. Section 4.1.5 will put these cross terms to good use calculating the retardance of the PEMs for any MSE measurement.

4.1.4 Intensity calculations for the C-Mod polarimeter

Equation (4.3) was evaluated using the algebraic package Maple. The expression was kept in algebraic form to gain insight to the resultant expressions. The full time-varying intensity expression is shown in Eqn. 4.23, arranged by Stokes elements (boldfaced). Terms representing families of frequency components are also boldfaced. Compared with Eqn. 4.15, the intensity formula with imperfect optics is more complex.

$$
\begin{aligned}
&4I = \qquad\qquad (4.23)\\
&(\mathbf{I}_{unp} + \mathbf{I}_\pi + \mathbf{I}_\sigma + \mathbf{I_c})\left[r_m + 1 + \left(\frac{r_m - 1}{2}\right)\{M\cos(2\chi) + L\sin(2\chi)\}\right] + \\
&(\mathbf{I}_\pi - \mathbf{I}_\sigma)\mathbf{cos(2\boldsymbol{\gamma}_{\boldsymbol{\pi}})}(1-d)\cdot \\
&\qquad \left[2\cos(2\chi)\left(\frac{r_m - 1}{2}\right) + M\left\{\cos^2(2\chi)\left(\frac{r_m + 1}{2}\right) + \sin^2(2\chi)\sqrt{r_m}\cos(\delta)\right\} + \right.\\
&\qquad \left. L\cos(2\chi)\sin(2\chi)\left\{\left(\frac{r_m + 1}{2}\right) - \sqrt{r_m}\cos(\delta)\right\} + J\sin(2\chi)\sin(\delta)\sqrt{r_m})\right] + \\
&(\mathbf{I}_\pi - \mathbf{I}_\sigma)\mathbf{sin(2\boldsymbol{\gamma}_{\boldsymbol{\pi}})}(1-d)\cdot \\
&\qquad \left[2\sin(2\chi)\left(\frac{r_m - 1}{2}\right) + L\left\{\sin^2(2\chi)\left(\frac{r_m + 1}{2}\right) + \cos^2(2\chi)\sqrt{r_m}\cos(\delta)\right\} + \right.\\
&\qquad \left. M\cos(2\chi)\sin(2\chi)\left\{\left(\frac{r_m + 1}{2}\right) - \sqrt{r_m}\cos(\delta)\right\} - J\cos(2\chi)\sin(\delta)\sqrt{r_m})\right] + \\
&\mathbf{I_C}(1-d)\left[-M\sin(2\chi)\sin(\delta)\sqrt{r_m} + L\cos(2\chi)\sin(\delta)\sqrt{r_m} + J\sqrt{r_m}\cos(\delta)\right]
\end{aligned}
$$

$$
\begin{aligned}
J &= 2\sin(2\beta)\,\mathbf{sin(A)} - 2\cos(2\beta)\,\mathbf{sin(B)}\,\mathbf{cos(A)}\\
K &= 2\sin(2\beta)\,\mathbf{cos(A)} + 2\cos(2\beta)\,\mathbf{sin(B)}\,\mathbf{sin(A)}\\
L &= -2\cos(2\beta)\sin(2\theta)\,\mathbf{cos(B)} + K\cos(2\theta)\\
M &= 2\cos(2\beta)\cos(2\theta)\,\mathbf{cos(B)} + K\sin(2\theta)
\end{aligned}
$$

Eqn. 4.23 was written as an IDL routine to simulate the MSE intensity signal using a time-varying retardances and user selectable optical property values. The signals are simulated at 1 MHz by setting timesteps at 1 μs to match the actual measured signals. These simulation signals are then run through a digital lockin to recover modulations amplitudes.

The complexity of the geometric terms in Eqn. 4.23 does not facilitate intuitive interpretations, so the terms are reorganized here into a more symbolic form, shown as Eqns. 4.24-4.27, to give better insight into the effect of imperfect optics.

$$\begin{aligned}
\cos(A) &\propto G_1 I_{total} + G_2[I_\pi - I_\sigma]\cos(2\gamma) + G_3[I_\pi - I_\sigma]\sin(2\gamma) + G_4 I_C && (4.24)\\
\cos(B) &\propto G_5 I_{total} + G_6[I_\pi - I_\sigma]\cos(2\gamma) + G_7[I_\pi - I_\sigma]\sin(2\gamma) + G_8 I_C && (4.25)\\
\sin(A) &\propto G_9[I_\pi - I_\sigma]\cos(2\gamma) + G_{10}[I_\pi - I_\sigma]\sin(2\gamma) + G_{11} I_C && (4.26)\\
G_n &= f(\theta, \beta, \chi, \delta, r_m) && (4.27)
\end{aligned}$$

where G_n are unknown geometric factors containing θ, the orientation of the polarimeter with respect to the tokamak coordinates, β, the angle of the linear polarizer in the polarizer, χ, the apparent angle of the composite model mirror, δ, the imposed phase shift of the composite mirror, and r_m, the reflectivity ratio of the composite mirror.

Comparing Eqns. 4.24-4.26 with 4.16-4.18, one can see that the effect of imperfect optics and geometry introduces cross terms to each set of harmonics not seen in the ideal MSE model. If the cross terms are not negligible, it would be important to include their effect in any calibration. In the next section, an invessel calibration will be performed that allows for solution of the unknown values of the optics properties and geometric constants.

4.1.5 Measuring the PEM retardances even with imperfect optics

In the intensity Eqn. 4.23, terms that give rise to families of frequency components are modified by the geometric terms identically. *Therefore, relationships between frequency components within the same family are independent of any optical properties and depend only on retardances.*

This property can be used to measure the retardance concurrently with each MSE measurement. The $\sin(A)\sin(B)$ term in Eqn. 4.23 is the product of two Bessel series shown in 4.19. The first few terms of this product is

$$\begin{aligned}
&\sin(A)\sin(B) = \\
&\quad 2\,[J_1(A_0)J_1(B_0)\cos(\omega_1 t)\cos(\omega_2 t) - \\
&\quad J_1(A_0)J_3(B_0)\cos(\omega_1 t)\cos(3\,\omega_2 t) - \\
&\quad J_3(A_0)J_1(B_0)\cos(3\,\omega_1 t)\cos(\omega_2 t)\ldots]
\end{aligned} \tag{4.28}$$

giving modulation frequencies at $(\omega_1 \pm \omega_2)$, $(3\,\omega_1 \pm \omega_2)$, and $(3\,\omega_2 \pm \omega_1)$. Taking ratios of the closest lying frequencies gives

$$\frac{J_3(A_0)}{J_1(A_0)} = \frac{\mathrm{A(38kHz)}}{\mathrm{A(42kHz)}} \tag{4.29}$$

$$\frac{J_3(B_0)}{J_1(B_0)} = \frac{\mathrm{A(46kHz)}}{\mathrm{A(42kHz)}} \tag{4.30}$$

By measuring the ratio of the amplitudes of several MSE components, one can solve for the peak retardance values through a mapping of the ratio of third to first order Bessel functions, shown in Fig. 4-4

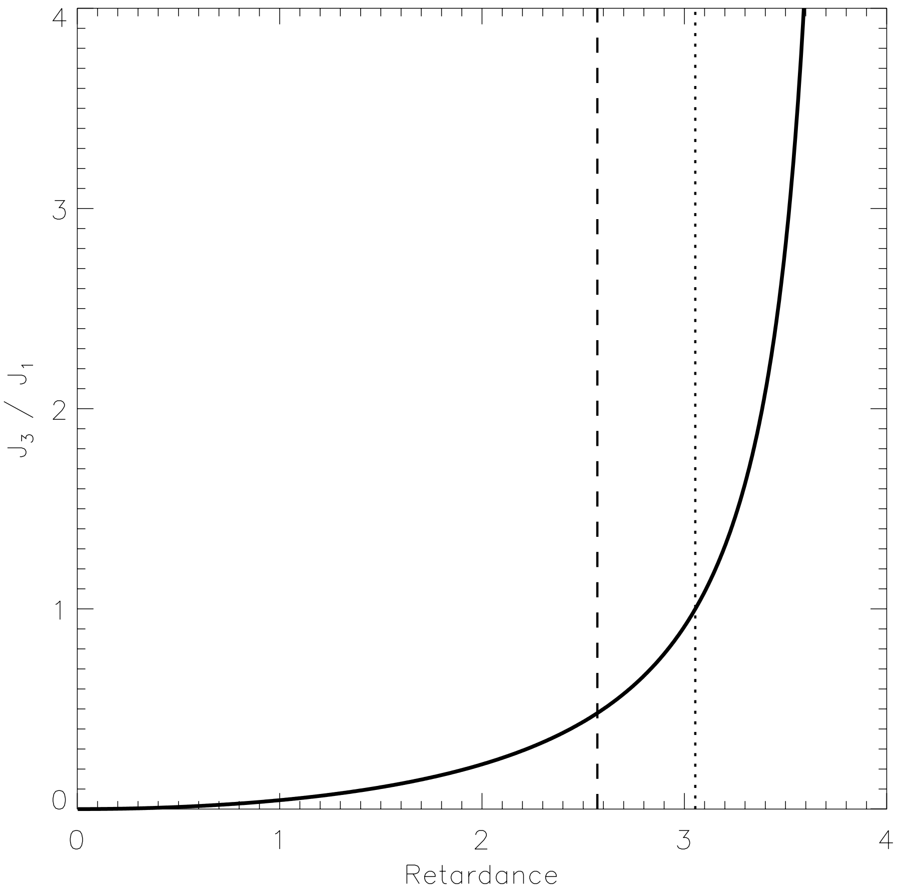

Figure 4-4: Ratio of J_3/J_1, the 3^{rd} order to 1^{st} order Bessel function of the first kind. Via Eqns. 4.29 and 4.30, this function provides a relation between PEM retardances and the ratio of the amplitudes of $(3\,\omega_1 - \omega_2)$, and $(3\,\omega_2 - \omega_1)$. Dotted line shows the ratio of 1 at the ideal MSE retardation value, dashed lines shows the mean measured value during the calibration with PEMs set at half wave retardation.

4.2 Absolute invessel calibration using known Stokes vectors

In order to understand the response of MSE to arbitrary input Stokes vectors, an invessel calibration where input Stokes vectors were fully known was necessary. To perform this calibration, an elaborate apparatus was designed for use inside the C-Mod vacuum vessel. This calibration apparatus and the calibration results is discussed in this section.

4.2.1 LED light source

MSE observes a narrow range of wavelengths a few nanometers red of Hα at 656.1nm. A high intensity, steady state, uniform, low voltage, and unpolarized source was desired to provide the basic source of light needed for the calibration apparatus. It was quite fortunate that the latest super bright GaAlAs Light Emitting Diodes, LEDs, have a central output wavelength of 660nm, with a spectral half width of 20nm, runs on low voltage DC, can be operated steady state, and is unpolarized. Having met almost all of the criterian, a custom PCB was fabricated containing approximately 500 5mm diameter LEDs with a sheet of pearl glass used to make the array appear more uniform.

4.2.2 Generating unpolarized light

The LED array was tested to be unpolarized to better than 0.1% in the lab, approximately the limit of the detection method used. For the test of unpolarized light, the array was aimed directly at the MSE objective lens. The pearl glass diffuser was excluded because it was found to increase polarization very slightly.

4.2.3 Generating linearly polarized light

To produce fully linearly polarized light with an absolutely calibrated angle accurate to 0.1° was more challenging than originally anticipated. Although thin sheet dichroic polarizers based on anisotropic molecules that conduct in one direction (e.g. Polaroid sheets) are widely available, none are available with calibrated polarization directions, or with specified directional uniformity. As a result, painstaking care was taken to calibrate the polarizer in house using two redundant methods.

To begin, a sheet polarizer was attached to a Newport precision rotation stage with a specified accuracy of $\pm 0.002°$. A Brewster's angle reflection method was used to generate a laser beam whose polarization angle aligned to gravity within 0.1° by using precisely positioned optical wedges. This beam was passed through the precisely rotating polarizer sheet while the transmittance was recorded with respect to angle.

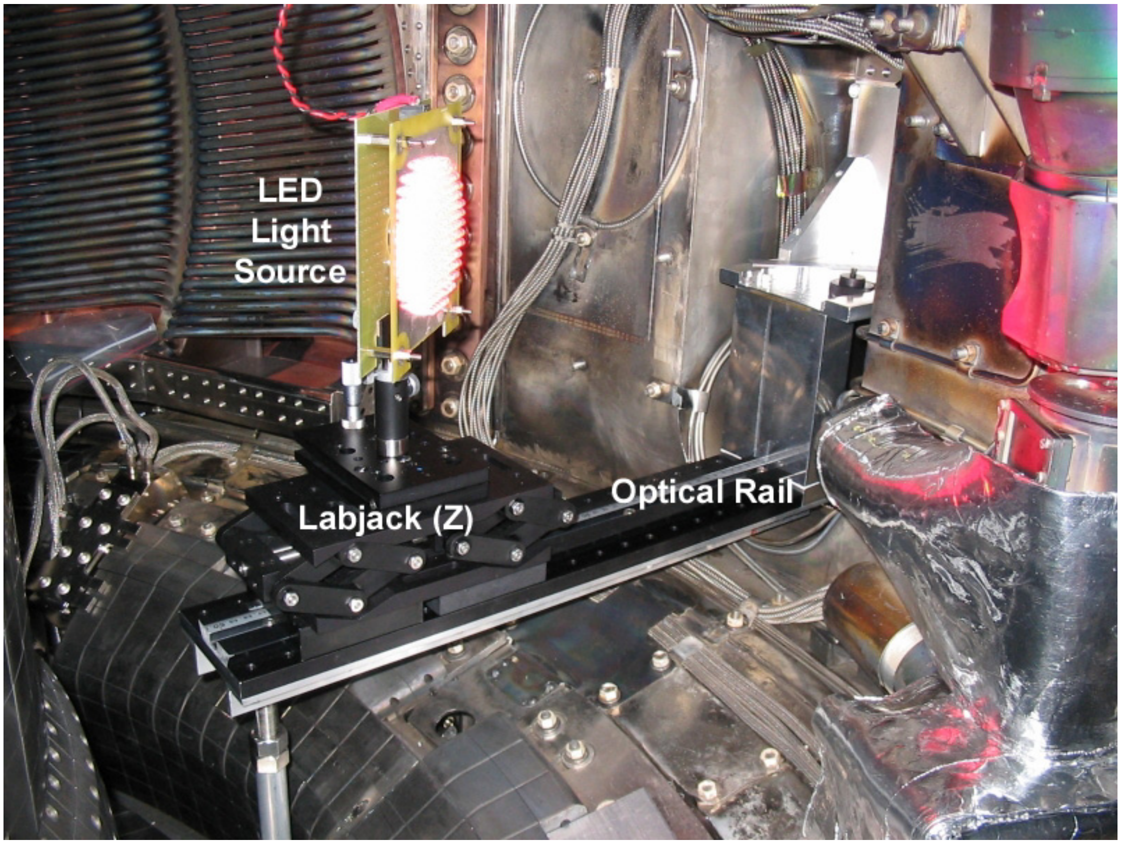

Figure 4-5: Unpolarized LED light source used for invessel calibrations. It is seen here sans other polarization optics to perform the unpolarized light calibration.

The expected $\cos^2(\theta)$ transmittance was fitted to determine the angle of the passing axis. While this method worked reasonably well, reproducibility at the 0.1° level was difficult due to the heavy reliance on mechanical alignment. A more robust method was found by using a polarizing cube, which consists of a pair of 45° prisms. Again, no specifications regarding polarization angle tolerances could be obtained, so once again an in-house calibration was performed. The polarization direction of the cube was found to be well aligned to the optical faces. Successive measurements of the apparent polarization direction was made while rotating the polarizing cube in small increments about two opposing faces. This procedure produced small perturbations in the polarization angle that allowed the polarizer to be calibrated to better than 0.01° accuracy.

Polarizer angular uniformity was originally tested by testing the passing intensity from different sections of the polarizer, but a competing effect rendered results from this method unuseful. Residual stresses in sheet polarizers makes them not optically flat, showing subtle surface warping when looking at a reflection. This can change the incidence angle, and thus transmitted fraction even more dramatically than passing angle non-uniformity. The uniformity was ultimately tested by comparing fitted passing angles tested on different annular regions of the polarizer sheet. This test showed the polarizer sheet to be uniform to 0.1° over a radius of 3cm from the center of the polarizer, increasing to 0.2° for larger areas. Sufficient care was taken during the invessel scans to use only the center 6cm the polarizer sheet.

The intensity through crossed polarizers and was determined to be about 0.5%. This translates into an extinction ratio of 200 and does not meet the typical manufacturer specified extinction ratio of 10^4 due to the extended incidence angle range used in the MSE bench test to reflect real calibration scenarios.

4.2.4 Generating circularly polarized light

Creating pure circularly polarized light also proved challenging. Although circular polarizers are available in sheet form, none are available in the wavelength required by MSE, so a custom tunable circular polarizer was designed. To create circularly polarized light, linearly polarized light is passed through a quarter waveplate oriented at 45° to the polarization direction (see the example in Appendix A starting with Eqn. A.17). A quarter waveplate specified at the proper wavelength was procured from Meadowlark Optics, but was found to require tilt tuning to match the desired 660nm wavelength.

The circularly polarized source was calibrated by measuring the transmitted intensity shown in Eqn. A.19. If the waveplate and polarizer are perfectly aligned and the waveplate were perfectly quarterwave (achieved via tilt tuning), then no intensity variation would occur by a rotation of the last polarizer. Any intensity variation resulting from a rotation of the final polarizer would signify residual linear polarization.

After extensive lab calibration and tuning, it was determined that approximately 1-3% of the light would remain linearly polarized, likely due to the fact that the light

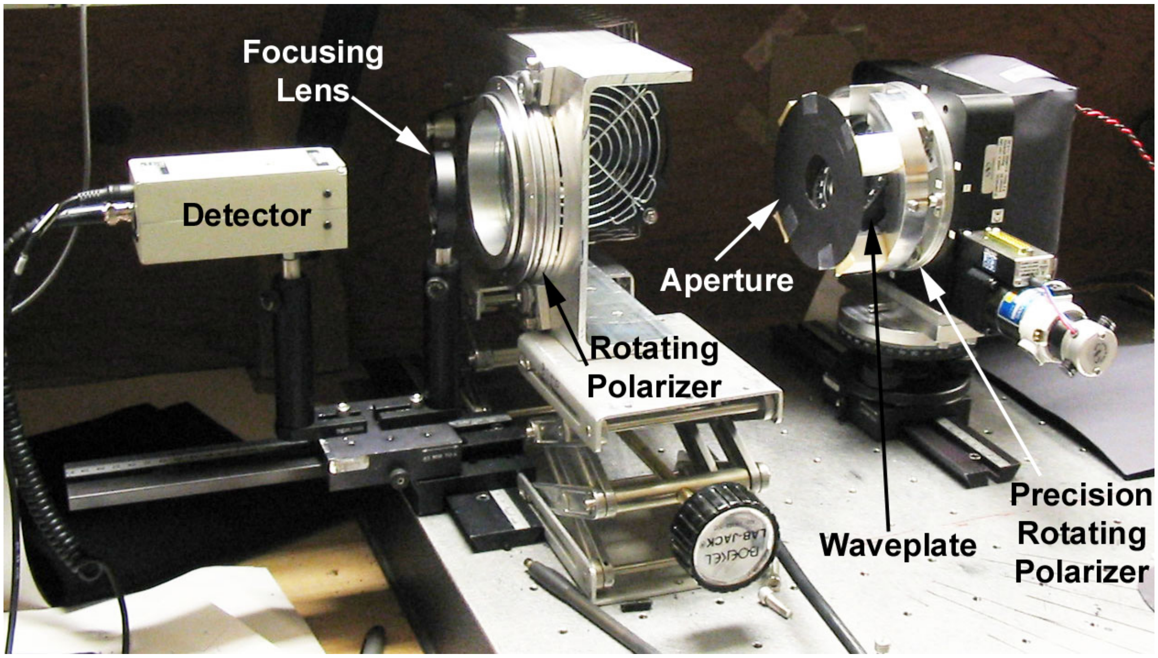

Figure 4-6: Using two rotating polarizers, the circular polarizer was calibrated on the bench. The optical setup used here is explained as an example in Appendix A.2.3.

source is not monochromatic. The residual linear fraction was measured using the bench test shown in Fig. 4-6 where light from the circular polarizing apparatus on the right was sent through a continuously rotating polarizer, a focusing lens, and then detected using a 1 cm^2 silicon photodiode. Variations of intensity in time would indicate residual linearly polarized light. One limitation of this setup is its inability to distinguish circularly polarized from unpolarized light, with both passing through the rotating polarizer with equal intensity and without variation with respect to the second polarizer angle. To measure the unpolarized intensity would have required an even more elaborate setup at significant additional equipment cost. More importantly, it was highly unlikely that such a complex optical setup would have errors below 1%, making possible results only marginally useful. Therefore, it was decided that the unpolarized intensity would have to be a free parameter (expected to be small) when the circular calibration is compared to simulation.

Since each MSE channel operates at slightly different wavelengths, it was not possible to know the exact residual linear fraction a priori. The measurement of

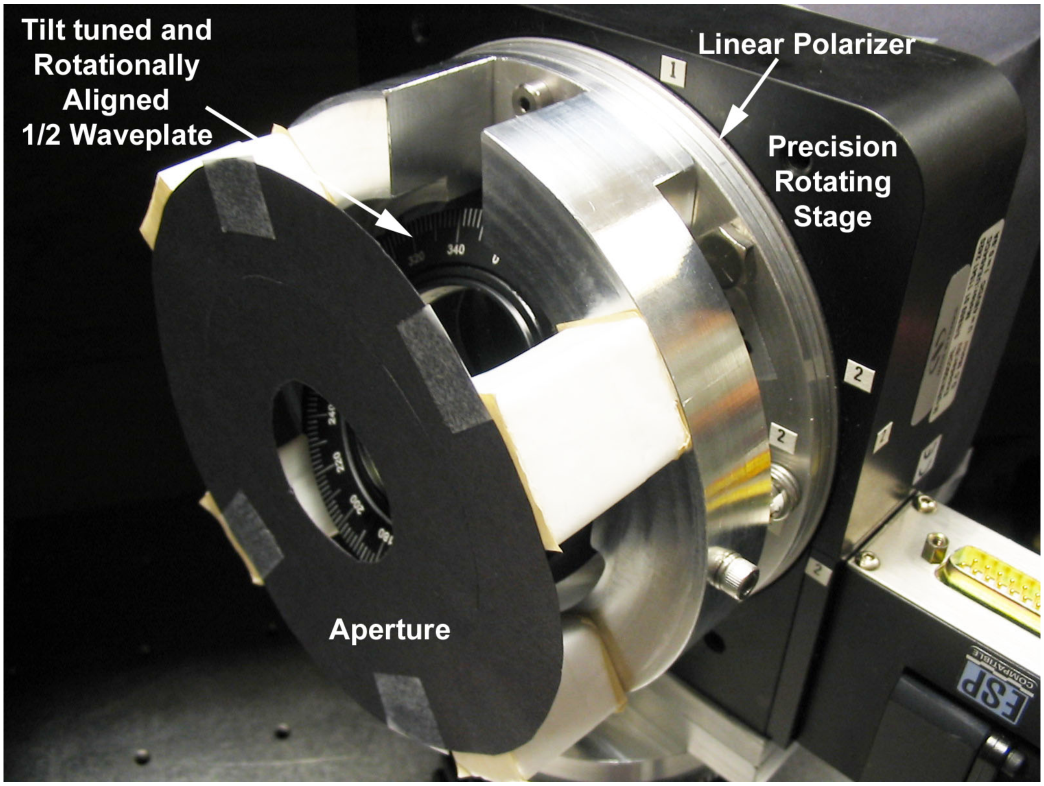

Figure 4-7: A close up photo of the circular polarizing apparatus, showing the tilt tuned waveplate mounted in front of the rotating polarizer, with both attached to the rotating stage. *Using this configuration, the waveplate rotated with the linear polarizer so that the angle of residual linearly polarized light would rotate.* The LED array and linear polarizer had emissive areas larger than the waveplate, so a black paper aperture was mounted in front of the waveplate.

mirror imperfections was desired to about a percent, so this uncertainty could not be tolerated.

A new approach was developed where the waveplate could be both tilt tuned in the lab, and also rotated along with the linear polarizer, shown in Fig 4-7. Rather than measure the MSE response to nominally circularly polarized light at one orientation, the circular polarizer was rotated through 360° exactly as was done for the linear polarizer calibration. Using this method, the angular dependent response due to the residual linear polarization could be subtracted from the results, leaving only the circular response.

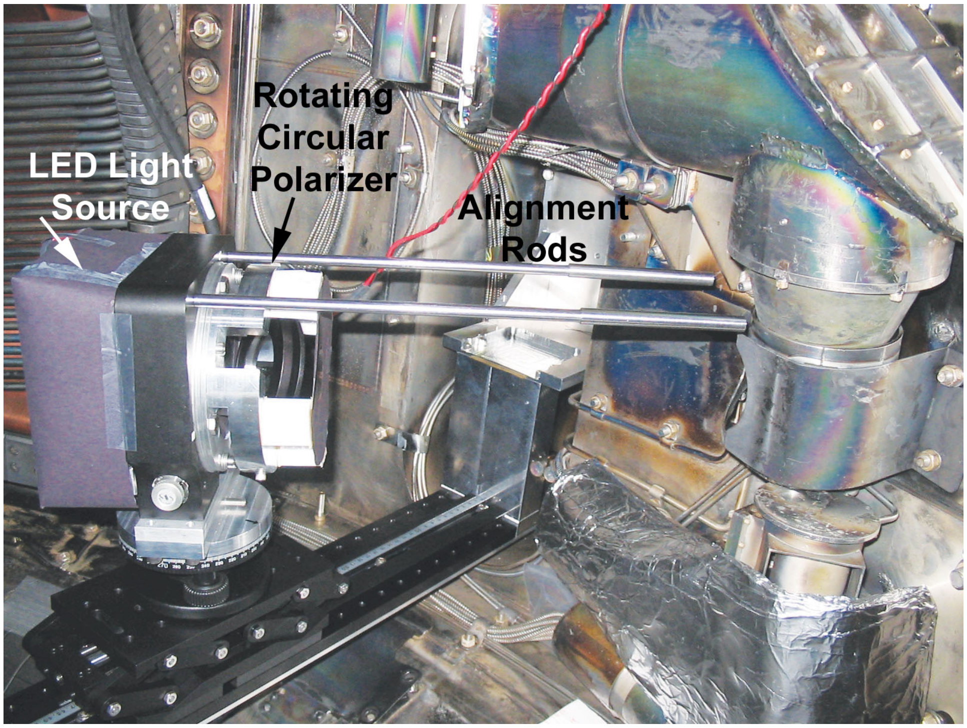

Figure 4-8: Circular source used invessel. By taking measurements through a whole rotation of the tilted waveplate with the linear polarizer, residual linear component could be subtracted.

4.2.5 Invessel alignment and calibration procedure

The linear polarizer procedure is conceptually illustrated in Fig. 4-9, showing the optical path through components of the optics train. The rotating invessel polarizer rotates clockwise in the calibration as shown, but produces the opposite rotation direction when seen at the end of the polarimeter due to reflections. The schematic is applicable to the configurations shown by Figs. 4-10 and 4-8.

The absolutely aligned polarizer was mounted invessel using an optical bench, assembled invessel, see Fig. 4-10. The optical bench consisted of optical rails and a precision jack allowing for R and Z alignment mounted on top of an optical table mechanically aligned to the beam axis. A three axis goniometer allowing for tilt and rotation about the z-axis was used to align the polarizer plane perpendicular to the MSE objective lens axis. This was a crucial step to prevent any projections of the linear polarization angle.

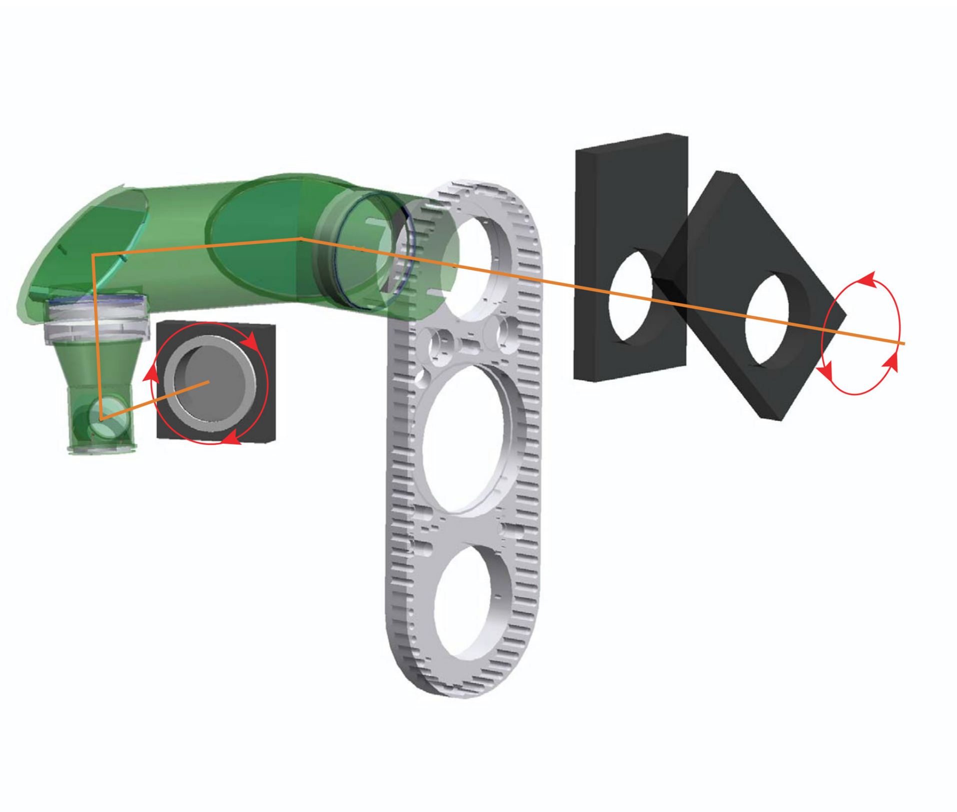

Figure 4-9: Solid model rendering of linear invessel calibration setup. The C-Mod vacuum vessel is hidden to show MSE optics canister with PEMs. A rotating invessel polarizer produces the opposite rotation direction when seen at the end of the polarimeter due to reflections. PEMs shown separated for clarity, air side relay optics are not shown for the same reason.

The calibration apparatus was absolutely aligned to gravity by leveling the rotation stage using a high precision digital level, with ±0.02° accuracy. This procedure was repeated invessel to ensure an identical alignment of the calibration apparatus with gravity. The digital level and procedure used can be seen in Fig. 4-10. The digital level is rotated as shown in the photo to measure the inclination angle of the MSE viewing chord, but oriented parallel to the rotation plane of the polarizer to zero the polarizer direction.

After alignment of the polarizer to MSE for a particular channel. The linear polarizer was positioned with a starting angle 10° counter-clockwise of true vertical, with *the vertical direction specified as the zero angle in the calibration.* A macro program was designed to execute an automated sequence in which the polarizer would be ad-

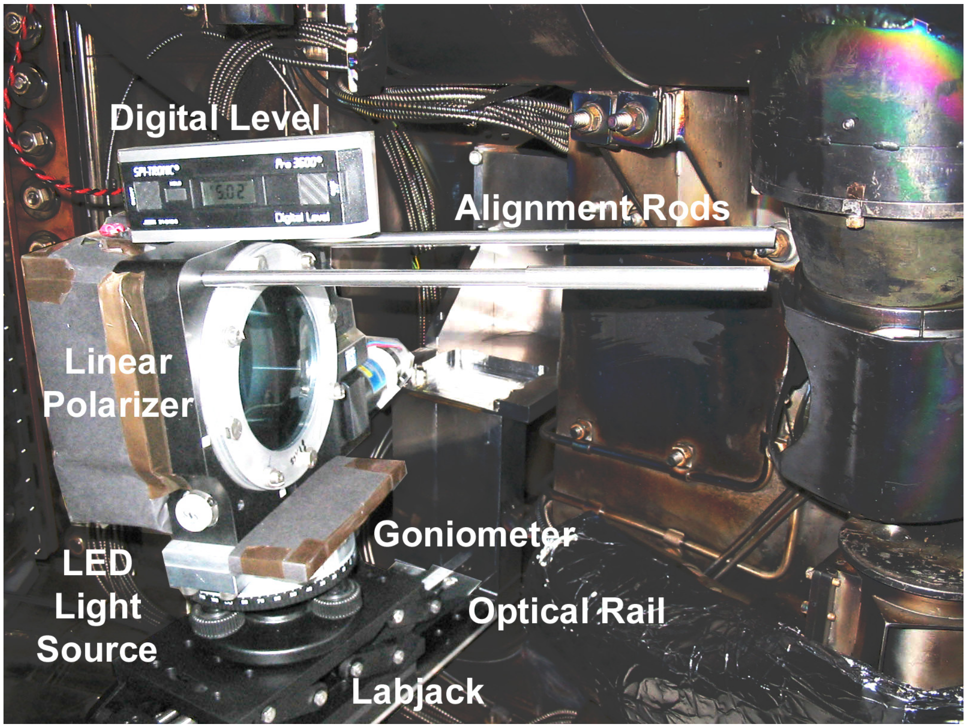

Figure 4-10: MSE absolute calibration apparatus seen here assembled invessel. Optical mounting allows alignment in R,Z and a goniometer allowed tilt alignmentto the MSE objective lens.

vanced in 5° (10° for the circular calibration) increments with a MSE measurement at each polarizer angle. The polarizer was was rotated through one full revolution.

The same procedure was used for the circular polarization calibrations to identify residual linear polarizations. In the end, well over one thousand test shots were taken. Recording only the channel being calibrated increased speed and reduced data storage requirements considerably.

4.2.6 Reflection measurements from ICRF antennas

Looking at fig. 1-3, one sees that almost all of the MSE chords end at the ICRF antennas. There was a concern that reflected unpolarized bremsstrahlung and line radiation from the plasma would become partially polarized by reflecting off copper and boron nitride surfaces of the antennas. Taking advantage of the new calibration equipment, this effect was tested invessel.

Using the high intensity LED source, reflectivity tests were conducted to test for the intensity and polarization of reflected light. The LED source was aimed at the antennas from equidistant locations to the antennas and the MSE objective lens. From the same locations, it was then pointed towards the MSE objective lens as a comparison.

The calibration results show that reflections from the ICRF antennas have very small intensities. Reflected intensities were typically well below 1% of the direct intensity when detectable. In the cases of detectable reflected intensities, there was no observed polarization of the reflected light, although this result has large error bars due to the low intensity.

This reflection result has implications for the MSE operation during RF power changes, suggesting that rather than plasma edge reflections, a local emissive source in the wavelengths observed by MSE develops directly in front of the antennas when the ICRF is operating. The polarized fraction of such RF-generated light is significant enough to affect the MSE measurement, but can be subtracted as part of the background during steady state RF operation. More study is required, however, more study to allow MSE measurements to be useful during *changes* in RF power.

4.3 Results from invessel calibration

Analysis of the invessel calibration data provides an absolutely calibrated response curves for pure linearly polarized light. These response curves include any imperfections in the optics that are present without magnetic fields or stresses induced by vacuum.

The linear response data were fitted to the functional form,

$$\gamma_{MSE} = K_0 + K_1 \gamma_{input} + K_2 \cos(2\gamma_{input} + \psi_2) + K_4 \cos(4\gamma_{input} + \psi_4) \tag{4.31}$$

where the MSE measured angle is represented by $\gamma_{MSE} = \frac{1}{2}\,\mathrm{atan}(\mathrm{A40}/\mathrm{A44})$, and the input angle using the linear polarizer (for which zero is aligned with gravity) is represented by γ_{input}.

An ideal MSE would have only a linear response with unity slope ($K_1 = 1$) with a constant offset reflect the rotation of the polarimeter. Non-Ideal angular components at angle harmonics are caused by imperfections in the optical train, with amplitudes and phases indicative of the orientation and severity of the optical imperfection. Only even multiples of γ_{input} are required because MSE is only sensitive to $2\gamma_{input}$. An example of values fit for the MSE edge channel is shown in Table 4.1

R [cm]	K_0 [deg]	K_1	K_2	ψ_2 [deg]	K_4	ψ_4 [deg]	Residual Error [deg]
86.8	25.46	1.000	0.920	-4.46	0.307	86.06	0.022
85.2	25.21	1.000	0.687	-2.63	0.199	87.59	0.020
83.6	25.26	1.000	0.525	-3.58	0.146	91.08	0.026
82.0	24.97	1.000	0.421	-4.36	0.097	93.98	0.015
78.5	24.62	1.000	0.349	-0.72	0.083	103.82	0.016
76.7	24.37	1.000	0.395	3.25	0.115	101.15	0.016
74.7	24.19	1.000	0.513	6.02	0.165	100.63	0.024
72.6	23.93	1.000	0.687	5.08	0.259	95.54	0.027
70.1	23.78	1.000	1.025	4.45	0.389	90.30	0.026
67.6	26.66	1.000	1.505	3.72	0.545	85.54	0.048

Table 4.1: Invessel calibration angular fit parameters corresponding to Eqn. 4.31.

4.3.1 Measured calibration retardances

Retardance for the invessel calibration was calculated using the procedure in Sec. 4.1.5. The measured values were quite different than the intended values of π. In order to post-calibrate data for the past run campaign, the retardance was kept the same as used during the campaign. Results from the retardance measurements are displayed in Table 4.2 and these value used in the simulations.

According the technical reference from the Hinds Corp.[53], the retardation of PEMs is not uniform over the exposed aperture. MSE uses a wide aperture bar-shaped model, and makes use of much of the exposed aperture area, with roughly a 8–10cm spot size, but with higher intensities towards the spot center. The PEM specification sheet shows a cosine variation in retardance along one axis, maximized at the aperture center, and constant retardance along the other. The specifications cites a 75% modulation efficiency at a diameter of 8.8cm, which is roughly consistent with the values measured.

Viewing Major R (cm)	A_0 20.3kHz	A_0 Std Error $[10^{-3}]$	B_0 22.3kHz	B_0 Std Error $[10^{-3}]$
86.8	0.819 π	3.02 π	0.800 π	4.49 π
85.2	0.817 π	8.09 π	0.822 π	2.38 π
83.6	0.825 π	3.86 π	0.831 π	1.01 π
82.0	0.831 π	2.68 π	0.843 π	1.89 π
78.5	0.832 π	1.24 π	0.840 π	1.63 π
76.7	0.829 π	2.36 π	0.825 π	6.60 π
74.7	0.837 π	2.08 π	0.833 π	2.54 π
72.6	0.828 π	1.16 π	0.813 π	2.38 π
70.1	0.821 π	0.78 π	0.784 π	1.46 π
67.6	0.802 π	0.79 π	0.736 π	2.86 π

Table 4.2: Retardance values measured during the invessel calibration. Radial locations were measured using a radial intensity weighting scan. Retardance used matches that used for the 2003-2004 C-Mod run campaign.

4.3.2 Measured and fitted responses

A number of diagnostic signals were needed to fit all of the unknown parameters in the simulation. The amplitudes of the 20, 40, and 44 kHz signals were separated and matched to simulated signals. Both simulated and measured signals were fitted to the form in Eqn. 4.32 to facilitate parameter fitting.

$$\frac{\text{Amplitude}(20, 40, 44\text{kHz})}{\text{Amplitude}(\text{DC})} = C_0 + C_2\cos(2\gamma_{input} + \phi_2) + C_4\cos(4\gamma_{input} + \phi_4) \quad (4.32)$$

In this fit, the dominant term should be $C_2 \cos(2\gamma_{input} + \phi_2)$, with an ideal MSE response containing only this term. No linear response with angle was observed. The values for the 40, 44, and 20 kHz coefficients are given in Tables 4.4, 4.5, and 4.6.

Polarization fraction

MSE measures linear polarization angles by taking the ratio of A40/A44, as described in Eqn. 4.21. Another unique quantity can be derived from the sum A40 and A44 signals, the linear polarization fraction, see Eqn. A.8. Two normalized linearly polarized Stokes vectors are identical if both the angle in Eqn. A.10, determined from A40/A44, and the polarization fractions are the same.

When analyzing measured data, it becomes evident that measuring the fractional polarization according to A.8 would be error prone because the total intensity, I, is the complicated function, Eqn. 4.23. Determining the measured I requires the measurement of the peaks in the raw data, difficult to do because of the slowest beat cycle times can occur at the same time scales as plasma background changes ($\approx$ 2kHz). An easier to compute quantity that is nonetheless related to the polarization fraction was adopted. This quantity representing the polarization fraction, P_f, is calculated by taking twice the sum of the 40 and 44 kHz modulation amplitudes and dividing by the mean of the intensity, represented as the DC amplitude (ADC), during the same period.

$$P_f = \frac{2|(A40 + A44)|}{ADC} \tag{4.33}$$

Disadvantages of this representative quantity is its angle dependence and that it can exceed one. To obtain useful calibrated $\mathrm{P_f}$ values, one normalizes this value by the calibrated values found during the invessel linear polarization calibration. $\mathrm{P_f}$ will be described as "calibrated" when this normalization is done. An example of how this quantity is matched to calibration measurements is shown in the right column of Fig. 4-12.*

---

*Actually, in Fig. 4-12 the quantity $2(|A40| + |A44|)/ADC$ is plotted to provide more visual matching features as a function of angle.

Results for linearly polarized light

Viewing Major R (cm)	I	Q	U	V
86.8	1	0.99982 $\cos(2\gamma)$	0.99982 $\sin(2\gamma)$	0.019
85.2	1	0.99982 $\cos(2\gamma)$	0.99982 $\sin(2\gamma)$	0.019
83.6	1	0.99982 $\cos(2\gamma)$	0.99982 $\sin(2\gamma)$	0.019
82.0	1	0.99982 $\cos(2\gamma)$	0.99982 $\sin(2\gamma)$	0.019
78.5	1	0.99976 $\cos(2\gamma)$	0.99976 $\sin(2\gamma)$	0.022
76.7	1	0.99969 $\cos(2\gamma)$	0.99969 $\sin(2\gamma)$	0.025
74.7	1	0.99969 $\cos(2\gamma)$	0.99969 $\sin(2\gamma)$	0.025
72.6	1	0.99969 $\cos(2\gamma)$	0.99969 $\sin(2\gamma)$	0.025
70.1	1	0.99964 $\cos(2\gamma)$	0.99969 $\sin(2\gamma)$	0.027
67.6	1	0.99955 $\cos(2\gamma)$	0.99955 $\sin(2\gamma)$	0.030

Table 4.3: Stokes vectors used to model the MSE invessel calibration response

Using the Stokes vectors shown in Table. 4.3 in the MSE model, simulated results are compared with linear calibration data. Tables 4.4 through 4.6 condense the results from fitting the measured responses from the invessel calibration using linearly and circularly polarized light as well as the simulated responses from the MSE model. Using the fitting coefficients from the measured response, the MSE response to any Stokes vector can be reconstructed. The optics properties deduced from simulations are discussed in the next section.

A limitation of the single mirror model was revealed when trying to reconcile simulations with measured data. A small constant term was present in the 20 kHz response, i.e. term C_0 in Table 4.6 could not be reproduced by the effects of a single mirror. A constant response in the 20 kHz response comes from the $\sin(A)$ term in Eqn. 4.23, which appears three times (the $\sin(A)$ comes from the J term, which appears in three places). One can show that the two J terms arising from linearly polarized light can be rewritten as,

$$\begin{aligned} J(\mathbf{I}_\pi - \mathbf{I}_\sigma)(1-d)\sin(\delta)\sqrt{r_m} &\quad [\cos(2\gamma_{input})\sin(2\chi) - \sin(2\gamma_{input})\cos(2\chi)] = \\ J(\mathbf{I}_\pi - \mathbf{I}_\sigma)(1-d)\sin(\delta)\sqrt{r_m} &\quad \cos(2\gamma_{input} + 2\chi) \end{aligned} \tag{4.34}$$

which cannot give rise to a constant A20 as a function of γ_{input}. The remaining A20 term arises from a response to an input angle inpendent circularly polarized light, which cannot be produced by a single imperfect mirror reflection (a cross term effect after multiple reflections). To reproduce the measured A20 response, light with a small degree of circular polarization (2–3%) was used in the simulation input Stokes vector.

	40 kHz Measured					40 kHz Simulated				
R [cm]	C_0 $[10^{-2}]$	C_2 $[10^{-1}]$	ϕ_2 [deg]	C_4 $[10^{-2}]$	ϕ_4 [deg]	C_0 $[10^{-2}]$	C_2 $[10^{-1}]$	ϕ_2 [deg]	C_4 $[10^{-2}]$	ϕ_4 [deg]
86.8	0.84	3.00	-39.5	1.21	-51.7	0.82	3.00	-39.5	0.96	-42.7
85.2	1.03	3.03	-39.7	1.46	-43.0	0.97	3.03	-39.7	1.16	-24.3
83.6	1.03	3.04	-39.5	1.51	-37.8	0.99	3.05	-39.5	1.34	-29.8
82.0	1.13	3.06	-40.0	1.69	-36.6	1.14	3.07	-40.0	1.53	-27.6
78.5	1.22	3.10	-40.6	1.73	-37.1	1.20	3.10	-40.6	1.54	-30.4
76.7	1.09	3.06	-41.1	1.61	-39.6	1.05	3.06	-41.2	1.35	-38.6
74.7	1.20	3.07	-41.4	1.69	-43.3	1.17	3.07	-41.5	1.50	-39.5
72.6	0.92	2.99	-42.1	1.33	-50.1	0.94	2.99	-42.1	1.17	-47.6
70.1	0.75	3.00	-42.5	1.08	-67.3	0.84	3.01	-42.5	0.91	-66.5
67.6	0.22	2.76	-42.8	0.71	-114.3	0.47	2.76	-42.8	0.64	-55.1

Table 4.4: Measured and simulated 40.6 kHz responses from the MSE invessel calibration using linearly polarized light. Values correspond to quantities in Eqn. 4.32.

As a check to determine if this adjustment to the Stokes vector is plausible, the magnitude of the last term of the Stokes vector, V, can be calculated using the model. After a reflection by an imperfect mirror which imposes a phase shift (equivalent to

	44 kHz Measured					44 kHz Simulated				
R [cm]	C_0 [10^{-2}]	C_2 [10^{-1}]	ϕ_2 [deg]	C_4 [10^{-2}]	ϕ_4 [deg]	C_0 [10^{-2}]	C_2 [10^{-1}]	ϕ_2 [deg]	C_4 [10^{-2}]	ϕ_4 [deg]
86.8	0.34	2.82	51.3	1.14	39.4	0.35	2.81	51.1	0.90	48.0
85.2	0.72	2.90	50.6	1.41	47.7	0.62	2.90	50.5	1.11	65.9
83.6	0.87	2.93	50.7	1.47	52.7	0.83	2.93	50.6	1.29	60.2
82.0	1.07	2.98	49.9	1.66	53.9	1.02	2.98	49.9	1.49	62.4
78.5	1.11	3.03	49.1	1.71	53.5	1.03	3.03	49.2	1.51	59.3
76.7	1.01	2.99	48.6	1.58	50.5	0.85	2.99	48.6	1.32	51.2
74.7	0.94	2.97	48.2	1.64	47.1	0.97	2.97	48.2	1.46	50.3
72.6	0.53	2.85	47.8	1.29	39.3	0.65	2.85	47.8	1.11	42.3
70.1	0.06	2.80	47.5	1.02	23.5	0.28	2.80	47.5	0.84	23.5
67.6	-0.64	2.50	47.4	0.67	-25.0	-0.35	2.50	47.3	0.58	-34.8

Table 4.5: Measured and simulated 44.6 kHz responses from the MSE invessel calibration using linearly polarized light. Values correspond to quantities in Eqn. 4.32.

	20 kHz Measured					20 kHz Simulated				
R [cm]	C_0 [10^{-3}]	C_2 [10^{-2}]	ϕ_2 [deg]	C_4 [10^{-3}]	ϕ_4 [deg]	C_0 [10^{-3}]	C_2 [10^{-2}]	ϕ_2 [deg]	C_4 [10^{-3}]	ϕ_4 [deg]
86.8	6.73	5.11	9.09	1.63	-15.6	6.78	5.08	9.09	1.63	5.98
85.2	6.89	3.7	17.5	1.97	10.8	6.72	3.73	17.5	1.44	32.8
83.6	6.79	3.44	21.7	1.68	24.3	6.68	3.44	21.7	1.51	31.4
82.0	7.11	3.13	25.7	1.66	30.9	6.66	3.12	26.0	1.56	38.5
78.5	7.50	2.47	32.7	1.29	39.1	7.26	2.49	32.7	1.24	42.8
76.7	7.67	1.88	41.4	0.89	47.2	7.68	1.89	41.2	0.83	43.8
74.7	7.46	1.34	45.6	0.63	66.1	7.37	1.35	45.2	0.66	47.3
72.6	6.48	0.46	110.5	-0.64	-22.4	6.82	-0.46	-69.7	0.178	104.7
70.1	7.85	-0.82	54.4	-0.71	15.3	7.67	-0.83	54.4	-0.25	30.4
67.6	8.65	-0.15	54.0	-0.92	3.09	8.57	-1.55	54.0	-0.36	-28.1

Table 4.6: Measured and simulated 20.3 kHz responses from the MSE invessel calibration using linearly polarized light. Values correspond to quantities in Eqn. 4.32.

a retardance), a small circular fraction can be created. This effect is discussed in Sec. A.2.4. Calculations show that the necessary circular fraction is consistent with the deduced values of δ for the mirror which will be shown in the next section.

The responses generated by the model from Eqn. 4.23 using optical properties discussed in the next section are shown overplotted with the measured responses in Fig. 4-11 for the 40 and 44 kHz components, and the left column in Fig. 4-12 for the 20 kHz component.

Results show that the model is able to reproduce the diagnostic behavior very well with a unique set of optical property values used in the model. The optical values used to generate responses that best fit the measured values are deduced to be the actual values. Fitted values for the simulation responses are shown next to the measured values in Tables 4.4 through 4.6 to quantitatively compare the quality of fit between simulation and measurement.

Some sensitivity was observed for each signal to the simulation parameters, but some signals proved to be particularly sensitive. For example, the parameter χ, the apparent mirror angle, had the strongest response on the phase difference between the A40 and A44 signals from the A20 signal. A unique value of χ was necessary to satisfy the observed $\phi_2[A40]$, $\phi_2[A44]$, and $\phi_2[A20]$ simultaneously. The mirror reflectivity ratio, r_m, strongly influences the $C_0[A40]$ and $C_0[A44]$, and was chosen to match observed values. The linear polarizer angle, β, had the heaviest influence on the parameter $C_2[A40]/C_2[A44]$. The phase shift imposed by the mirror, δ, primarily influenced $C_0[A20]$. The polarimeter angle θ was chosen to satisfy the combination of $\phi_2[A40]$ and $\phi_2[A44]$. The retardances used in the simulation were determined by measurement of A38, A42, and A46 (from the previous section). The retardance values uniquely determine the value $C_2[A40] + C_2[A44]$, and the model consistently satisfies this value using the measured values of retardance.

Results for circularly polarized light

Using the calibration device as described in Sec. 4.2.4, the response to circularly polarized light was obtained by taking the average of the the response over a full

TOP: Ch 1 (R=86.6cm), MIDDLE: Ch 5 (R=78.5cm), BOTTOM:, Ch 8 (R=72.6cm)

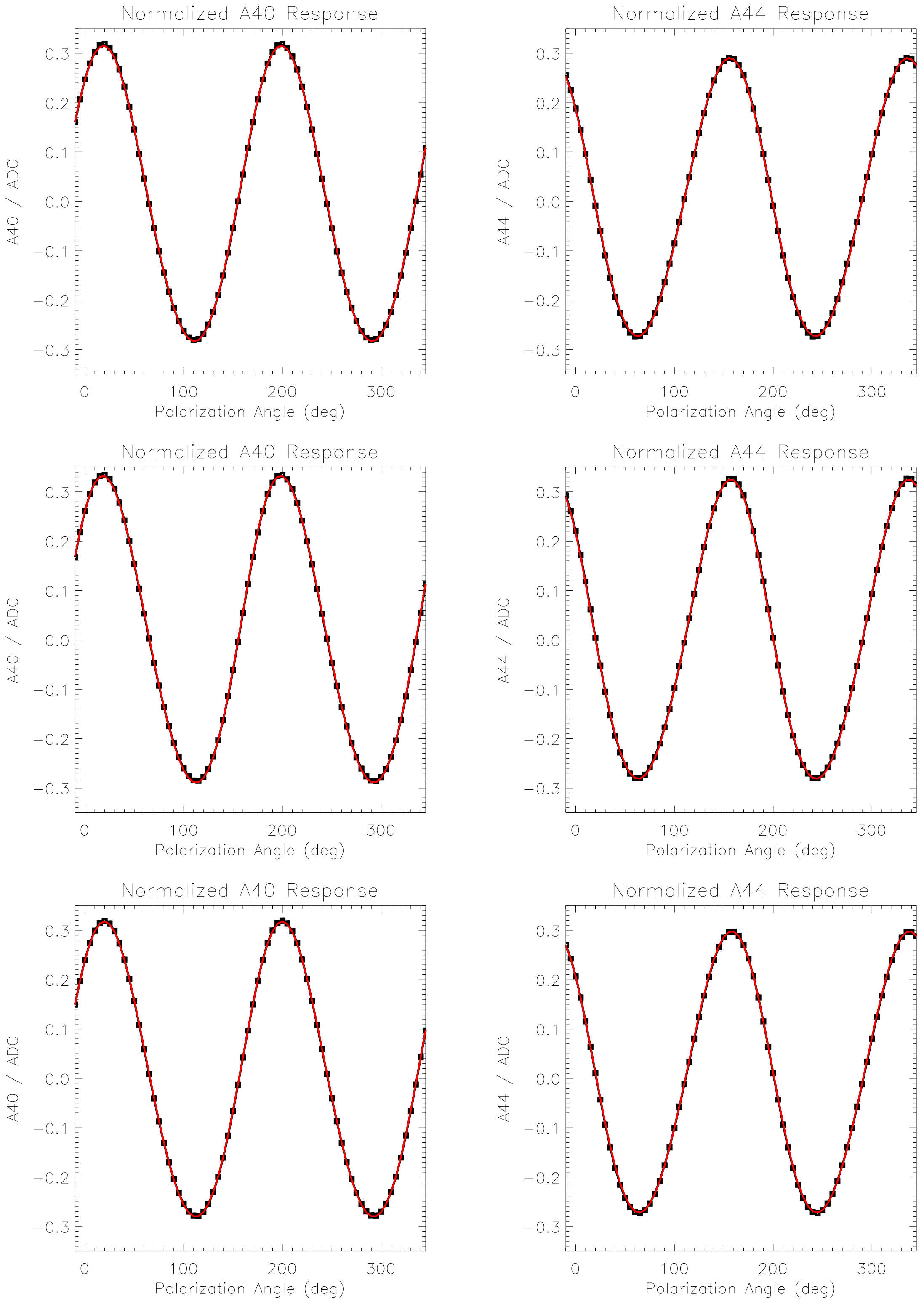
Normalized A40 Response

Normalized A44 Response

Normalized A40 Response

Normalized A44 Response

Normalized A40 Response

Normalized A44 Response

Figure 4-11: MSE linear response curves of A40 and A44 for linearly polarized light. Black points show measurement, with the red curve showing simulated data.

TOP: Ch 1 (R=86.6cm), MIDDLE: Ch 5 (R=78.5cm), BOTTOM:, Ch 8 (R=72.6cm)

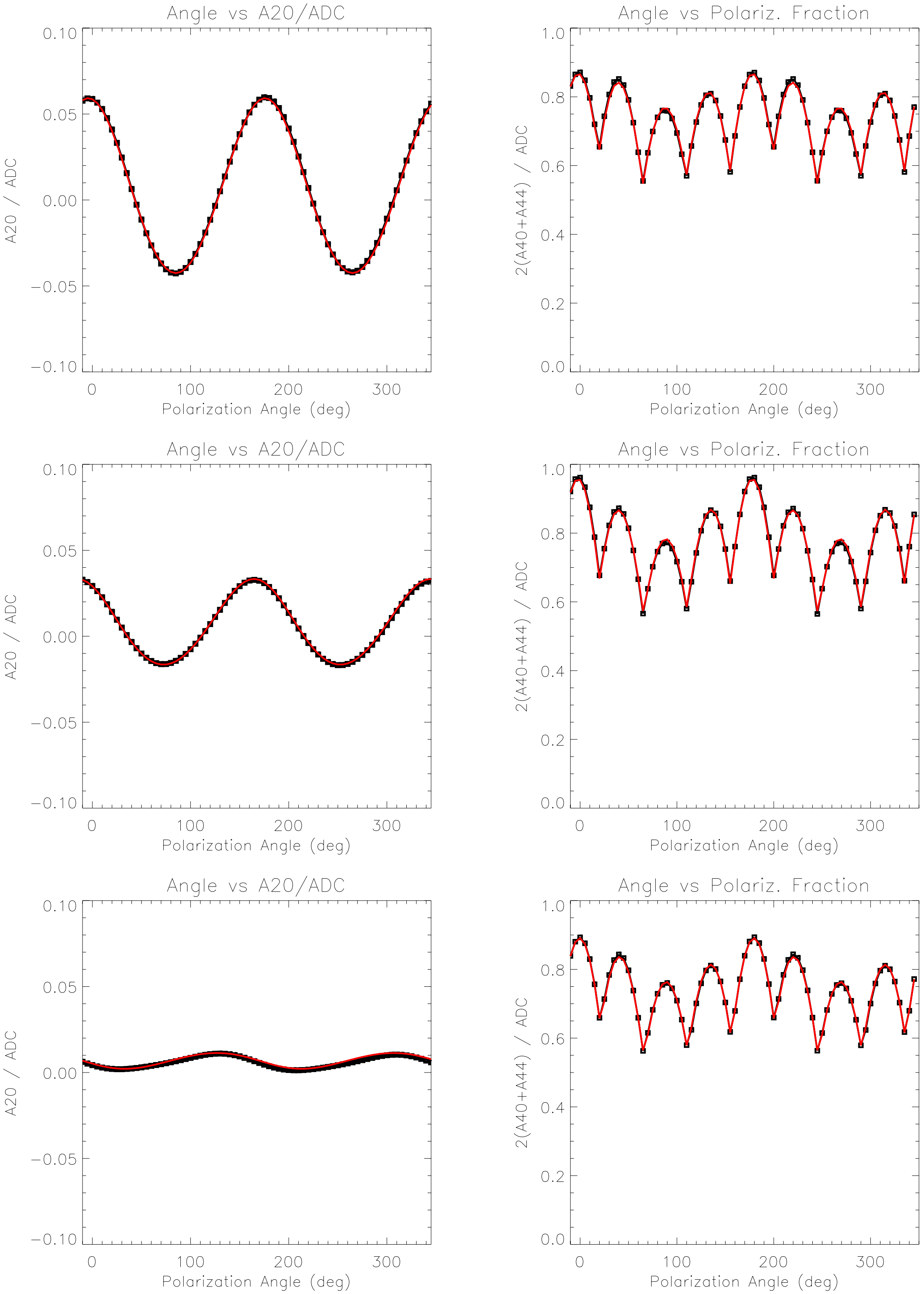

Figure 4-12: MSE response curves of A20 for linearly polarized light. The polarization fraction shown on the right hand column is actually $2(|A40|+|A44|)/ADC$, a variation of Eqn. 4.33. Black points show measurement, with the red curve showing simulated data.

View	Measured			Simulated		
R (cm)	20kHz C_0	40 kHz C_0	44 kHz C_0	20kHz C_0	40 kHz C_0	44 kHz C_0
86.8	0.299	-0.031	-0.028	0.300	-0.028	-0.034
85.2	0.297	-0.020	-0.025	0.307	-0.015	-0.029
83.6	0.291	-0.018	-0.027	0.302	-0.014	-0.027
82.0	0.293	-0.015	-0.026	0.299	-0.009	-0.027
78.5	0.299	-0.010	-0.022	0.303	-0.004	-0.022
76.7	0.299	-0.006	-0.017	0.303	-0.001	-0.017
74.7	0.296	-0.003	-0.012	0.298	0.001	-0.012
72.6	0.299	-0.003	-0.002	0.300	0.004	-0.002
70.1	0.304	-0.009	0.006	0.308	-0.001	0.007
67.6	0.297	-0.011	0.011	0.296	-0.001	0.012

Table 4.7: Measured and fitted responses from the circular MSE invessel calibration. Values correspond to C_0 in Eqn. 4.32 and all angle dependent terms have been discarded as the residual linear contamination.

revolution of the circularly polarized light generator. This removes any response attributed to the residual linear polarization. The measured response was compared to the simulated response using the same mirror properties from Table 4.8 derived from the linear calibration. Results are summarized in Table 4.7.

As expected from Sec. 4.2.4, a small unpolarized intensity was necessary in the simulation Stokes vector to match the input calibration light. For this calibration, this fraction was determined to be 4.8%.

4.3.3 Values of optical properties used in MSE simulation

The invessel calibration procedure was simulated with the MSE model by varying the values of the optical properties until the responses matched calibration responses for each MSE channel. Due to the size and nonlinear sensitivity of the parameter space, a brute-force optimization of all parameters was abandoned in favor of human intuition. All of the following fitted parameters were arrived by iterative parameter scans. Values of the optical properties that best matched the calibration responses are shown in Table 4.8.

Fig. 4-13 shows plots of how small and large phase shifts influence quantities such as the ratio of amplitudes of the 20 and 40 kHz, and the 20 and 44 kHz. These signals provide a good diagnostic of angular terms such as χ (the apparent rotation angle of the mirror), δ (the phase difference imposed between s&p components after a reflection), θ (the polarimeter offset angle), β (the polarimeter linear polarizer angle), and r_m (the mirror s to p reflectivity ratio), because they are sensitive to phase differences.

View R (cm)	θ	β	χ	δ	r_m	Depolarization Fraction
86.8	25.40°	23.10°	130.50°	−9.20°	0.990	7.0%
85.2	25.21°	23.15°	126.38°	−6.60°	0.975	6.2%
83.6	25.25°	23.10°	124.18°	−6.15°	0.990	6.3%
82.0	24.95°	23.00°	122.00°	−5.60°	0.985	6.0%
78.5	24.65°	22.90°	118.50°	−4.40°	0.985	4.5%
76.7	24.35°	22.75°	113.90°	−3.35°	0.995	4.8%
74.7	24.18°	22.90°	111.50°	−2.40°	0.995	5.7%
72.6	23.93°	23.00°	76.47°	−0.88°	1.00	7.6%
70.1	23.75°	23.00°	109.00°	1.55°	1.00	6.2%
67.6	23.64°	22.80°	108.25°	2.90°	1.00	11.6%

Table 4.8: MSE Mirror Properties and geometric constants. All variables correspond to the MSE model, given by Eqns. 4.3, and the subsequent MSE intensity, Eqn. 4.23.

TOP: Ch 1 (R=86.6cm), MIDDLE: Ch 5 (R=78.5cm), BOTTOM:, Ch 8 (R=72.6cm)

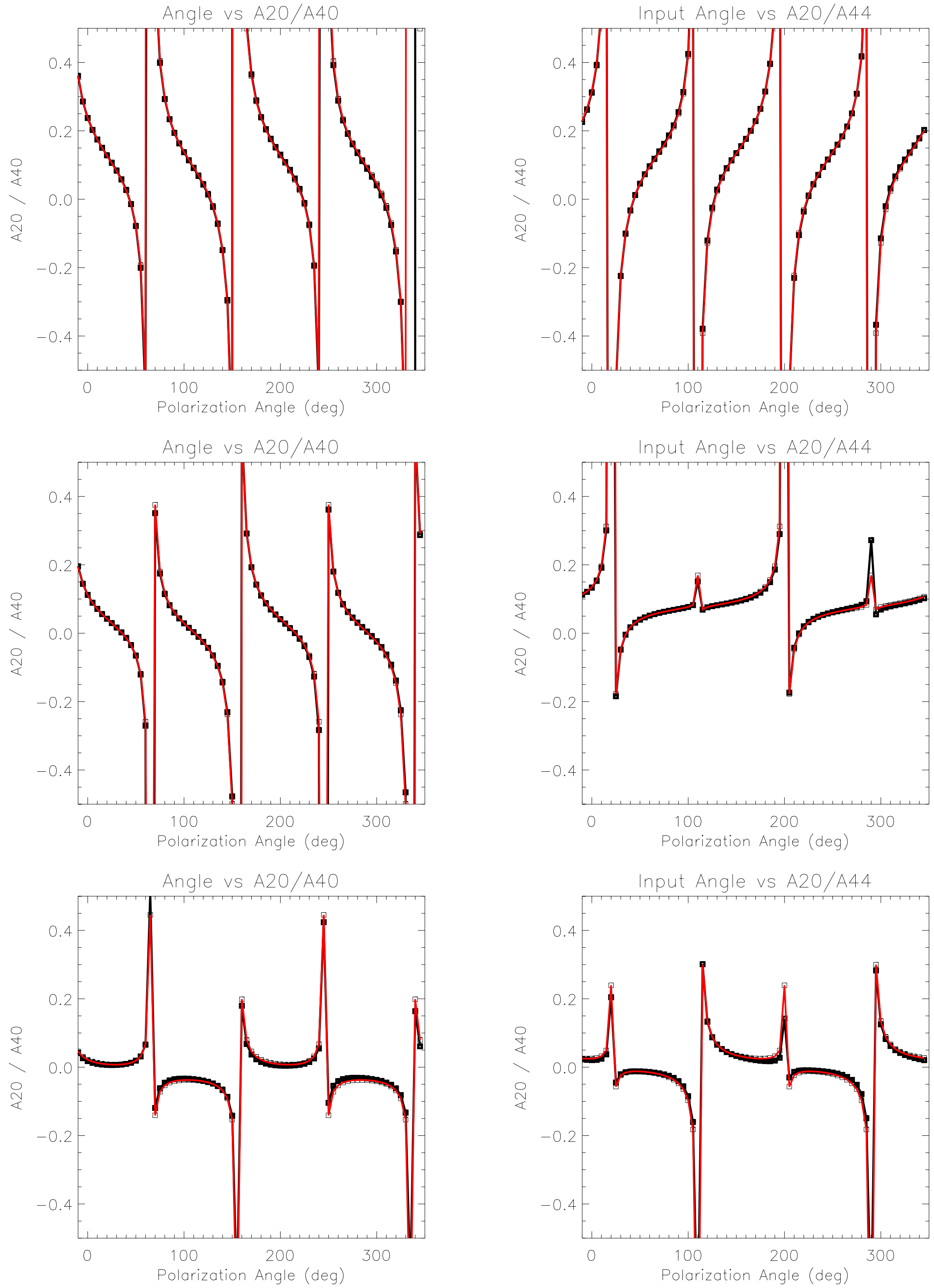

Figure 4-13: Ratio of 20 kHz to 40 kHz and 20 kHz to 44 kHz modulation amplitudes. This signal provides an excellent visual check of the simulation's fit (red curve) to measured data (black points). Each of the quantities, $\theta, \beta, \chi, \delta, r_m$, and the depolarization fraction must be modeled accurately to reproduce the measured data in these figures.

r_m, Mirror relative reflectivity

Unpolarized light calibration showed that the relative mirror reflectivities were within specifications. r_m, the ratio of reflectivities in the s and p directions, is better than 0.99 for *each mirror* in all channels, or 0.97 for the composite mirror in the model. The polarized fraction observed for an input of completely unpolarized light ranged from about 0.3% near the optical axis to 0.7% for the the edge channel, but with large error bars of roughly ±0.3% due to the small number of shots were taken using unpolarized light. Sensitivity tests using the simulation indicates that the polarized response to unpolarized light is rather insensitive to r_m. The values measured from the unpolarized tests only served to limit the range of r_m to between 0.97 and 1 for the composite mirror.

An improvement in sensitivity to the composite mirror r_m comes from looking at the angle independent offset of the responses to linearly polarized light. This more sensitive term, shown as C_0 in Eqn. 4.32 and Tables 4.4 to 4.6 was used to generate the values shown for r_m in Table 4.8 and is in agreement with the results from the unpolarized light tests.

The composite effect of non-unity r_m of multiple mirrors may be diminished via two effects. First, since the MSE mirrors are oriented such that each axis is roughly perpendicular to the axis of next mirror, the effects of r_m may cancel when examined as a whole. In particular, for optical ray propagating along MSE's optical axis, the s-orientation at Mirror 2 becomes the p-orientation at Mirror 3. Second, lenses between mirrors and between the last mirror and the polarimeter may also serve to partially depolarize any polarization created by the mirrors, although the measured upper limit of this effect is shown as the total system depolarization fraction shown in Table 4.8.

χ and δ, Mirror phase shift and orientation

Measured signals at the fundamental PEM1 frequency of 20 kHz indicate a circular response to the pure linear polarized light. The magnitude of the 20 kHz response is most sensitively related to δ, the parameter representing the phase difference between s and p components imposed by a mirror reflection. The phase of the 20 kHz component with respect to the linear angle is determined by χ, the apparent angle of the mirror optical axis. The fitted quantities for these parameters are shown in Table 4.8, showing that the phase shift is worst at the edge channel, reaching a minimum and then changing sign for the last two core channels.

4.3.4 Geometric properties used in MSE simulation

θ, Polarimeter orientation

The phases of the dominant terms in the 40 and 44 kHz components, shown as ϕ_2 in Tables 4.4 and 4.5, are sensitive to the rotation of the polarimeter relative to true vertical and were used to identify θ in Eqn. 4.3.

The reason for each channel to have a different zero is due to reflections and the nominal offset angle of 22.5°. Because the light from each channel enters the polarimeter at slightly different angles, the nominal 22.5° offset is projected slightly differently, resulting in small changes in the apparent polarimeter angle.

Using this data, one can compare the measured angle from a beam into pure toroidal field to θ to calculate any Faraday rotation.

β, Linear polarizer orientation

The simulations also provided several important geometric properties of the MSE setup. When the MSE fixed polarizer was installed, there was no method to precisely measure its passing direction.

The linear polarizer for the MSE polarimeter is designed to have its passing angle bisect the optical axes of the two PEM, i.e., oriented at 22.5° for PEMs at 0° and 45°. This was achieved by aligning one edge of a sheet polarizer, specified by the manufacturer to be the passing direction, to the bisecting angle of the PEMs. However, since no tolerances were available, it was previously not possible to determine the accuracy of the linear polarizer passing direction.

Using the MSE model, this angle β was determined for all channels. Values in

Table 4.8 shows a mean angle of, 22.97°, with a standard deviation of 0.1° most likely due to passing angle non-uniformity across the polarizer surface (4" diameter). The 0.5° deviation from the optimal angle has no effect on a calibrated measurement, and is one reason a small difference between the 40 and 44 kHz response amplitudes, or C_2, in Eqn. 4.32 with values in Tables 4.4 to 4.5. The other reason for this difference can be due to the inequality of retardation between the two PEMs.

4.3.5 Additional optical properties

Throughput of optical system

During the 2001 upgrade, the optical throughput of the invessel periscope was measured. The input aperture was uniformly illuminated, and light exiting Lens 3 was focused to measure the intensity. An identical test was done but using only the MSE obective lens to match the aperture. The intensity ratio measured was 82%, and combines all effects of vignetting, internal reflections, and less than perfect reflectivity from each mirror within the periscope.

MSE has a considerable number of material transitions within its optics train which may attenuate the input light despite the use of antireflective coatings. Each transition causes a 4% loss without an AR coating, and AR can reduces the loss to 1% for normal incidence. All MSE lenses are AR coated with the exception of the vacuum window. Optics measured in the throughput test included *ten of twenty* total material transitions with AR coatings, and three mirror reflections. Using a nominal value of 1% loss at each AR surface, this would be consistent with a 90% transmission through the components *inside* the invessel housing, compared with the measured 82%. The difference of 8% can may be mostly attributed to optical vignetting and to a smaller extent, mirror reflection losses. Accounting for the vacuum window and air side optics, the intensity is expected to be attenuated to 68% when the light reaches the polarimeter.

Despite these losses, MSE is in no way photon statistics limited. Dark count, stray light, and electronic contributions to the noise observed in the lockin signals is minimal. The internal losses do provide a plausible explanation for the observed depolarization fraction.

Depolarization fraction

The depolarizing nature of the MSE optics does not affect any angular measurements and has previously gone unnoticed until the absolute Stokes vector response could be both modeled and measured. However, it does reduce the sensitivity of the diagnostic by several percent, so this effect is discussed briefly here. The depolarization of entering light prior to reaching the polarimeter is suspected to be caused by either the internal reflections within the optical structure or by a small depolarizing effect of passing through each antireflective coating or material interfaces.

In the previous section, it was discussed how internal reflections reduced the single pass fraction of the MSE light to 68%. The light that is not transmitted would be incident upon the internal surfaces of the MSE optics housing and could be scattered back into MSE channels as unpolarized light. To achieve the observed depolarization fraction, 14-36% of this internally reflected light would need to scatter into MSE channels, quite unlikely if only light originally destined for MSE channels is considered. However, this may be plausible in the invessel test (as well as plasma) because MSE accepts light for the entire image plane, and only a small fraction of the total light enters the fibers. Light entering the MSE objective lens around the vicinity of the accepted optical channel can contribute to the internal scattering.

This effect does not extend to the total acceptance cone into the MSE periscope. A radial viewing extent calibration used to determine the extent of each viewing chord showed that each MSE channel is localized in light acceptance. This test involved using a 2 mm by 10 cm light source scanned along the beam axis. This test, while not covering the entirety of the plasma volume, showed that optical crosstalk does not extend a few millimeters beyond the expected imaging area for each channel determined from backlighting calibrations (passing light in the reverse direction of normal operation to illuminate the viewing area).

It is also possible that passage through all the lenses and AR coatings could have a depolarizing effect on the light. Even a small effect at each interface would compound to a noticible fraction due to number of such interface changes.

Both of these conjectures are consistent with the observation that the depolarization fraction changes with channel, minimizing at the optical axis, where optical vignetting is minimized and the rays pass through lenses most perpendicularly.

4.3.6 Limitations of the single-mirror model

The single mirror model has proven to be quite successful in reproducing the response of the diagnostic to each element of the Stokes vector. However, there are a few parameters that the single mirror model was incapable of reproducing exactly.

For example, the phase of the 4γ response, ϕ_4, for each of the 40, 44, and 20 kHz components is not well matched, and the amplitudes are not as well matched as for the 2γ response. In fitting the linear responses, one also had to make an assumption that the unmodeled mirrors introduces circularly polarized light.

These effects can be largely attributed to the cross terms present when multiple mirrors at different angles each possessing imperfections. Building upon the success of the current effort, a more sophisticated model may be constructed to capture the effect of all of the components. The most important addition to the model should be the effect of stray fields on the PEM crystals. This effect is not currently included explicitly, relying on the single combined Faraday rotation term which may not be accurate.

The model in this work gives good matches to measured data from the calibration, and gives good confidence that the diagnostic's response can be predicted. The model can also be used to explore sensitivities of the system to various hypothetical changes in experimental parameters and geometries, such as retardance changes, or polarizer rotations.

4.3.7 Effect of unpolarized and circularly polarized light

This extensive calibration and modeling effort was undertaken to answer the question of whether the optics introduced errors in angular measurements when other elements of the Stokes vector were present. Results of the calibration showed that this is certainly possible, particularly with circularly polarized light at the edge channels. Calibration results showed linear sensitivities to circularly polarized light at up to 10% of the sensitivity to linear light. Through the optical model, this effect has been attributed to the phase shift between s and p components induced by the invessel mirrors.

The case is improved with unpolarized light, where measurements, consistent with simulations, show very small fractions of the light becoming polarized by the mirrors.

With the optical imperfections quantified, it will be shown in the subsequent chapters that in all cases for beam-into-gas measurements (Chapter 5) and for most plasma measurements (Chapter 6), the contamination from unpolarized and circularly polarized light is insufficient to explain measured results.

4.4 Chapter summary

A Stokes vector and Müeller matrix model of MSE was used successfully to simulate the measured MSE responses. Unknown optical properties and geometries of MSE were deduced in the process of reconciling simulation results with measurements. A painstakingly absolutely calibrated apparatus with 0.01° angular resolution and capable of producing nearly pure unpolarized, linearly polarized, and circularly polarized light was constructed. Using this calibration invessel, a detailed invessel calibration was taken, covering the entire basis set of Stokes vectors.

Using the fitted results from the calibration, the response of MSE can be understood for any arbitrary Stokes vector. Although it was not possible to produce mathematically perfect Stokes vectors using the calibration apparatus, imperfections of the Stokes vector on the order of a few percent were successfully modeled with simulation and accounted for.

Model results provided the values of many key sensitive parameter intrinsic to the diagnostic. Quantities such as the dielectric mirror reflectivity ratio and phase shifts between s and p components, the composite mirror axis angle, the polarimeter rotational offset, the polarimeter linear polarizer angle, and the depolarization fraction were all matched to measured results using parameters scans in the simulation.

Issues with ICRF antenna reflection were largely resolved during the calibration procedure. Results showed that ICRF antenna reflections are unlikely to cause MSE measurement errors, with both reflected fraction and polarization of reflections at a very low level.

A new method to measure the PEM retardances for each MSE measurement was made possible by using digital lockins to measure additional harmonics, including the typically parasitic frequencies $(3\,\omega_1 - \omega_2)$, and $(3\,\omega_2 - \omega_1)$. The ratio of these harmonics, belonging to the same harmonic family, are unaffected by imperfect optics, allowing the retardance to be measured routinely for each MSE measurement.

Having absolutely calibrated the instrument and developed a working understanding of the sensitivity parameters, the following chapters will focus on measurements made both for beam-into-gas and plasmas.

Chapter 5

Beam-into-gas Calibration

The invessel calibration discussed in Chapter 4 has provided a complete calibration for MSE except for changes in conditions between an up-to-air invessel calibration and plasma operation. These changes can include Faraday rotation by transmissive elements due to magnetic fields, stress induced birefringence in the vacuum window, and factors that can change PEM retardances. A method capable of calibrating these effects is to use DNB injection into a gas-filled torus with vacuum fields. However, current calibrations seem to observe polarized light that is not emitted by the beam. In this chapter, the beam-into-gas calibration is discussed.

The beam-into-gas calibration is performed by injecting the neutral beam into the tokamak filled with low pressure deuterium gas, with toroidal and vertical fields generated by equilibrium coils. Without the plasma current, the vacuum fields can be fully reconstructed from magnetic measurements using the vacuum field reconstruction code, MFLUX. An equilibrium coil current scan provides the full range of pitch angles needed for an absolute MSE angle calibration. Originally, the beam-into-gas was intended to provide the primary calibration for MSE, as it more closely reproduces plasma operation conditions. However, beam-into-gas measurements exhibited large nonlinear deviations from expected angles as well as unexpectedly strong sensitivities to viewing chord angle, and small changes in filter bandpass. Simulated spectra were also unable to reproduce measured beam-into-gas spectra.

Previous beam-into-gas calibration results from Levinton [28] on TFTR, as well as informal discussions with other MSE diagnosticians indicate that the beam-into-gas calibration is still not well understood throughout the MSE community. A detailed look at the beam-into-gas data is motivated by the fact that although the idea of gas-filled torus calibrations has been around since the first MSE installation, several MSE diagnostics have not been able to apply the results from such a calibration directly to plasma measurements. A literature search shows no published work providing a thorough explanation for observed beam-into-gas discrepancies. C-Mod's MSE diagnostic may provide some new understanding of these calibration issues due to its unique viewing geometry.

Several conditions contribute to the confidence in the validity of MSE beam-into-gas measurements made during the Winter 2004 campaign. First, the absolute calibration confirms the instrumental angular response and quantifies contamination from optical imperfections. Second, bench measurements of Verdet constants place upper limits on the expected Faraday rotation. Third and most importantly, the invessel optics were verified after the run to have remained stationary during the run campaign. These results suggest that mechanisms not associated with the MSE instrument must be found to explain beam-into-gas results.

In this chapter, a hypotheis that explains both MSE and spectral measurements made during beam-into-gas calibrations will be presented. A definitive experiment to test the hypothesis will be proposed. A simulation of the expected MSE spectra for beam-into-gas will be presented first, followed by measured spectra.

5.1 Spectra Simulation

MSE relies on careful spectral filtering to maximize the measured intensity of π lines in the Stark-Zeeman multiplet while rejecting orthogonal σ lines. Maximizing the polarization fraction in this way optimizes the instrument sensitivity and signal-to-noise. Modeling the Stark-Zeeman spectra is necessary to determine the optimal filter tuning to maximize the polarization fraction. A 2D simulation was written to simulate the MSE spectra.

To begin, this section will assume statistical populations, and consider degeneracy-summed Stark-Zeeman lines only, rather than individual degenerate transitions. This reduces the Stark-Zeeman polarization directions to the Stark directions, so lines containing Stark-Zeeman-v will be simply referred to as σ lines and lines containing Stark-Zeeman-E will be referred to as π lines. Line splittings will be disucssed in units of $q_0/2 \approx q_1/6$ per Eqns. 2.43 and 2.44. The validity of using statistical states will be examined in a later section.

5.1.1 Beam effect on observed spectra

Doppler Shift

The Doppler shift is crucial for MSE because it separates the beam Stark-Zeeman lines from the background Dα. For a plasma, background Dα can come from excitation, recombination, and charge-exchange events at the plasma edge, as well as beam charge-exchange in the plasma core. During beam-into-gas, the beam can excite and ionize gas atoms to cause background Dα.

The Doppler shift can be calculated using Eqn. 5.1, the relativistic form is only given for completeness as the beam is only travelling at 1% the speed of light. A more useful form is also given normalized to C-Mod conditions. In Eqn. 5.2, θ is the angle between the sightline and $\mathbf{v_{beam}}$, given in Table 1.2.

$$\nu = \nu_0 \sqrt{\frac{1+v/c}{1-v/c}} \tag{5.1}$$

$$\Delta\lambda_{Doppler} = 68.1 \cos(\theta) \sqrt{\frac{E_{beam}}{50\,\mathrm{keV}}}\ \text{Å} \tag{5.2}$$

The range of viewing angles ranges from 52° for the magnetic axis view to 80° for the edge view. This translates into Doppler shifts of 42Å for the core, but only 12Å at the edge.

Beam Energy Components

The neutral beam is not monoenergetic. In addition to atomic hydrogen ions, H^+, molecular ions, H_2^+, H_3^+, and H_2O^+, can also be accelerated. These molecules then disassociate into hydrogen atoms with lower energies. This results in hydrogen beam neutrals with $\frac{1}{2}$, $\frac{1}{3}$, and $\frac{1}{18}$ of the full beam energy. Doppler shifts of these partial energy components are diminished compared to the full energy component, and can be comparable to the Zeeman-Stark splitting, resulting in overlapped spectral lines.

The π and σ components of the multiplet can overlap between different beam energy components. When this occurs, as is the case for most channels on C-Mod, MSE must choose a spectral region that has a strong net polarization, otherwise π and σ line will combine to give unpolarized light. For C-Mod's case, the only lines that are not overlapping are the redshifted $-2\pi, -3\pi$, and -4π lines from the full energy beam component.

5.1.2 Broadening Mechanisms

Aperture Broadening

The most significant mechanism of line broadening for the C-Mod MSE is finite aperture broadening. The objective lens diameter of MSE is 5.5cm, with the image between 32cm (edge) to 40cm (axis) away. This creates a range of angular acceptance and correspondingly, a range of Doppler shift for each sightline. This results in parabolic line shapes for circular lenses [54].

The range of aperture broadening for the full energy component of the beam on C-Mod's MSE ranges from a FWHM of 5Å for the axis view, to 9Å for the edge view. This may be slightly counterintuitive, as the Doppler shift is minimal at the edge. However, the image is both closer at the edge and the derivative of $\cos(\theta)$ in Eqn. 5.2 is larger at the edge.

The effect of aperture broadening is only important for species with a mean velocity, such as beam atoms. For thermal distributions, the broadening mechanism of importance is the Gaussian shape determined by the distribution temperature.

Beam Angular and Energy Distribution

There can be an angular distribution within the beam. The neutral beam is composed of numerous beamlets coming out of a curved acceleration grid with a focal point. At the point of observation, there is a Gaussian distribution of angles. This effect contributes very slightly here due to the low divergence angle ($\lesssim 1^\circ$) of the beam used.

Beam ions can neutralize between the acceleration grids, causing some hydrogen neutrals to have less than full energy. It is also possible for molecular species to decompose in the acceleration grids, via the reactions shown as Eqn. 5.3. Product ions in these reactions will be accelerated to greater energies while product molecules will end up with lower energies. The reaction is written one way as the reverse reaction is unlikely, given the acceleration difference between ions and neutrals within the grid.

$$\begin{array}{rcrlcll} \mathrm{H}_3^+ & \rightarrow & 2\mathrm{H} & (<\mathrm{E}/3) & + & \mathrm{H}^+ & (>\mathrm{E}/3) \\ \mathrm{H}_2^+ & \rightarrow & \mathrm{H} & (<\mathrm{E}/2) & + & \mathrm{H}^+ & (>\mathrm{E}/2) \\ \mathrm{H}_2\mathrm{O}^+ & \rightarrow & 2\mathrm{H} & (<\mathrm{E}/18) & + & \mathrm{H}^+ & (>\mathrm{E}/18) \end{array} \tag{5.3}$$

Although this effect will create wings on the otherwise monoenergetic beam components, it was not included in the simulated spectra due to the lack of data that quantifies its magnitude.

Neglected Broadening Mechanisms

The following list of broadening mechanisms are negligible when compared with the aperture, angular, and energy broadenings. See [55] for more detailed information on each mechanism.

- Thermal broadening for room temperature gas
- Natural line broadening
- Pressure (Stark) broadening

5.1.3 Simulated spectra

MSE viewing chords integrate through the 8-10 cm neutral beam, and has an aperture size comparable to other scale lengths, so a 2D simulation is more accurate for determining the view averaged line shapes. The key mechanisms that need to be accounted for are aperture broadening, magnetic field variation along the chord integration, and finite image size effects. Filter functions can be used in the code to predict the polarization fraction.

The beam is modeled in a 2D R-y grid, where R is the radial direction, and y is the toroidal direction at the beam axis. Each viewing chord is divided into discrete rays within each MSE channel's viewing area, and each ray is divided into individual emissive elements along its intersection with the DNB. Each emissive element contributes to the total signal according to the relative local beam neutral density and the distance from the lens. So far only beam-into-gas specta have been simulated, so calculations of local beam brightness have not been necessary.

The transition probabilities are incorporated into the simulation as relative intensities of the multiplet components based on the Stark-Zeeman line structure in Chapter 2. Equating transition probabilities with relative intensities in this way implies the assumption of a statistical population of upper states.

Figure 5-1 shows simulated spectra using conditions from a 6.1T beam-into-gas shot (1040304027). Relative intensities of the background Zeeman-split Dα components emitted by the deuterium fill gas are calculated by using the viewing angle with respect to the magnetic field, shown in Fig. 2-6, in Eqn. 2.21. Zeeman line profiles are obtained by scaling a measured line from a lamp calibration, and should include all instrument effects. This implied the assumption that the fill gas is at the same temperature as the gas in the calibration lamp. No attempts were made to simulate the intensities of the Zeeman lines, rather the total intensity of the Zeeman lines were made to agree with measured values.

Fig. 5-1[TOP] shows the simulation results showing the Stark-Zeeman split and Doppler shifted beam emission compared to the Zeeman split Dα. The bottom figure

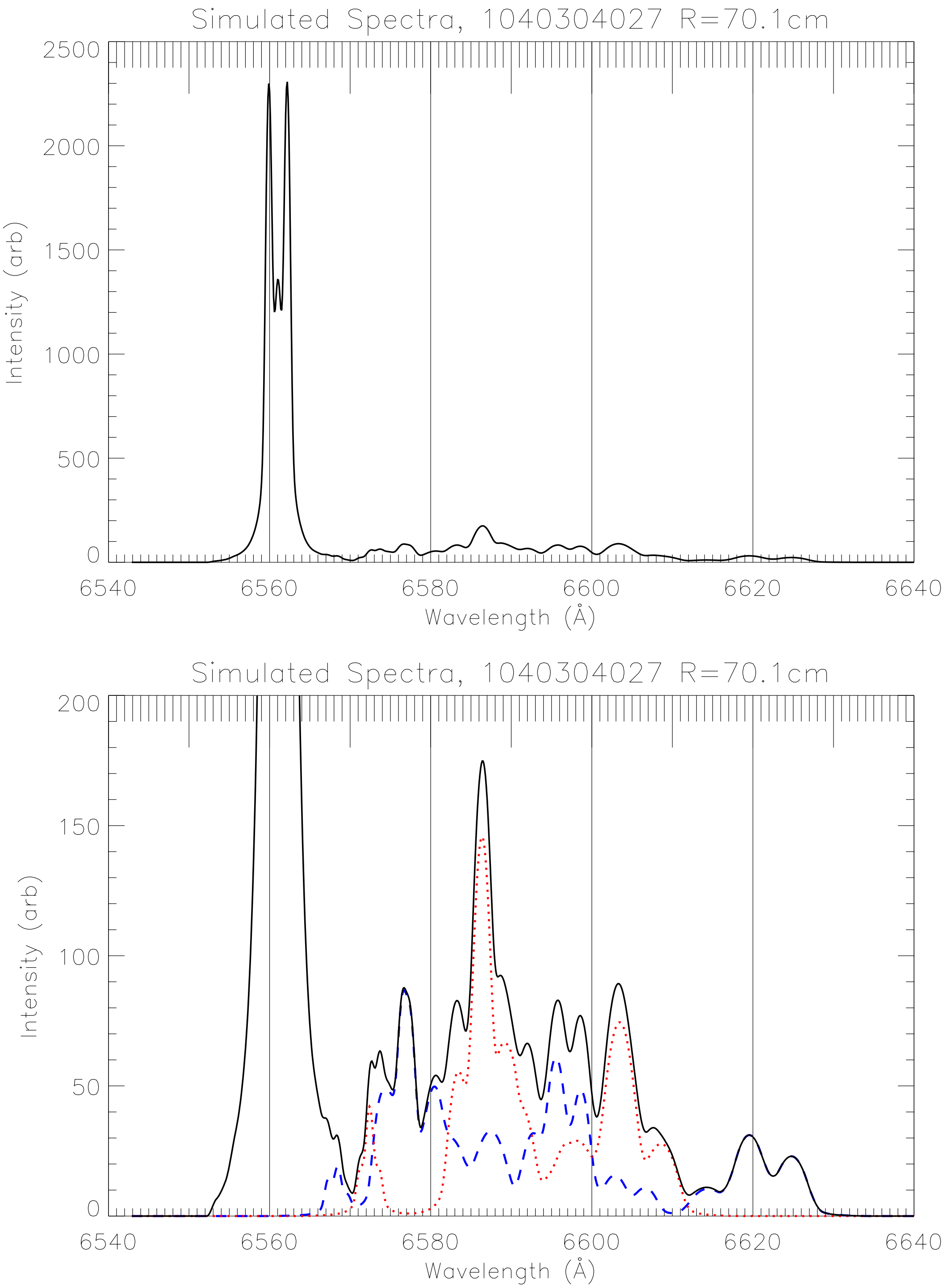

Figure 5-1: Top: Simulated spectra for a 6.1T beam-into-gas shot. The intense emission centered at 6561 Å is Zeeman split Dα from fill gas excitation.
Bottom: Same data, scaled to focus on beam emission. Simulation includes the measured beam species mix, realistic geometry, and assumes statistical upper state populations. Dashed blue lines shows π line intensity, and dotted red line shows σ line intensity. MSE chooses to observe the three redshifted π components from the full energy beam component at around 6620Å because they do not overlap with σ lines.

shows the beam emission in more detail, showing both σ polarized intensity as a red dotted line and π polarized intensity as a a blue dashed line. The simulation makes it clear why MSE on C-Mod measures the -2π, -3π, and -4π lines of the full energy beam component around 6620Å, as these are the only lines free from overlap with σ lines.

For this simulation, the local beam species intensities, of full (37.2%), half (12.7%), third (43.5%), and eighteenth (6.5%) energy components at the measurement location were used. These values were based on a spectrum without magnetic field measured just after the simulated shot.

Non-statistical populations have previously been reported by Levinton [41] in beam-into-gas calibrations. Using techniques developed in Chapter 2, one can calculate the effect on observed multiplet component intensities from perturbations to upper states populations. Inclusion of this effect in the spectra simulation should allow one to match intensities in the observed spectra and deduce the upper state population. However, an attempt to do so revealed discrepancies between the simulated and measured spectrum.

5.2 Measured spectra

Several attempts have been made in the past several years to couple the MSE fiber arrays to a spectrometer via a patch fiber. These attempts proved to be too inefficient to produce useful spectra. In January 2004, a flexible XYZ translation plus rotation stage was fabricated to allow MSE fibers to be optimally positioned directly in front of the spectrometer's entrance slit. By removing all intermediate components, this setup has reached the etendue coupling limit for the MSE optics and the spectrometer. The improvement in spectra counts was several fold and produced the spectra presented here.

The following MSE spectra were taken with the MSE fiber viewing R=70.1cm during beam injection into deuterium gas with a 6.1T (on-axis) field. This channel provides sufficient Doppler shift between beam components to separate Stark features.

Several shots were taken without disturbing the optical setup while changing field conditions from 6.1T to 2.7T, then to zero field.

Spectrometer calibration

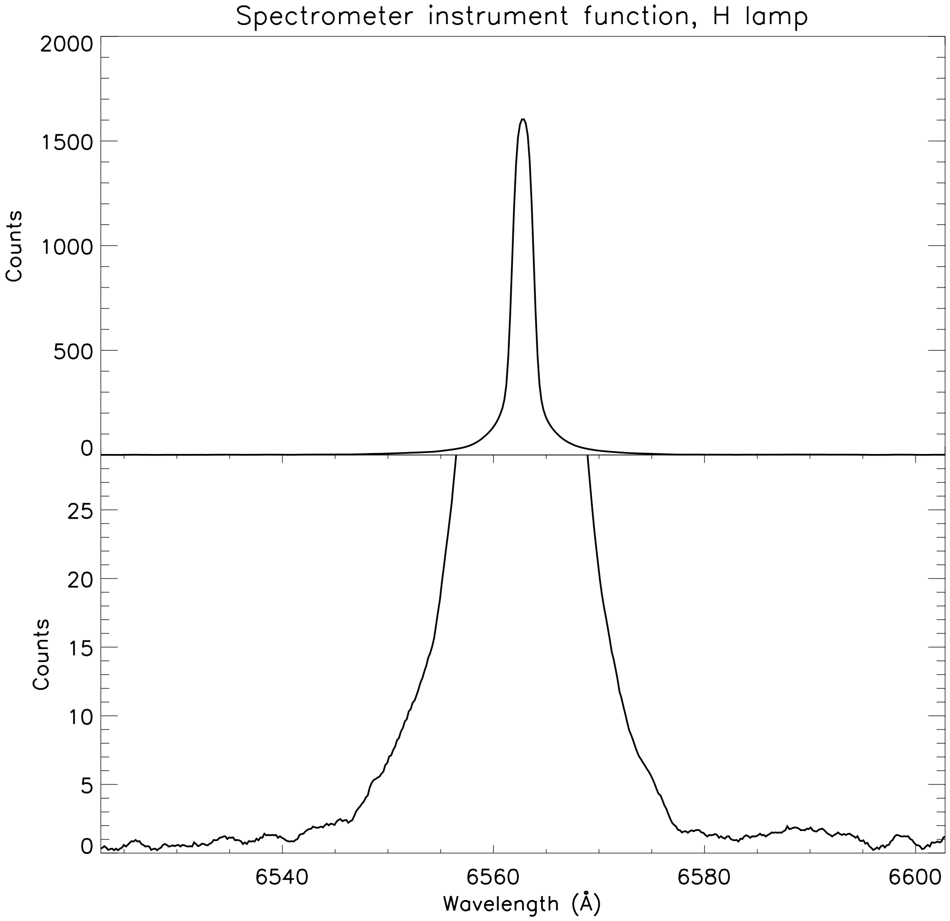

Figure 5-2: McPherson 2051 Instrument function, taken using a hydrogen lamp. Scaled in lower figure to show falloff to noise floor of 1–2 counts.

All spectra was taken with a 1 m McPherson 2051 Czerny-Turner monochromator. The instrument dispersion was calibrated by measuring lines from a neon calibration lamp. Calibration for measurements of spectra near the Dα wavelength typically uses NeI lines at 6506.53 Å, 6532.88 Å, 6598.95 Å, 6678.28 Å, depending on the desired range. A measurement of the Hα line from a hydrogen calibration lamp was performed. This line profile is shown in Fig. 5-2. This line profile, which included all spectrometer broadening mechanisms, will be used repeatedly in the following sections to fit room temperature lines. Because some arguments will be based on low count features, the instrument function is shown down to the noise floor of 1–2 counts. The line shapes for neon lines were compared to the hydrogen line and found to be essentially identical.

Special thanks goes to William Rowan from U. of Texas at Austin for operating the spectrometer during the MSE beam-into-gas calibration, as well as taking the lamp calibration data.

5.2.1 Beam-into-gas spectra

Figure 5-3 compares measured spectra in varying magnetic field conditions. Fig. 5-3[Top] shows the four beam energy components Doppler shifted in zero field. Fig. 5-3[Middle] was taken at 2.7T (on-axis) and shows the Stark-Zeeman splitting of each energy component. The calculated positions of each of the Stark-Zeeman components are shown as vertical lines, using blue for π and red for σ. The beam energy components are differentiated using linetype, with full energy in solid, half using dash-dotted, third using dashed, and eighteenth using dotted lines.

To improve photon statistics, Fig. 5-3[bottom] shows the summed counts from two spectra with identical conditions (1040304027 and 028). For these two shots the toroidal field coils were run at 167.5kA to produce a 6.1T field at the magnetic axis. This is 5.8T locally at R=70.1cm and both values will be used to refer to this high field condition. The torus was filled with deuterium gas at 1.4 mTorr for all spectra taken. Figure 5-4 is identical to Fig. 5-3[middle] and [bottom] but rescaled to focus on beam emission.

The measured spectra in Fig. 5-3[bottom] and Fig. 5-4[bottom] do not appear to match the simulated spectra in Fig. 5-1, although the predicted locations of the Stark split lines appear to be correct based on the differences observed between the 2.7T and 6.1T spectra.

Two non-beam emission features stand out as unexpected differences between measured and simulated spectra. The measured spectra show unshifted background

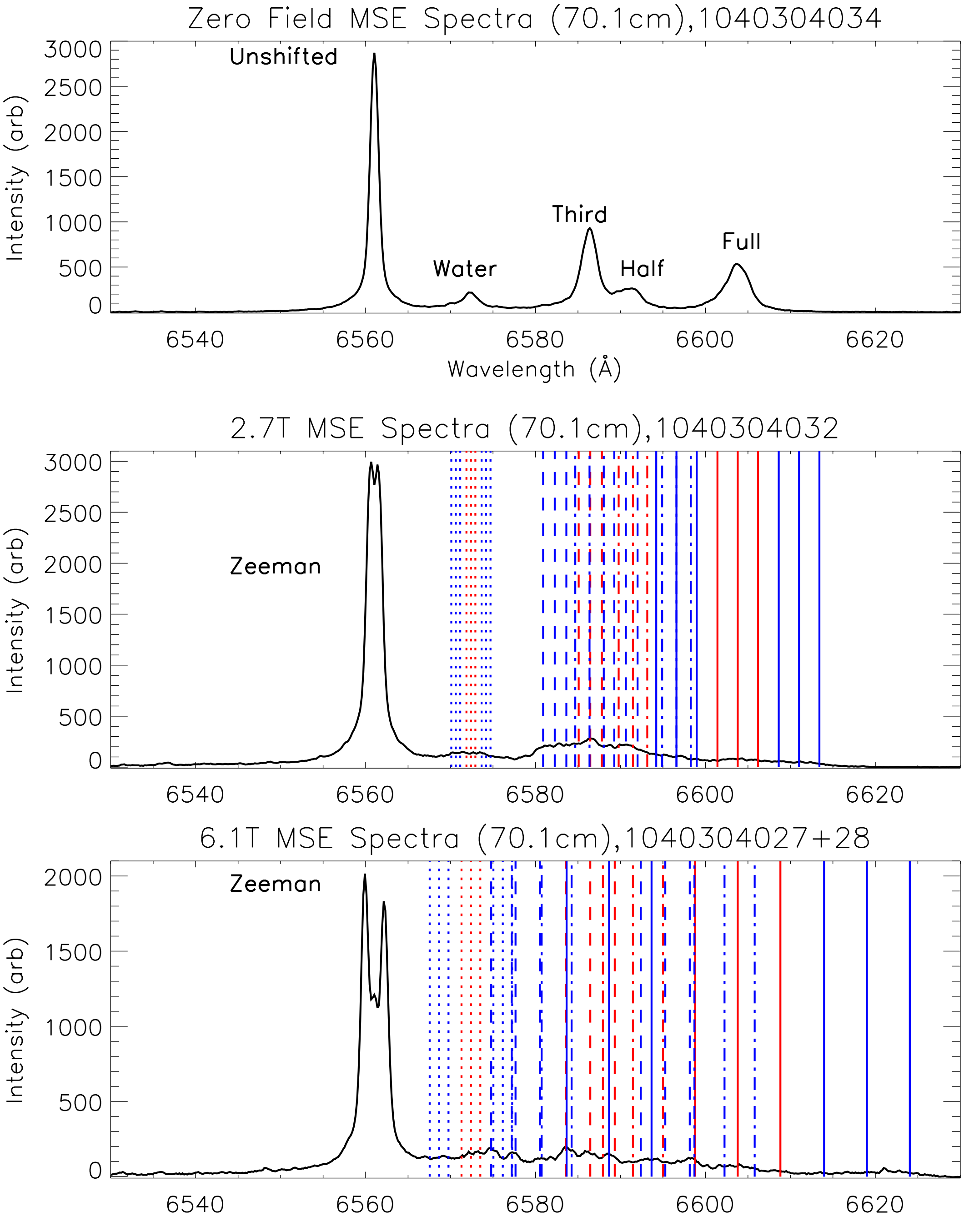

Figure 5-3: Measured spectra taken with the MSE fiber viewing R=70.1cm.

Top: Spectra of beam into deuterium gas, zero field. Leftmost peak shows the unshifted Dα from excitation of the fill gas followed by the Doppler redshifted beam components with eighteenth (water), third, half, and full energies.

Middle/Bottom: With an on-axis magnetic field of 2.7T [Middle] and 6.1T [Bottom], each beam component has split into nine Stark-Zeeman components, while Dα has split into three Zeeman components. Expected Stark-Zeeman lines are shown in red for σ and blue for π. Solid lines represent lines from the full energy component, dash-dotted for half, dashed for third, and dotted for water.

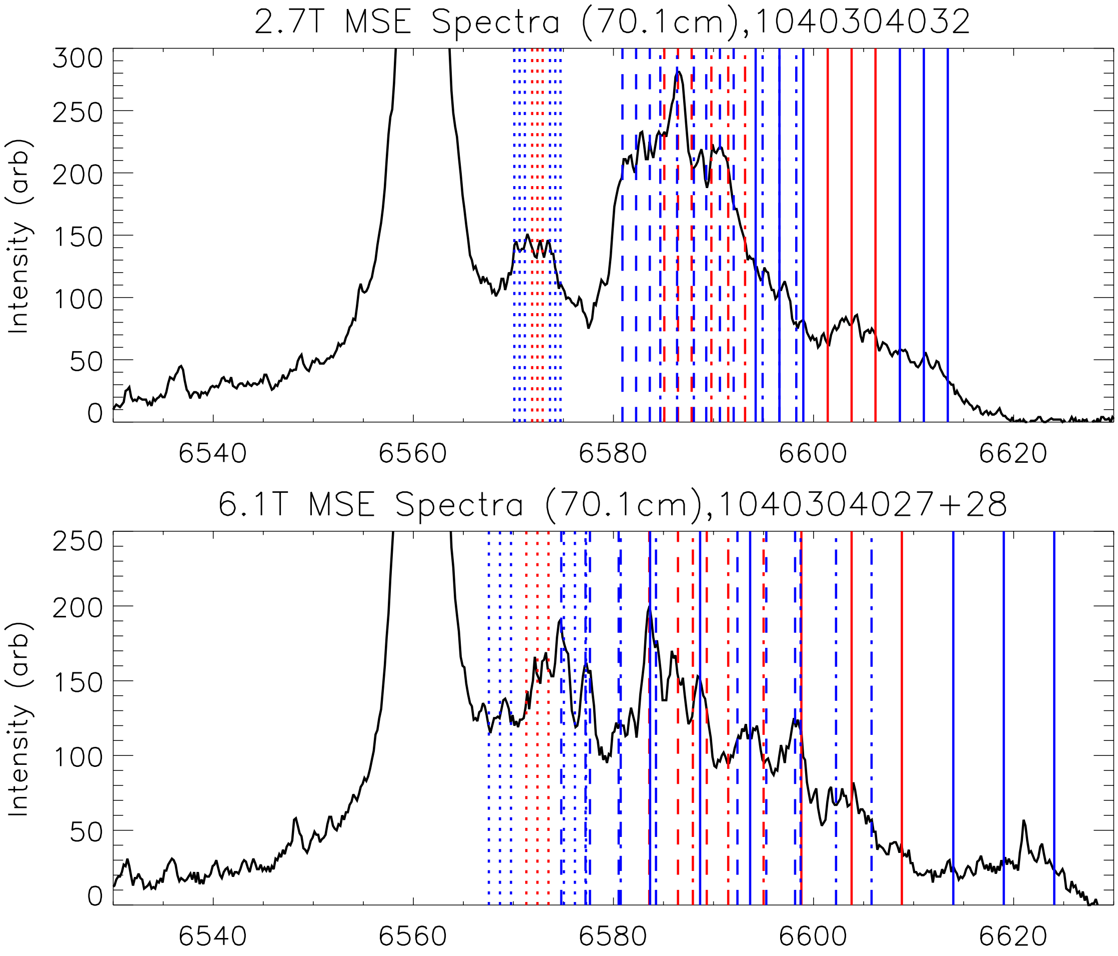

Figure 5-4: Same as Fig. 5-3: MIDDLE and BOTTOM, but scaled to focus on Stark-Zeeman components. Again, the expected Stark-Zeeman lines are shown in red for σ and blue for π lines. Solid lines represent lines from the full energy, dash-dotted for half, dashed for third, and dotted for water.

Zeeman peaks of uneven intensity in the 6.1T spectra. The unequal Zeeman peaks is evident for the Zeeman-σ peaks at 6.1T, but much less so for the 2.7T peaks (where the Zeeman-π peak is also not resolved). The difference in the Zeeman shifts between the two fields is 0.6Å, suggesting that a narrow line might exists at 6559.9Å with a peak around 200 counts.

The measured spectra also show intensity on the blue side of the Zeeman split Dα, where the simulation shows the intensity falling to zero. While discrepancies in the shape of the beam emission might be explained as inaccuracies in the simulation, non-beam emission differences suggest there may be an additional source of emission.

5.2.2 D_2 molecular lines in beam-into-gas spectra

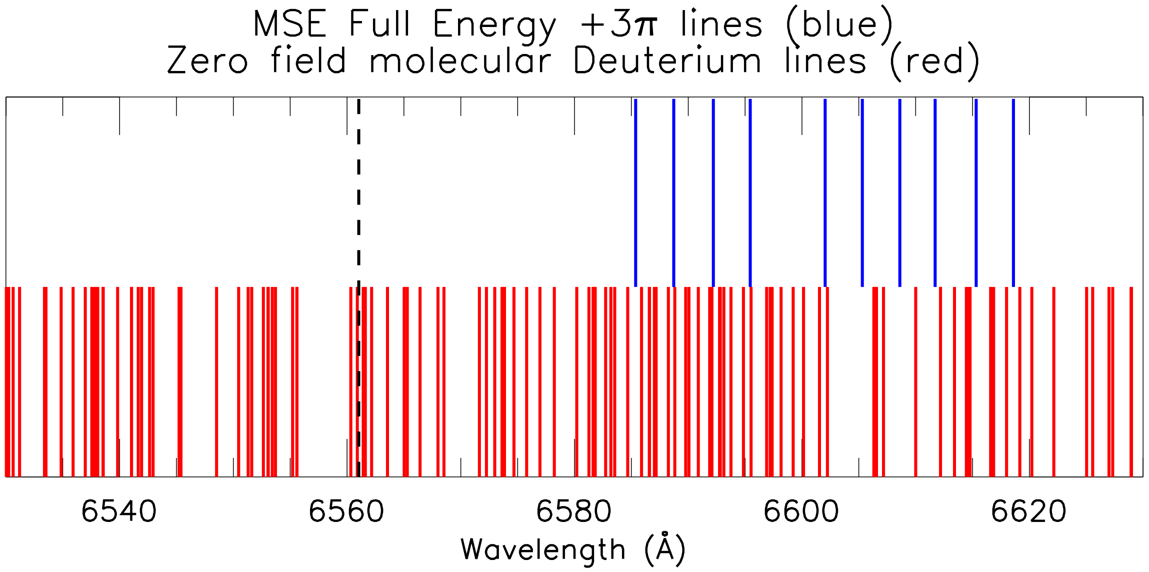

Figure 5-5: Deuterium molecular lines within the MSE spectral region. Data shown from Freund [56] are for zero field. Red lines on the lower half shows wavelengths of deuterium molecular lines, blue lines above show where the nominal centers of MSE tuned filters for each spatial channel. A black dashed line shows unshifted Dα as a reference. 133 unshifted and unsplit D_2 lines are shown.

The unequal intensity of the Zeeman-σ peaks and emission below the wavelength of Dα suggests the presence of additional lines unaccounted for in the MSE spectra model. In this section, D_2 molecular emission is considered as a possible source of additional light. Fig. 5-5 shows over one hundred D_2 lines in the MSE region of interest. The line locations were taken from the extensive analysis of Dieke's spectrographs by Freund [56], which unfortunately does not provide intensity data. No references could be found showing D_2 molecular line intensities even remotely matching the MSE condition of high energy neutral beam impact on room temperature, low pressure deuterium gas under strong magnetic fields. For the purposes of this work, the lines intensities must be assumed to be unknown, and readers should not assume that D_2 lines shown in Fig. 5-5 are of equal or even similar intensities.

Another caveat for the data shown is that it is for zero field. Molecular lines will Zeeman split in a magnetic field in a far more complicated manner than atomic Zeeman splitting, [57, 58]. Fig. 5-6 is reproduced from Jost [57] showing that different

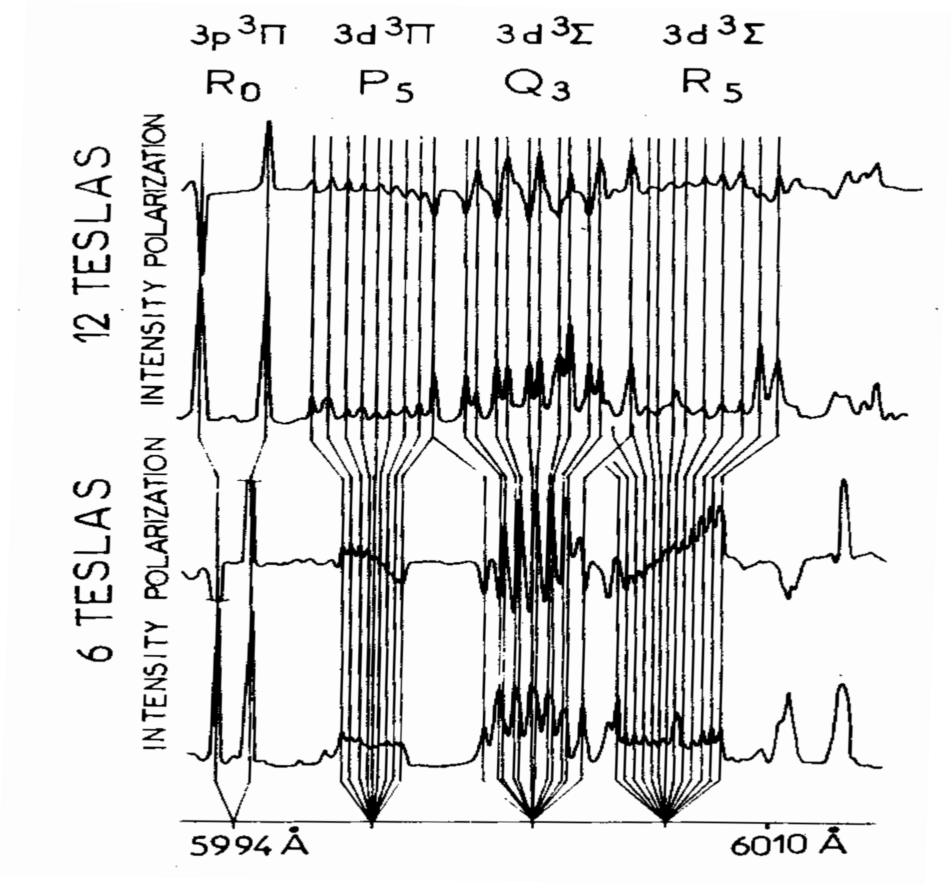

Figure 5-6: Measured polarization pattern for a few sample lines of D_2 shows its complexity. At 6T, the widths of the separation is about 3Å. MSE filter transmission decreases by about a decade in 3Å. Reproduced from Jost [57].

rotational-vibrational ("rovibrational" in the literature) states can split into doublets and a variety of multiplets in a magnetic field, with the width of the splitting as high as 3Å for the 6T case in the figure. The intensity and polarization state are complex as well, with the figure showing Zeeman-σ polarization above the centerline and Zeeman-π polarization below the centerline.

Since the molecular lines are not Doppler shifted, neither their width nor wavelength should vary dramatically with MSE channel, although the 1/R variation in magnetic field will slowly change the Zeeman splitting. Therefore, even though the spectra was taken for the R=70.1cm channel, molecular lines are expected to be present in all other MSE channels.

Emission between beam components

Molecular lines are usually ignored as they are a small fraction of the Balmer-α intensity. The shape of the beam component lines should follow a parabolic line shape convolved with the instrument function taken from a lamp calibration. As shown below, fitting this shape to the zero field spectra shows counts between the lines that cannot be explained. In addition, unexplained peaks appear in several places between atomic components.

The zero field spectrum shown in Fig. 5-7 has been fitted using calculated line centers and line profiles previously described. As the widths of the aperture broadening scale with Doppler shift, the parabolic widths of the fractional energies are scaled by the square root of their energy fraction. The unshifted line was fitted by scaling the instrument function. Good fits were obtained for the atomic lines, as seen in Fig. 5-7[TOP], but a surprising amount of unexplained intensity remains between the lines. Fig. 5-7[BOTTOM] shows this in more detail. The unfitted intensity exists throughout the region between the unshifted line and the full energy beam component. When integrated over this range of 6565-6610Å, the unfitted intensity, i.e. the area between the solid and dashed line in Fig. 5-7, is 18% of the *total* measured intensity in the same region.

Since the lines have been fitted to the peaks of the measured spectra, the regions where the discrepancy is most evident lies in the areas between beam components. Some of this "unexplained" intensity is likely due to the beam energy distribution described in 5.1.2, where molecular breakup and ion neutralization in the accelerator grid made it possibile to have wings to the energy distribution of each beam component, but it is unlikely that as much as 18% of the beam is in the energy wings. Looking again at Fig. 5-7[BOTTOM], it appears that there are many small peaks in the regions between beam components that can not be explained by the beam energy distribution. It is unfortunate that these suspected molecular features are overlapped with other features, such that their peaks are less than one Poisson error above the backbround intensity and making their presence less than definitive.

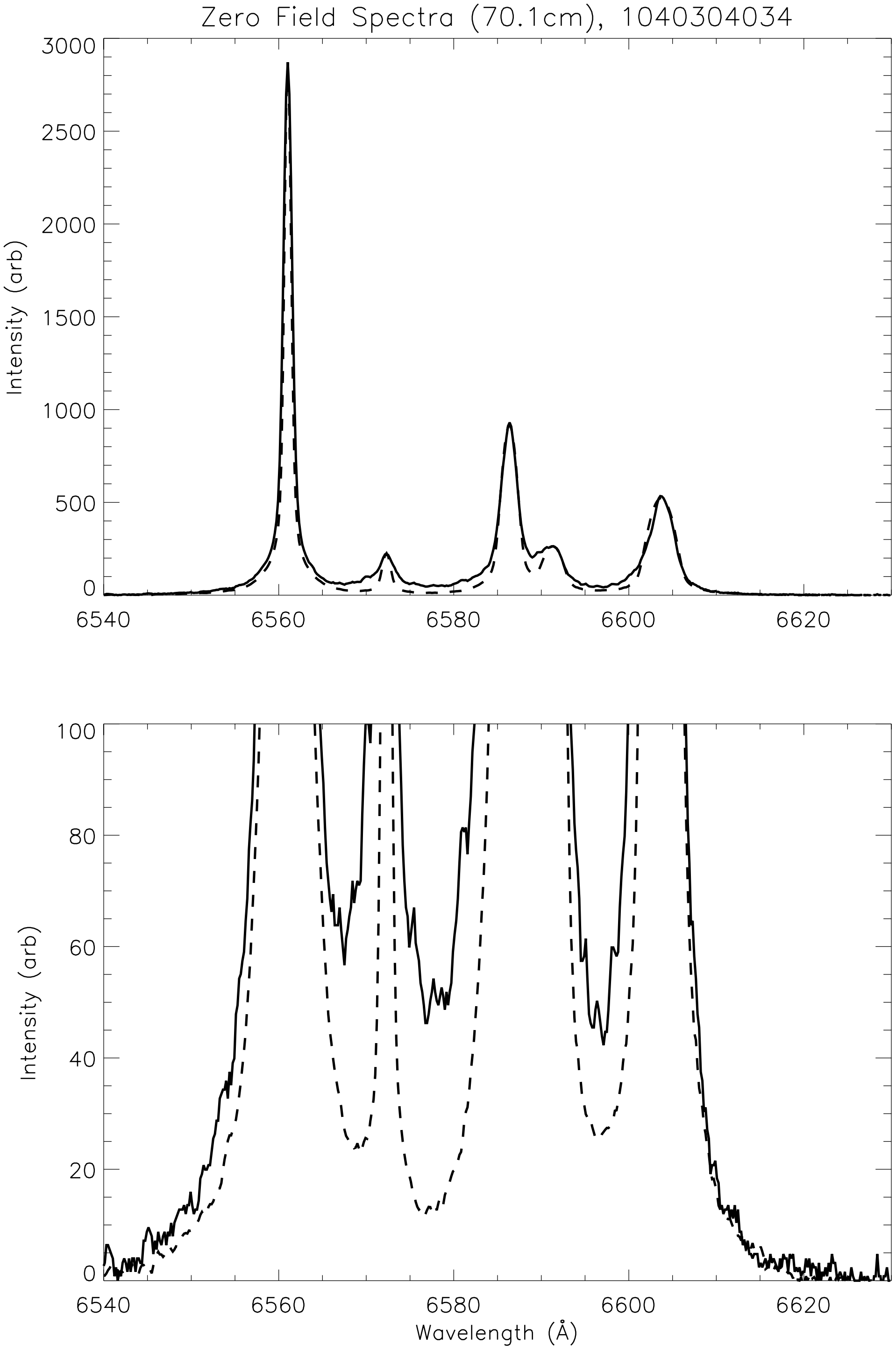

Figure 5-7: Fitted zero field spectra shows unexplained intensity between peaks suspected to be D_2 molecular lines.
Top: Calculated spetra (dashed) fit the measured profile (solid) well expect between beam components.
Bottom: Same as Top but with zoomed range shows small unexplained features throughout the spectra.

One troubling fact is the lack of emission on the red side of the full energy emission. One might have expected to observe emission in this region, around 6620 Å for both the zero field spectrum in Fig. 5-7[BOTTOM] as well as in the low field spectrum in Fig. 5-4[TOP]. The lack of emission in this region does not support the D_2 hypothesis.

Emission blue of the unshifted lines

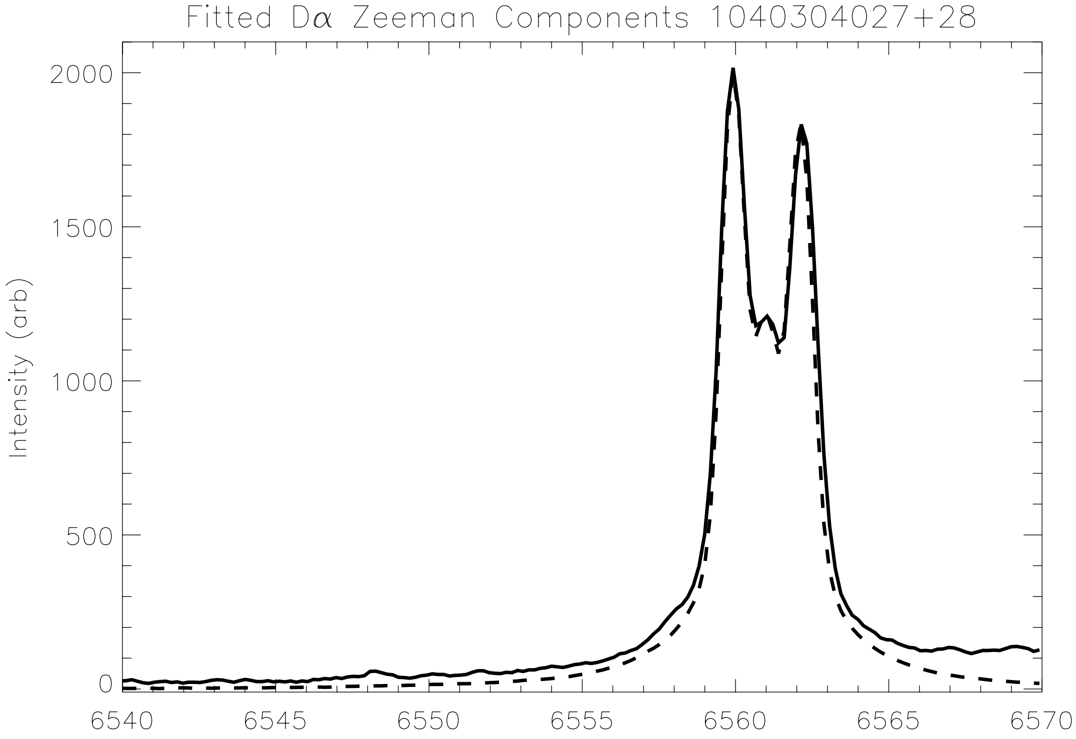

Figure 5-8: Zeeman components fitted using three scaled instrumental functions. There is no emission expected on the blue side of Dα, suggesting another source such as molecular D_2. Fig. 5-9 zooms into the area of interest and compares with the zero field spectra.

Looking blue of unshifted Dα lends more support for the existence of D_2 molecular lines. Since beam atoms appear redshifted for MSE viewing geometry, there should be no light on the blue side of the unshifted line due to the beam. However, unexpected emission on the blue side of Dα is seen in all three spectra. The Zeeman components of Dα are fitted using instrument function line shapes, as shown in Fig. 5-8. Three instrument function shapes were scaled to fit the three Zeeman lines and summed to

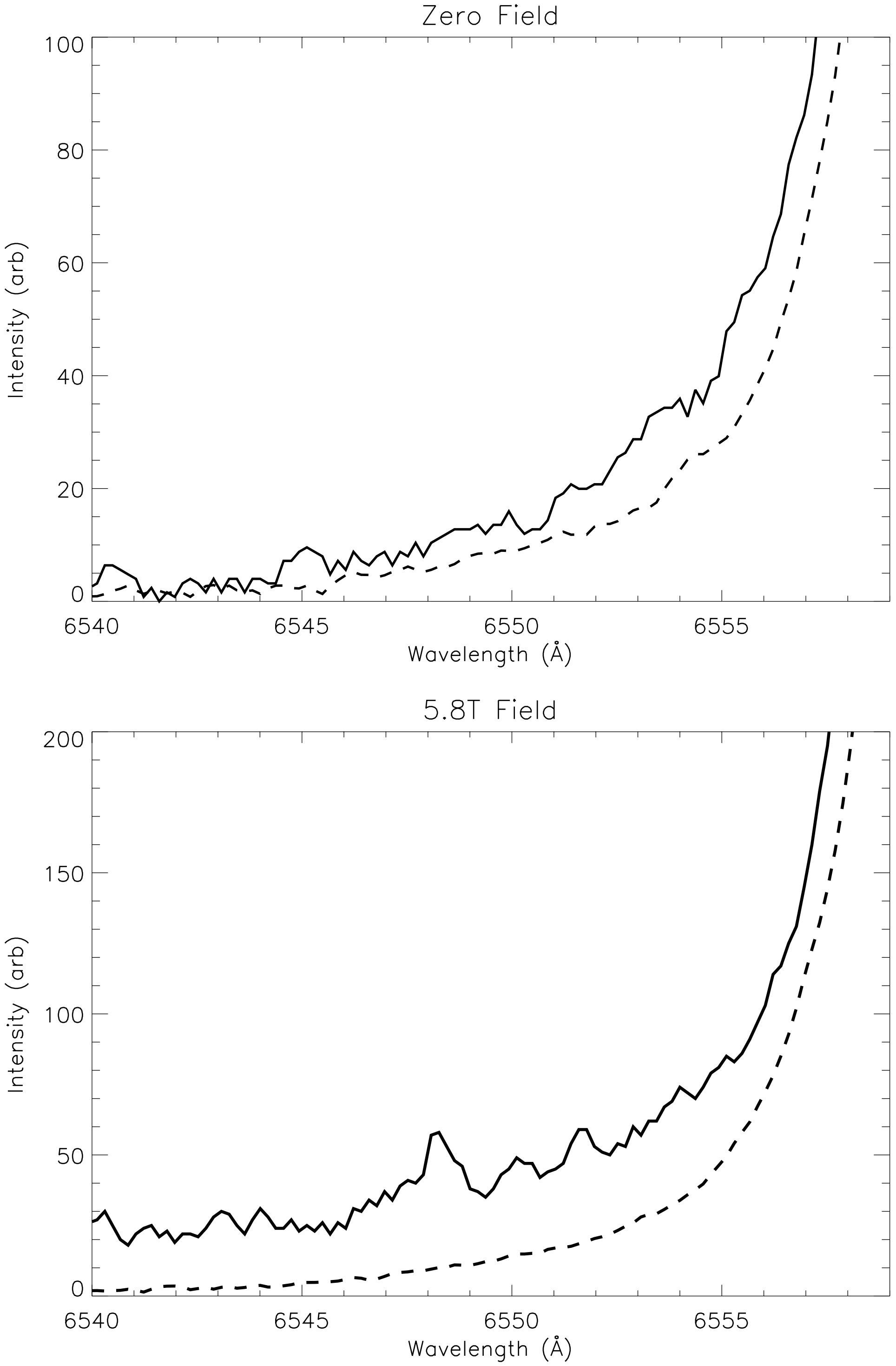

Figure 5-9: Zoomed area blue of unshifted Dα from Fig. 5-7[TOP] and Fig. 5-8 [BOTTOM]. Dashed line shows best fit using scaled instrument function. Wavelengths below Dα shows significant broadband intensity. Other than molecular deuterium lines, there is no currently no other plausible explanation for this emission. Comparing the measured intensity in this range between spectra shows that the magnetic field increases the emission by a factor of between five to eight.

give the dashed line. The unequal Zeeman-σ lines were fitted independently to give the most conservative falloff on the blue side.

The emission is expected to approach zero as shown by the dashed line, but counts well above the noise floor of the spectrometer persist all the way to the edge of the detector 20 Å away. The area of interest for both a zero field and a high field case is shown in Fig. 5-9, with the dashed line showing the expected intensities.

While counts above noise can be seen in the zero field spectra of Fig. 5-9[TOP], the effect is more dramatic in the spectra with magnetic field, Fig. 5-9[BOTTOM]. The only current explanation for the presence of this emission is deuterium molecular lines. Fig. 5-5 does show numerous D_2 molecular lines blue of Dα that might account for the counts observed in spectra.

Comparing the spectra in Fig. 5-9 shows that the suspected molecular line emission becomes more intense with a magnetic field. This suggests that the D_2 rovibrational excited population changes in the two conditions. Little is known about this effect, but this work suggests that the effect could be due to the confinement of beam ions and to a lesser extent free electrons generated as the neutral beam undergoes ionization events. In the case without field, ions generated from the neutral beam continue to travel radially without perturbation but in a magnetic field, ions are confined where they ionize, and are lost vertically through ∇B and to a much lesser extent (due to the radial velocity of the beam) curvature drifts. *This differs significantly from other MSE configurations because the C-Mod beam is injected purely radially, and has no mean toroidal velocity component.*

Assuming conservatively that the ion energy loss is negligible throughout the beam drift, the drift velocity is calculated to be about 250 times slower than the atom velocity. This allows the ion to transfer 250 times more energy to free electrons or to directly excite D_2 molecules. The same calculation also applies to free electrons within the MSE viewing volume, but electrons will stream along field lines, assuming a symmetric velocity distribution. These effects combine to greatly increase the density of charged particles responsible for molecular excitation, and could possibly explain the apparent 5-8 fold increase in molecular lines.

From the fitted zero field spectra in Fig. 5-7, one can compute the widths of each beam atom line, including all broadening mechanisms present in both MSE optics and the spectrometer. Aperture broadening is invariant with Stark-Zeeman splitting, so widths for each multiplet components is identical to the unsplit line. Lines from the room temperature fill gas, both atomic and molecular, should be characterized by the instrument function because they are low temperature and not affected by aperture broadening. It might be possible, therefore, to try to distinguish between molecular and beam lines by their widths. Unfortunately, attempts to distinguish molecular lines from atomic lines were inconclusive due to their spectral overlap and the variable Zeeman splitting of molecular lines.

Polarization of deuterium molecular lines

The presence of unexpected lines would not be an issue for MSE unless the light were polarized. Fig. 5-10 shows two overlaid spectra using otherwise identical setups, without (black) and with (blue) the MSE linear polarizer. The polarized spectra have been normalized to match the integrated Dα intensity to compare the spectra. The indistinguishable dashed and dotted lines show the expected intensity falloff from the sums of all Zeeman components. Because the polarizer is not aligned with either Zeeman-σ or Zeeman-π components, areas in the spectra where the blue line is greater than the black should be interpreted as having light polarized more in alignment with the polarizer, and areas where the blue line is below the black as more perpendicular. Comparing the spectra shows the a complex polarization pattern.

The unforeseen complexity of the MSE spectral region still limits the conclusiveness of current measured spectra. Small spectral features suspected of being D_2 molecular lines are within one or two Poisson errors or were not well reproduced from one shot to the next. The C-Mod DNB used in this work was limited to 50ms per C-Mod pulse, making it inefficient to integrate enough photons for spectra of sufficient counts to draw firmer conclusions. The situation could be significantly improve with the installation of a new long pulse beam, with a 1.5s pulse. This is well matched to the C-Mod pulse length, and could potentially provide the equivalent photon count

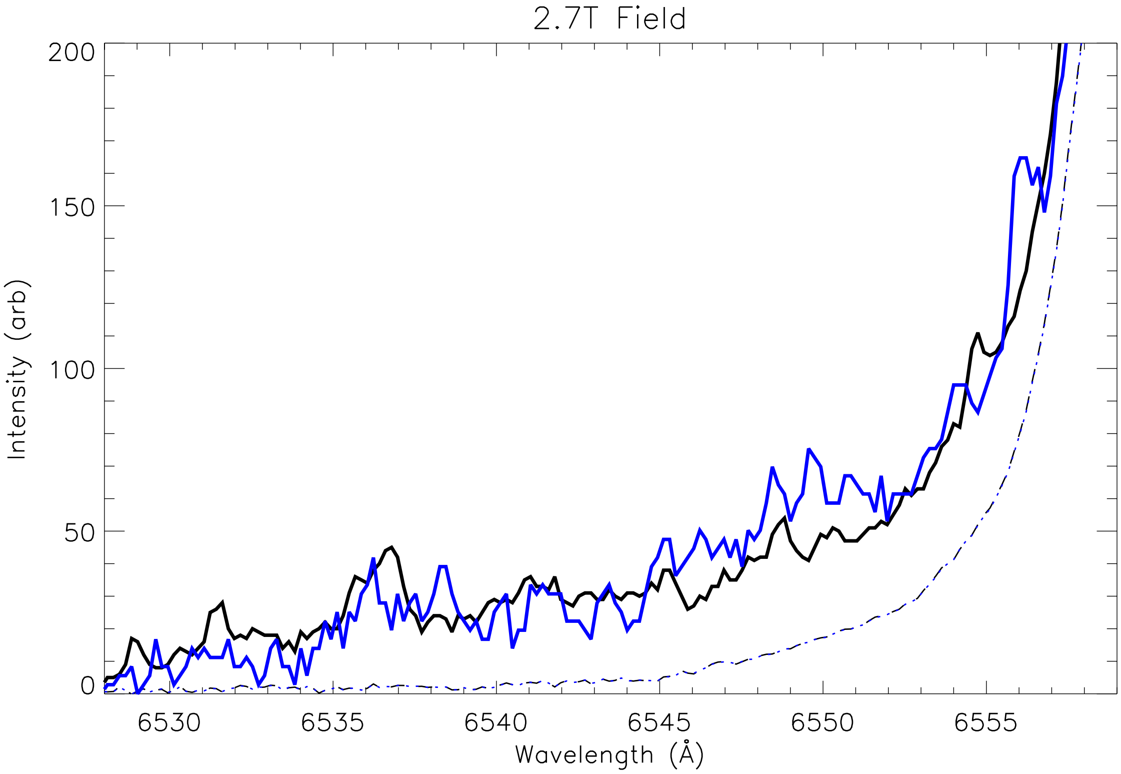

Figure 5-10: Polarization of D_2 lines on the blue side of Dα. A scaled Fig. 5-3[MIDDLE] is shown in black, taken without a polarizer. Another 2.7T spectra taken with the MSE linear polarizer in place is shown in blue. The two spectra have been normalized to match the total Dα intensity. Dashed and dotted lines (indistinguishable) show the expected intensity falloff. Differences in intensity shows that the emission is partially polarized.

in a single shot that would have required one entire C-Mod run day using the 50ms beam.

5.2.3 Excited state population for C-Mod beam-in-gas

In addition to contaminating the MSE angular measurement, the overlapping molecular lines of unknown intensity also complicate the benchmarking of Stark-Zeeman excited state populations. Although it would have been highly desirable to determine the *entire* excited state population, it is currently not possible to do so using available spectra containing D_2 line contamination.

The intensity of the D_2 lines appear diminished for the most redshifted MSE

Component	-2π	-3π	-4π
Statistical	0.32	1.00	0.74
C-Mod Measured	0.83	1.00	0.75
TFTR Measured	0.76	1.00	1.25

Table 5.1: An estimate of the excited state population used in the fit shown in Fig. 5-11. Values are normalized to the 3π component. The C-Mod data does not match either statistical expectations nor previous data from Levinton [41].

lines at the core channels, so an excited population fit may be possible for several π components of the multiplet. Fig. 5-11 centers around the 6620Å region, where MSE observes the -2,-3, and -4 π lines of the full energy beam component. The relative intensities of these lines are fitted and Table 5.1 lists the measured line intensities for these components, calculated intensities assuming a statistical intensities, and those measured by Levinton on TFTR [41]. The C-Mod data differs from both Levinton's results and statistical expectations.

Figure 5-11 shows two fits to the data using the values in Tab. 5.1, one using statistical populations (dashed line) and the best fit (solid line). A statistical ratio cannot be scaled to fit all three π components. From the fitted data, it appears that the original assumption that this spectral region contains only beam emission lines is somewhat invalid. About 20% of the emission in the fitted region shown in Fig. 5-11 cannot be accounted for. The 20% figure likely underestimates the D_2 intensity since overlapping lines are fitted and assumed to be beam emission.

5.3 MSE Beam-into-gas measurements

In the previous section, spectral data suggesting the presence of polarized D_2 molecular lines were shown. Despite the presence of several spectral features that need to be explained by a wideband, low-intensity source, the low count spectra had unfavorable Poisson statistics and almost no emission was observed the red side of the full energy beam component. The whole of these observations do not unequivocally

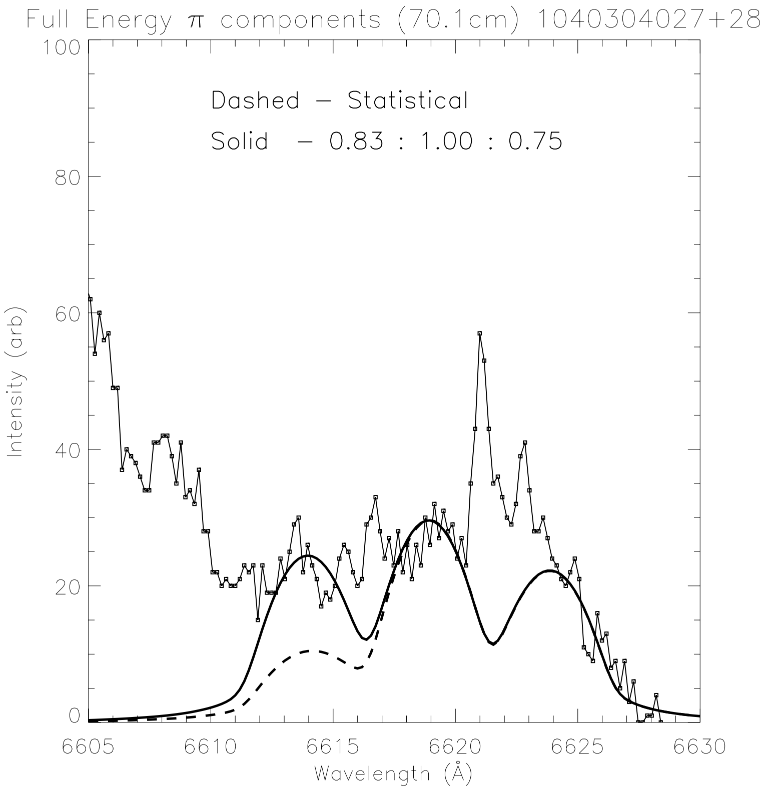

Figure 5-11: Same data as Fig. 5-3 [Bottom] with fitted -2,-3, and -4 π components. Dashed statistical population curve cannot be scaled to simultaneously fit all π components. The presence of additional lines can be seen as slightly over 20% of the measured intensity cannot be accounted for in the region between 6612-6629Å.

establish the presence of polarized D_2 lines in the spectra. In this section, the MSE measurements of beam-into-gas will be discussed, showing polarization measurements that differ dramatically from the expected values.

This section shows that the MSE measurements are consistent with observing a sum of partially linearly polarized light oriented perpendicular to the magnetic field, (Zeeman-σ) along with the expected Stark-Zeeman-E beam emission. This model will simultaneously satisfy the measured linear angles, the observed polarization fraction, as well as explain several observed sensitivities.

5.3.1 Beam-into-gas run parameters

The beam-into-gas calibration in this section was performed on run day 1040422, using 2.0 to 2.5 mTorr of deuterium. The toroidal field was set to 5.4T to reproduce the majority of C-Mod pulses. To generate the magnetic field line pitch angle, a combination of equilibrium field coils EF3 and EF4 were used. While EF4 provides a field that is essentially vertical, it is not capable of enough current to produce the full range of MSE observed angles during plasma, so EF3 was used in conjunction. EF3 has a more pronounced radial component as well, but due to the radial nature of the DNB this is not an issue.

The MSE filters are tuned to reduce the leakage of σ light as they would be for normal plasma operation. The centers of the filters are set to the greater wavelength of the -3π component, or 10Å beyond the peak of the -1σ component. This reduces the filter transmission to at most 5% of the peak transmission at the -1σ wavelength. Tuned in this manner, spectral simulations, such as the one shown in Fig. 5-1, calculates the integrated intensity due to $\Delta E = 0, -1$ lines to be less than 1% of the integrated intensity from $\Delta E = -2, -3, -4$ lines. The tuned filter function is plotted with the measured spectra, reproduced from Fig. 5-4[BOTTOM].

The filters were measured using the McPherson spectrometer using a broadband source to verify their central wavelengths. The filters had also been measured by Andover at the time of purchase. Neither measurements could test the filter function far from the bandpass center at very low transmissions. Transmissions below 10% of peak (≈6% absolute), are based on Andover specifications, available online at (www.andcorp.com/Web_store/General_info/Filter_type_3.html). Observation of ECDC plasma, a low temperature electron cyclotron discharge cleaning plasma, provided an additional confidence check. MSE could not detect Dα above electronic noise levels when observing ECDC plasmas. No instrumental calibration of the relative intensity of ECDC and beam induced Dα was performed, but visual inspection shows that ECDC plasmas are brighter than the beam.

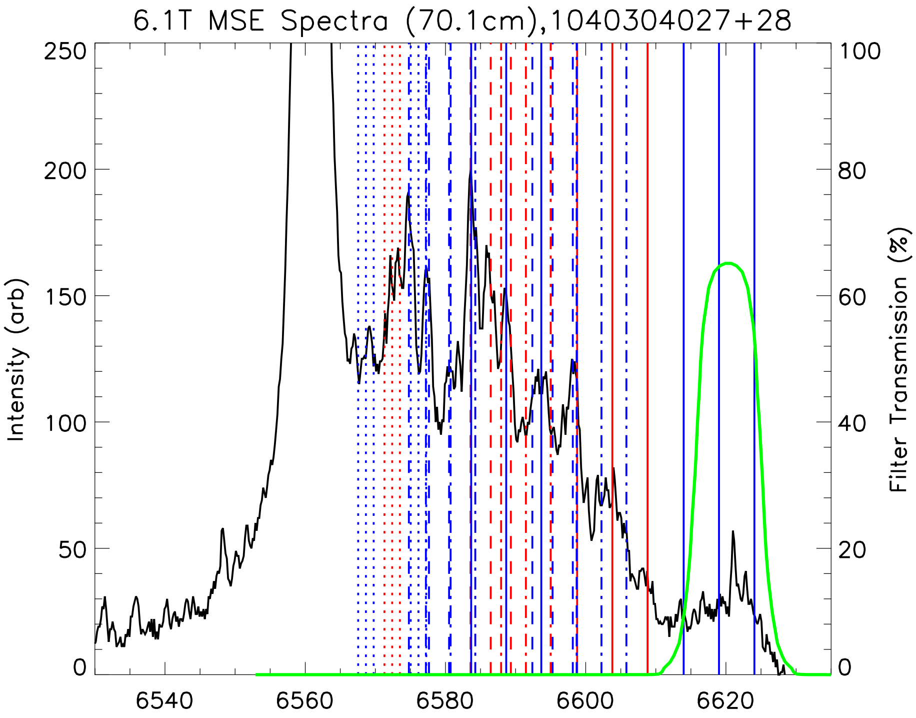

Figure 5-12: MSE filter function, shown in green, overlaid on beam-into-gas spectra from Fig. 5-4[BOTTOM].

5.3.2 Beam-into-gas measured angles

Angles measured during the beam-into-gas calibration for the edge MSE channel is shown in Fig. 5-13[TOP] and for a core channel in Fig. 5-13[BOTTOM]. The abscissa is the MFLUX reconstructed pitch angle. The solid line represents the expected measurement based on the invessel calibration. The difference between observed and expected angles is not only large but also not linear. For beam-into-gas calibration measurements, the MSE random uncertainties during a single shot are roughly the size of the plotting symbols used. The discrepancies between MSE measured angles and MFLUX angles exceed 20°. The strong curvature of the measured response was particularly puzzling, as there are no instrumental effects known to produce non-linearities. Even more interesting is the strong channel dependency when comparing the two channels in Fig. 5-13, with the discrepancy decreasing significantly for the MSE channels that view closer to the torus center.

For this range of pitch angles, vertical fields change essentially linearly with the

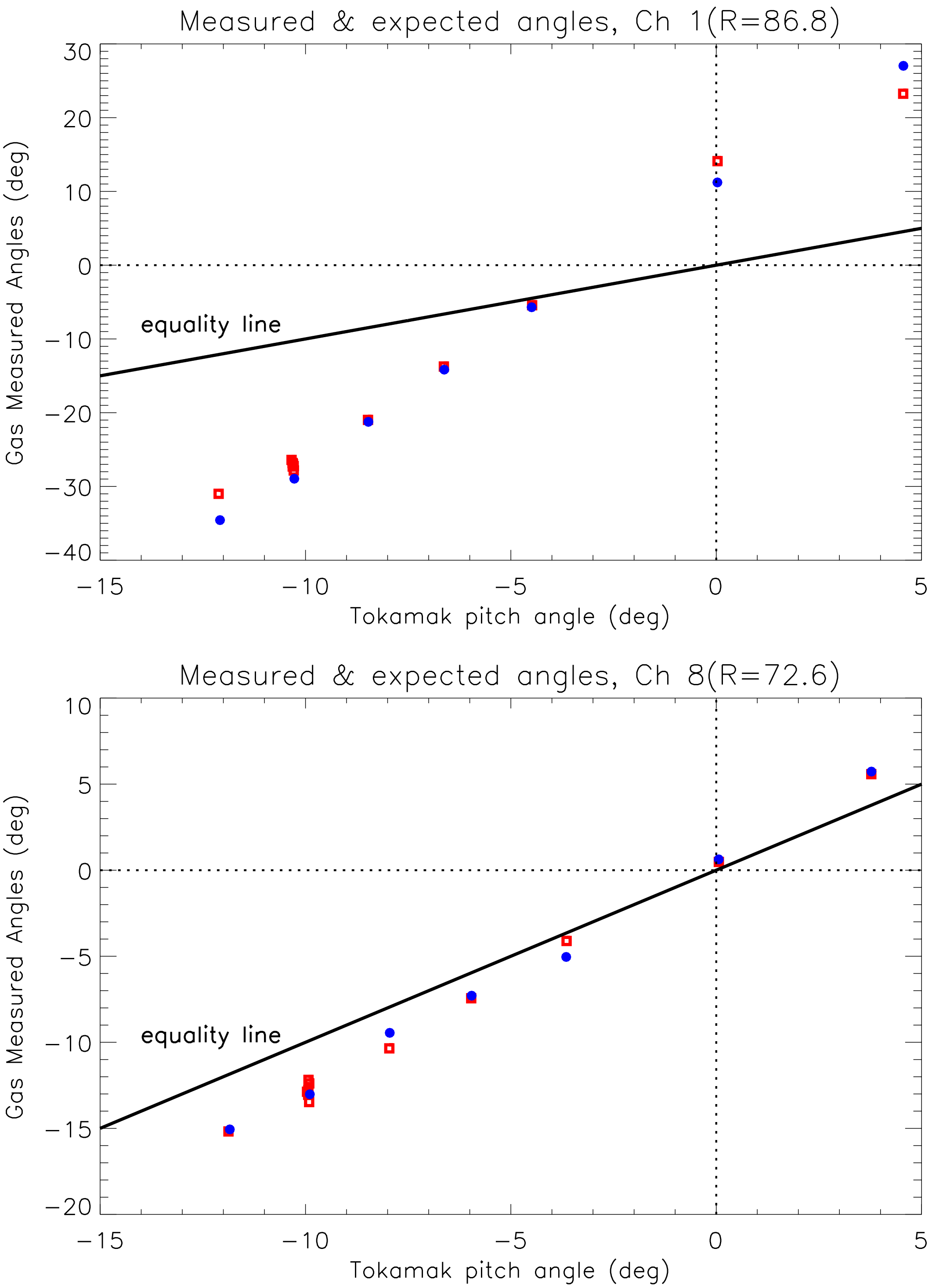

Figure 5-13: Beam-into-gas measured angles. Uncertainties are about the size of ploting symbols. Red squares show data at nominal MSE filter temperatures and blue circles show data with filters at +20°C of nominal, a +3.4Å shift in filter bandpass. Solid line shows expected MSE measurements using invessel calibration data. Note the large discrepancies of ±20° on the edge channel, and the strong channel to channel dependence.

pitch angle, so all mechanisms arising from stray fields, such as Faraday rotation or magnetic field interactions with PEM retardance are expected to scale linearly with pitch angle, and would not exhibit such strong nonlinearities.

5.3.3 Unexpected polarization fraction

Fig. 5-14 shows the operational polarization fraction curve (P_f defined by Eqn. 4.33) from the beam- into-gas calibration discussed in the previous section. The [TOP] figure shows the measured P_f for the edge channel, and below, the expected values for fully polarized Stark-π [BOTTOM LEFT] and Zeeman-σ [BOTTOM RIGHT] components.

The MSE observed P_f is the intensity weighted average of P_f for all observed light, and thus the comparison of the observed P_f with that of pure Stark-π and Zeeman-σ components is immediately suggestive. The observed light does not appear to be fully polarized Stark-π light, with values below that shown in [BOTTOM LEFT]. Second, the observed P_f has curvature with a maximum at $-4.9°$, the inclination angle of the MSE sightline. *The fact that the polarization fraction curves shows shape characteristics resembling Zeeman-σ suggests that light polarized in the direction perpendicular to* $\mathbf{B}$ *is being observed.*

Aside from the addition of a Zeeman-σ component, an unpolarized component is also necessary to reproduce the observed P_f. The Stark-Zeeman-E lines are expected to be fully polarized so the presence of unpolarized light is also unexpected. One possible source for unpolarized light is leakage of the $\Delta E = 0, -1$ lines, since equal intensities of perpendicularly polarized will combine incoherently to produce unpolarized light.

For this calibration, the MSE filters were tuned to the red of -1σ by at least 10Å to avoid any σ leakage. 10Å represents a little over 1 FWHM for the MSE filters, and the tranmittance is reduced to $\leq 5\%$ at the -1σ location. The filters were then tuned even further by +3.4Å, shown as blue circles in Fig. 5-13. This shift results in an increase in the discrepancy with MFLUX, and a slight reduction of P_f, the opposite of what one would expect if one suspected that σ leakage was the cause of the reduced polarization fraction.

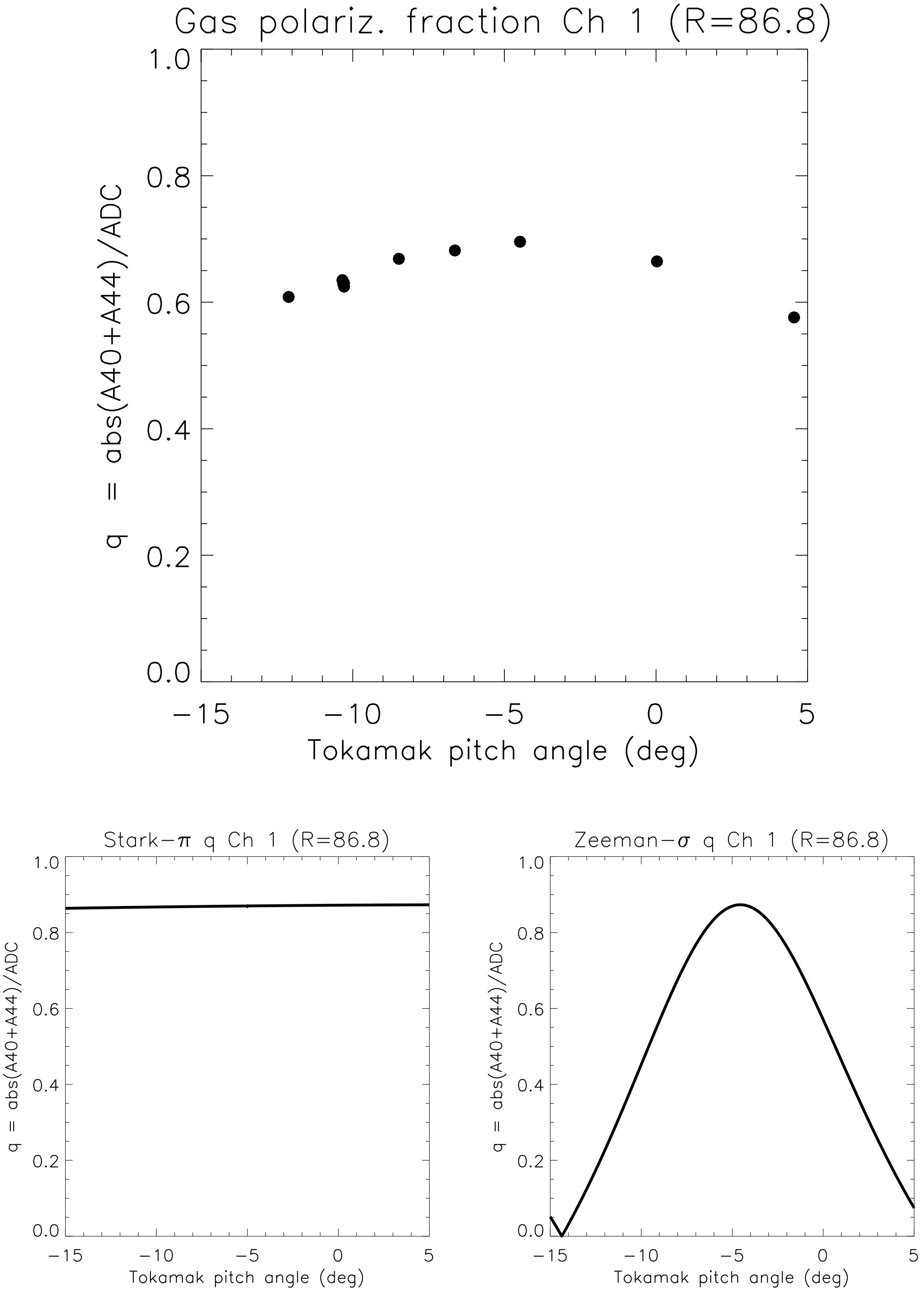

Figure 5-14: Beam-into-gas operation polarization fraction, P_f. Observed P_f is the intensity weighted average of P_f for all observed light and does not appear to be the expected pure Stark-π P_f shown in [BOTTOM LEFT], but rather mixed with Zeeman-σ [BOTTOM RIGHT] characteristics.

The filter functions had been measured using a spectrometer recently prior the calibration, so there was no question as to their location. Confidence in the ability to calculate beam emission line locations comes from measured spectra in Fig. 5-4, where predicted line locations show agreement with measured spectra.

Knowing the MSE line locations, widths, and the filter functions should allow one to predict the polarization fraction. From simulated spectra, this fraction was predicted to be essentially 100%. However, Fig. 5-14 shows significantly lower polarization fraction, around 75%.

5.3.4 Non-statistical upper state populations

Even though Stark-σ lines are thought to be essentially completely filtered out by the MSE filters, their inclusion is one possibility for the lower than expected polarization fraction. The question then becomes whether Stark-Zeeman-v and Stark-Zeeman-B transitions can produce the angles observed in the calibration.

For statistical populations, the answer is simply no, as statistical intensities of degenerate Stark-Zeeman-v and Stark-Zeeman-B combine to give polarization in the Stark-σ direction. This would combine with the perpendicular Stark-Zeeman-E (Stark-π) direction to produce the same angle at a reduced polarization fraction assuming the intensity of the Stark-Zeeman-E were greater. However, Sec. 2.3 discussed the possibility of observing Stark-σ at non-orthogonal angles as an effect of non-statistical populations, especially with the Stark-σ_{-1} component.

To explore this possibility, all possible MSE responses to combinations of linear Stokes vectors with angles aligned to Stark-Zeeman-E, Stark-Zeeman-v, and Stark-Zeeman-B were simulated. *The results show that no combination of light from the beam emission alone is capable of producing the observed angles.* The addition of any Stark-Zeeman-v or Stark-Zeeman-B in non-statistical proportions resulted in worse agreeement with measurements while addition in statistical proprotions only reduced the polarization fraction without changing the angle. These calculations combined with the filter data shows that Stark-σ line leakage cannot be the reason for the beam-into-gas observed angles.

5.3.5 Instrumental effects

Faraday rotation

In order for Faraday rotation to explain the observed discrepancies, the sensitivities to vertical field alone must account for the total range of discrepancies, about 44° for the edge channel in Fig. 5-13[TOP] and 4.8° for the core channel in Fig. 5-13[BOTTOM], since the toroidal field is held constant for each scan. Faraday rotations need to be measured in the MSE frame, so the angle values need to be divided by the error magnification ratio. A 7.7° Faraday rotation is needed for the edge channel and 4.8° for the core channel to explain the discrepancy.

Using EFIT on an enlarged grid to calculate the vacuum field values for the MSE optical components shows the change in field to be maximum through L2, which experiences a $\Delta \mathrm{B_z} = 1.3\mathrm{T}$ varying linearly with pitch angles used in Fig. 5-13. Radial fields for the PEM and external optics experience only a $\Delta \mathrm{B_r} = 0.04\mathrm{T}$ change during for the full range of pitch angles.

The Verdet constants necessary for these effect are two orders of magnitude beyond values measured in the lab. Faraday rotation is also unable to explain the curvature, channel to channel dependence, dependence with filter temperature.

Stress-induced birefringence

A calculation of the effect of stress-induced birefringence on vacuum lenses for polarized light transmission was performed by Lubin [59]. Since the MSE vacuum window can be thought of as a lens with zero curvature, the results should apply. The birefringefence, φ, depends on the difference of the integrals of the radial and circumferencial stress through the thickness,

$$\varphi = \frac{2\pi}{\lambda}(q_1 - q_2)(I_{rr} - I_{tt}) \tag{5.4}$$

$$I_{ij} = \int_0^L \sigma_{ij}\, d\ell \tag{5.5}$$

where L is the thickness of the window, q_1 and q_2 are the photoelastic constants (photoelastic constants could not be found for SFL6, but many optical glasses have similar photoelastic constants, see [60, 61]). The calculations from [59] show that for symmetric geometries, i.e. symmetric surfaces on the vacuum side and the air side, the stresses are nearly odd across the thickness of the plate, causing I to approach zero.

MSE rays nominally exit the center of the window, although over an expanded area. At the center of the window, $I_{rr} = I_{tt}$ due to symmetry, causing no birefringence. The MSE window is also small (6 cm radius), compared to windows where stress-induced birefringence is expected to cause noticable effects. If the birefringence is on the order of a few degrees, then the only effect expected will be similar to that from the mirrors already modeled, where linear light become partially circularly polarized. Very little natural (non-optics induced) circularly polarized light is observed for both beam-into-gas and plasma shots, so the converse effect of circular light affecting linear measurements negligible.

Stress-induced birefringefence cannot explain the beam-into-gas observations because it lacks any sensitivity to the scanned parameters. With a static stress state, stress-induced birefringefence can at best explain a small fixed discrepancy from the invessel calibrations.

PEM retardances during beam-into-gas

Using the retardance calculation described in Sec. 4.1.5, the beam-into-gas PEM retardances are compared with the invessel calibration in Fig. 5-15. The retardance settings on the PEM controllers are maintained at the same values for both data sets. What is relevant for measuring magnetic field pitch angles is actually the change in the ratio of retardances, shown in [BOTTOM LEFT]. The actual effect on the measured angle is the ratio of ratios, ranging from 0-2%, shown in [BOTTOM RIGHT]. These corrections were applied to the beam-into-gas data when fitting to the invessel calibration.

The errors were reduced due to the use of the ensemble data from the entire beam-

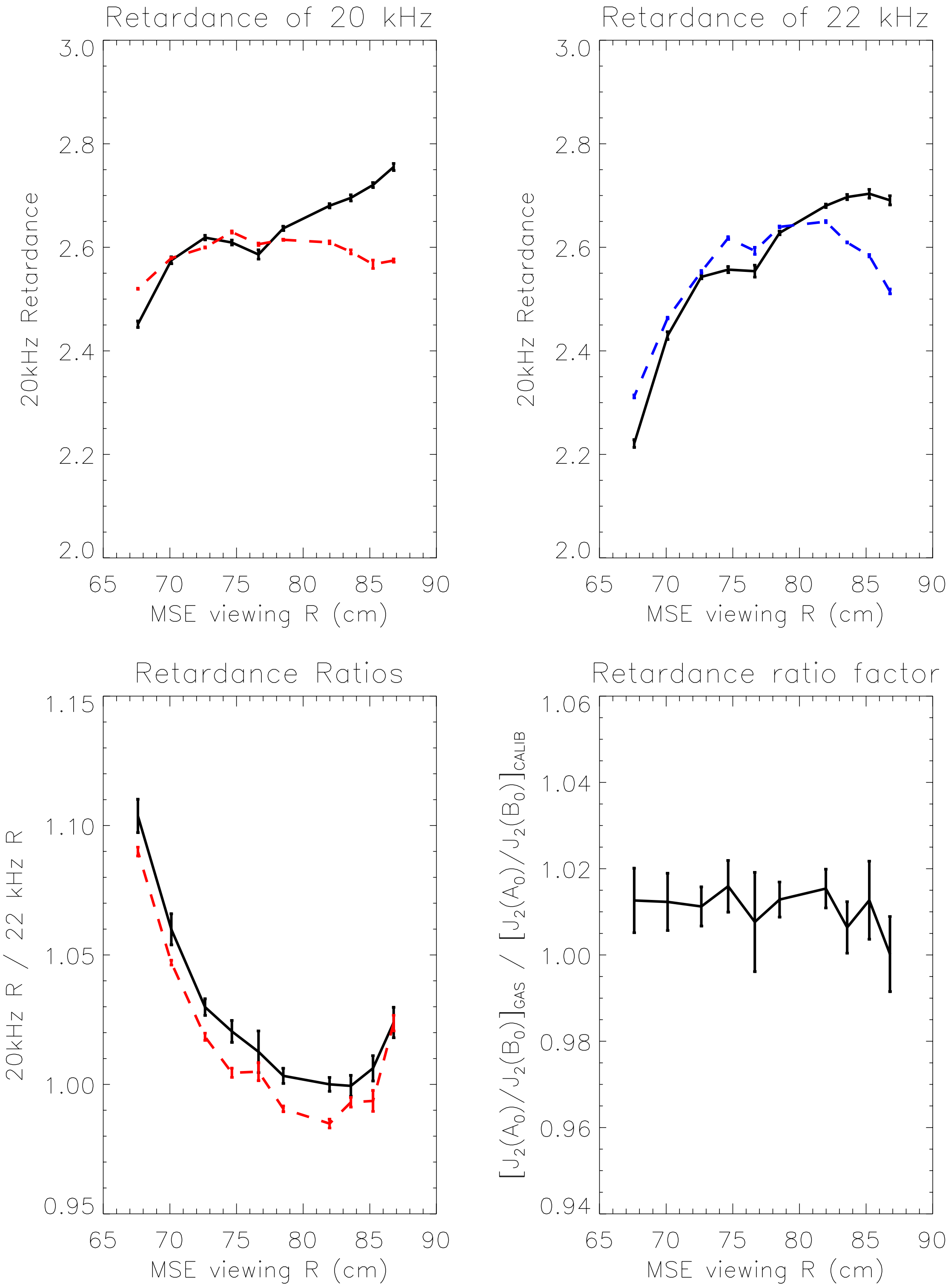

Figure 5-15: Beam-into-gas retardances compared with invessel calibration. Dashed lines are used for data from the invessel calibration. Top figures show changes in retardance, but only small relative changes [Bottom left]. Actual changes in measured angles results from taking the ratio of the lines in [Bottom left], and is shown to be between 0-2% in [Bottom right].

into-gas run, 29 measurements, and 70 for measurements for the invessel data. One can see from Fig. 5-15, the normalized errors sum at each step along the process, resulting in relatively large errors in the final results that affects the measured angle.

The significant changes observed in PEM retardances need to be studied more carefully, as the ratio of retardances is a direct factor in the MSE measured ratio of A40/A44, shown in Eqn. 4.21. Each 1% uncertainty in the ratio of retardances will results in a pitch angle uncertainty of 0.2° uncertainty for core views to 0.7° for edge views. There is no observed strong channel dependence in the PEM retardance changes, so this effect is unlikely to explain the beam-into-gas observed angles.

In trying to isolate the sensitive parameter with which the retardance varied, no statistically meaningful trends were observed with pitch angle and consequently stray fields. This is likely due to the error bars present for individual retardance measurements, and may require repeated measurement in the lab to achieve useful statistics.

Although the radial stray fields were only approximately 0.02T during the beam-into-gas tests, EF4 does product as much as a -0.15T vertical at the PEM location. It is not known if such a field can alter the retardances of the PEMs. Other environmental effects may also affect PEM operation such as PEM temperatures, which were not recorded between the invessel calibration and the beam-into-gas test.

It is important to conclude this discussion of PEM retardance variations with the observation that although the retardance needs to be maintained more carefully, the angular uncertanties introduced due to changes in retardation ratios and their uncertainties are too small to account for the observed discrepancies between MSE and MFLUX for beam-into-gas as well as discrepancies between MSE and EFIT for plasma measurements.

5.4 Resolution via molecular D_2 lines

Previous sections presented spectroscopic data suggesting that partially polarized molecular D_2 may be observed by MSE. D_2 lines would be Zeeman polarized either

View R [cm]	**86.8**	85.2	83.6	82.0	78.5	76.7	74.7	**72.6**	70.1	67.6
Stark-π	**0.63**	0.68	0.72	0.69	0.69	0.75	0.75	**0.75**	0.74	0.74
Zeeman-σ	**0.10**	0.11	0.13	0.13	0.14	0.15	0.15	**0.15**	0.16	0.16
Unpolarized	**0.27**	0.21	0.15	0.18	0.17	0.09	0.10	**0.10**	0.10	0.10

Table 5.2: Estimated mixture of MSE observed light used to construct responses shown in Fig. 5-16. Bold columns show channels shown in Fig. 5-16.

parallel or perpendicular to the magnetic field. For consideration of the pure Zeeman effect, the viewing angle ψ is the only necessary parameter, and is shown for each MSE channel in Fig. 2-6[LEFT]. Over the range of calibration pitch angles, atomic Zeeman-σ lines will have a larger intensity than that of Zeeman-π lines for all MSE channels. It is assumed that molecular lines behave similarly. An atomic example of this has already been shown in Fig. 5-8, where the Zeeman-σ lines are more intense than the Zeeman-π line in the center.

5.4.1 Zeeman-σ polarization response

The projected direction of Zeeman-σ polarization, i.e. perpendicular to $\mathbf{B}$, is shown in Fig. 3-1[MIDDLE, RIGHT AXIS]. Using the calibration data from Sec. 4.3.2, the A40 and A44 response curves for Stark-π and Zeeman-σ projected directions are shown as a function of pitch angle in Fig. 5-16. One can see the dramatic change in response as a function of pitch angle for the edge channels. This comes about due to the rapidly changing angle of the projected magnetic field shown in Fig. 3-1[MIDDLE].

MSE responds linearly to Stokes vectors, so an intensity weighted linear combination of the response functions will predict what MSE measures for a mixture of light. Fig. 5-17 shows the best fit response function for a mixture of Stark-π, Zeeman-σ, and unpolarized light as the black solid line, with the mixtures used to create the responses listed in Table 5.2. The Stark-π and Zeeman-σ response curves are reproduced from Fig. 5-16 for each plot. Data points from the same calibration data shown in Fig. 5-13 are shown for two filter settings, red (nominal) and blue (+3.4 Å). A good

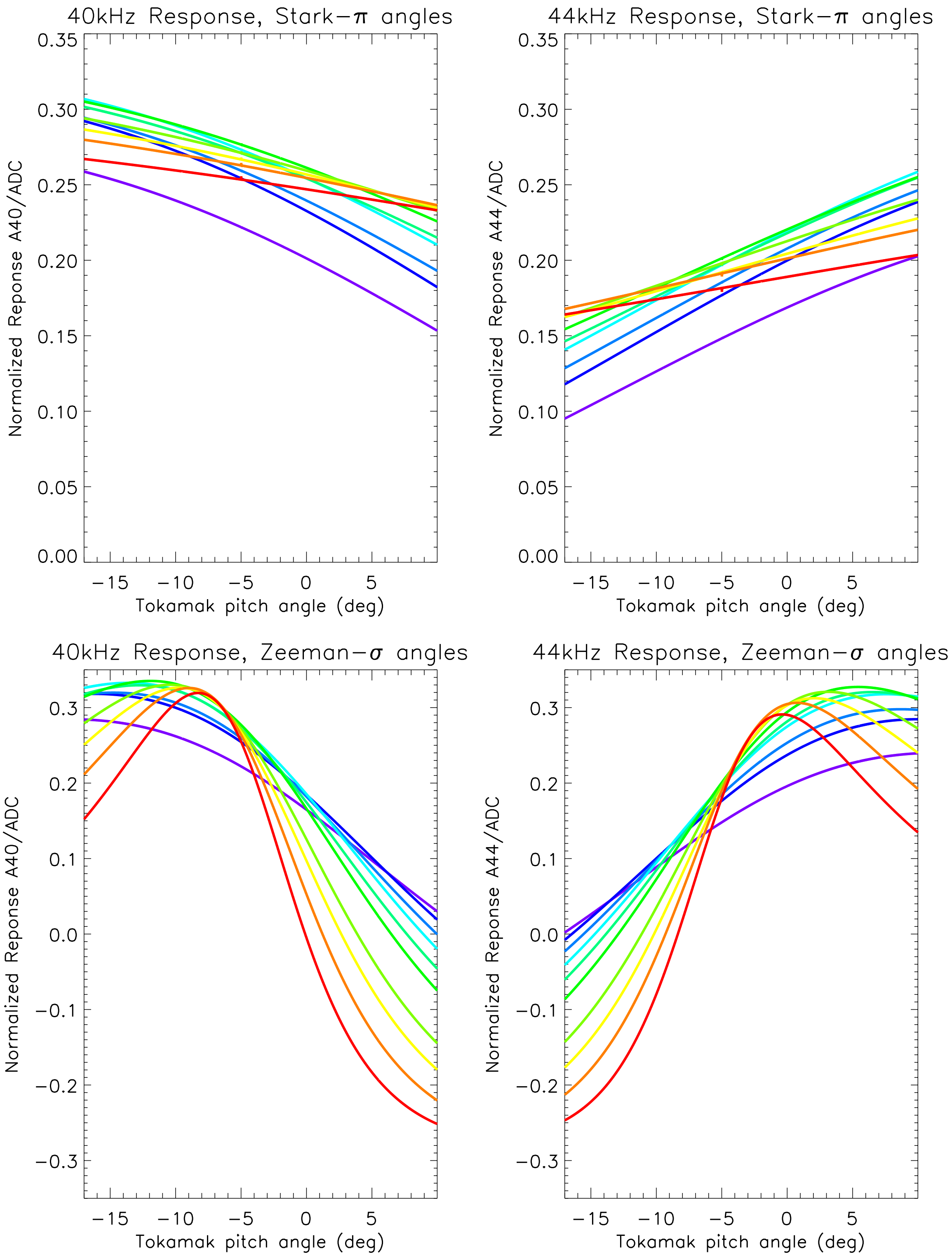

Figure 5-16: MSE calibrated harmonic amplitude responses. Red shows the edge channel going to violet for the innermost channel. [Top Left:] 40 kHz Stark-π [Top Right:] 44 kHz Stark-π [Bottom Left:] 40 kHz Zeeman-σ, [Bottom Right:] 44 kHz Zeeman-σ.

match for the responses in both A40 and A44 using the same light composition can be achieved. Matching both the A40 and A44 responses simultaneously shows both angle and polarization fraction agree with measured results.

The response curves shown in Fig. 5-17 were constructed by fitting a ratio of Stark-π, Zeeman-σ, and unpolarized light at a particular pitch angle (the inclination angle). However, each line varies in intensity as a function of pitch angle. For the Stark-Zeeman-E line, the relative intensity curve is shown in Fig. 2-7. However, the relative intensity of molecular lines as a function of pitch angle is not known, so an ad hoc intensity curve for the atomic Zeeman-σ intensity from Eqn. 2.21 is used. This ad hoc assumption is a likely source for some remaining discrepancies.

Figure 5-18 shows the expected angle for the response curves shown in Fig. 5-17. The curvature of the measured data as well as the channel-to-channel differences are reproduced. One can see the sensitivity to Zeeman-σ light for the edge MSE channel in the dotted lines of Fig. 5-17, where the fractional composition of Zeeman-σ was adjusted by ±2%.

Fig. 5-18 shows that at the MSE inclination angle ($-4.9°$), the measured angle is insensitive to the ratio of Stark-π to Zeeman-σ, but angles become increasingly sensitive to the composition ratio away from this pitch angle value, especially at the edge channel. One would expect that the extremes in the calibration pitch angle range would be most sensitive to small changes in the ratio of Stark-π to Zeeman-σ intensities. This is seen in the edge channel data in Fig. 5-18[TOP], where a slight change in the ratio of Stark-π to Zeeman-σ caused by a 3.4Å change in filter tuning shows up most dramatically as changes between the red (nominal) and blue (+3.4Å) points.

There appears to be an additional systematic offset in Fig. 5-17[BOTTOM] and the point closest to the inclination angle in the [TOP] figure that is not capable of being fitted using this technique. This offset could be the Faraday effect that the beam-into-gas was intended to measure, as it is in the right range of values (≈1° in pitch angle, or ≈0.5° in the MSE measurement frame). However, with Zeeman-σ affecting the current measurement, the error bars in this result makes it not quantitatively

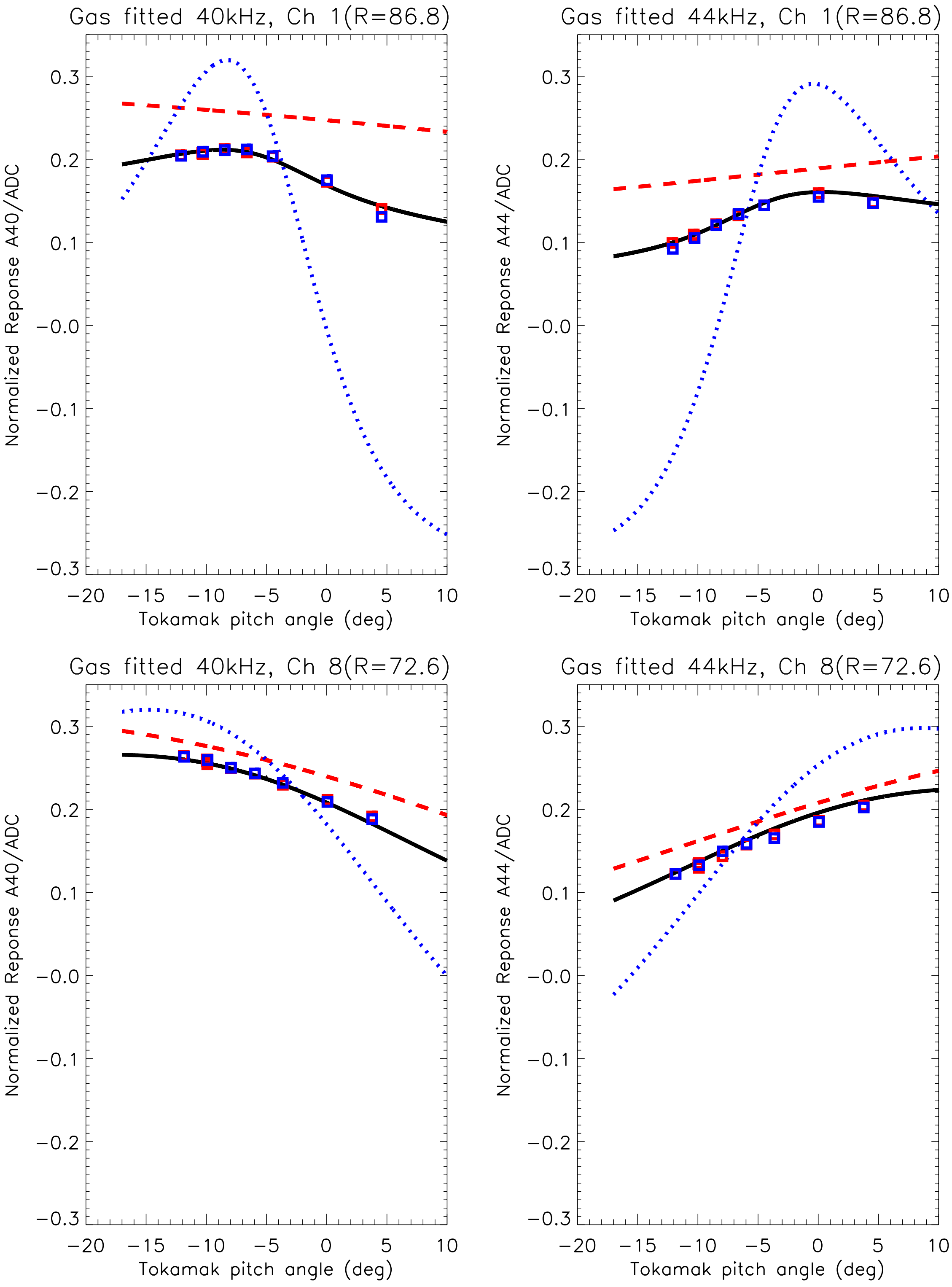

Figure 5-17: Fitted response functions matching beam-into-gas measurements. Net response curves shown as solid black lines are linear combinations of the of Stark-π (red dashed), Zeeman-σ (blue dotted), and unpolarized light. Two channels are shown, with both 40 and 44 kHz responses fitted by the same light composition, matching both measured angles and the polarization fraction.

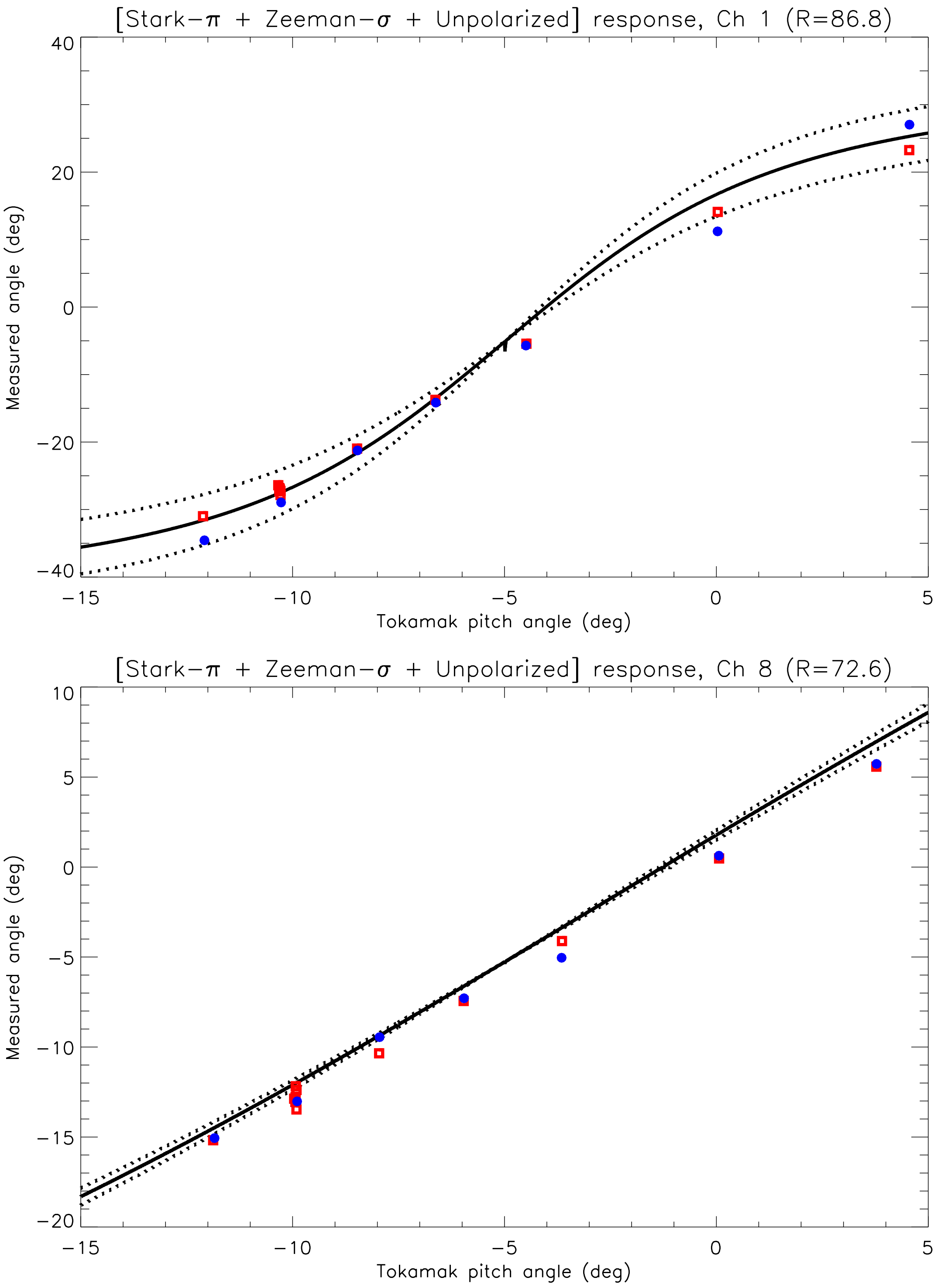

Figure 5-18: Beam-into-gas measured angles in red squares (nominal filter tuning) and blue circles (+20°C) compared with the expected angles using the best fit of Stark-π, Zeeman-σ, and unpolarized light. Dotted lines show the effect of a ±2% adjustment to the Zeeman-σ fraction of total intensity.

useful.

The total amount of D_2 *light, composed of Zeeman-*σ *and unpolarized light required to match the measured response for all channels ranges between 20-30% for all channels.* This is roughly consistent with the conservative spectral estimate of 18% in Sec. 5.2.2 and 20% in Sec. 5.2.3.

5.4.2 Zeeman linear polarization fraction

For both Zeeman and Stark atomic polarizations, the net polarization when integrating over all emission is zero, independent of angle. However, the fact that one can observe net polarization when not all of the emission is observed is one of the underlying principles of MSE. This is the situation when the observed Zeeman polarized D_2 lines falls under the exponentially decreasing regions of the filter function. Fig. 3-18 shows that aside from the roughly 5Å wide (FW90%M) plateau region of maximum transmission, essentially all of the rest of the filter function is exponentially decaying. This can lead to the preferential transmission of one Zeeman polarization component.

From fitting of the measured response curves with Stark-π and D_2 light, it appears that the linear polarization fraction of the D_2 light is 27% for the edge channel increasing monotonically to 60% for the core channels. This comes from taking the ratio of the Zeeman-σ row in Table 5.2 to the sum of the Zeeman-σ and unpolarized rows. While this is the trend one would expect with increasing ψ, the angle between the viewing chord and $\mathbf{B}$ shown in Fig. 2-6 [LEFT], the values of the observed linear polarization fractions are impossible with the atomic Zeeman triplet. Atomic Zeeman polarization was calculated using MSE geometry and results show primarily circular rather than linear polarization for the range of MSE observation angles, especially at the edge channels. This makes it impossible to observe linear fractions above a few percent and also serves to rule out unshifted atomic Zeeman leakage as the contaminant light source.

For molecular lines, the situation is not clear. The reason that the atomic Zeeman-σ linear polarization fraction is low is because the transition is from a spherically symmetric atom, which is inappropriate for diatomic molecules. The simplest classical shape one can imagine for the diatomic molecule electron distribution is an ellipsoid, with projected elliptical orbits. "Elliptical" orbit transitions can result in radiation which differ significantly in linear polarization fraction than transitions from "circular" orbits. Unfortunately, data on D_2 Zeeman linear polarization fractions as functions of observation angle could not be found in the literature.

From available literature, the shapes of Zeeman lines are quite varied, as seen in Fig. 5-6, with polarization fraction, splitting width and the number of lines all varying with transition type. Without having identified the transition nor knowing the intensity as a function of wavelength, it is currently not possible to reconcile the apparent linear polarization fraction of D_2 during the beam-into-gas calibration.

It is important to conclude this discussion with the observation that despite the effort in this work to understand molecular line properties, *the solution to MSE beam-into-gas calibration does not require a detailed understanding of* D_2 *polarization, but rather the elimination of* D_2 *lines from observation.* This can be done by performing the beam-into-gas calibration using a different fill gas, such as helium. The realization of possible molecular line contamination occured after the return of the loaned DNB, so experiments crucial validate the hypothesis could not be included in this work.

5.5 Chapter conclusions & Next steps

The beam-into-gas calibration can provide important information for MSE, complementing the invessel calibration with measurements of the Faraday rotation, stress induced birefringence, and stray field effects on PEM retardances using conditions that are very similar to plasma pulses. However, current beam-into-gas measured angles shows large discrepancies with expected results, strong channel-to-channel sensitivities, non-linear behavior as a function of pitch angle, and sensitivity to MSE filter tuning.

A hypothesis that D_2 light was responsible for contaminating the MSE beam-into-gas calibration was put forth, drawing from available spectral data as well as measurements made by MSE.

Available spectra suggests the presence of additional light in the beam-into-gas calibration. Evidence of the following was shown:

- Unexpected intensity on the blue side of Dα well above the noise floor of the spectrometer
- Uneven Zeeman-σ components at one value of magnetic field but not another
- A significant amount of unexplained intensity between beam component lines
- Unexplained emission in the MSE Stark-Zeeman components

These observations suggest that an another emissive source is present in the beam-into-gas calibration. Compiled wavelength data shows that numerous D_2 molecular lines lie in the MSE spectral region. Spectra taken with a polarizer suggests that the suspected D_2 light is partially polarized.

It is unfortunate that features thought to be D_2 lines have statistical uncertainties too high to be definitive. Measurements from MSE provided additional polarization observations supporting the hypothesis that MSE observes D_2 lines during the beam-into-gas calibration.

The conclusion that MSE measures an unexpected polarized source during beam-into-gas calibration was reached after a variety of proposed error mechanisms were discounted, including,

- Faraday rotation
- Stress-induced birefringence
- Non-statistical upper state populations
- PEM retardance changes
- Unshifted Dα leakage

Motivated by spectral evidence of D_2 light, a partially polarized source in the Zeeman-σ direction was considered as a possible contaminant source. The result of adding between 20–30% of light partially polarized in the Zeeman-σ direction resulted in matching expected angles to observed angles for all MSE channels. Additionally, the following measured quantities were also reconciled with expected values. No major discrepancies remain between expected and observed MSE measurements with the inclusion of D_2 lines.

- Polarization fractions
- Non-linearities in angle response
- Channel-to-channel sensitivity
- Qualitative sensitivity trends for filter temperatures changes

It is likely for the reasons discussed above that beam-into-gas with known pitch angle calibration have not provided the absolute MSE angle calibration desired. Unfortunately, the realization of possible D_2 contamination occured after the DNB used for this work had been removed from C-Mod, so experiments that will definitively test the hypothesis were not possible. These experiments will be forthcoming using C-Mod's new DNB.

5.5.1 Next steps

Several experiments can provide data to test the D_2 hypothesis. The first is most definitive.

Comparing beam-into-gas spectra using two different fill gases, deuterium and helium, should definitively show if D_2 lines are present in the beam-into-gas calibration. A comparison of MSE measurements made between D_2 and an atomic background gas would show if the fill gas affects the measured angle. This experiment is highly recommended as part of the C-Mod MSE calibration run during the next run campaign. The new fill gas should also not have any lines interfering with the MSE wavelength range (6585Å to 6630Å) to avoid contamination. Helium would be a good choice, with the two closest helium lines at 6560.1Å (HeII Brackettβ, n=6→4) and a HeI line at 6678.2Å ($3d^1D \rightarrow 2p^1P$). Since the unshifted Dα line will be absent, these He lines could serve as useful calibration lines. It will be important to eliminate all deuterium in the vacuum vessel, due to the sensitivity of MSE to D_2 light. The unshifted Dα wavelength should be included in the measured spectral range to verify that deuterium has been sufficiently reduced.

The D_2 contaminant lines must be eliminated to properly simulate the MSE beam-into-gas spectra. Once this is accomplished, the simulation spectra can be used to deduce the excited state population by matching observed multiplet line intensities.

The second experiment verifies the location and existence of unshifted D_2 lines by taking spectra of the low temperature ECDC plasmas. This experiemnt has the distinct advantage of being easy, not even requiring tokamak run time, and the ability to sum over numerous frames of spectrometer data to reduce the error of the low intensity molecular lines.

Although measuring ECDC plasma is simple to do, it does not verify the structure of Zeeman split deuterium molecular lines. To do so will require significantly more work as ECDC does not work at full toroidal field. A proposal has been submitted at the 2004 IDEAS forum to develop ICDC, that is, using the ICRF antennas at low power with full field to breakdown the gas. If this cannot be achieved, another method is to fire a helium neutral beam into deuterium. This excites the molecular lines while removing the beam emission. To do this experiment will require a DNB engineering effort. It is unknown if the DNB can be made to operate using helium at this point.

If proven to be correct, the resolution of the beam-into-gas MSE measurements will be useful for the entire MSE community trying to use this calibration to accurately determine Faraday effects, polarimeter offsets, and stray field effects crucial for making accurate MSE plasma measurements.

Comparision of PEM retardances between the invessel calibration and the beam-into-gas calibration motivates a more careful measurement of PEM retardance sensitivities. Due to the accuracy requirements of MSE measurements, PEM retardances must be maintained with high precision. It is not yet clear what is causing the PEM retardances to change. While stray magnetic fields is the most obvious difference, other changes in conditions such as ambient temperature might also be possible.

Chapter 6

Plasma Measurements

In Chapter 5, it was shown that the beam-into-gas calibration may be compromised by molecular emission. Therefore, analysis of MSE data for plasma measurements will be based entirely on the invessel calibration shown in Chapter 4. This chapter will discuss how MSE performs in measurements of magnetic pitch angles in plasmas.

A key benchmark for MSE compares measured pitch angles with magnetic reconstruction (EFIT) pitch angles at the plasma edge. This comparison reveals significant discrepancies between MSE and EFIT measurements. At the plasma edge, the magnetic pitch angle is essentially independent of the plasma internal current profile, so magnetic reconstructions are accurate. Inconsistencies between EFIT and MSE at the plasma edge must therefore be due to error in the MSE measurement. Discrepancies between the EFIT and MSE for plasma measurements are much smaller than the discrepancies between MFLUX and MSE for beam-into-gas angles, but they are still beyond what is acceptable for useful measurements. Possible causes for the disagreement will be the focus of this chapter.

Three mechanisms are proposed here to explain the differences between MSE and EFIT pitch angles at the plasma edge. The first mechanism comprises statistical uncertainties in MSE plasma measurements. The second group involves errors introduced by the instrument itself, such as Faraday rotation and PEM retardance variation. The third, and perhaps the most difficult to evaluate with available data, attributes the differences to contaminant polarized light.

This chapter examines data measured during the 2003-2004 run campaign to determine if any of the proposed mechanisms can explain the observations. Since the exact cause of the discrepancies has *not* been identified, many of the discussions presented will result in negative results, but serves to document the state of MSE understanding.

6.1 Uncertainty analysis of plasma MSE measurements

Statistical error analysis is a crucial part of the measurement because MSE is most useful when the measurement achieves an accuracy of $\lesssim 0.2°$ in pitch angle. Uncertainty analysis will determine whether MSE can produce useful measurements, which is particularly challenging at the plasma edge due to unfavorable viewing geometry effects discussed in Sec. 1.5

6.1.1 Sources of uncertainty

To calculate the uncertainty in an MSE angular measurement, one propagates the uncertainties from the quantities MSE actually measures, beginning with the intrinsic instrumental statistical uncertainty of the amplitudes in the relevant frequency components. This is obtained by taking the timepoint to timepoint standard deviation of the invessel calibration at the relevant angles observed in plasma. Since MSE makes angle measurements by taking the ratio of two measured quantities, the *fractional* uncertainties of the A40 amplitude and that of the A44 amplitude add. The fractional quantities in the measured ratio are shown in Table 6.1.

These uncertainties account for effects such as electronic noise, photon statistical noise, and digital lockin apodization effects, and will be included as part of the total uncertainty for plasma measurements. The timepoint-to-timepoint standard deviation for 5 ms time window measurements is given here as opposed to the standard error of the total 50 ms measurement (a $\sqrt{10}$ difference in this case).

MSE R [cm]	86.8	85.2	83.6	82.0	78.5	76.7	74.7	72.6	70.1	67.6
σ^R_{inst} [%]	0.21	0.33	0.38	0.18	0.13	0.19	0.32	0.28	0.31	0.32

Table 6.1: Instrumental standard deviation of MSE, given as the fractional uncertainty in the measured ratio, R=A40/A44, using 5ms sampling windows. Valid for the range of observed C-Mod plasma pitch angles.

No additional uncertainty results from fitting the MSE response curve to angles measured during the invessel calibration. The MSE response to all angles was fitted using 72 discrete angle measurements taken over one full revolution of an invessel linear polarizer, with the fitting coefficients shown in Table 4.1. Residual errors between the fitted curves and the measured points, also shown in Table 4.1, are no larger than the errors from a single measurement, with all values $\leq 0.05°$.

A third source of random measurement error arises from uncertainties in background subtraction. This is the dominant source of uncertainty for essentially all plasma measurements.

6.1.2 Plasma Background Subtraction

For high accuaracy MSE measurements, careful subtraction of the plasma background, i.e. lockin signal from emission other than beam emission, is always necessary even when the plasma signal does not appear significant relative to the beam signal, an example of which is shown in Fig. 6-1. A small signal in the lockin frequencies A40 and A44 from background light indicates that the background is either weakly polarized or contains broadband intensity variations in phase with the MSE signal. The reason why the plasma background would be weakly polarized is not known, as invessel calibration show that reflections from antennna surfaces are small with no measurable polarization. All viewing chords integrate through the plasma edge, and it is possible that the observed edge impurity light may be weakly polarized, e.g. molecular deuterium emission.

To subtract the background, each frequency amplitude signal is linearly interpolated using measurements made in 10ms time intervals immediately before and after

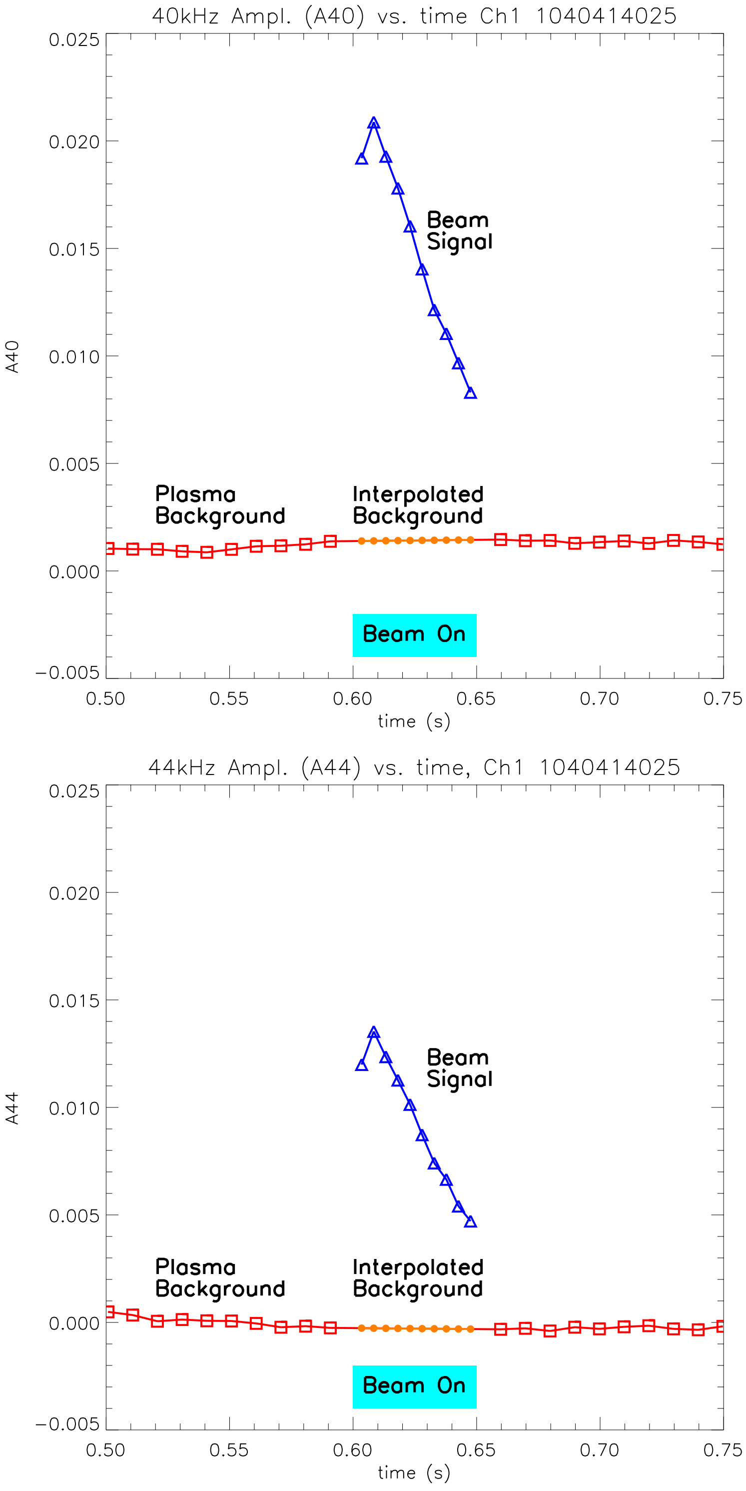

Figure 6-1: 40 and 44 kHz (A40 and A44) amplitudes as a function of time for the edge MSE (R=86.8 cm) channel. Shown are outputs from the digital lockin analysis. A linearly interpolated background (orange circles), using the two background measurement points (red squares) immediately before and after the beam, is subtracted for the signal during the beam pulse (blue triangles).

the beam pulse. The plasma background is analyzed using 10 ms time windows as opposed to the 5ms time window that is used during the beam pulse because the polarized plasma signals are significantly weaker. The interpolated plasma background for each harmonic signal is subtracted from the measured signal during the beam pulse, as shown in 6-1. This method works for each harmonic component because MSE behaves linearly with respect to input Stokes vectors, so one can subtract the plasma response from the combined beam with plasma light.

The interpolated background has uncertainties that have been estimated using two methods. The first method defines the uncertainty as a fraction of the change in background from before to after the beam pulse, i.e. the interpolation range. One can set the fraction to reflect the desired conservatism, however, there aren't good guides to help in the selection. The background signals can be reasonably stationary during quiescent plasmas, ELMs (Edge Localized Modes), L-mode to H-mode (L-H) transitions, and density ramps can change the observed background significantly over 50ms.

A second method works well for quiescent plasmas in which the background undergoes only smooth variations over the entire 0.25 second MSE signal acquisition time. This condition applies for all plasmas presented here.

For the quiescent plasmas considered in this work, a decent starting assumption is that the plasma background varies linearly for intervals of roughly 50ms. One can estimate the uncertainties of linear interpolations of the background using a procedure similiar to error analysis for a least squares linear fit.

The error estimate relies on taking the mean of interpolation errors during intervals of background before and after the beam pulse. The calculation of interpolation errors for any given period of background is identical to a calculation of the uncertainty for a linear fit, but in this case, a linear interpolation using the interval endpoints is used rather than fitting over all data. This is done to simulate the actual interpolation during the beam pulse.

A schematic of the procedure is shown in Fig. 6-2, where the A44 signal from 0.5–0.6s, prior to beam injection, is shown. Horizontal bars show 60ms time intervals

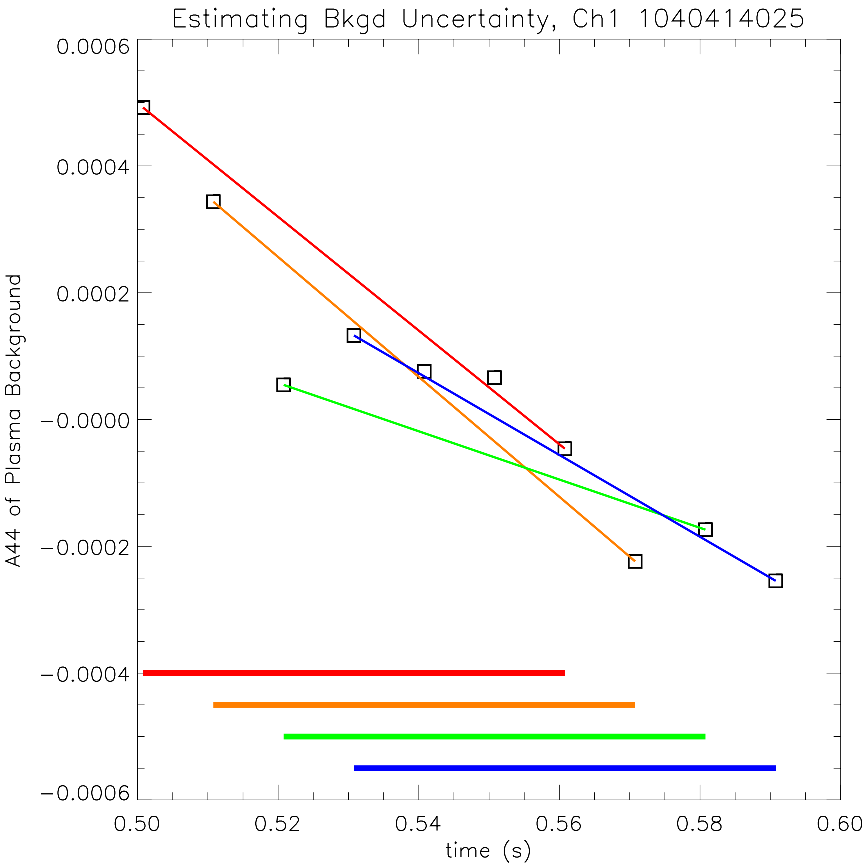

Figure 6-2: Uncertainties in interpolating plasma background. Points are the measured background A44 signal from early times (0.5–0.6s) in Fig. 6-1[BOTTOM] prior to beam injection. Horizontal solid lines near the bottom represent 60ms time intervals. Measured points at interval endpoints are used create a linear interpolation for the entire interval. The mean standard deviation between measured and interpolated points over all such interpolations is used to estimate the uncertainties for the interpolation during the beam.

where linear interpolations are performed using the measured datapoints at the endpoints of the intervals. For each time interval there are N+1 points (N+1=7 typically used for a 60 ms window). The endpoints are used for the interpolation but are not included in the standard deviation calculation. Each data point is subscripted i, from 0 to N. The standard deviation for a single interpolation is,

$$A_i^{interp} = A_0 + i\left(\frac{A_N - A_0}{N}\right) \tag{6.1}$$

$$\sigma_{interval} = \sqrt{\frac{1}{N-2}\sum_{i=1}^{N-1}[A_i^{meas} - A_i^{interp}]^2} \tag{6.2}$$

$$\tag{6.3}$$

where A_i^{meas} are measured data, A_i^{interp} are interpolated values, and $\sigma_{interval}$ is the standard deviation using the difference between interpolated points and measured data for only the internal points. The $1/(N-2)$ factor equals the reciprocal of the number of points used minus one to give the sample standard deviation.

$\sigma_{interval}$ is calculated for all possible intervals before and after the beam pulse. Under normal circumstances as shown in Fig. 6-2, there are four frames before and four frames after the beam. The mean of the interval standard deviations is used as the standard deviation for the interpolation during the beam pulse. This background uncertainty is calculated for each MSE harmonic of interest.

$$\sigma_{bkgd} = \overline{\sigma_{interval}} \tag{6.4}$$

After the interpolated background has been subtracted from each MSE timepoint, the weighted average of the ratio of A40 to A44 is calculated. For a series of measurements of a harmonic signal such as A40 or A44, individual datapoints are subscripted i and the weighted average of the ratio is calculated as, from [62]

$$R_i = \frac{A40_i}{A44_i} \tag{6.5}$$

$$\sigma_{bkgd}^{R_i} = \frac{\sigma_{bkgd}^{A40}}{A40_i} + \frac{\sigma_{bkgd}^{A44}}{A44_i} \tag{6.6}$$

$$\sigma_{total}^{R_i} = \sqrt{[\sigma_{bkgd}^{R_i}]^2 + [\sigma_{inst}^{R}]^2} \tag{6.7}$$

$$w_i = \frac{1}{[\sigma^{R_i}_{total}]^2} \tag{6.8}$$

$$R_{Wavg} = \frac{\sum R_i w_i}{\sum w_i} \tag{6.9}$$

$$\sigma(R) = \frac{1}{\sqrt{\sum w_i}} \tag{6.10}$$

where subscripted variables denote values for a single datapoint.

Eqn. 6.6 represents the uncertainty for a ratio data point as the simple sum of fractional errors for the numerator and denominator rather than a quadrature sum. This is done to be conservative as it is not clear that A40 background uncertainties are independent of those for A44, since both arise from plasma light. Instrumental uncertainties (from Table 6.1) are summed in quadrature with background interpolation uncertainties in Eqn. 6.7 because these errors are believed to be independent. The weights for each datapoint is expressed by Eqn. 6.8, and the weighted average ratio and its uncertainty expressed in Eqns. 6.9 and 6.10.

A weighted average is necessary due to the dramatic decrease in beam intensity during the 50ms beam pulse, which can be seen in Fig. 6-1. This beam "droop" effect is discussed next.

6.1.3 Beam current effect on MSE signal to noise

MSE makes use of light only from the full energy beam component within the viewing volume (3cm(z)×1cm(R) area through the beam), so the magnitude of MSE signals depend on not only on beam current, but also the beam species mix and beam diameter. This sections shows that the MSE signal increases faster than the measured beam current and how MSE uncertainties would be reduced by improving beam conditions.

Beam full energy fraction

The reader may have noticed the strong falloff of the MSE signal with time during the 50ms beam pulse, falling to only 35% of the peak value by the end of the beam pulse in a steady state plasma. Over this time period, the effect can be attributed to decreases in the full energy DNB neutral component and an increase in width of the DNB. This results in MSE signal decreases that are larger than the decrease in the beam current, shown in Fig. 6-3[TOP]. BES measured beam widths shows the beam reaches perviance of 8 cm (minimum 1/e diameter) at the design current of 5A, increasing to roughly 10 cm at 3A. This effect alone cannot explain the MSE observed decreases in signal, so the remainder is attributed to a decrease of full energy fraction with decreasing beam current.

The largest uncertainty for MSE measurements is from interpolation of the plasma background during the beam pulse. The decrease in MSE signal over the beam pulse reduces the total weight of the weighted average used to calculate the MSE ratio, or conversely increases the uncertainty. The beam pulse shown in Fig. 6-3[TOP] is representative of the typical conditions near the end of the 2004 run campaign, during which all the plasma data presented in this work was taken. For the beam pulse shown, the peak beam current was 4A, and droops to around 2.6A at the end of the pulse, a decrease of 35%. The MSE signal for the same period, shown directly beneath the beam current in Fig. 6-3[TOP], is reduced by 65% relative to the peak.

When normalized using the peak values for both the beam current and the MSE signal, Fig. 6-3[BOTTOM] shows that the relative loss in MSE signal is 1.8 times that indicated by the beam current. This degradation effectively halves the integrated beam signal compared to a constant beam pulse at peak value. Therefore, the measurements taken in the plasmas presented in this work have uncertainties characteristic of measurements using a 4A, 25ms duration beam pulse.

This leaves potential for improving the MSE uncertainties, which decrease as the square of the total weight of the signal. It is unclear how full energy fractions will vary with the peak beam current when comparing different beams during actual operation,

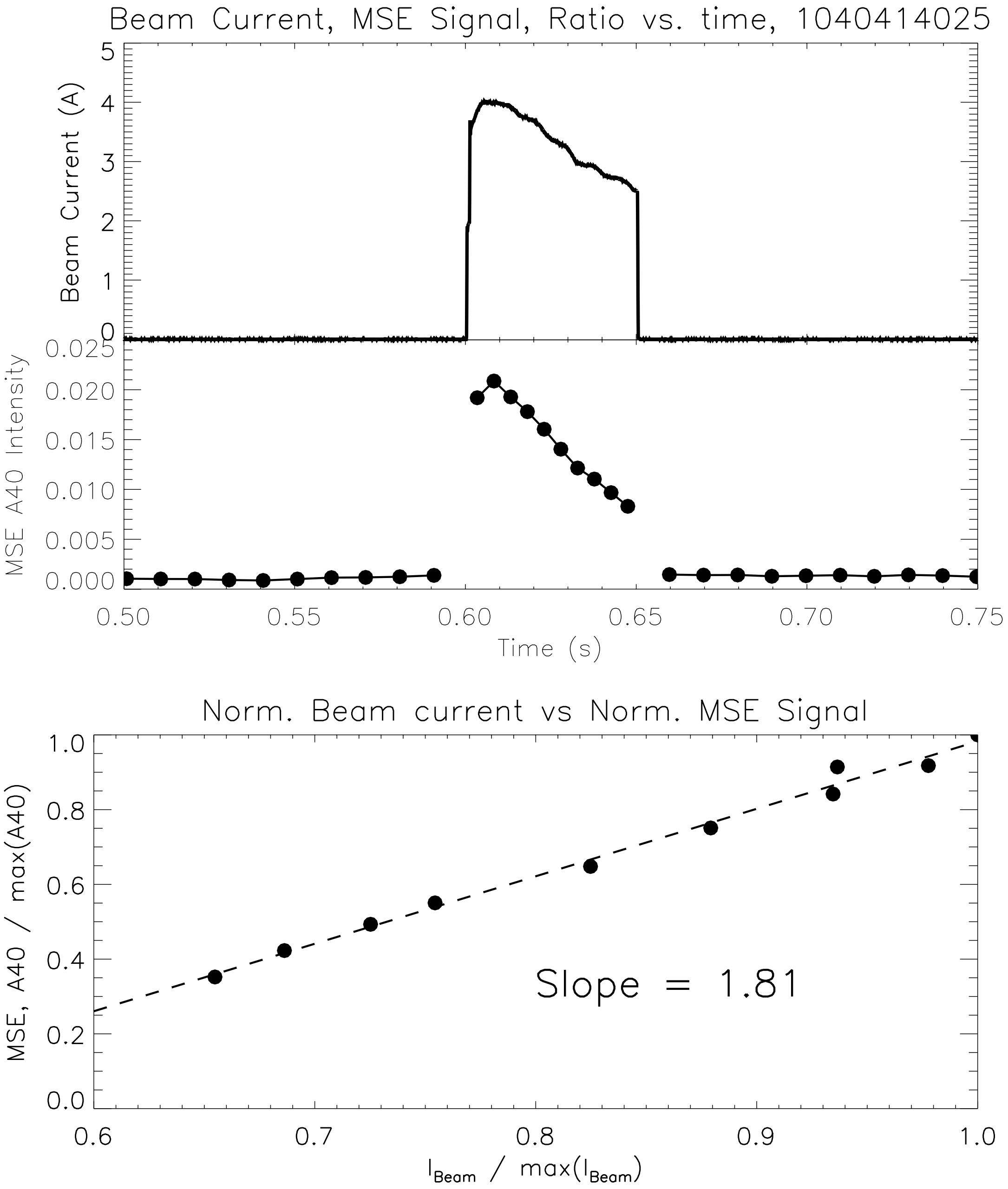

Figure 6-3: Beam current degradation over a single beam pulse and its effect on MSE signals. As the beam current “droops” over the 50ms pulse length, the MSE signal, which observes only the full energy component, decreases at a steeper rate. The calculated rate of full energy fraction decrease is 1.8 times that indicated by the beam current. By the end of the 50ms pulse, the MSE signal is only 35% of its peak value. This reduces the total usable signal by half compared to a beam pulse operating at peak current for the entire pulse.

so it is assumed here that species mix remains constant. Using this assumption, if the new 1.5s long pulse beam is able to *maintain the maximum current of 7A* for periods of 50ms, the MSE uncertainties would decrease by a factor of 1.9 ($=\sqrt{2 \cdot 7/4}$). If the measurement time is also increased to 100ms, then current uncertainties could be reduced by as much as 62% (assuming that 100ms background interpolations produce no increases in uncertainties).

6.1.4 Angular uncertainty

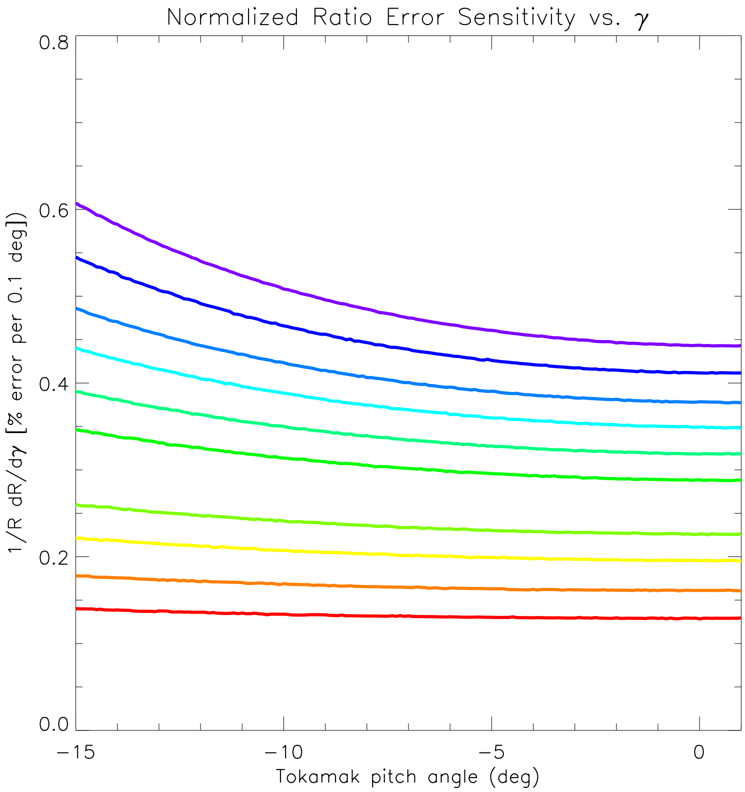

Figure 6-4: Uncertainty sensitivity for MSE channels. The y-axis shows the fractional error, in %, that would result in a 0.1° angular uncertainty. The low angular sensitivity/large error magnification for the edge channels (red, orange, yellow) is manifested as a low value of uncertainty required to produce a 0.1° angular uncertainty.

Until now, the uncertainties have been propagated as a fraction of the measured ratio of A40 to A44, since these errors are comparable between MSE channels. However, as they are converted from ratio uncertainties to angular uncertainties, the viewing geometry (or error magnification) discussed in Sec. 1.5 becomes evident.

Fig. 6-4 plots the derivative of the MSE angular response curve, illustrating the effect of the error magnification on the angular uncertainty. From this figure, one can see at the edge channel, a 0.18% uncertainty in the A40/A44 ratio yields an error of 0.1° in pitch angle, so the harmonic components A40 and A44 need to be measured to slight better than one part in a thousand to achieve a $\approx 0.1°$ accuracy.

6.1.5 Uncertainties vs. density

One outstanding question regarding the usefulness of MSE on C-Mod is the range of densities over which MSE can provide useful measurements. The MSE uncertainty in 49 ohmic, L-mode plasmas over a range of densities is shown in Fig. 6-5. Overall, the results show *increasing uncertainties with increasing plasma density*, but there is considerable scatter, suggesting that density may not always be the dominant factor.

From the data shown in Fig. 6-5, one can see that the uncertainties due to background typically remain mostly below 0.3° except for the edge channel to $\bar{n}_e$ of about 1.5×10^{20}. This suggests that errors for the edge channel may be dominated by plasma edge radiation rather than beam attenuation.

6.2 Comparison with EFIT at the plasma edge

Edge MSE measured pitch angles compared to values calculated by EFIT for 49 quiescent, ohmic, L-mode plasmas are shown for the four edgemost MSE channels in Fig. 6-6. These plasmas were all at 5.4T toroidal field, with the range of averaged electron densities between 2.6×10^{19} to $2.0\times10^{20}\text{m}^{-3}$, plasma currents between 0.77–1.1 MA, peak electron temperatures between 1.2–3.9 keV, and elongations between 1.46–1.70. This plasma data set will be used extensively for the remainder of this chapter, and all plots of plasma data will be from this set of plasmas unless otherwise noted. EFIT reconstruction is most accurate at the plasma edge, but should be reasonably reliable for the radii shown for L-mode plasmas.

MSE measurements are plotted against EFIT calculated values in Fig. 6-6, with

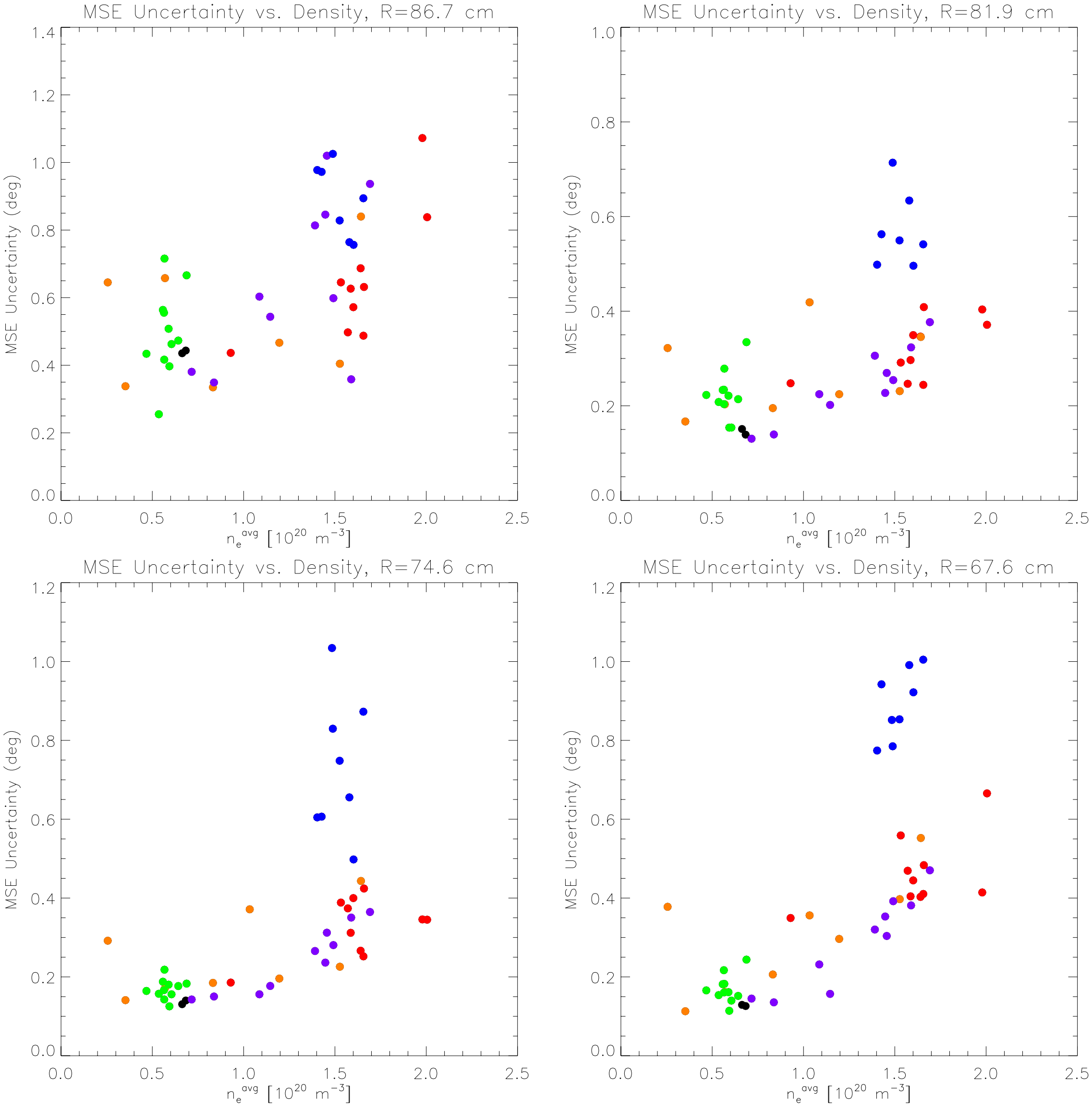

Figure 6-5: MSE uncertainties as a function of plasma density. Uncertainties are given in tokamak pitch angles, including the error magnification. Densities are given as $\bar{n}_e$, in [m^{-3}]. Four of ten MSE channels are shown, including the edge channel, at about 2 cm from the last closed flux surface, and the innermost channel, about 1 cm from the magnetic axis. Different colors represent different run days.

error bars calculated from the ratio error in Eqn. 6.10 and Fig. 6-4. One sees that the discrepancy with EFIT can be up to to 4.5° at the edge channel, improving to $\approx 2.0°$ for most measurements in other edge channels. In the three edgemost channels, MSE systematically measures a larger angle than EFIT, while the situation is reversed in the fourth channel. Many discrepancies are outside error bars. To illustrate this better, Fig. 6-7 shows the discrepancies with EFIT plotted versus MSE uncertainties.

In Fig. 6-7, points below the equality line do not have sufficient uncertainty to resolve their discrepancies with EFIT pitch angles. From these data, one can conclude that MSE discrepancies with EFIT angles cannot be accounted for by the statistical MSE uncertainties, which include the the background subtraction of plasma light, the intrinsic error of the instrument, and the fitting errors in the MSE angular calibration (negligible).

The dotted horizontal lines in Fig. 6-7 show the one standard deviation point for this data set, i.e. 68% of uncertainties fall below the line. The values of this uncertainty σ are given in Table 6.2. Note that the run day shown with blue points show systematically higher uncertainties. The color scheme for plasmas will be kept consistent for all plots showing this dataset.

MSE R [cm]	86.8	85.2	83.6	82.0	78.5	76.7	74.7	72.6	70.1	67.6
Uncertainty (68% range) [deg]	0.72	0.48	0.42	0.34	0.34	0.25	0.35	0.50	0.47	0.42

Table 6.2: Uncertainty statistics for MSE plasma measurements. For the 49 plasmas analyzed, 68% of uncertainties fall below this value. This values is a function both of the signal to noise, which decreases going from plasma edge to core, and the error magnification, which also decreases from edge to core.

Assuming EFIT to have errors negligible to MSE errors near the plasma edge, one can attempt to use the discrepancies between EFIT and MSE to calibrate MSE. This was the method with which Levinton calibrated the TFTR MSE [63]. The ensemble set of L-mode discharges presented here could be used in a similar calibration procedure for the *edge* MSE view. Figure 6-8 shows the weighted averages of the

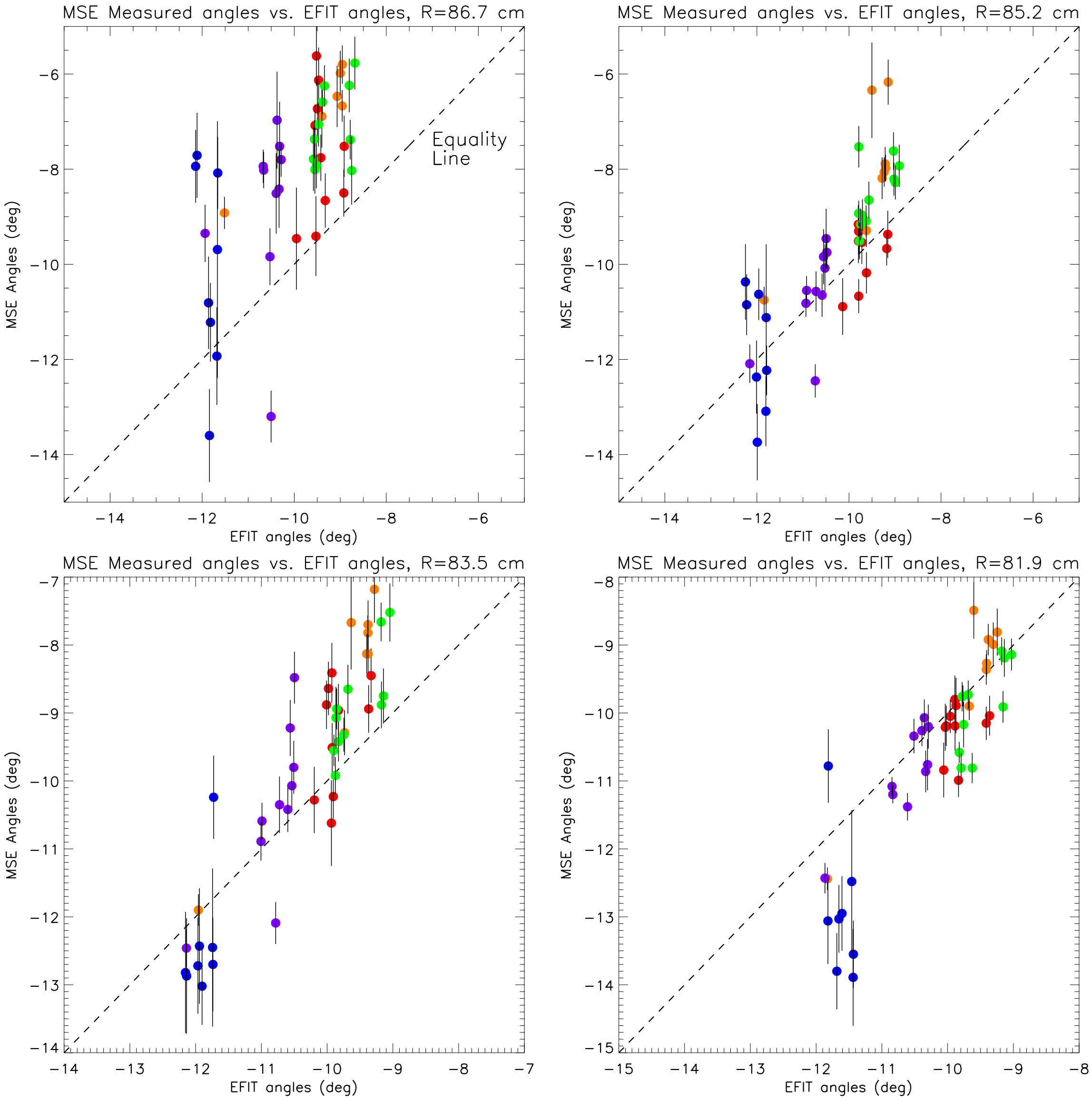

Figure 6-6: MSE measured angles compared with EFIT for 49 MSE measurements made during quiescent ohmic L-mode plasmas. Error bars are the total random MSE errors. Different colors represent different run days.

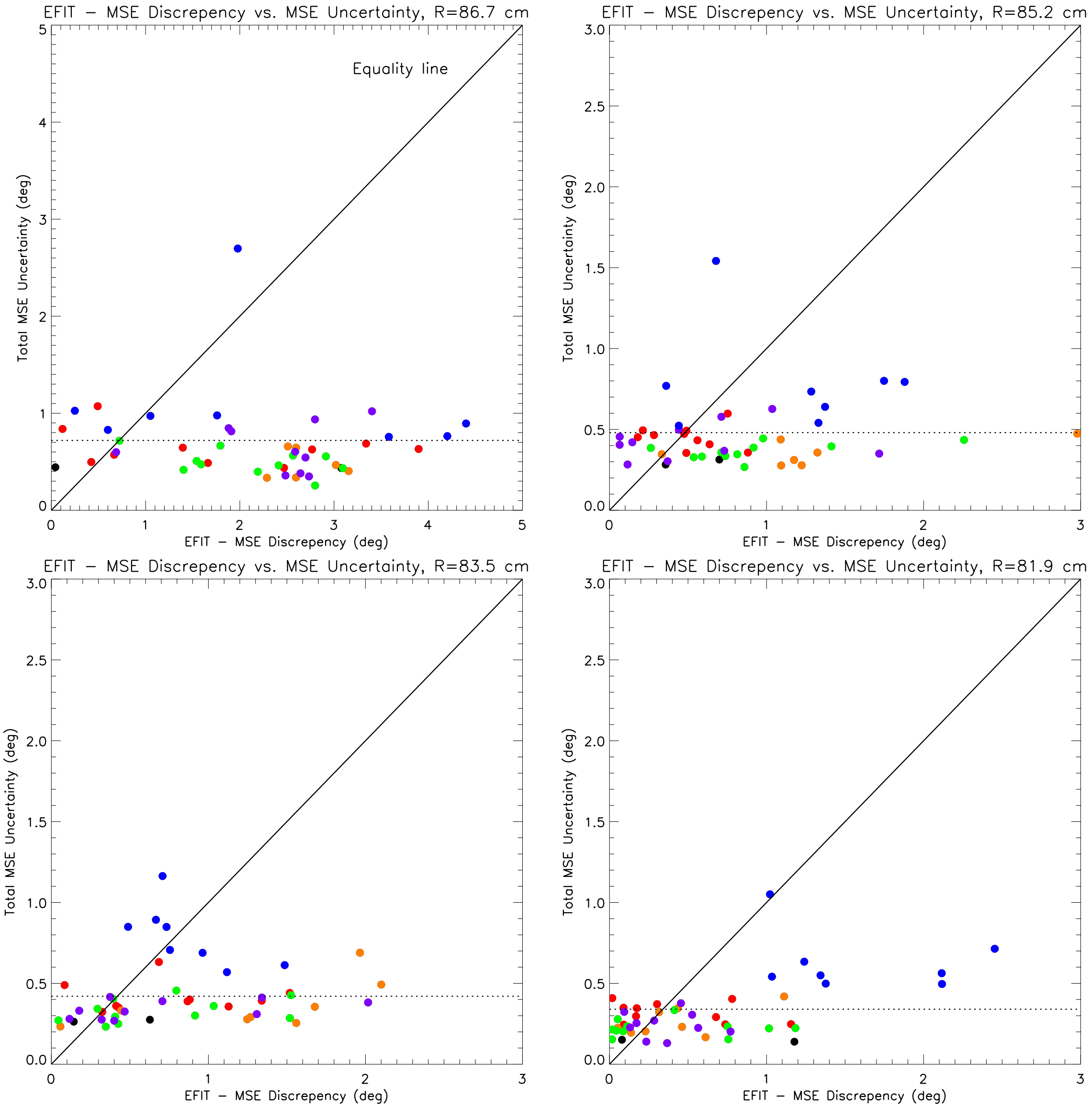

Figure 6-7: MSE uncertainties compared to discrepancies with EFIT for the same plasmas as Fig. 6-6. The absolute value of the discrepancy with EFIT is plotted. Points below the equality line cannot reconcile discrepancies with EFIT angles using the MSE uncertainty. Different colors represent different run days. 68% of uncertainties lie below the dotted horizontal line.

MSE/EFIT discrepancies and standard deviations for each channel. All MSE channels are shown, but the reader should be aware that EFIT reconstruction errors can increase dramatically going towards the plasma center. The standard deviations in Fig. 6-8 shows that plasma edge calibration is unlikely to work for C-Mod's MSE unless the source of additional scatter is removed. The standard deviation of discrepancy values is significantly larger than the uncertainties shown in Table 6.2. These results suggest that additional errors in MSE exist and need to be found for calibrated measurements. The dynamic range of the additional error must also be at least ±1.8° for the edge channel, and about ±1.0° for other channels.

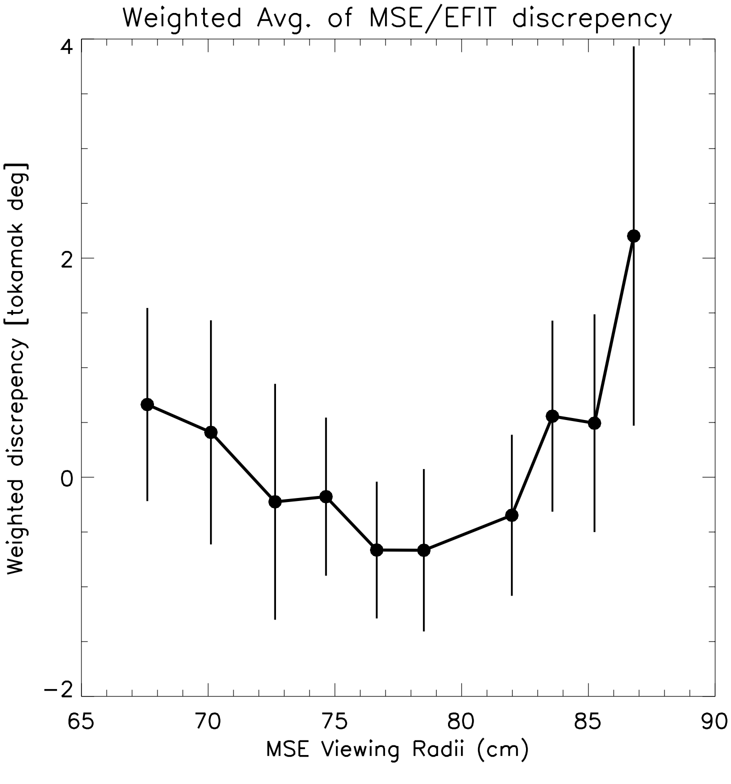

Figure 6-8: Variations in the EFIT/MSE discrepancies for 49 L-mode plasma discharges. Weighted average and standard deviation (1σ) of the discrepancies between EFIT and MSE. All MSE channels shown, but reader should be aware that EFIT reconstruction errors can increase dramatically going towards the plasma center.

Element	L1	L2A/B	L3A/B	V.W.	L4A	L4B	L5	L6
Z Location [m]	0.92	0.92	1.09	1.36	1.40	1.50	1.69	1.85
R Location [m]	0.03	0.18	0.23	0.23	0.23	0.23	0.23	0.23
Thickness [cm]	0.5	2.6	3.0	1.3	1.0	1.0	2.0	1.0
Relavant Field	B_t	B_z	B_r	B_r	B_r	B_r	B_r	B_r
Mean Field [T]	-3.94	0.53	-0.27	-0.09	-0.10	-0.11	-0.04	-0.003
95% range [T]	0.12	0.05	0.03	0.03	0.03	0.04	0.02	0.007
Faraday Rot. [deg]	0.052	0.036	0.021	0.003	0.003	0.003	0.002	0.000
95% range [deg]	0.002	0.004	0.002	0.001	0.001	0.001	0.001	0.000

Table 6.3: Estimate of Faraday rotation in MSE optics based on lab measured Verdet constants. Optics locations in R and Z are shown, along with the thickness of each element. The relevant component of the magnetic field and the mean values over all 49 plasma pulses along with the 95% (2 standard deviations) range are given next. Faraday rotations are calculated using the lab measured Verdet constant of 0.0265 deg/(cm Tesla).

6.2.1 Faraday rotation

One important effect not yet considered is the still uncalibrated Faraday rotation. Without a Faraday effect calibration, a sizable correction can be missing from the MSE measurements. For the set of plasma data presented, fields through each MSE component was calculated using EFIT. Faraday rotations are calculated using the mean lab measured Verdet constant of 0.0463 rad/(m T) or 0.0265 deg/(cm T). Estimated Faraday rotations are shown in Table 6.3. All lens pairs are considered to be in the same location save L4A/B, where the pair is separated by 10 cm. All rotations are assumed to be in the same direction in this calculation to give the most conservative estimate. Future raytracing results will show the sign of each rotation relative to the image at each optic.

Table 6.4 lists the total Faraday rotation by summing over all optics, and applying the error magnification factor for each channel to make the values applicable to pitch angle errors. Results show that these estimates of the total Faraday rotation are insufficient to explain the discrepancies between MSE measurements and EFIT, and

View R [cm]	Total Faraday Rotation Estimate [tokamak deg]
86.8	0.69 ± 0.07
85.2	0.54 ± 0.05
83.6	0.45 ± 0.04
82.0	0.38 ± 0.04
78.5	0.30 ± 0.03
76.7	0.27 ± 0.03
74.7	0.25 ± 0.02
72.6	0.23 ± 0.02
70.1	0.21 ± 0.02
67.6	0.20 ± 0.02

Table 6.4: Total Faraday rotation summed over all elements in Table 6.3 with error magnification applied for each channel.

the expected range of Faraday rotation in the optics cannot account for the range of discrepancies between EFIT and MSE. Although the effect of Faraday rotation for the PEMs have not been explicitly included, $\mathrm{B_r}$ values at the PEMs (identical to that for L6) are very low, with a mean of -30 gauss and a 95% range of ±70 gauss.

6.2.2 Radial electric field

Another effect present in plasma could be a radial electric field. MSE directly measures the angle of the total electric field, and would be affected by such static fields. The same viewing geometry projection that makes MSE edge views insensitive to pitch angles also makes these views sensitive to radial electric fields. Table 6.5 shows the sensitivity of MSE channels to radial electric fields as the $\mathrm{E_r}$ necessary to change the measured pitch angle by 1.0°

From poloidal rotation measurements of magnetic fluctuations by Hutchinson [64], $\mathrm{E_r}$ is believed to be as high as 200–250 kV/m during H-mode plasmas for a narrow region at the plasma edge. These value of $\mathrm{E_r}$ would give rise to $\mathbf{E} \wedge \mathbf{B}$ drifts matching the measured magnetic fluctuation rotation velocities of up to 50–60 km/s at the

MSE View Radii [cm]	86.8	85.2	83.6	82.0	78.5	76.7	74.7	72.6	70.1	67.6
E_r [kV/m]	39	50	63	76	106	124	145	167	196	226

Table 6.5: Radial electric field sensitivity. Radial electric field necessary to the measured pitch angle by 1.0° for each MSE channel, at typical pitch angles measured by each channel.

edge (mapped to the outboard midplane). Although significant rotation velocities are rarely observed in L-mode plasmas using magnetic fluctuation measurements, spectroscopic measurements of core toroidal velocities (using trace Ar impurities) can give an equivalent E_r of up to 30 kV/m if the plasma edge rotates as fast as the core. This value of E_r can have a significant effect on edge MSE measurements. Due to the sensitivity of MSE to E_r at the edge, more work needs to be done to assess the effect of plasma rotation on MSE measurements, even for L-mode plasmas. Routine plasma rotation velocity profiles from charge-exchange recombination spectroscopy (CXRS) is not yet available, but would be very helpful in resolving this issue.

The large radial electric fields observed during H-mode are believed to exist locally in the steep gradient region (3–4mm wide) of the H-mode pedestal just a few millimeters inside the separatrix. The edge MSE channel observes at R=86.8 cm, about 2–3 cm inside the separatrix, with a radial channel extent of 1.5 cm. It is possible that E_r has decayed significantly even for the edge MSE channel. Otherwise, a strong influence on the MSE measured pitch angle will be observed. The MSE sensitivity to E_r may turn out to be an advantage once MSE is reconciled with EFIT at the plasma edge. Because EFIT provides accurate pitch angles at the plasma edge, it would be possible to measure E_r using the discrepancy between MSE and EFIT. Using the edge value of Table 6.5, one sees that an edge MSE measurement with a ±0.5° errors would be capable of measuring the local (1.5 cm width) E_r with about a ±20 kV/m accuracy.

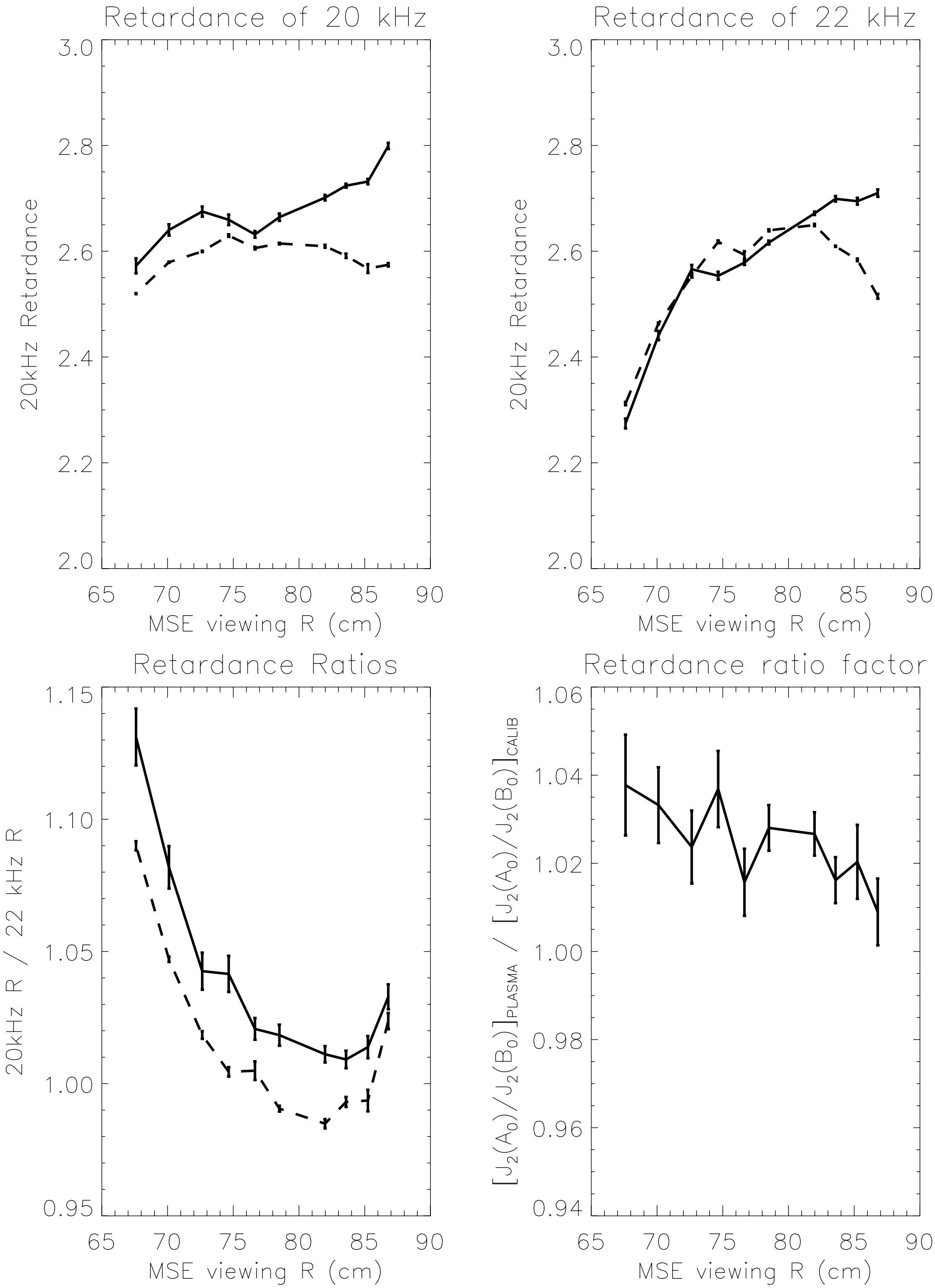

Figure 6-9: Plasma retardances compared with invessel calibration. Dashed lines are used for data from the invessel calibration. [Top] figures show retardances for each PEM (in radians), with resulting relative changes shown in [Bottom left]. Actual changes in measured angles result from taking the ratio of the lines in [Bottom left], and is shown to be between 1-4% in [Bottom right].

6.2.3 PEM retardances during plasma measurements

PEM retardances were measured for all plasmas in the 49 shot ensemble and shown in Fig. 6-9. All plasma measurements used identical PEM settings compared to values used during the invessel calibration, yet PEM retardances appear to shift between plasma conditions and invessel calibration conditions.

The retardance measurement uncertainties for plasma shots are greater than uncertainties in the beam-into-gas and invessel calibration cases. Even though the retardance calculation is independent of pitch angle and plasma brightness, broadband intensity fluctuations can still contribute noise to the three frequency components used to measure retardance.

Figure 6-10 shows no clear trend data when the retardance ratio is plotted against the discrepancies with EFIT. Retardance measurements for individual plasmas also contain too much noise to correct possible shot-to-shot variations in retardance of $\leq 1\%$. However, there does appears to be a systematic change in PEM retardances between the invessel calibration and the invessel calibration from the ensemble data.

The inability to measure the PEM retardances sufficiently accurately for every shot implies that retardances need to be carefully maintained. A lab calibration will be necessary to isolate the sensitive parameter that causes the PEM retardance to vary. This is slightly problematic on C-Mod, possessing only a single pair of PEMs (est. $60k per pair), so perhaps this test could be performed at another site.

C-Mod is believed to be the first MSE to routinely measure the PEM retardance because no publications could be found showing measured PEM retardances for other MSE diagnostics. This makes comparisons between the results found on C-Mod and other MSE diagnostics difficult. Operationally, the C-Mod PEMs are power cycled daily, but those on DIII-D are left on for months at a time. Whether this difference is important, or other variables, such as environmental conditions and stray fields experienced by the PEM also need to explored.

From the vendor PEM FAQ (www.hindsinstruments.com/PEM_Components/faq.aspx), the optical head of the PEMs are stable with respect to magnetic, electric, and slow

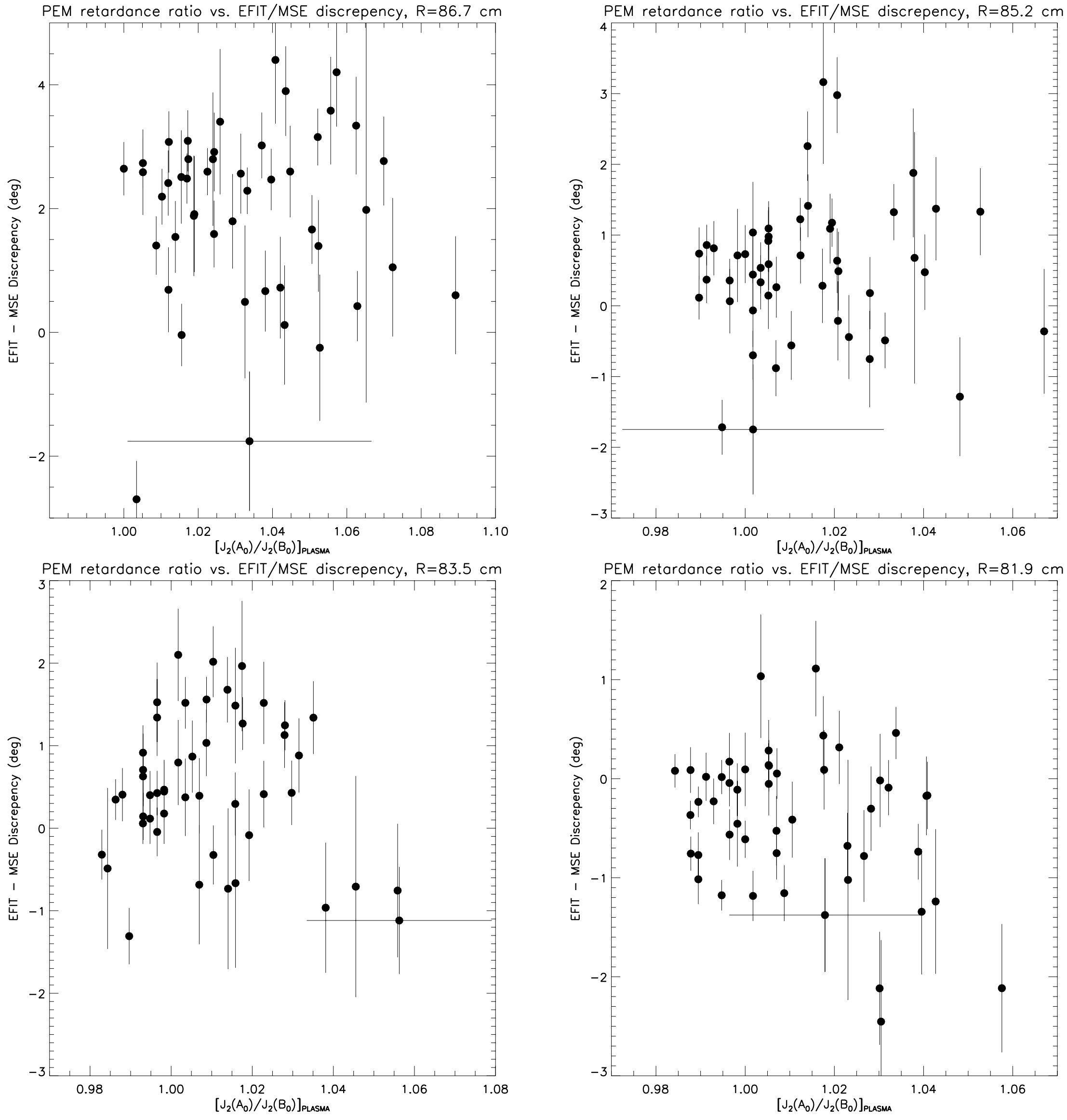

Figure 6-10: Retardance ratio measurements in plasma shots versus the discrepancy between MSE and EFIT. No clear trend is observed. Horizontal error bars (typical shown for each channel) shows retardance ratio measurement errors are likely too large to correct for on a shot-to-shot basis.

changes in temperature. The electronic head is kept far from the tokamak (10 m) and should not experience fields larger than the maximum 100 gauss specified by the manufacturer.

6.2.4 EFIT discrepancies vs. density and Z_{eff}

While the MSE uncertainties increase with plasma density, one might suspect that discrepancies with EFIT might do the same. Fig. 6-11 show that this is not the case.

Similarly, if one suspected that the MSE discrepancy is due to the effect from a dominant impurity species, then one might expect to see the EFIT discrepancy to scale with Z_{eff}. Fig. 6-12 shows that this is also not the case.

6.3 Polarization fraction of beam emission

The MSE bandpass filters were measured using a spectrometer in April, 2004, and for all plasma MSE measurements shown filters were tuned such that for each channel, the σ_1 line was at least 1.2 FWHM away (10Å) from the center of the filter bandpass. This assures that the filter function is reduced to $<5\%$ peak transmission by the σ_1 wavelength. Spectral simulations show that this filter setup reduces the amount of integrated 0 and -1σ intensity to be $<1\%$ of the intensity of the -2,-3, and -4π lines. Therefore, after the plasma background is subtracted, leaving only the beam emission, MSE should see calibrated polarization fractions very close to unity. This is the same argument made of the beam-into-gas data that led to the search for additional contaminant light.

Figure 6-13 show the mean polarization fraction of the same 49 plasmas used in the previous sections. The beam emission does not appear to be fully polarized, suggesting that the beam may be producing light other than the Stark-Zeeman Hα lines within the wavelength range accepted by MSE.

Figure 6-14, shows the outer four channels plotted against the EFIT calculated pitch angle. A group of plamas all from the same run day show up with consistently

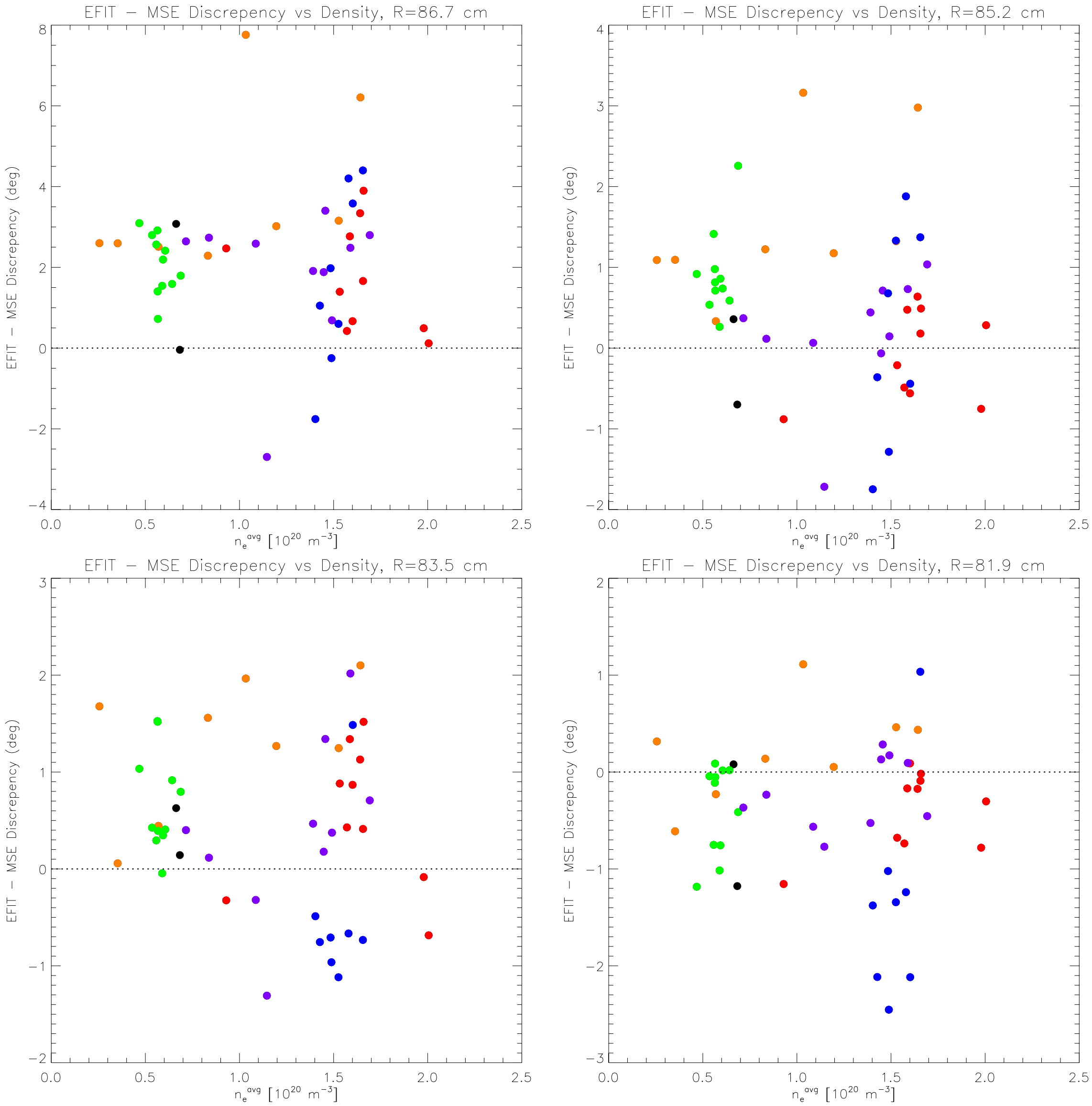

Figure 6-11: MSE discrepancies with EFIT plotted against plasma density shows no clear trends

.

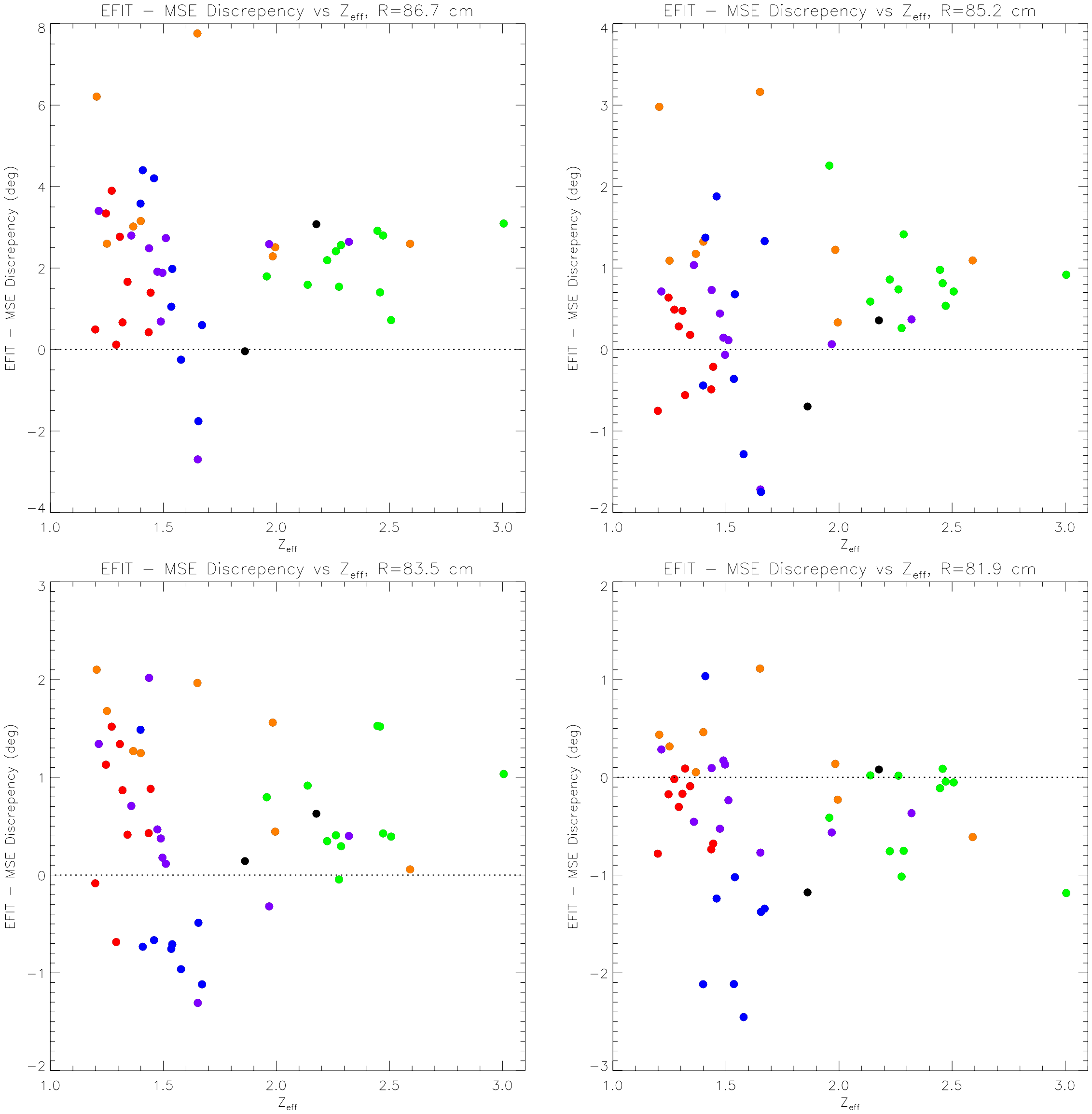

Figure 6-12: MSE discrepancies with EFIT plotted against plasma Z_{eff} shows no clear trends.

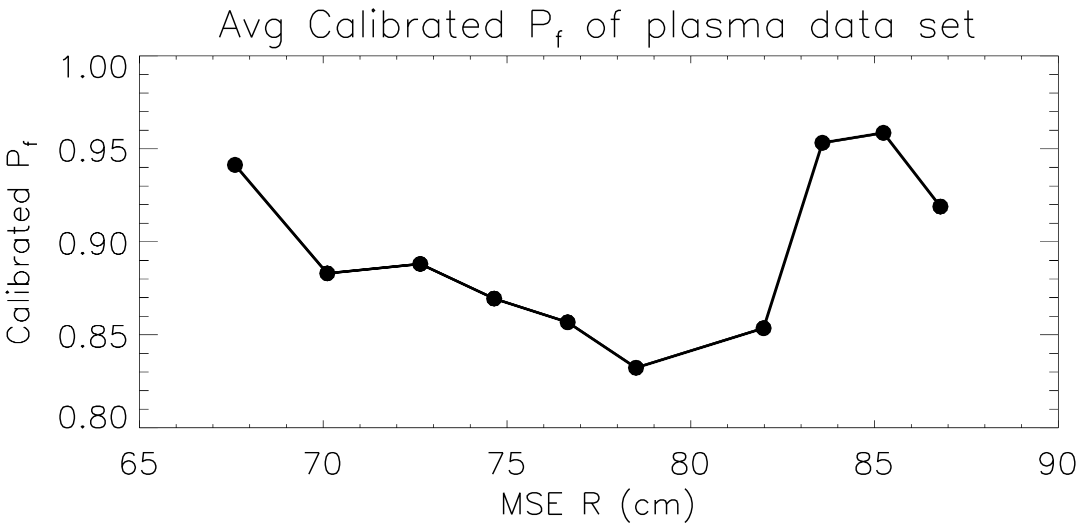

Figure 6-13: Average calibrated P_f of plasma data set. The expected value for full polarization is 1.

lower polarization fractions is shown as blue points.

This group of plasmas has no particularly distinctive features compared with the other data. One difference is the addition of a small ^{3}He minority for the RF experiment, but He does not have any lines within the MSE accepted wavelength range. All measurements were taken during periods *without* RF input power.

MSE filter temperature and retardance logs were checked to ensure that the filters were all tuned identically and the measured retardances are within error bars for the entire data set. The beam voltage and current were also verified to be consistent with the remainder of the data set. With all of these parameters identical, there are few reasons left for the dramatic observed changes to polarization fraction. One hypothesis suggests an increase of an impurity that produces beam induced charge exchange emission within the bandpass wavelength range of MSE.

Figures 6-15 and 6-16 shows that measurements with low polarization fraction lie within the middle of the range for both density and Z_{eff}, and shows no trend with either quantity. This results suggests that possible impurities responsible for MSE contamination are not the majority impurity species.

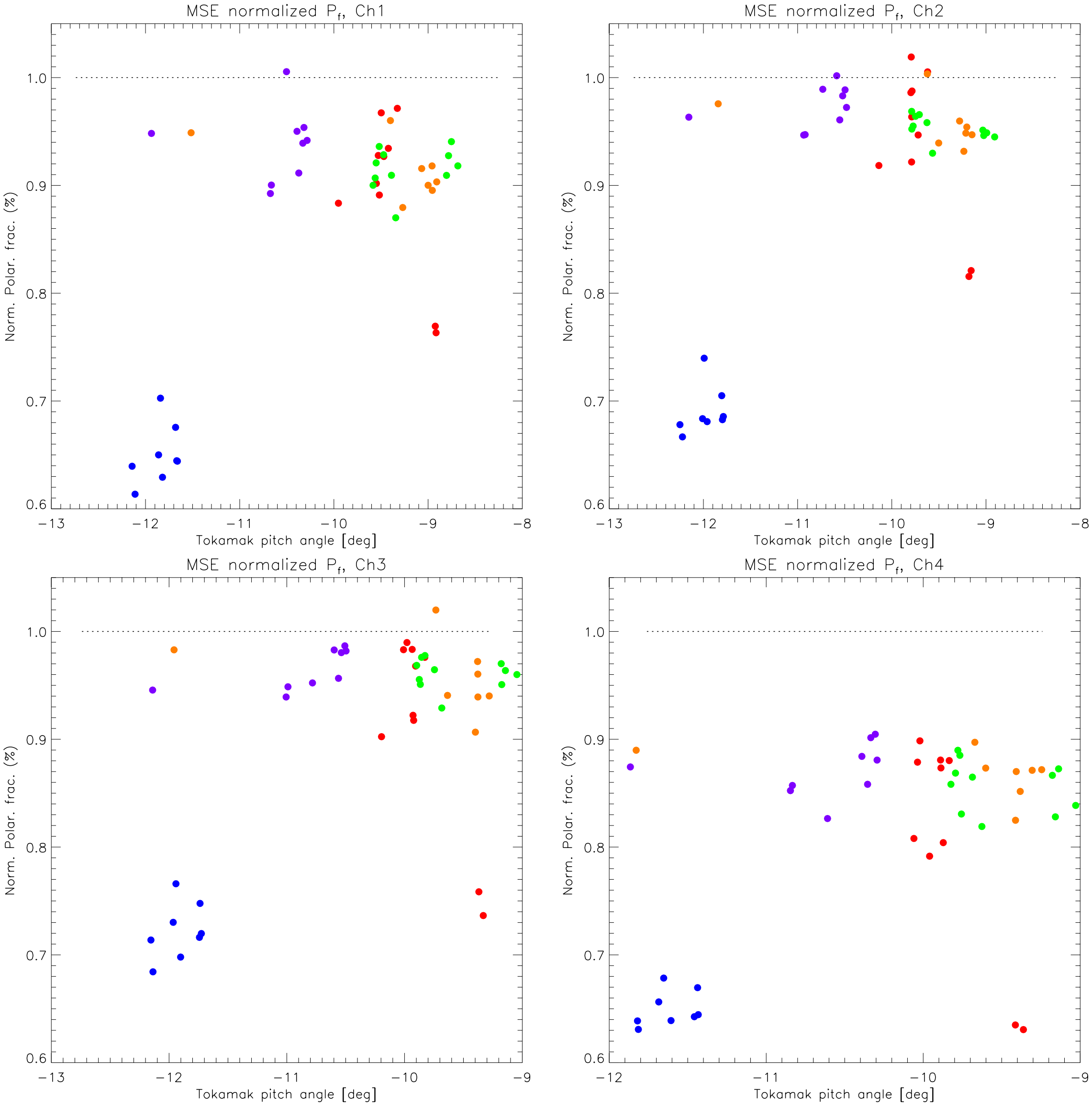

Figure 6-14: Calibrated polarization fraction of plasma measurements. The polarization fraction plotted as a function of the pitch angle. Full polarization is expected to be have a value of 1.

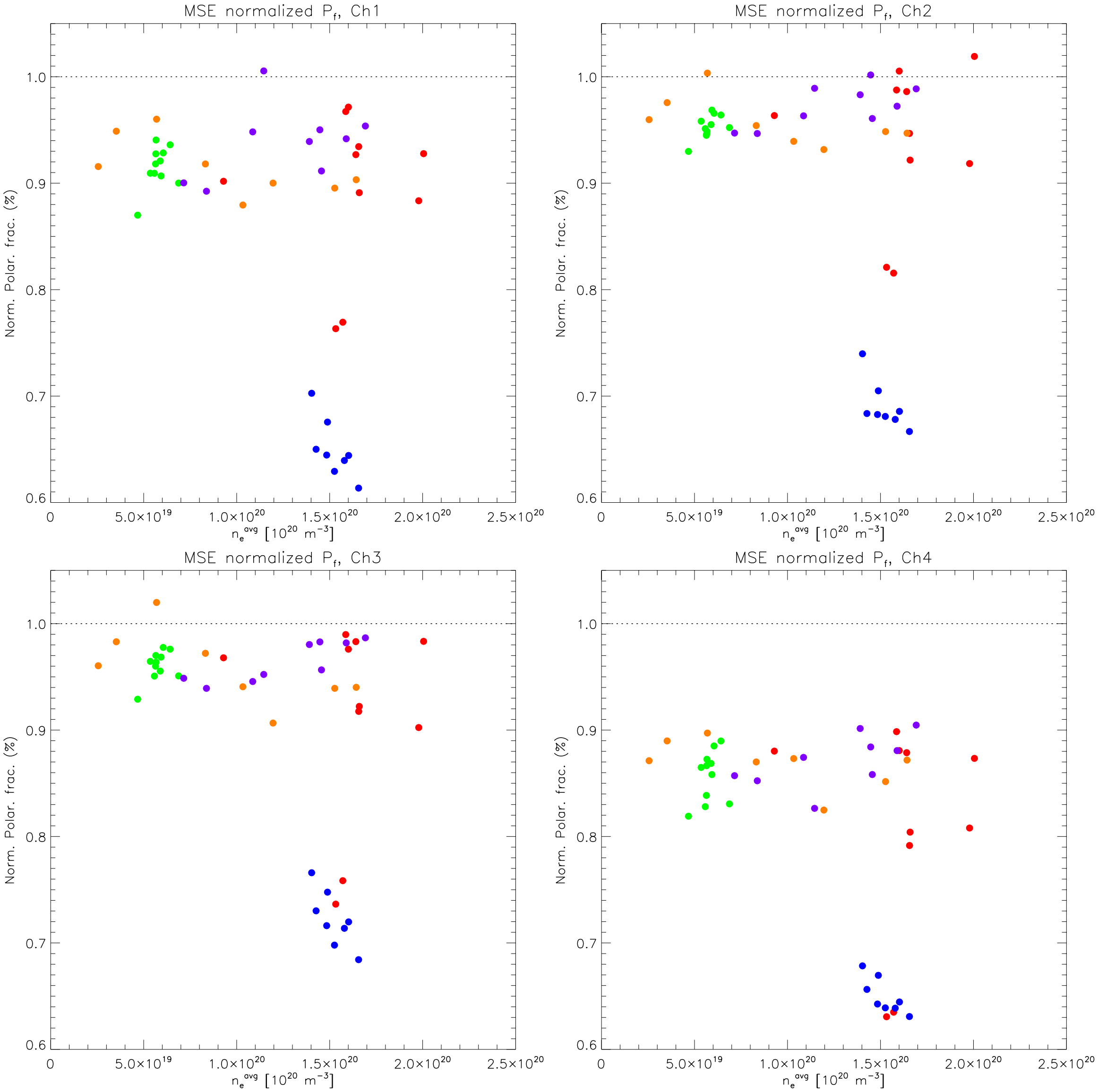

Figure 6-15: Calibrated polarization fraction of plasma measurements. The polarization fraction plotted as a function of plasma density.

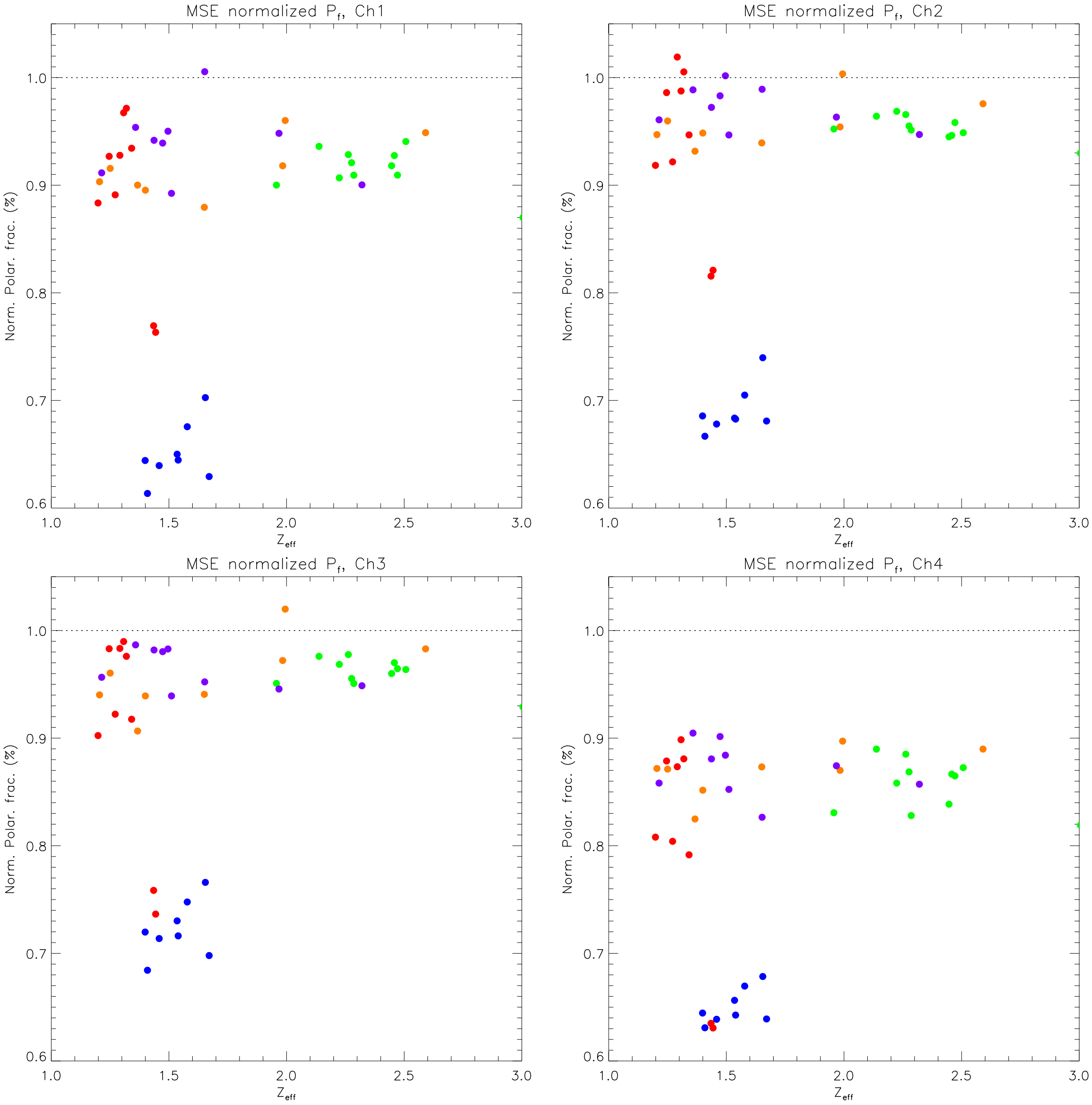

Figure 6-16: Calibrated polarization fraction of plasma measurements. The polarization fraction plotted as a function of the Z_{eff}.

It is also of interest to note that the plasmas which display lower polarization fractions are the same ones that display systematically higher uncertainties for a given density in Fig. 6-5. This would be the case if background (not beam induced) charge exchange at the plasma edge produced a background signal with higher polarization fraction when the impurities were present in higher concentrations. These observations are consistent with the hypothesis that trace impurity species are producing partially polarized line emission within the MSE spectral region. Background charge exchange from the edge would be detected as a partially polarized background and can be subtracted, but beam-induced charge exchange would produce weakly polarized contaminant light indistinguishable from beam emission by MSE.

Following this line of logic, one might expect that the discrepancy with EFIT would trend with the polarization fraction. Figure 6-17 shows EFIT/MSE discrepancies versus calibrated P_f for the four edge MSE channels. Results are not clear for the two edge channels, but for the third and fourth MSE channels do seem to show a trend of greater discrepancies with decreasing P_f.

6.4 Observation of edge emission on MSE

On shot 1040505003, MSE observed a plasma event that may provide some clues to MSE observation of impurities. A series of edge intensity oscillations occured during the MSE digitization period, prior to the beam injection. The intensity fluctuations were observed in every MSE channel, as well as the Dα diode, but were not seen by the Z-meter, which measures visual bremsstrahlung ($\propto Z_{eff} n_e^2$). This section will treat this edge intensity oscillation as a uniform, thin, emissive slab at the plasma edge.

The plasma in question had global parameters of 5.4T, 1MA, $\bar{\mathrm{n}}_\mathrm{e} = 10^{20}\mathrm{m}^{-3}$, with steady 1MW of RF injection at the time of measurement. The data was taken between 0.95s to 0.99s, in the flattop of both $\mathrm{I_p}$ and RF power. The plasma is in L-mode, with injected RF power too low to cause an H-mode transition. On this run day, observed MSE intensities were not observed to vary with changes in RF power (this

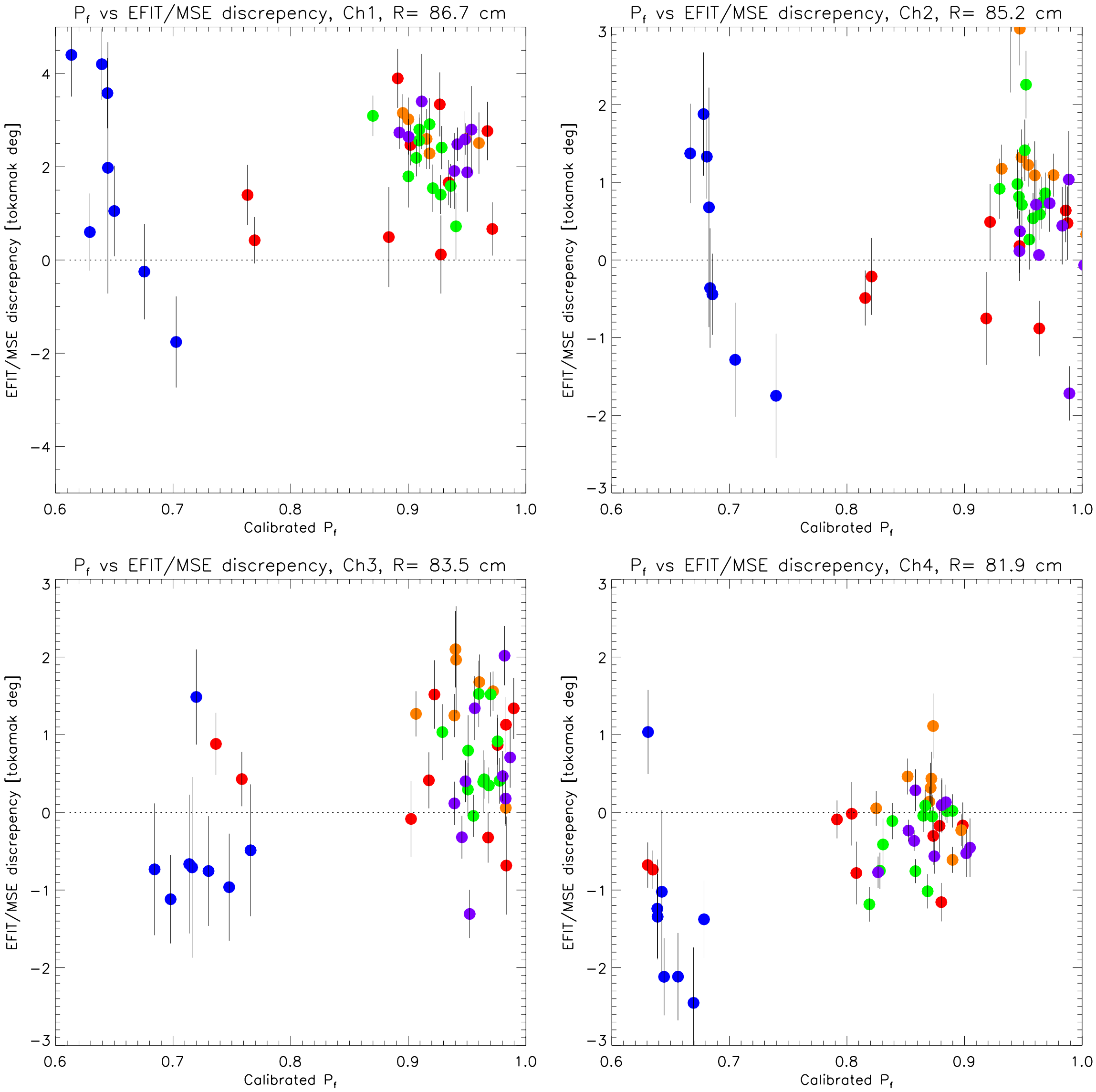

Figure 6-17: Calibrated polarization fraction vs. EFIT/MSE discrepancy. Error bars are MSE error bars, with EFIT uncertainties for these edge channels assumed small compared to MSE uncertainties.

varies from run day to run day).

6.4.1 Correlation with Dα diode data

Fig. 6-18 shows a series of intensity fluctuations caused by the edge dithering as a function of time, showing the intensity response of all MSE channels, as well as the Dα and Z-meter signals. The strong time correlation of all MSE channels (to $\lesssim 50\ \mu s$) and with the Dα diode (to $\lesssim$ 0.3 ms) suggests that the fluctuations observed by MSE are all localized at the plasma edge. For the shot being considered, the channel with a filter bandpass closest to Dα (the edge channel) has a center filter wavelength at 6590.8Å, making the filter transmission at $\lambda_{D\alpha}$ roughly 8×10^{-5} reducing to about 10^{-5} transmission for the core channels. The Z-meter in the lowest [BOTTOM RIGHT] panel shows that the visual bremsstrahlung do not display the same oscillations observed by MSE and the diode.

The period of the oscillations are about 2.5 ms. Digital lockin analysis using time intervals at around 1.25ms proved to be too noisy to determine if the light from the edge oscillation were significantly more polarized than the background light.

To illustrate the amplitude of the fluctuation better, three peak to peak values were measured and averaged. This was compared to the average value of the MSE signals over the 0.95-0.98s time period. Fig. 6-19 shows the ratio of intensities of the edge fluctuations to the MSE chord integrated total intensity. The dotted line shows the same calculation for the Dα diode signal.

By naively assuming that Dα leakage through MSE filters is wholly responsible for the MSE fluctuation intensity, one can show using data from subsequent plasmas that this cannot be true. If Dα leakage were the sole cause for the intensity fluctuations observed on MSE, one could compare $\Delta I_{D\alpha}/I_{D\alpha}$ to $\Delta I_{MSE}/I_{MSE}$ to deduce how much of the total MSE background is due to Dα. This is shown with the right hand axis in Fig. 6-19. This “cross calibration” leads to the conclusion that 75% of the MSE background is Dα leakage at the edge channel. However, over the next several shots, observations show that this assumption cannot be true. With visual bremsstrahlung at an identical value, all MSE signals decrease by at least 37% while the Dα signal

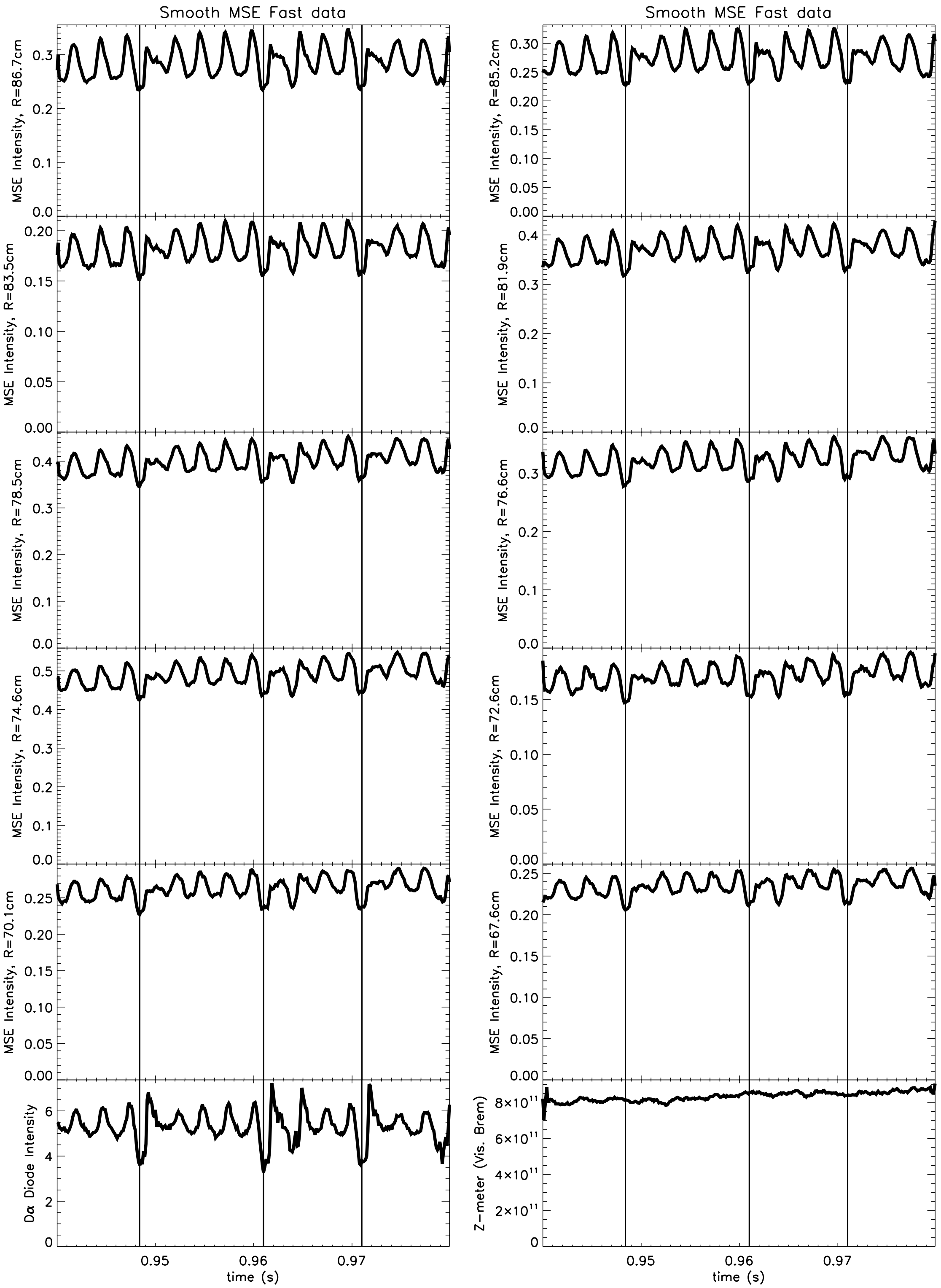

Figure 6-18: Plasma edge fluctuations as observed by MSE, the Dα diode [BOTTOM LEFT], and the Z-meter (visual bremsstrahlung) [BOTTOM RIGHT].

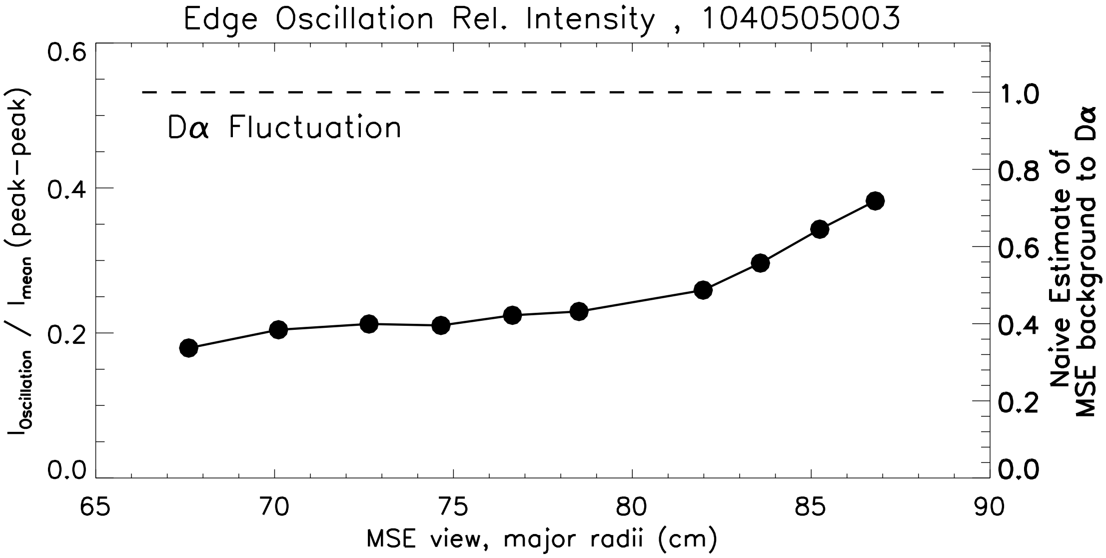

Figure 6-19: Plasma edge fluctuation intensity as a fraction of the mean MSE observed intensity. Dashed line shows same fraction for the Dα diode signal.

decreases by only 5%. The conclusion from these results is that at least one third of MSE observed fluctuation intensity is *correlated with, but not* Dα on shot 1040505003.

Since the Z-meter signal does not show the same fluctuations, the entirety of the *fluctation* can be assumed to be from the plasma edge. As both Dα and bremsstrahlung have been eliminated from consideration, only impurity lines and molecular deuterium remain as viable candidates. Unfortunately, for this analysis, there isn't any method that would allow differentiation between these two types of lines.

The edge fluctuations on shot 1040505003 can now be considered as a "stardard candle" being observed by MSE. Assuming that the emission is from a thin uniform slab at the plasma edge, MSE intensities need to scaled by a $\cos(\Omega)$ term, where Ω is the angle between the viewing chord and the toroidal field, to account for the different chord integral lengths. A relative intensity calibration of MSE channels was performed by McDermott [65] using beam into gas data. Her results were applied to the MSE fluctuation amplitudes.

After applied these calibration factors to each channel, one might now expect to see channel to channel differences based primarily on variations in filter bandpass for each MSE channel. If the observed emission is broadband, intensities should not vary based on filter center locations. In essence, this turns MSE into a low resolution spectrometer with overlapping wavelength bins. The FWHM of MSE filters at 9Å is larger than differences in their central wavelengths (≈3-4 Å). Figure 6-20 show the results from this analysis, with the data plotted versus MSE viewing radii in the left figure, and the filter center wavelengths in the right.

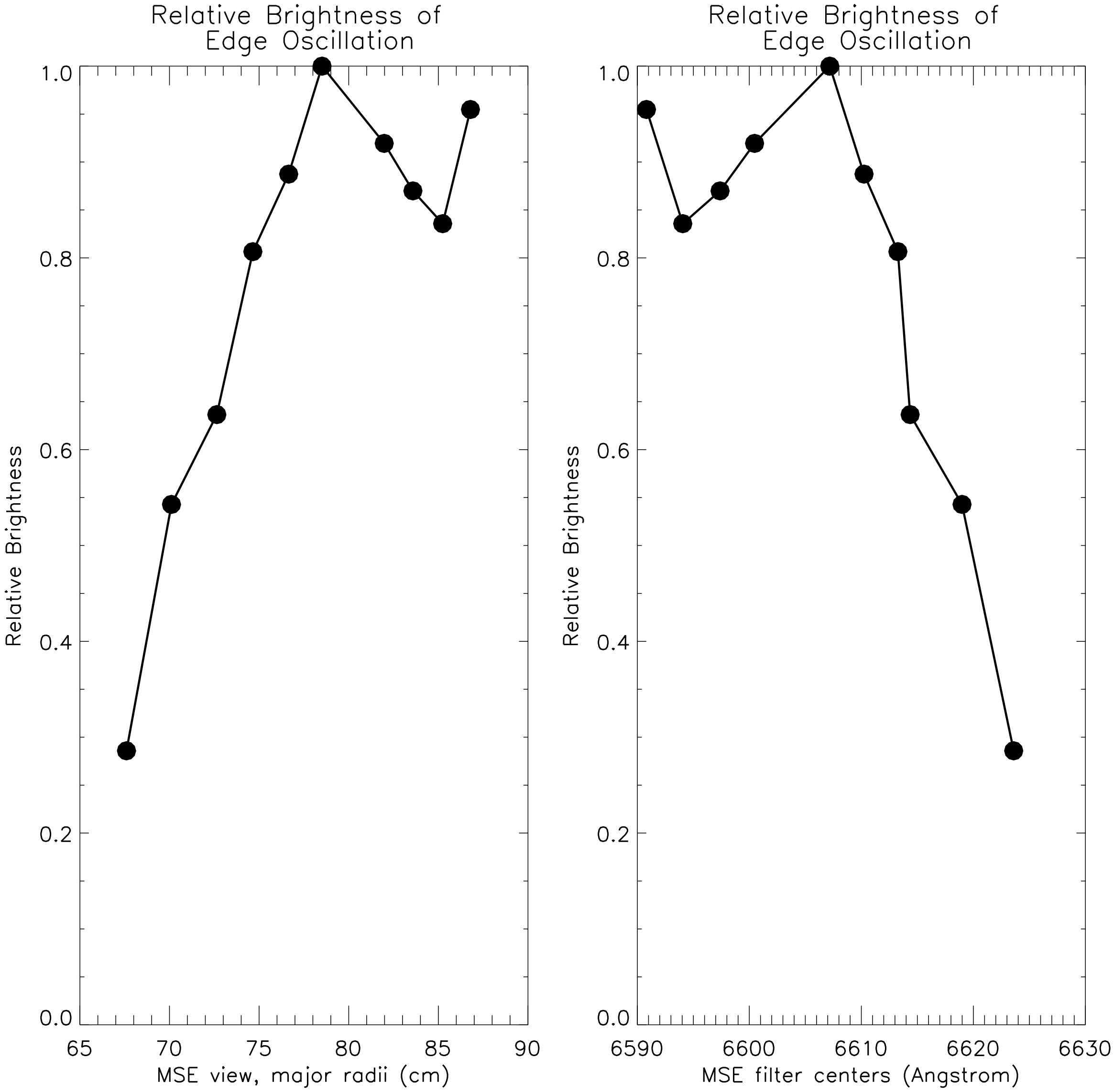

Figure 6-20: Edge emission relative brightness as observed by MSE. Plotted versus view radii on the left and versus the central bandpass wavelength on the right.

This result suggests that there might be two lines within the MSE wavelengths, one near 6608.5Å and the other near or below 6590.8Å. Sampsell has presented [66] measured intrinsic impurity lines around this region, such as CII (6578.0Å), CI (6578.8Å), CII (6582.9Å), and FIII (6583.9Å). As BES was not interested in wavelengths beyond the beam near the edge (low Doppler shifts), no work was done to study impurity lines in the spectral region beyond 6600Å.

Comparing Fig. 6-20 with the average polarization fraction plot of Fig.6-13 shows a qualitative inverse relation, with the channel at 78.5 cm and the edge channel showing local brightness maxima as well as local polarization minima. This inverse relationship corroborates the hypothesis of having *two impurity charge exchange or* D_2 *lines within the MSE channels*, contaminating the MSE measurement with a partially polarized signal.

If the lines are from D_2, then possible sources for MSE polarized contamination remain elusive because D_2 should not exist inside the plasma, so there is little chance for the beam to cause D_2 emission in the plasma.

If the lines suggested by the previous analysis are indeed impurity lines, it remains unclear why they appear partially polarized and contaminate the MSE measurement. Another caveat in this analysis is that the charge states covered by this analysis only extend to those that can exist at the plasma edge. It is possible that the charge states observed in the edge emission no longer exist in higher temperature plasma core.

The beam-into-gas calibration chapter revealed the sensitivity of the edge channels to Zeeman linear polarizations. The introduction of roughly 2% linearly polarized light in the Zeeman directions will produce the roughly 4° discrepancies observed at the edge. This sensitivity will likely require that MSE avoid observing any Zeeman polarized light, because measuring such small signals with adequate uncertainties may not be possible.

6.5 Chapter Summary & Next Steps

6.5.1 Summary

Agreement between EFIT and MSE measurements is currently only within two degrees for the edgemost channel, and between 0.5–1.0 degrees for all other channels. While this level of agreement may be sufficient for some uses of MSE data, such as a measurement of the plasma inductance or intrashot measurements of local current density changes, more demanding uses such as magnetic shear constraint and on-axis safety factors still require better calibration. This chapter showed a number of mechanisms than might explain the cause(s) of MSE errors.

MSE uncertainties were measured and totalled, including instrumental statistics, fitted response curve uncertainties, and the dominant uncertainty of subtracting the background plasma signal. The uncertainties were found to be too small to explain the discrepancies with EFIT, indicating an unknown source of error.

Error analysis indicates that MSE is not fundamentally limited by signal-to-noise for plasmas up to $\bar{n}_e = 1.5 \times 10^{20}$ for all channels using the 50ms 4A beam. Sensitivity analysis of MSE uncertainties with respect to DNB parameters show the possibility for dramatic reductions in the MSE uncertainty (over a factor of 2) using the new DNB. Even in its current state, MSE should have sufficiently low statistical uncertainties to make *relative* pitch angle measurements if the unknown contaminant emission source remains constant through the measurement.

Faraday rotation from optics remains to be calibrated *in situ*. Lab measurements place upper bounds on the expected values of these effects. Even if Faraday rotation were larger than expected, there is currently little evidence to suggest that it could have a large enough dynamic range during plasmas to match the observed uncertainties. Further, Faraday rotations cannot explain decreases in polarization fraction, only changes in angle. Although the plasmas considered in this work were all L-mode, the sensitivity of MSE to radial electric fields makes it necessary to have better rotational data than is currently available to fully resolve this issue. With only core toroidal rotation data, an assumption that the edge plasma rotates at velocities equal to the core gives values of E_r that can have a significant influence on edge MSE channels.

PEM retardances changes do have the potential of introducing a large uncertainty with a significant dynamic range. Because the ratio of retardance ratios (between in-vessel calibration and plasma) have large error bars, it may be possible for retardance changes to be an important factor. If this is the case, then decreased polarization fractions must be due to fully unpolarized light, and the trend data with polarization fraction would have to be a coincidence.

One remaining hypothesis at this point is that a partially polarized, beam-induced charge exchange impurity line is contaminating the MSE angular measurement. Estimating from the polarization fraction, intensity of this contamination is small, comprising of between approximately 5% to 20% for all MSE channels.

Support for the presence of an impurity line is currently mostly circumstantial. The 50ms beam used for this work is not well-suited for taking detailed survey spectra of the MSE wavelengths due to its short length. Plasma background subtraction of spectra taken through MSE fibers have sufficient noise to obscure small features such as the weak impurity lines being searched for. In addition, impurity calibration at the plasma edge is complicated by the fact that MSE only observes the full energy beam component, but charge exchange can occur (with even larger cross-sections) for the lower energy beam components. Without a routine measurement of the beam species composition, it is especially difficult to isolate sensitivities of MSE observations to beam parameters or plasma conditions.

With the installation of the long pulse beam, it should be possible to take detailed spectra with low Poisson statistical noise to study the MSE spectral region. This should provide direct evidence of any impurity lines that may be present.

This work motivates a detailed spectral study by making use of MSE observations of lower than expected polarization fractions of the beam emission. A set of data showing dramatically lower polarization fraction appears for an unknown reason. By examining all possibilities, such as MSE filter tuning, MSE retardance drift, beam current and energy, a hypothesis was formed that a trace impurity was present in a larger quantity for those plasmas. The same plasmas with reduced polarization fractions also showed larger discrepancies with EFIT in two MSE channels.

The lack of correlation betweeen the discrepancy with either density or Z_{eff} is consistent with the theory that the contaminant light is due to beam induced charge exchange with a trace impurity that does not influence global plasma parameters.

Another piece of evidence came from the analysis of an edge fluctuation. By comparing to the Dα diode and visual bremsstrahlung signals, the intensity fluctuation was deduced to be from a thin emitting shell from the edge. Using knowledge of the filter function, Dα can be excluded as a possible source. Without similar fluctuations from the visual bremsstrahlung, density fluctuations were excluded, leaving only molecular lines and impurity lines. Using a simple thin emissive slab assumption and a MSE channel to channel relative calibration, the fluctuation amplitudes were converted to relative intensities. This effectively transformed MSE into a low resolution spectrometer, with results showing that two likely impurity lines exist in the MSE spectral range, one near 6608.5Å and the other near or below 6590.8Å. A final comparison between the MSE "spectrograph" and the average polarization fraction over a large series of plasma measurements shows qualitative agreeement to support the conclusion of two impurity lines.

6.5.2 Next Steps

The next step for MSE is to *study the spectral region within the MSE filter bandpass* carefully, looking for impurity lines that are only a fraction of the intensity of the MSE Stark-π lines. One approach already being implemented is to inject some suspected impurities, carbon and fluorine. By observing MSE signals when these impurities are injected, one will immediately know if these trace impurities are responsible for the MSE contamination.

Spectroscopic identification of the contaminant lines will be the first step to determining the possibility of avoiding their observation. It is currently not known if there are filters available that would be capable of rejecting enough impurity light to make all MSE channels viable or if certain MSE channels will not be able to make measurements using the current viewing geometry.

Determining the Faraday rotation during plasma shots is already well underway with the installation of an invessel fixed polarizer, which will be able to measure the Faraday rotation without using beam-into-gas. More detailed studies of PEM retardance sensitivities in the lab must be conducted. Currently, retardance sensitivities remain an important unknown, and the measurement of retardance changes between the invessel calibration and plasma remains a significant uncertainty.

The installation of the new, long pulse neutral beam is progressing well, and should provide numerous advantages for both MSE calibration and measurements. Previously tasks that would have required a tremendous number of plasmas at great cost using a 50ms beam should be greatly facilitated with the new DNB. Experiments such as plasma major radius jogs using small minor radii plasma now have much greater benefit to cost ratios, and could be pursued. Plasma spectra currently unusable due to large uncertainties after background subtraction can be improved to test several hypotheses presented in this work.

Chapter 7

Summary and Future work

This dissertation documents the work done to implement and calibrate a Motional Stark Effect diagnostic in the difficult environment prevalent on C-Mod. Initial efforts focused on strengthening the invessel periscope to survive the large accelerations of C-Mod disruptions. Once a robust design was implemented, efforts shifted to an absolute invessel calibration to determine the instrumental response. When trying to reconcile invessel calibration measurements with a complementary calibration technique using DNB injection into a gas-filled torus with known fields, significant differences were found. Additional discrepancies are discovered when measurements in plasmas are compared to either set of calibrations.

The remainder of the effort focused on theoretical and experimental initiatives to resolve observed discrepancies. This chapter summarizes the progress that has been made to date, documents the current state of understanding, and identifies future studies necessary to complete the calibration of MSE in order to realize its potential of measuring the internal magnetic pitch angle profile accurately.

7.1 Summary

7.1.1 Atomic Physics

New discoveries were presented in Chapter 2 regarding the polarization nature of hydrogenic Balmer-α transitions in $\mathbf{E} \wedge \mathbf{B}$ fields, where both Stark and Zeeman effects are present. The following new features are found for the Balmer-α transitions by coherently adding components of the transition dipole and examining all thirty-six possible transitions.

- Three transition types exist for MSE relevant cases where the atom emits in crossed $\mathbf{E} = \mathbf{v}_\perp \wedge \mathbf{B}$ and $\mathbf{B}$ fields. These can be labeled by their linear orientation in the limit where the Stark effect is dominant. All three transitions are present regardless of the strength of the magnetic field.
  - Stark-Zeeman-E ($\parallel \mathbf{E}$)
  - Stark-Zeeman-v ($\parallel \mathbf{v}_\perp$)
  - Stark-Zeeman-B ($\parallel \mathbf{B}$)
- Stark-Zeeman-E and Stark-Zeeman-v ($\Delta E \neq 0$) emission is elliptically polarized while Stark-Zeeman-B and Stark-Zeeman-v ($\Delta E = 0$) emission is linearly polarized.
- Summed over degenerate transitions for each energy level, lines containing Stark-Zeeman-v are perpendicular to lines containing Stark-Zeeman-E only for statistical upper hybrid state populations.

Diagnostics that observe $\Delta E = 0, \pm 1$ lines must verify that upper state populations are statistical to have confidence that the measured emission is polarized perpendicular to the local electric field. MSE diagnostics that measure the $\Delta E = \pm 2, \pm 3$, and ± 4 lines (Stark-Zeeman-E) can avoid the need to verify statistical state populations by carefully excluding all $\Delta E = 0, \pm 1$ line emission (Stark-Zeeman-v, Stark-Zeeman-B).

7.1.2 Hardware

Major hardware components of the MSE diagnostic have been described, including vacuum optics, air-side optics, the polarimeter, transfer fibers, photomultipliers and digitization hardware. The methods for monitoring and tuning MSE filter temperatures, photomultiplier high voltages, and PEM retardances were discussed. The digital lockin used to analyze fast raw MSE intensities was also discussed.

The mechanical mounting of every MSE vacuum side components has been redesigned at least once, motivated by disruption damaged optics. The engineering experience can be summarized in the following four principles which should be applicable for most optics installations in tokamaks that suffer from large disruption forces.

- ♣ Prevent any metal to glass contact
- ♡ Trap all Teflon volumetrically or mechanically
- ♠ Put only compressive stresses on optics
- ♢ Protect against direct impact

Current C-Mod MSE optics have survived for at least one full run campaign without any damage.

7.1.3 Calibration & Modeling

An absolute invessel calibration was performed using an invessel optical apparatus capable of generating arbitrary calibrated Stokes vectors, including both linear and circularly polarized components. C-Mod is believed to be the first MSE installation to have performed such a full Stokes polarimetry calibration. Results from the calibration were combined with a Müeller matrix model of MSE including real geometry and one imperfect mirror. The following MSE geometric and optical properties were deduced by matching simulated results with measured results.

- The retardance or phase shift of the dielectric front surface mirror
- The orientation of the mirror optical axis relative to the polarimeter axis
- The mirror reflectivity ratio of s to p components
- The polarimeter orientation
- The angle of the linear polarizer in the polarimeter
- The retardance of each PEM

Good agreement between the model and data was achieved over the entire angular range with unique values of optical properties. MSE model and measured responses was shown to agree for the 20, 40, and 44 kHz harmonics in both amplitude and phase.

A new method of measuring the PEM retardances concurrently with MSE measurements by using sum and difference frequency harmonics at $(3\omega_1 - \omega_2)$, $(3\omega_2 - \omega_1)$, and $(\omega_1 + \omega_2)$ was found to be consistent between the model and measurements.

7.1.4 Beam-into-gas calibration

A hypothesis has been proposed suggesting that deuterium molecular emission contaminates the MSE measurement during beam-into-gas calibrations. Spectroscopic and MSE polarization data was shown to support this argument. The inclusion of a partially polarized source oriented in the Zeeman-σ ($\perp \mathbf{B}$) direction at between 20–30% the total observed intensity resolves all known discrepancies between expected and observed values, including both the linear polarization angle and the polarization fraction. Observed non-linearities, channel-to-channel differences, and sensitivity to filter tuning for certain angular ranges were all reproduced when this polarized source, believed to be molecular D_2 on the basis of measured spectra, was included. Proposed tests of this hypothesis were identified.

7.1.5 Plasma Measurements

MSE measurements of plasmas calibrated using invessel calibration data currently agree with EFIT to within 1° for L-mode plasmas for all but the edge channel, which can differ by over 2°. Statistical uncertainties are insufficient to explain the observed differences. Analysis shows that MSE statistical uncertainties are $\leq 0.4°$ for channels other than the edge channel for plasma densities up to $\bar{n}_e = 1.5 \times 10^{20}$ m^{-3}. An estimate of Faraday rotation using bench measured Verdet constants show a systematic error with a narrow dynamic range. Three mechanisms found to require further exploration were,

- PEM retardance variations. PEM retardances need to be precisely maintained with changing environmental, operational, and stray field conditions.

- Radial electric fields from plasma rotation. Due to the sensitivity of MSE at the edge, values of E_r as low as 40kV/m can perturb the MSE measurement by 1°. Routine plasma rotation profiles will likely be needed to fully resolve this issue.

- Weakly polarized emission from beam-induced charge exchange within the MSE spectral region that cannot currently be subtracted from the signal. A spectral search for weak line emission from trace impurities will be possible with the new long pulse beam.

7.2 Future Work

The calibration of C-Mod's MSE is mostly complete. The absolute calibration conducted has provided a fairly complete understanding of the instrument. Only two instrumental effects remain to be calibrated, an *in situ* Faraday rotation measurement, and verification of PEM retardance stability.

The remaining outstanding issues for MSE measurement are actually physics based. For the beam-into-gas calibration, a straightforward test of the D_2 hypothesis using helium as the fill gas during the calibration is imminent. The results may help explain a number of previously unexpected observations both at C-Mod and at several other MSE installations.

Perturbations to plasma measurements are more subtle. Verification of the effect of E_r on MSE is subject to the availability of rotation measurements at the MSE measurement locations. Acquiring convincing correlation evidence will require routine measurements of rotation profiles.

A careful spectral survey to find weak beam-induced charge exchange lines will be facilitated by a long pulse beam. Because the effect of Zeeman oriented polarized contamination are most evident at the edge, routine measurements of the beam species mix would be helpful. The ratio of Balmer-α emission from the full energy beam component to beam-induced charge exchange emission from trace impurities is dependent on the local beam species mix because all beam neutrals can undergo charge exchange (lower energy species typically have larger cross-sections) while MSE observes only the full energy component.

If impurity lines are found to lie in the MSE spectral range, the implications are not yet clear. It will likely be necessary for MSE to avoid observation of such contaminant light altogether, and it is not clear if filter exists filters suitable for this application. In the likely event that some MSE filters will need to have a narrowed bandpass, improvements in DNB parameters will be necessary to maintain current statistical uncertainties.

If it is not possible to avoid observing contaminant lines around the MSE Balmer-α lines for certain channels, it should be possible to observe the Balmer-β line, which are polarized and split in roughly the same manner as Balmer-α, albeit with a more complex pattern. For this reason, a spectral survey around the Balmer-β line ($\lambda_{\mathrm{H}\beta} =$ 486.1nm) is also highly recommended.

Appendix A

Stokes Vectors and Müeller matrix representation for polarization optics

A.1 Stokes vector representation of partially polarized light

The Stokes vector is a convenient way of representing incoherent polarized light. Any polarization state can be represented, including partially polarized states.

The Stokes vector represents intensities, it is well suited for comparing incoherent radiation where fields do not vectorally add. An advantage of using Stokes vectors is that multiple vectors can be simply added together, analogous to superimposing multiple sources of incoherent light. Another mathematical representation for polarized light sometimes used is the Jones vector, which uses a two element complex vector to represent fully polarized linear and circular polarization directions. However, MSE does not generally receive input light that is fully polarized, so the Jones vector is not discussed here.

Stokes vectors takes the form of a four element column vector,

$$\mathbf{S} = \begin{bmatrix} & I_{total} & \\ I_{0^\circ} & - & I_{90^\circ} \\ I_{45^\circ} & - & I_{-45^\circ} \\ I^{RH}_{circ} & - & I^{LH}_{circ} \end{bmatrix} = \begin{bmatrix} & I_{total} & \\ 2I_{0^\circ} & - & I_{total} \\ 2I_{45^\circ} & - & I_{total} \\ 2I^{RH}_{circ} & - & I_{total} \end{bmatrix} = \begin{bmatrix} I \\ Q \\ U \\ V \end{bmatrix} \tag{A.1}$$

The first element of the Stokes vector is the total intensity. The second element is the difference in intensity between passing the light through an ideal linear polarizer at 0° (horizontal) and one at 90° (vertical). The third element is the difference in intensity between passing the light through an ideal linear polarizer at 45° and one at −45°. The final element is the difference in the intensity between passing the light through an ideal right hand circular polarization blocker and a left handed polarization blocker. Another equivalent and often seen definition is also shown.

For monochromatic light, the Stokes vector elements can be related to the electric field components of the light,

$$\mathbf{E} = \mathbf{E_x} + \mathbf{E_y} = E_{0x}\cos(kz - \omega t + \delta_x)\hat{\mathbf{x}} + E_{0y}\cos(kz - \omega t + \delta_y)\hat{\mathbf{y}} \tag{A.2}$$

$$I = E_{0x}^2 + E_{0y}^2 \tag{A.3}$$

$$Q = E_{0x}^2 - E_{0y}^2 \tag{A.4}$$

$$U = 2E_{0x}E_{0y}\cos(\delta) \tag{A.5}$$

$$V = 2E_{0x}E_{0y}\sin(\delta) \tag{A.6}$$

where $\delta = \delta_y - \delta_x$.

The fractional polarizations, each < 1, can be determined for any Stokes vector as

$$V_{elliptical} = \sqrt{\frac{Q^2 + U^2 + V^2}{I^2}} \tag{A.7}$$

$$V_{linear} = \sqrt{\frac{Q^2 + U^2}{I^2}} \tag{A.8}$$

$$V_{circular} = \sqrt{\frac{V^2}{I^2}} \tag{A.9}$$

A.1.1 Common Stokes Vectors

Example polarization states include,

Table A.1: Table of common Stokes vectors

Polarization State	Stokes Vector	Polarization State	Stokes Vector
Linearly Polarized Horizontal, 0°	$\begin{bmatrix} 1 \\ 1 \\ 0 \\ 0 \end{bmatrix}$	Linearly Polarized Vertical, 90°	$\begin{bmatrix} 1 \\ -1 \\ 0 \\ 0 \end{bmatrix}$
Linearly Polarized +45°	$\begin{bmatrix} 1 \\ 0 \\ 1 \\ 0 \end{bmatrix}$	Linearly Polarized -45°	$\begin{bmatrix} 1 \\ 0 \\ -1 \\ 0 \end{bmatrix}$
Circularly Polarized Right handed	$\begin{bmatrix} 1 \\ 0 \\ 0 \\ 1 \end{bmatrix}$	Circularly Polarized Left handed	$\begin{bmatrix} 1 \\ 0 \\ 0 \\ -1 \end{bmatrix}$
Unpolarized, “natural light”	$\begin{bmatrix} 1 \\ 0 \\ 0 \\ 0 \end{bmatrix}$	Elliptically Polarized linear angle = 0° ellip. angle = 22.5°	$\begin{bmatrix} 4 \\ 2 \\ 0 \\ 2 \end{bmatrix}$

The linear polarization angle and ellipticity angle can be defined using the Stokes parameters,

$$\theta = \frac{1}{2}\arctan(U/Q) \tag{A.10}$$

$$\epsilon = \frac{1}{2}\arcsin\left(\frac{V}{\sqrt{Q^2+U^2+V^2}}\right) \tag{A.11}$$

where the ellipticity angle, ϵ, is the arctan of the minor over major radius of the ellipse, or $\tan(\epsilon) = b/a$.

A.2 Müeller Matrix representation for optical components

A.2.1 Polarization Optics

Hans Müeller devised a mathematical method to represent polarizing optics compatible with the usage of Stokes vectors in 1943 as a physics professor at MIT. Some common polarization optics are shown here.

Table A.2: Müeller matrix representations of common polarization optics

Optical Element	Müeller Matrix
Linear Polarizer, Horizontal	$\frac{1}{2}\begin{bmatrix} 1 & 1 & 0 & 0 \\ 1 & 1 & 0 & 0 \\ 0 & 0 & 0 & 0 \\ 0 & 0 & 0 & 0 \end{bmatrix}$
Linear Polarizer, Vertical	$\frac{1}{2}\begin{bmatrix} 1 & -1 & 0 & 0 \\ -1 & 1 & 0 & 0 \\ 0 & 0 & 0 & 0 \\ 0 & 0 & 0 & 0 \end{bmatrix}$
Quarter Waveplate, Fast axis horizontal	$\begin{bmatrix} 1 & 0 & 0 & 0 \\ 0 & 1 & 0 & 0 \\ 0 & 0 & 0 & 1 \\ 0 & 0 & -1 & 0 \end{bmatrix}$
Arbitrary Waveplate, Fast axis horizontal, retardance R	$\begin{bmatrix} 1 & 0 & 0 & 0 \\ 0 & 1 & 0 & 0 \\ 0 & 0 & \cos(R) & \sin(R) \\ 0 & 0 & -\sin(R) & \cos(R) \end{bmatrix}$
Circular Polarizer, Right handed	$\frac{1}{2}\begin{bmatrix} 1 & 0 & 0 & 1 \\ 0 & 0 & 0 & 0 \\ 0 & 0 & 0 & 0 \\ 1 & 0 & 0 & 1 \end{bmatrix}$

A.2.2 Rotation Matrices

It is often necessary to mathematically rotate Müeller matrices to represent the real geometry of optical components. To to this, one places rotation matrices on either side of a Müeller matrix to rotate the light into the optical axis of the optical component, operate on it with the Müeller matrix, and rotate it back.

The clockwise and counterclockwise rotational matrices are

$$R_{CW}(\chi) = \begin{bmatrix} 1 & 0 & 0 & 0 \\ 0 & \cos(2\chi) & \sin(2\chi) & 0 \\ 0 & -\sin(2\chi) & \cos(2\chi) & 0 \\ 0 & 0 & 0 & 1 \end{bmatrix} \tag{A.12}$$

$$R_{CCW}(\chi) = \begin{bmatrix} 1 & 0 & 0 & 0 \\ 0 & \cos(2\chi) & -\sin(2\chi) & 0 \\ 0 & \sin(2\chi) & \cos(2\chi) & 0 \\ 0 & 0 & 0 & 1 \end{bmatrix} \tag{A.13}$$

where χ is the rotation angle. The rotation matrices can also be used to describe the ideal rotator optical element, which simply rotates the linear components of incoming light.

For example, a quarter waveplate with the optical axis at 45° can be generated using,

$$\mathbf{W_{45^\circ}} = \mathbf{R_{CCW}(45^\circ)} \cdot \mathbf{W_{0^\circ}} \cdot \mathbf{R_{CW}(45^\circ)} \tag{A.14}$$

$$= \begin{bmatrix} 1 & 0 & 0 & 0 \\ 0 & 0 & 1 & 0 \\ 0 & -1 & 0 & 0 \\ 0 & 0 & 0 & 1 \end{bmatrix} \cdot \begin{bmatrix} 1 & 0 & 0 & 0 \\ 0 & 1 & 0 & 0 \\ 0 & 0 & 0 & 1 \\ 0 & 0 & -1 & 0 \end{bmatrix} \cdot \begin{bmatrix} 1 & 0 & 0 & 0 \\ 0 & 0 & -1 & 0 \\ 0 & 1 & 0 & 0 \\ 0 & 0 & 0 & 1 \end{bmatrix} \tag{A.15}$$

$$= \begin{bmatrix} 1 & 0 & 0 & 0 \\ 0 & 0 & 0 & -1 \\ 0 & 0 & 1 & 0 \\ 0 & 1 & 0 & 0 \end{bmatrix} \tag{A.16}$$

A.2.3 An Example Optical Train

To operate on a Stokes vector with multiple optical components in an optical train, order the matrices right to left such that the Stokes vector is operated on in the order of light passage through the components. An example of light passing through crossed polarizers will be used to illustrate this. Unpolarized light is passed through a horizontal linear polarizer, followed by a quarter waveplate at 45°, and finally a vertical linear polarizer. This optical setup is used is used in Section 4.2.4, but with the second polarizer rotating in time. In this optical train composed of ideal optics, note that the total intensity term, I, in the resultant Stokes vector is independent of the second polarizer angle. This property was used to determine the degree of circular polarization, Eqn. , of the circular polarizer used in the invessel calibration.

$$\mathbf{P_{90^\circ}} \cdot \mathbf{W_{45^\circ}} \cdot \mathbf{P_{0^\circ}} \cdot \mathbf{S} \tag{A.17}$$

$$\frac{1}{2}\begin{bmatrix} 1 & -1 & 0 & 0 \\ -1 & 1 & 0 & 0 \\ 0 & 0 & 0 & 0 \\ 0 & 0 & 0 & 0 \end{bmatrix} \cdot \begin{bmatrix} 1 & 0 & 0 & 0 \\ 0 & 0 & 0 & -1 \\ 0 & 0 & 1 & 0 \\ 0 & 1 & 0 & 0 \end{bmatrix} \cdot \frac{1}{2}\begin{bmatrix} 1 & 1 & 0 & 0 \\ 1 & 1 & 0 & 0 \\ 0 & 0 & 0 & 0 \\ 0 & 0 & 0 & 0 \end{bmatrix} \cdot \begin{bmatrix} 1 \\ 0 \\ 0 \\ 0 \end{bmatrix} \tag{A.18}$$

resulting in the expected Stokes vector showing vertical linearly polarized light,

$$\frac{1}{4}\begin{bmatrix} 1 \\ -1 \\ 0 \\ 0 \end{bmatrix} \tag{A.19}$$

A.2.4 A low retardance waveplate

Several elements in the MSE optics train can act like a waveplate with a small retardance (or equivalently a phase shift between s&p components) in an arbitrary orientation. An imperfect mirror reflection and stress induced birefringence can both have this behavior. This example shows the effect of such a waveplate, with optical axis oriented at χ relative to horizontal and retardance R, on a vertically polarized Stokes vector, $\mathbf{S_v}$.

$$\mathbf{S_v} = \begin{bmatrix} 1 \\ -1 \\ 0 \\ 0 \end{bmatrix} \tag{A.20}$$

$$\mathbf{S_{out}} = \mathbf{R_{CCW}}(\chi) \cdot \mathbf{W_{0^\circ}}[\mathbf{R}] \cdot \mathbf{R_{CW}}(\chi) \cdot \mathbf{S_v} \tag{A.21}$$

$$= \begin{bmatrix} 1 \\ -\cos^2(2\chi) - \sin^2(2\chi)\cos(R) \\ -\cos(2\chi)\sin(2\chi) + \cos(2\chi)\sin(2\chi)\cos(R) \\ -\sin(2\chi)sin(R) \end{bmatrix} \tag{A.22}$$

This result varies with both the waveplate angle and its retardance. when χ is a odd multiple of 45°, i.e. $(2n+1)\pi/4$, the Stokes vector reduces to (even multiples result in alignment of the waveplate axis with the polarization angle which results in no effect),

$$S_v = \begin{bmatrix} 1 \\ -\cos(R) \\ 0 \\ \sin(R) \end{bmatrix} \tag{A.23}$$

which has the effect of introducing a small circular component, but does not change the polarization angle for small values of retardance.

For arbitrary retardances and arbitrary orientations, linear angles calculated from

Eqn. A.22 are shown in Fig. A-1. Results show that a small linear angle change occurs. The effect increases for a given retardance from $\chi = 0°$, reaches a maximum at $\chi = 22.5°$, and decreases back to zero at $\chi = 45°$.

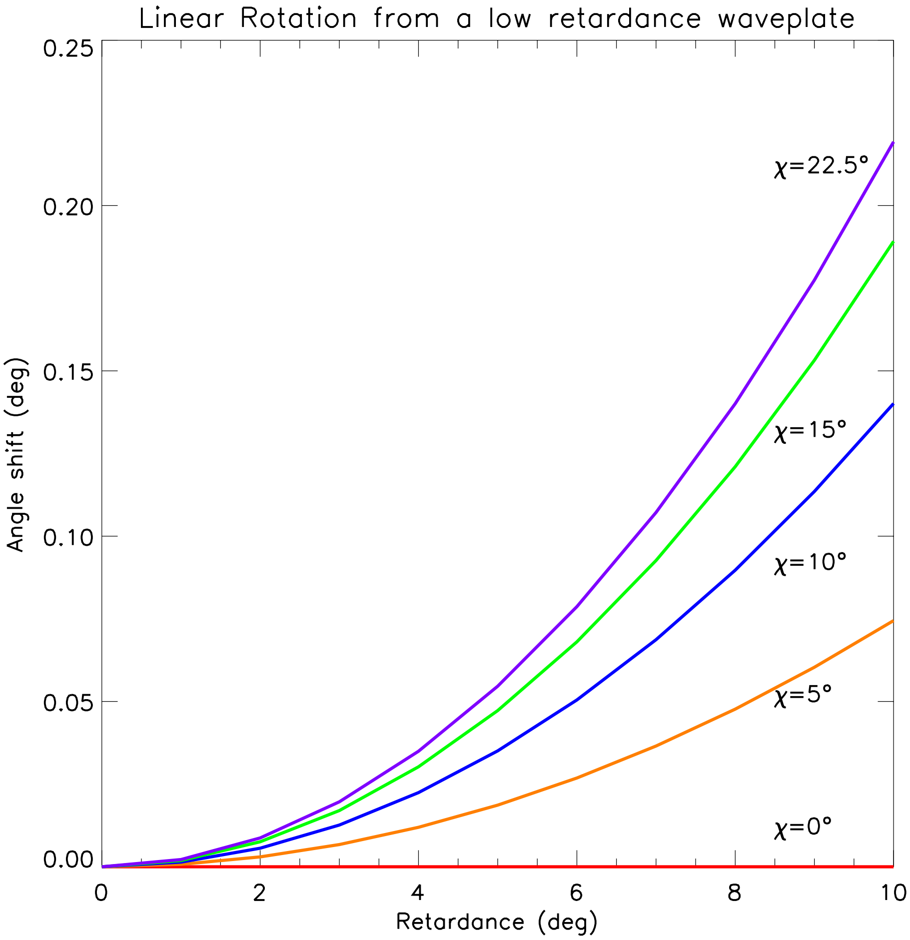

Figure A-1: Change in linear angle through a low retardance waveplate at arbitrary orientation.

Appendix B

Current interation of MSE invessel optics

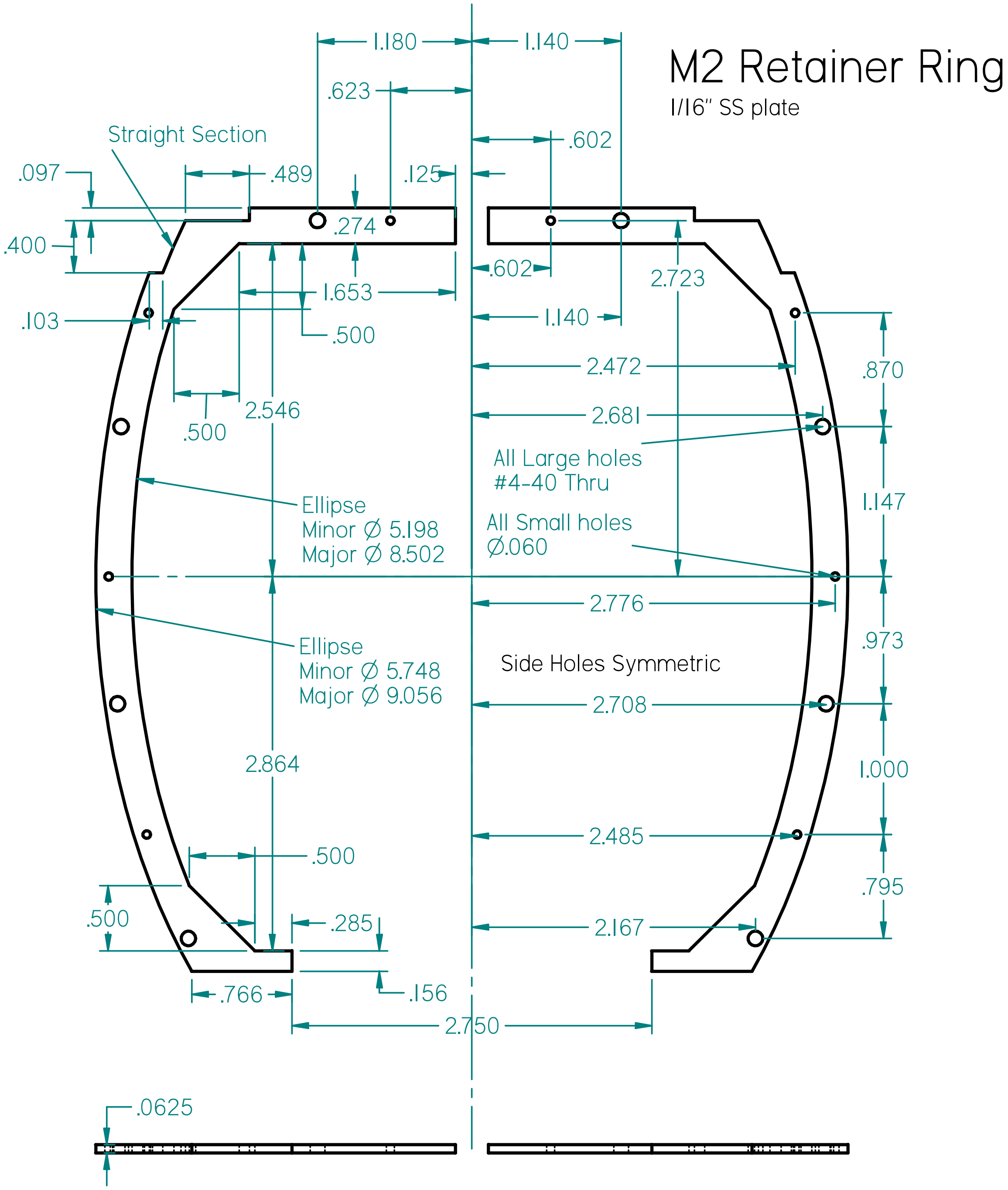

Figure B-1: M2 retainer. An identically shaped piece of 20 mil thick Teflon is used as a gasket under the metal retainer, mechanically trapped by the bolts.

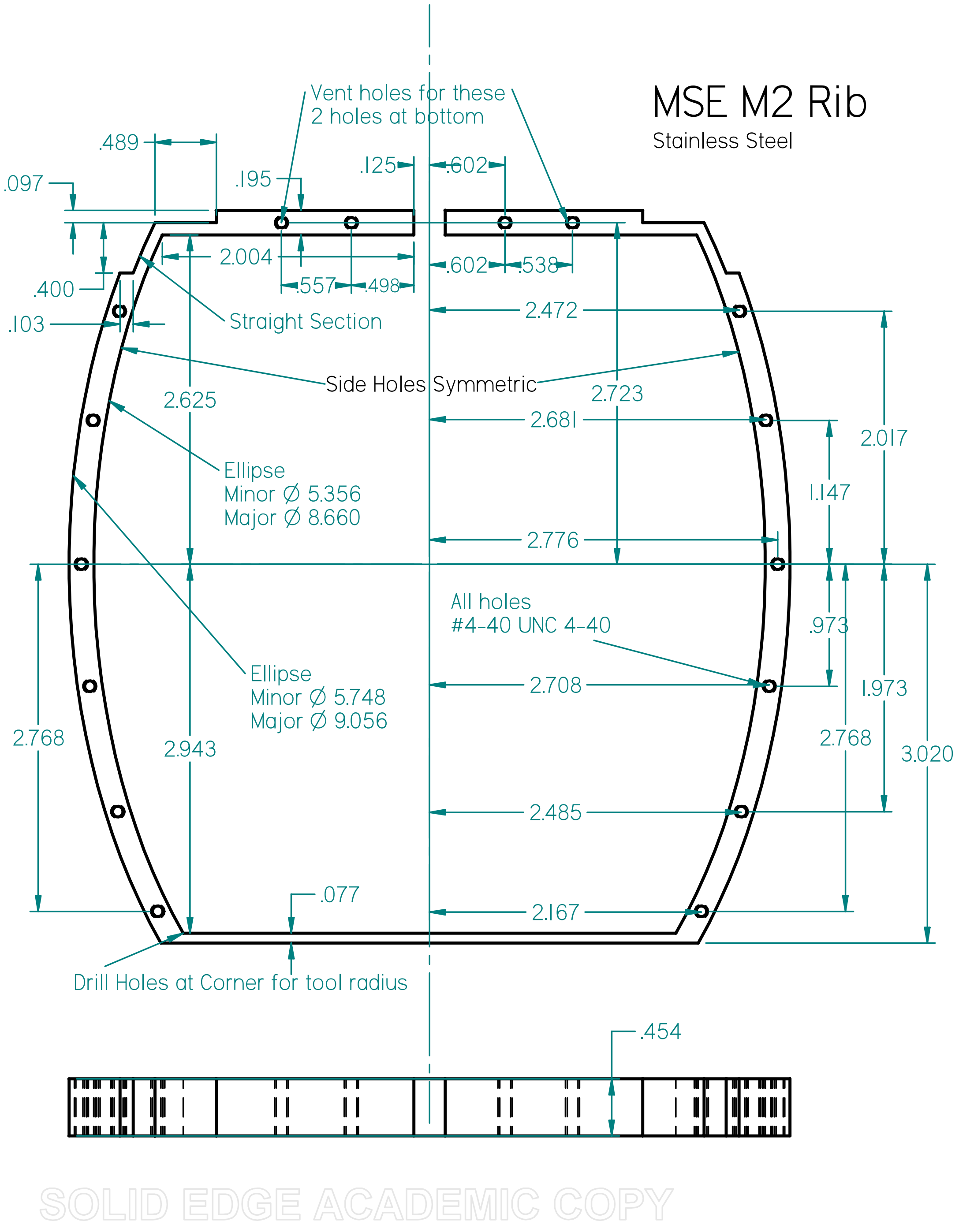

Figure B-2: M2 rib. A 20 mil strip of Teflon is placed between the inner wall of the rib and the mirror.

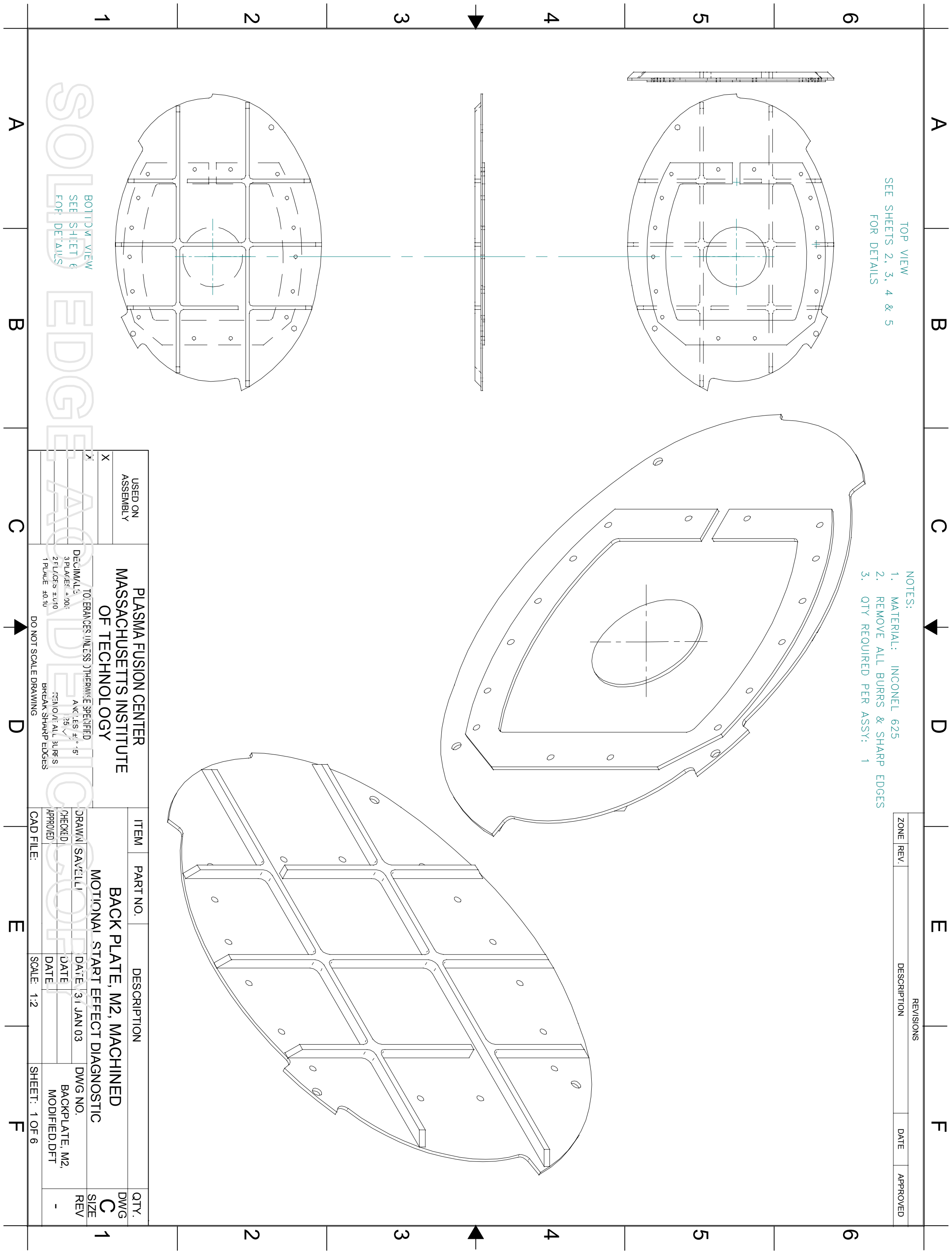

Figure B-3: M2 backplate. Constructed of Inconel with broken ribs on the back to increase stiffness but not increase eddy current loops.

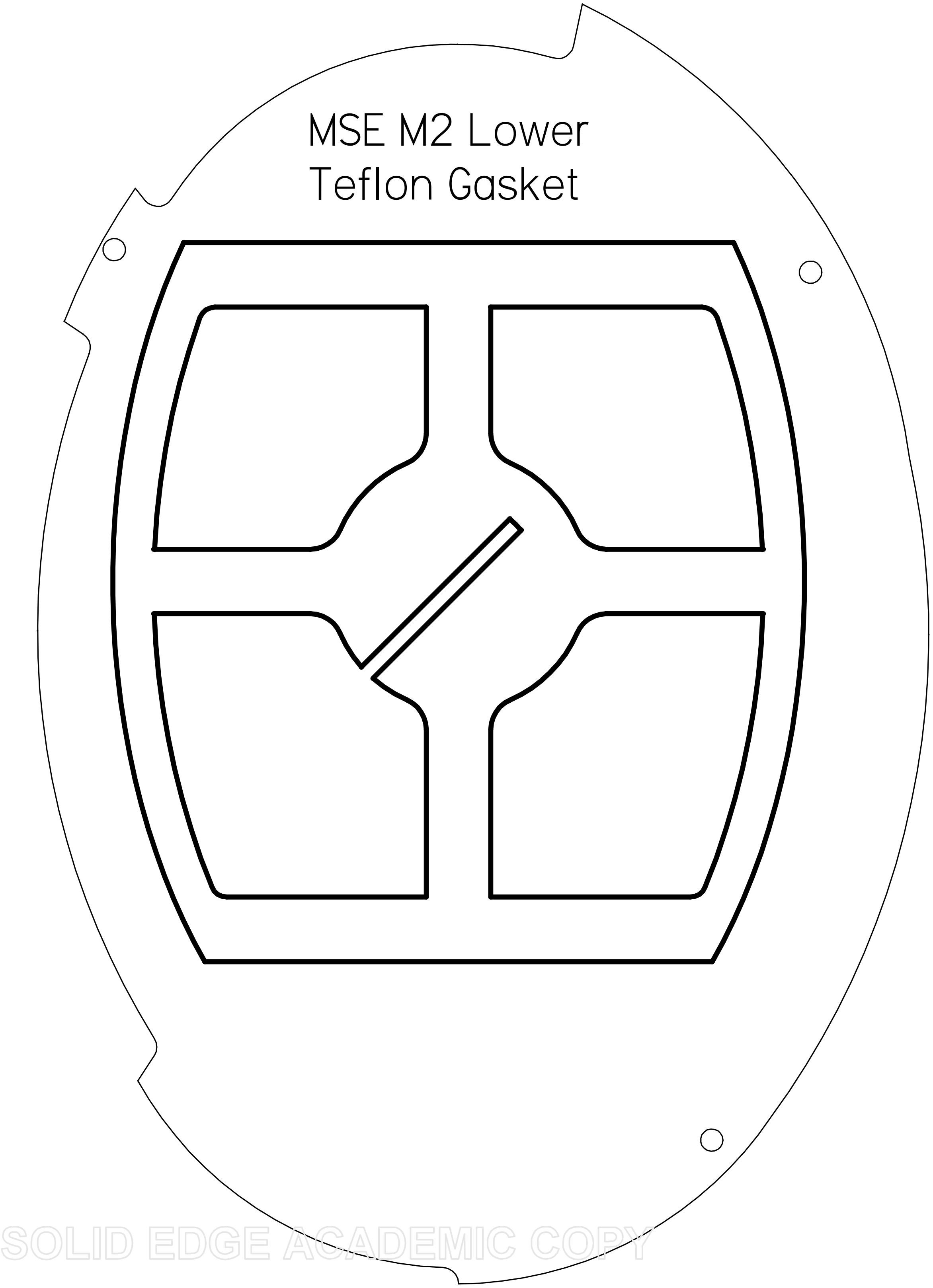

Figure B-4: M2 gasket shown by thick black lines. Cut from 30 mil Teflon sheet and placed under the mirror.

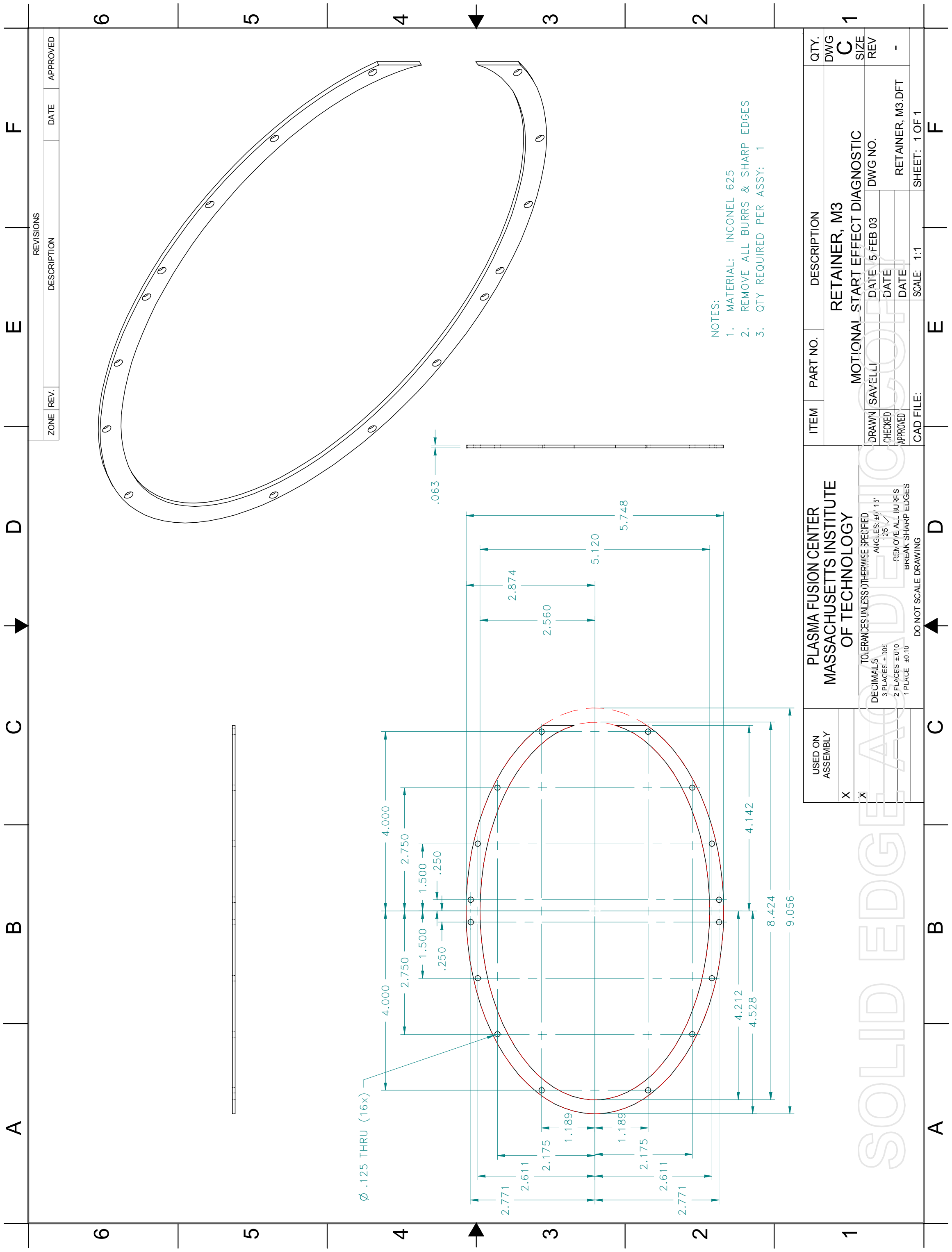

Figure B-5: M3 retainer. An identically shaped piece of 20 mil Teflon is used as a gasket under the metal retainer, mechanically trapped by the bolts.

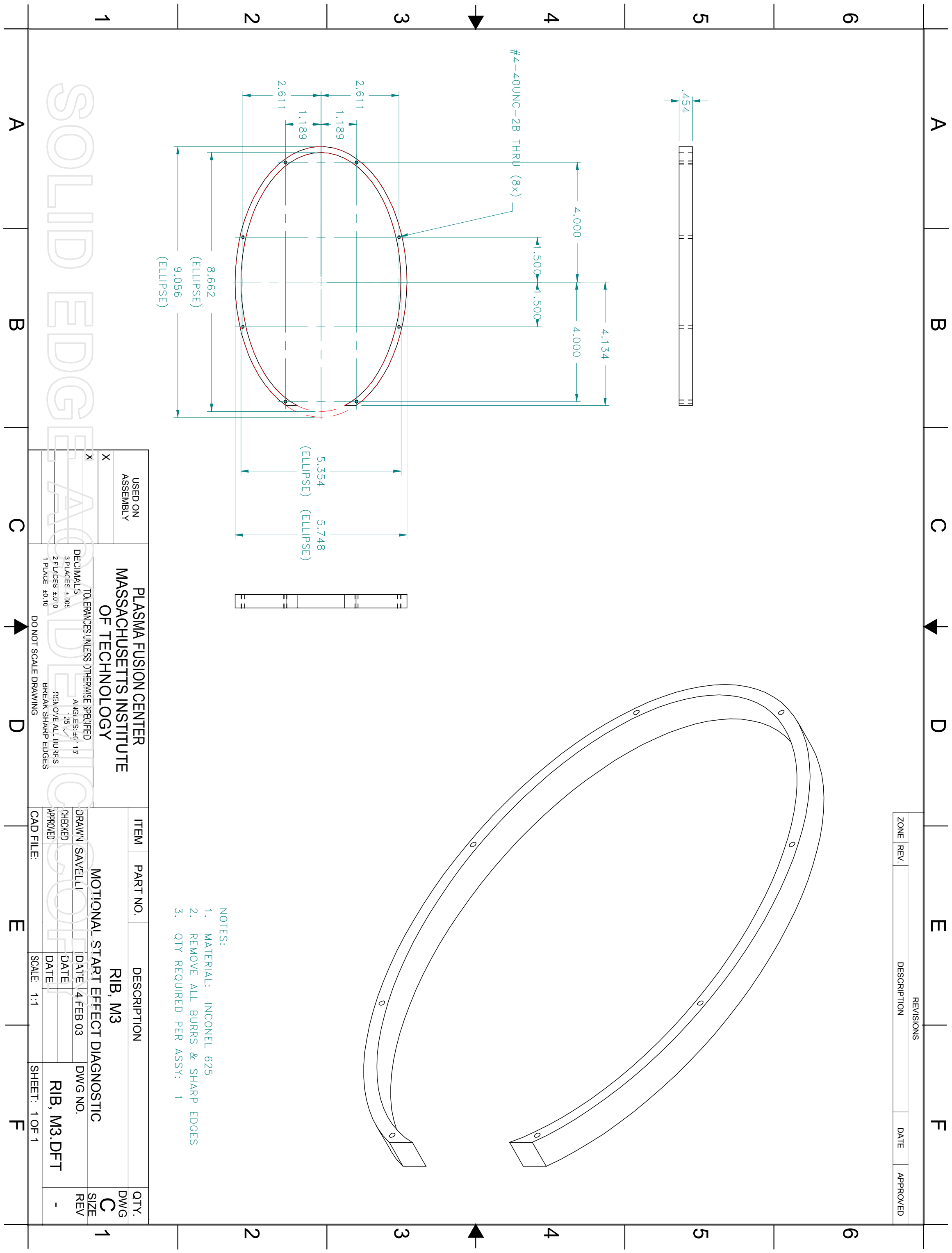

Figure B-6: M3 rib. A 20 mil strip of Teflon is placed between the inner wall of the rib and the mirror.

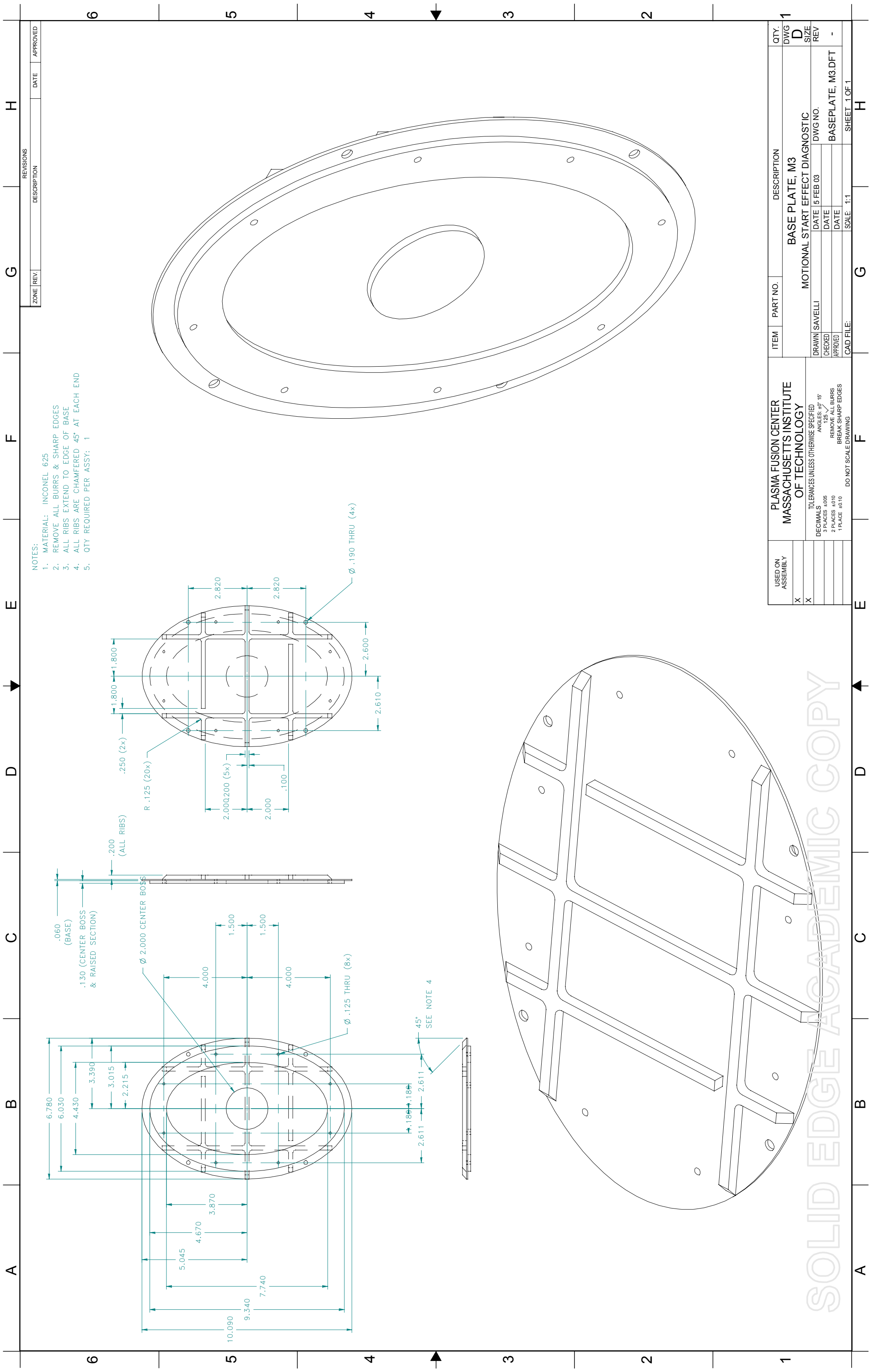

Figure B-7: M3 Backplate. Constructed of Inconel with broken ribs on the back to increase stiffness but not increase eddy current loops.

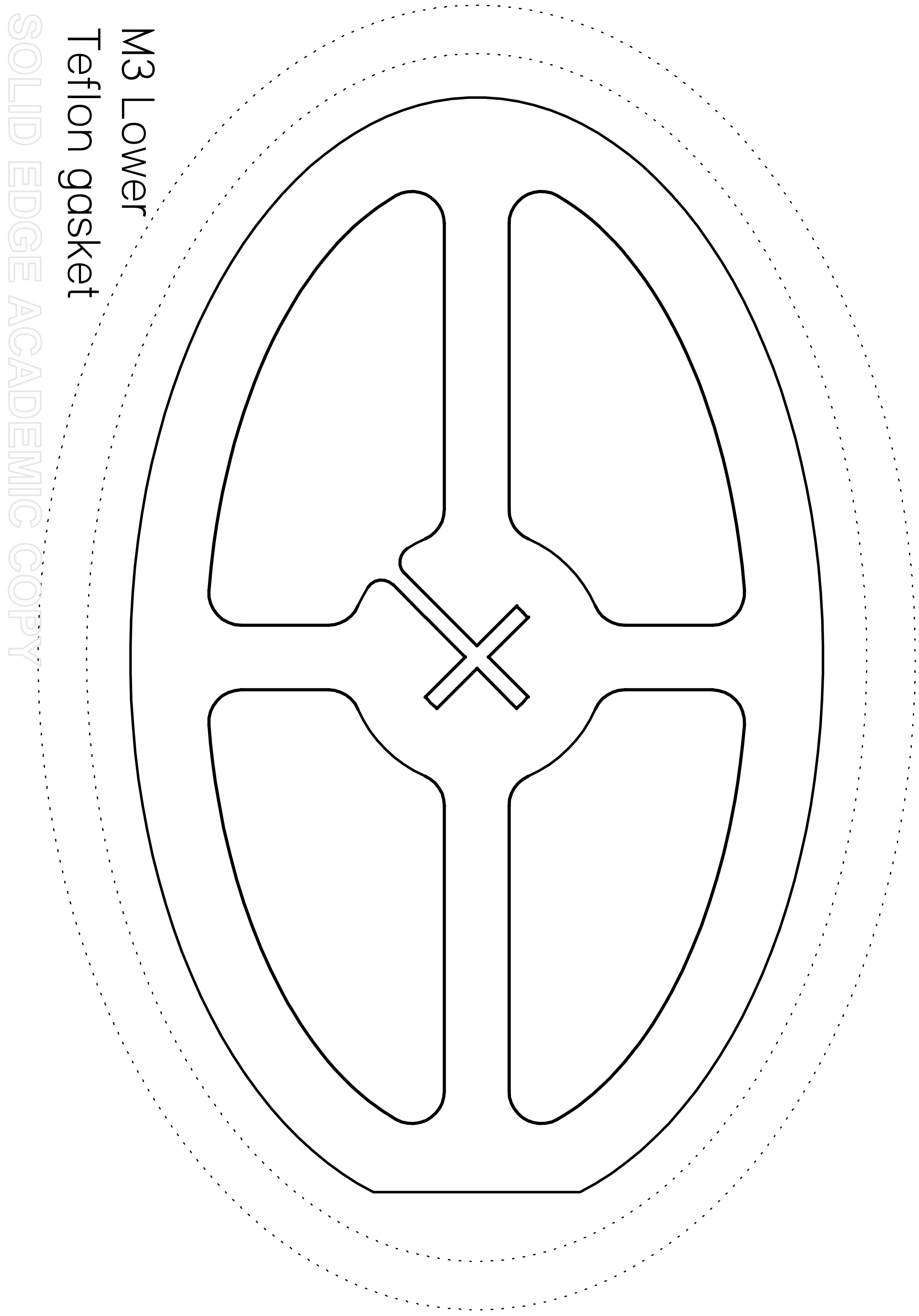

Figure B-8: M3 gasket shown by thick black lines. Cut from 30 mil Teflon sheet and placed under the mirror.

Bibliography

[1] John Wesson. *Tokamaks.* Oxford University Press, New York, NY, 1997.

[2] F. Levinton, S.H. Batha, M. Yamada, and M.C. Zarnstorff. *Phys. Fluids B*, 5(7):2554–2561, 1993.

[3] C.C. Petty, Y.R. Lin-Liu, T.C. Luce, M.A. Makowski, R. Prater, D.I. Schuster, H.E. St. John, and K.L. Wong. Localized measurements of electron cyclotron current drive using MSE spectroscopy on the DIII-D tokamak. *Nuclear Fusion*, 41(5):551 – 566, 2001.

[4] J.E. Menard, B.P. LeBlanc, J.R. Wilson, S.A. Sabbagh, D. Stutman, and D.W. Swain. Profile modifications resulting from early high-harmonic fast wave heating in NSTX. *AIP Conf. Proc.*, (595):158 – 61, 2001.

[5] A.A. Tuccillo and et.al. Recent heating and current drive results on JET. *AIP Conf. Proc.*, (595):209 – 16, 2001.

[6] N.C. Hawkes, B.C. Stratton, T. Tala, C.D. Challis, G. Conway, R. DeAngelis, C. Giroud, J. Hobirk, E. Joffrin, P. Lomas, P. Lotte, J. Mailloux, D. Mazon, E. Rachlew, S. Reyes-Cortes, E. Solano, and K.-D. Zastrow. Observation of zero current density in the core of JET discharges with lower hybrid heating and current drive. *Phys. Rev. Let.*, 87(11):115001, 2001.

[7] T.C. Luce, C.C. Petty, D.I. Schuster, and M.A. Makowski. Determination of the electron cyclotron current drive profile. *Fusi. Eng. and Design*, 53:337 – 42, 2001.

[8] R. Kaita and et. al. Current and pressure profile modification experiments with lower hybrid current drive and ion bernstein wave heating in pbx-m. *Plasma Physics and Controlled Nuclear Fusion Research 1992. Proceedings of the 14th International Conference on Plasma Physics and Controlled Nuclear Fusion Research*, pages 635 – 48, 1993.

[9] F. Paoletti and et. al. Motional stark effect plasma equilibria during LHCD experiments on PBX-M. *AIP Conf. Proc.*, (289):131 – 4, 1994.

[10] P.M. Ryan, D.W. Swain, J.R. Wilson, J.C. Hosea, B.P. LeBlanc, S. Bernabei, P. Bonoli, M.D. Carter, E.F. Jaeger, S. Kaye, T.K. Mau, C.K. Phillips, D.A. Rasmussen, and J.B. Wilgen. High harmonic fast wave current drive experiments on NSTX. *AIP Conf. Proc.*, (694):209 – 12, 2003.

[11] O. Naito, Z. Cui, S. Ide, T. Suzuki, T. Oikawa, M. Seki, T. Hatae, T. Fujita, T. Kondoh, H. Shirai, Y. Ikeda, and K. Ushigusa. Evolution of lower-hybrid-driven current during the formation of an internal transport barrier. 89(6):065001, 2002.

[12] Y. Ikeda, S. Ide, T. Suzuki, A. Kasugai, K. Takahashi, K. Kajiwara, A. Isayama, T. Oikawa, K. Hamamatsu, Y. Kamada, T. Fujita, K. Sakamoto, S. Moriyama, M. Seki, R. Yoshino, T. Imai, K. Ushigusa, and T. Fujii. ECRF experiments for local heating and current drive by fundamental o-mode launch from the low-field side on JT-60U. *Nucl. Fusion*, 42(4):375 – 82, 2002.

[13] Yu.F. Baranov, X. Garbet, N.C. Hawkes, B. Alper, R. Barnsley, C.D. Challis, C. Giroud, E. Joffrin, M. Mantsinen, F. Orsitto, V. Parail, and S.E. Sharapov. On the link between the q-profile and internal transport barriers. *Plasma Physics and Controlled Fusion*, 46(8):1181 – 1196, 2004.

[14] T. Fujita, T. Fukuda, Y. Sakamoto, S. Ide, T. Suzuki, H. Takenaga, K. Ida, H. Idei, T. Shimozuma, A. Fujisawa, S. Ohdachi, and K. Toi. Formation conditions for electron internal transport barriers in JT-60U plasmas. *Plasma Physics and Controlled Fusion*, 46(5 SUPPL A):35–43, 2004.

[15] T. Oikawa, A. Isayama, T. Fujita, T. Suzuki, T. Tuda, and G. Kurita. Evolution of the current density profile associated with magnetic island formation in JT-60U. *Phys. Rev. Lett.*, 94(12):125003 – 1, 2005.

[16] R.J. Jayakumar, M.A. Makowski, S.L. Allen, M.E. Austin, A.M. Garofalo, R.J. LaHaye, H. Reimerdes, and T.L. Rhodes. Observation of magnetohydrodynamic instability and direct measurement of local perturbed magnetic field using motional stark effect diagnostic. *Rev. Sci. Inst.*, 75(9):2995 – 3001, 2004.

[17] A.A. Ivanov, P.A. Bagryansky, P.P. Deichuli, S.A. Korepanov, A.A. Lizunov, S.V. Murakhtin, V.Ya. Savkin, G. Fiksel, and D. Den Hartog. Local measurements of plasma beta in GDT using MSE diagnostic. *Fusion Sci. Tech.*, 43(1T):265 – 7, 2003.

[18] S.P. Hirshman, D.K. Lee, F.M. Levinton, S.H. Batha, M. Okabayashi, and R.M. Wieland. Equilibrium reconstruction of the safety factor profile in tokamaks from motional stark effect data. *Phys. Plasmas*, 1(7):2277 – 90, 1994.

[19] F.M. Levinton, S.H. Batha, M. Yamada, L. Zakharov, and M.C. Zarnstorff. Sawtooth studies with q-profile measurements on TFTR. *Rev. Sci. Instrum.*, 66(1):372, 1995.

[20] S. Bernabei, R.V. Budny, E.D. Fredrickson, N.N. Gorelenkov, J.C. Hosea, C.K. Phillips, R.B. White, J.R. Wilson, C.C. Petty, R.I. Pinsker, R.W. Harvey, and A.P. Smirnov. The combined effect of epms and taes on energetic ion confinement and sawtooth stabilization. *Nuclear Fusion*, 41(5):513 – 518, 2001.

[21] M. Yamada, F.M. Levinton, N. Pomphrey, R. Budny, J. Manickam, and Y. Nagayama. Investigation of magnetic reconnection during a sawtooth crash in a high-temperature tokamak plasma. *Phys. Plasmas*, 1(10):3269 – 76, 1994.

[22] B.W. Rice, K.H. Burrell, L.L. Lao, and Y.R. Lin-Liu. Direct measurement of the radial electric field in tokamak plasmas using the stark effect. *Phys. Rev. Lett.*, 79(14):2694 – 7, 1997.

[23] B.W. Rice, D.G. Nilson, K.H. Burrell, and L.L. Lao. Simultaneous measurement of q and E_r profiles using the motional stark effect in high-performance DIII-D plasmas (invited). *Rev. Sci. Inst.*, 70(1 II):815 – 820, 1999.

[24] B.W. Rice, K.H. Burrell, and L.L. Lao. Effect of plasma radial electric field on motional stark effect measurements and equilibrium reconstruction. *Nucl. Fusion*, 37(4):517 – 22, 1997.

[25] S.R. Cortes, N.C. Hawkes, P. Lotte, C. Fenzi, B.C. Stratton, J. Hobirk, R. De Angelis, F. Orsitto, and C.A.F. Varandas. Measurement of the plasma radial electric field by the motional stark effect diagnostic on JET plasmas. *Rev. Sci. Inst.*, 74(3):1596 – 600, 2003.

[26] J. Hobirk, N.C. Hawkes, P.J. McCarthy, D. Merkl, and R.C. Wolf. Measurements of the poloidal magnetic and radial electric field profiles in ASDEX upgrade and JET. *Int. Conf. on Adv. Diag. for Magnetic and Inertial Fusion*, pages 197 – 204, 2002.

[27] A.J.H. Donne. Diagnostics for current density and radial electric field measurements: overview and recent trends. *Plas. Phys. Cont. Fusion*, 44(12B):137 – 58, 2002.

[28] F. Levinton, G.M. Gammel, R. Kaita, H.W. Kugel, and D.W. Roberts. *Rev. Sci. Instrum.*, 61(10):2914–2919, 1990.

[29] N.C. Hawkes and et al. *Rev. Sci. Inst.*, 70(1):894, 1999.

[30] D. Wroblewski, K.H. Burrell, and et al. *Rev. Sci. Inst.*, 61(11):3552, 1990.

[31] T. Fujita, H. Kuko, N. Isei, and K. Ushigusa. *Fus. Eng. and Design*, 34-35:289, 1997.

[32] Wolfram Research. WebMathematica explorations: Hydrogen atom (http://library.wolfram.com/webMathematica/Physics/Hydrogen.jsp), 2005.

[33] E. Schrödinger. *Ann. der Physics*, 80:457, 1926.

[34] Epstein. *Phys. Rev.*, 28:695, 1926.

[35] E.U. Condon and G.H. Shortley. *The Theory of Atomic Spectra*. University Press, Cambridge, New York, N.Y., 1951.

[36] H. Bethe and E. Salpeter. *Quantum Mechanics of One and Two-Electron Systems*. Academic Press Inc., New York, N.Y., 1957.

[37] R. Isler. *Phys. Rev. A*, 14:1015, 1976.

[38] C. Breton, C. Michelis, and et al. *J. Phys. B*, 13:1703, 1980.

[39] E.K.Souw and J.Uhlenbusch. *Physica B & C*, 122:353, 1983.

[40] I. H. Hutchinson. Private Memoranda, October 2004.

[41] F. Levinton. *AIP Conference Proceedings*, 381:143–150, 1996.

[42] R. Jaspers, B.S.Q. Elzendoorn, J.H. Donne, and T. Soetens. *Rev. Sci. Inst.*, 72(1):1018, 2001.

[43] M. Glass-Maujean et. al. *J. of Phys. B*, 33:4593, 2000.

[44] S. Lauer et. al. *J. of Phys. B*, 31:3049, 1998.

[45] E. Flemming and et. al. *J. of Chem. Phys.*, 103:4090, 1995.

[46] H. Weissmann, W. Hartmann, and D.S. Burch. *Z. Phys.*, D7:119, 1987.

[47] I D Willams, J Geddes, and H B Gilbody. *J. Phys. B*, 15:1377, 1982.

[48] R. Fonck, D. S. Darrow, and K.P. Jaehnig. *Phys. Rev. A*, 29:3288, 1984.

[49] N. Bretz, R. Bravenec, H. Yuh, and et al. *Rev. Sci. Inst.*, 72(1):1012, 2001.

[50] D.L. Simon, N.L. Bretz, E. Marmar, R. Bravenec, and R.F. Parsells. Optical and mechanical design of c-mod motional stark effect diagnostic. pages 349 – 351, 1999.

[51] Hamamatsu Photonics K.K. Multiplier tube r943-02 specification sheet. Technical report, 1997.

[52] G. Arfken. *Mathematical Methods for Physicists.* Academic Press, Inc., San Diego, CA, 1985.

[53] Baoliang Wang. Useful aperture of PEMS. Technical report, 1997.

[54] L C Marquet. *J. of the Optical Soc. of America*, 57(7):878, 1967.

[55] I. H. Hutchinson. Principles of plasma diagnostics, 2004.

[56] R.S. Freund and J.A. Schiavone. *J. Phys. Chem. Ref. Data*, 14(1):235–383, 1985.

[57] R. Jost and M. Lombard. *Molecular Physics*, 37(5):1605–1620, 1979.

[58] G.H. Dieke and F.T. Byrne. *Phys. Rev.*, 92(1):81–88, 1953.

[59] Olivier Lubin and Olivier Heuzé. Modelling of stress-induced birefringence in vacuum barrier lenses. *Pure and Applied Optics: Journal of the European Optical Society Part A*, 7(4):699–708, 1998.

[60] P. Benassi, V. Mazzacurati, G. Ruocco, and G. Signorelli. Elasto-optic constants in silicate glasses: experiment and theory. *Phys. Rev. B, Condens. Matter*, 48(9):5987 – 96, 1 Sept. 1993.

[61] William Primak and Daniel Post. Photoelastic constants of vitreous silica and its elastic coefficient of refractive index. *Journal of Applied Physics*, 30(5):779–788, 1959.

[62] John R. Taylor. *An Introduction to Error Analysis, 2nd Ed.* University Science Books., Sausalito, CA, 1982.

[63] F.M. Levinton, S.H. Batha, and M.C. Zarnstorff. Calibration of the upgraded motional stark effect diagnostic on TFTR. *Rev. Sci. Inst.*, 68(1):926 – 9, 1997.

[64] I. H. Hutchinson *et al.* Edge transport barrier phenomena in Alcator C-Mod. *Plas. Phys. and Cont. Fusion*, 41(3A):A609–A616, 1999.

[65] R. McDermott, S. Scott, H. Yuh, and W.Rowan. *Bulletin of the APS*, 49(8):74, 2004.

[66] M. Sampsell and *et. al. Bulletin of the APS*, 47(9):235, 2002.